High-resolution speleothem record of climate variability during the late Pleistocene from Spring Valley Caverns, Minnesota

A THESIS
SUBMITTED TO THE FACULTY OF THE GRADUATE SCHOOL
OF THE UNIVERSITY OF MINNESOTA
BY

Julia Anne Nissen

IN PARTIAL FULFILLMENT OF THE REQUIREMENTS
FOR THE DEGREE OF
MASTER OF SCIENCE

R. LAWRENCE EDWARDS

February, 2018

© Julia Anne Nissen 2018
ALL RIGHTS RESERVED

Acknowledgements

I would like to thank those who have made this research possible. First, to my advisor Larry Edwards, for his guidance and support throughout my time at the University of Minnesota. I would also like to thank my committee members Calvin Alexander and Josh Feinberg, as well as prior committee members Andy Wickert and Katsumi Matsumoto, for their mentorship.

I would like to acknowledge John Ackerman for his generosity in allowing me to work in Spring Valley Caverns and thank him for his continued support for scientific research at the University of Minnesota. This work would not have been possible without his contributions. Additionally, thanks to Martin Larsen and other members of the Minnesota Caving Club for their support during caving trips. Their dedication to caving ensures the preservation of these amazing sites.

This research was made possible through the work of staff at the Characterization Facility at the University of Minnesota, the University Imaging Centers, and the stable isotope laboratory at Xi'an University. A big thanks to Javier Garcia Barriocanal and Guillermo Marques for their help and patience.

I cannot thank the current and former individuals at the Isotope Lab enough for their assistance and camaraderie during my time at the University of Minnesota. To Yanbin Lu and Julie Retrum for their help in introducing me to laboratory procedures. To Mellissa Warner for her impressive work in *Python*, which inspired me to find new ways of improving data processing using programming. To Pu Zhang, who works tirelessly to ensure the lab is running smoothly and is never too busy to answer questions. To Zongyi Wang for his help in writing the *Python* programs. To Mathieu Pythoud for being the best office mate, and to Akemi Berry, I cannot imagine these past few years without you.

Dedication

This work is dedicated to those who supported me unconditionally throughout its development. To my amazing parents, to my brother and sister-in-law, and most of all, to Laura.

Abstract

Understanding how the Earth's oceanic and atmospheric systems responded to abrupt climatic forcings in the past is crucial in determining potential effects of anthropogenic climate change. This is of particular importance in the mid-continental United States, an agricultural hub that produces much of the world's corn and soybeans. High resolution paleorecords in the region remain sparse, restricting the predictability of global climate models and limiting our knowledge of atmospheric teleconnections across North America.

This study analyses the growth and stable isotopic concentration of late Pleistocene speleothem samples from Spring Valley Caverns, located in SE Minnesota. Timing of growth for six samples was determined using ^{230}Th dating and confocal microscopy, recording ages between 114 - 29 ky BP. This places all sample growth within the last glacial period. Sample growth largely correlates with warm conditions in the North Atlantic, indicating elevated temperature and moisture availability. Growth during MIS4 may be due to enhanced anticyclonic activity over the Laurentide Ice Sheet, resulting in anomalous southerly moisture transport.

High resolution stable isotope analysis was completed for two samples, showing both long term trends and short term variability. Samples show a steady decrease in δ^{13}C values from 104 - 29 ky BP, suggesting a transition from C4 to C3 dominated ecosystems consistent with global cooling. However, δ^{18}O values climb steadily throughout this period. This is indicative of drier conditions and an increase in Gulf of Mexico sourced moisture in the region. Short term variability from 64 - 44 ky BP shows impressive correlation to global paleorecords. North Atlantic cold events are shown as an increase in δ^{18}O values, and North Atlantic warm events as a decrease δ^{18}O values. As δ^{18}O and δ^{13}C generally covary during this period, elevated δ^{18}O values suggest regional aridity. The transport of Gulf of Mexico summer moisture into the region appears significantly susceptible to changes in North Atlantic climate, most likely through large scale atmospheric systems such as the North Atlantic Oscillation and Pacific-North America teleconnection.

The results of these records agree with a previous study of Spring Valley Caverns from the Holocene (Dasgupta, 2008). This signifies that large scale dynamics present during the last glacial period continue to affect regional climate, and thus these results may prove useful not only in improving our understanding of abrupt climate events during the late Pleistocene

but in predicting impacts on the region from anthropogenic warming.

Executive Summary

Speleothem samples from Spring Valley Caverns were studied in order to determine the primary drivers behind long and short term climate variability in SE Minnesota during the last glacial period. While a study looking at Holocene climate in Spring Valley indicated that the site experienced effects of abrupt North Atlantic events, preliminary site data from the last glacial period were inconclusive (Dasgupta, 2008, MacKinney et al., 2013, Shapiro, 2007).

In Chapter 1, we introduce specifics of long and short term climate variability during the late Pleistocene and discuss advantages and primary methods of speleothem research. While glacial-interglacial cycles are largely paced by orbital forcing, frequent changes in thermohaline circulation resulted in abrupt climate change throughout the last glacial period. The effects of these events are present in paleorecords globally, but the methods of transmission remain unknown in certain regions. For instance, while late Pleistocene sites in western North America are largely controlled by variation in Pacific-sourced winter precipitation and sites along the Gulf Coast are dominated by changes in Atlantic-sourced summer precipitation, records in the mid-continent are both sparse and inconclusive. Speleothems are invaluable as paleorecords as they are able to be dated at high resolution using ^{230}Th and confocal microscopy. Additionally, they retain signatures of oxygen and carbon isotopic variability inherited from changes in hydrological and environmental conditions, and thus can be used to make paleoclimate interpretations.

Chapter 2 discusses the modern climate in SE Minnesota, in order to better understand how conditions may have changed during the last glacial period. Southern Minnesota currently receives much of its precipitation during the summer months, and moisture is largely derived from Gulf of Mexico (D. Baker et al., 1978, Simpkins, 1995). When compared to large scale sea surface temperature patterns in the Atlantic and Pacific basins, higher than average temperatures in the Atlantic appear to contribute to a regional decrease in annual precipitation, while temperature anomalies in the Pacific do not appear to have a clear correlation to precipitation amount. Stronger correlations occur between regional precipitation amount and large scale atmospheric patterns. A damping of the ridge-trough system across North America during the winter months, characteristic of a negative Pacific-North American (PNA) teleconnection index, is associated with a strengthening of the Great Plains Low Level Jet and an increase in southerly summer moisture flow and regional precipitation (Higgins et al., 1997). Additionally a weakening of pressure systems across the North Atlantic, characteristic of a negative North Atlantic Oscillation (NAO) index, is also associated with higher than average summer precipitation. Modern data from the Twin

Cities shows that the oxygen isotopic signature of precipitation is positively correlated to temperature, as is modern calcite at Spring Valley Caverns (Mohr, 2000, Dasgupta, 2008). However, a calcite Holocene records indicates that temperature is likely not the primary driver behind oxygen isotopic variability over time (Dasgupta, 2008).

Original research is presented in Chapter 3. Six samples were dated by ^{230}Th and confocal microscopy, and two samples were analyzed for stable isotopic variation. Dating and stable isotope sampling resolution was significantly improved on samples SVC06 and SVC05, and a method of automatic band counting resulted in improved estimates for the duration of SVC05 growth phases. Growth phases largely correlate to Greenland interstadial events, indicating an increase in regional temperature and moisture availability. Additionally, four samples experienced the start of a growth phase in the middle of MIS4. This is most likely due to an increase in anti-cyclonic activity over a heightened Laurentide ice sheet in the NE. This activity may have strengthened southerly summer flow, increasing available summer moisture to the region. Stable isotope values show an increase in δ^{18}O and a decrease in δ^{13}C values throughout the last glacial period. In order to achieve higher δ^{18}O values at a lower annual temperature compared to modern, SE Minnesota would either need to experience an increase in fraction of moisture remaining during moisture trajectory or an increase in proportion of Gulf of Mexico moisture. Based off models and proxy records, it seems likely that both rain out and moisture source are affecting the oxygen isotopic signature in SE Minnesota throughout the last glacial period. Additionally, abrupt climate changes correlating to global paleorecords are identifiable in the δ^{18}O record of SVC06. Greenland interstadials and Heinrich stadials correlate to lower and higher δ^{18}O values at Spring Valley, respectively. Assuming a dominant Gulf of Mexico moisture source, this indicates Spring Valley is largely recording regional aridity, and appears to negatively correlate to records in the southwest United States.

If regional precipitation has a significantly higher δ^{18}O signature during the last glacial period than previously thought, it is possible that Mississippi-drained meltwater estimates during the last deglaciation have been underestimated. Models that used varying end member values for both the δ^{18}O of melt and of regional precipitation resulted in estimates of southerly-routed Laurentide sea level rise contribution that were up to 3.3m higher than previous estimates (Carlson, 2009).

Contents

List of Tables

List of Figures

Chapter 1

Introduction

1.1 Late Quaternary Climate Change in North America

1.1.1 Introduction

The Quaternary was marked by both long term and abrupt climate change. The Quaternary began with the formation of permanent continental ice sheets around 2.75 mya, due to long term cooling throughout the mid-Cenozoic (Clark, 1999, Ruddiman, 2010). Since then Earth has experienced numerous glacial-interglacial cycles, driven by orbital changes. First identified by Milutin Milankovitch, periodicities in the eccentricity, obliquity, and precession of Earth's orbit result in regular changes to Northern Hemisphere summer insolation (NHSI, Milankovitch, 1930). In the 1950s, it was discovered that the δ^{18}O signal of benthic foraminifera from deep sea sediment illustrated remarkable synchronicity with the solar insolation curve (Emiliani, 1955). It was later shown that much of the deep water signal was driven by continental ice volume, which appeared to be responding linearly to changes in obliquity and precession (Imbrie et al., 1984).

Through the benthic record it was also shown that Earth's system responds non-linearly through oceanic-atmospheric feedback to changes in eccentricity, resulting in gradual glaciations and rapid deglaciations every ≈100 ky (Shackleton, 2000). These orbital cycles every ≈ 20, ≈ 40, and ≈ 100 ky result in regular changes not only in foraminifera δ^{18}O and global ice volume, but sea level, surface and deep sea temperature, atmospheric carbon dioxide concentrations, atmospheric and ice δ^{18}O, and the location of atmospheric circulation features (Mesolella et al., 1969, Hastings et al., 1998, Emiliani, 1955, Chappell et al., 1986, Lorius et al., 1988, Bender et al., 1985, Dansgaard et al., 1993, Lorius et al., 1985, Y. Wang et al., 2001).

In addition to the climatic responses to solar insolation, Earth frequently experienced abrupt changes in oceanic and atmospheric processes. First identified in the Greenland record, abrupt changes in the δ^{18}O of ice occurred throughout the last glaciation (Dansgaard et al., 1993). These changes in δ^{18}O values were determined to be temperature oscillations, with 24 anomalous warm periods dubbed Dansgaard-Oeschger (DO) events. These saw-tooth oscillations were divided in Greenland into warm phases (DO events/interstadials) and cold periods (stadials). Progressive cycles of Greenland temperature oscillations would result in gradually cooler stadials, until an abrupt warming event restarted the cycle (Bond et al., 1993). These were seen not only in Greenland air temperatures, but North Atlantic sea surface temperatures.

In 1988, layers of ice rafted debris were found in deep-sea sediment cores from the North Atlantic (Heinrich, 1988). Six carbonate-rich events found in marine cores throughout the North Atlantic were attributed to large iceberg armadas largely originating from the area surrounding the Labrador Sea (Bond et al., 1992, Hemming et al., 1998). These detrital layers- dubbed Heinrich events- occurred at the end of cooling cycles, during periods of extremely low temperature in the North Atlantic. Whereas Greenland interstadials occur typically every few thousand years, Heinrich events occur every $\approx$7 ky (Stocker, 2000). Figure 1.1 illustrates the correlation between North Atlantic temperature events, ice rafted debris, and cooling cycles. North Atlantic air temperature is indicated by the Greenland δ^{18}O record, and North Atlantic sea surface temperature by the dominance of cold water planktonic foraminifera. Heinrich events are located at the end of cooling cycles, and associated with low sea surface temperature in the North Atlantic and high δ^{18}O values, indicating extensive global ice cover.

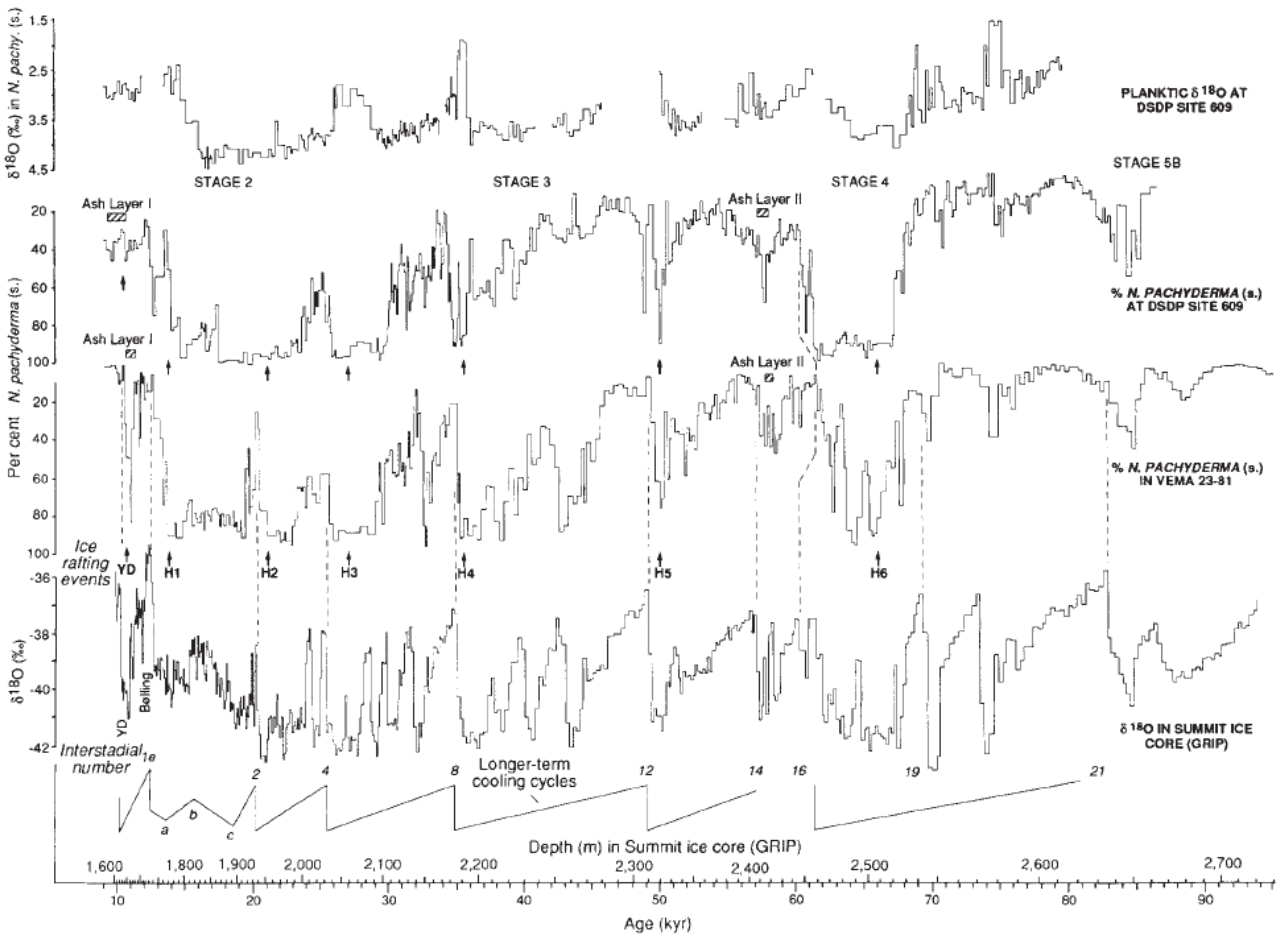

Figure 1.1: Data from North Atlantic paleorecords, showing correlation between Greenland air and sea temperature, global ice volume, and ice rafting events. The planktonic δ^{18}O value is negatively correlated to amount of global ice volume, whereas the δ^{18}O of GRIP Greenland ice core is positively correlated to temperature. The two cores recording percentage of planktonic foraminifera *N. Pachyderma* species are indicative of sea surface temperature, as the species lives in water less than 10°C. Ice rafting events occur at the end of cooling cycles, and correlate to high global ice volume, low sea surface temperature, and low Greenland air temperature. From Bond et al., 1993.

These events have been linked to changes in Atlantic meridional overturning circulation (AMOC), which induces thermohaline circulation (THC) by transporting warm and saline surface waters to the North Atlantic. Once there, the water is atmospherically cooled and descends, forming North Atlantic Deep Water (NADW) and ultimately returning southward (Stocker, 2000 *and references therein*). The formation of NADW is dependent on maintaining a high enough density of surface waters where physical descent is possible, through low temperature and/or high salinity. If THC slows, reducing the rate of deep water formation, a reduction in meridional heat transport results in significant cooling of surface temperatures in the Northern Hemisphere. During DO events, elevated temperatures in the North Atlantic result in melt water discharge from continental ice sheets and an enhancement in the hydrological cycle, resulting in a freshwater cap on the North Atlantic sea surface. This slowly reduces THC, until the melt water either ceases or is able to mix and warm, saline waters are brought to the surface, resulting in the rapid resumption of THC. This proposed explanation would account for the saw-tooth patterns of DO cycles in Greenland temperatures, but the exact mechanisms behind THC reduction remain contested (Stocker, 2000 *and references therein*).

It appears that Heinrich events actually follow a slowdown in the AMOC, and do not act as its precursor (Alvarez-Solas et al., 2013). Previous hypotheses proposed that Heinrich discharge events were a response to internal ice sheet dynamics, whereby the Laurentide ice sheet would "purge" itself following a prolonged build up in volume, which in turn would shut down NADW formation (MacAyeal, 1993). However, it has been shown that ice rafting events accompanied the cold periods of multiple DO cycles during the last glacial period at a much higher frequency than an ice build up mechanism would allow for (Bond et al., 1995). Additionally, there is evidence that the AMOC may have lost strength prior to the most prominent iceberg calving events (Hall et al., 2006, Gutjahr et al., 2010). As overturning circulation slows, convection can no longer efficiently cool subsurface waters in the North Atlantic, leading to subsurface warming (Marcott et al., 2011). Warmer subsurface waters result in basal melting of the Labrador ice shelf, producing calving in the shelf and ultimately the acceleration of ice-streams around the Labrador Sea and extensive iceberg discharge (Alvarez-Solas et al., 2011, Alvarez-Solas et al., 2013). The largest discharge events, illustrated by Heinrich layers, occur during periods of prolonged subsurface warming (Alvarez-Solas et al., 2013). This extensive discharge results in a near shutdown of the AMOC, replicated in freshwater hosing simulations (Kageyama et al., 2010). Note that while a Heinrich event refers to the deposition of ice rafted debris accompanying iceberg calving, the longer period of heightened cold conditions is referred to as a Heinrich stadial.

Different paleorecords appear to have varied responses to DO events and Heinrich stadials,

with tropical sites showing a heightened sensitivity to Heinrich stadials. In Greenland, events such as Heinrich stadials and the Younger Dryas (sometimes referred to as Heinrich stadial 0) - which entailed a dramatic decrease in NADW formation - resulted in extreme winter temperatures (Severinghaus et al., 1998, Denton et al., 2005). These frigid temperatures were made possible by extensive sea ice cover, which prevented oceanic heat release (Broecker, 2006). As shown through general circulation models by Chiang and colleagues, the location of the Inter Tropical Convergence Zone (ITCZ) is highly sensitive to polar sea ice (Chiang et al., 2003). If the North Atlantic gains significant winter sea ice, the ITCZ -and thus the tropical rain belts- would be displaced southward (Chiang et al., 2003, Broecker, 2006). This displacement during Heinrich stadials is seen in changes in monsoonal activity, with a decrease (increase) in monsoonal strength in the Northern Hemisphere (Southern Hemisphere) (X. Wang et al., 2004, Y. Wang et al., 2001). This is accompanied by a drop in atmospheric methane production, due to a decrease in tropical wetland productivity in the Northern Hemisphere (Chappellaz et al., 1993). Additionally, Antarctic temperatures rise in response to the change in cross-equatorial heat transport, indicating the presence of a "bipolar see-saw" (Blunier et al., 2001).

The responses of global atmospheric systems to perturbations in thermohaline circulation during the last glacial period are complex and remain ill-defined in certain geographical locations, particularly continental areas removed from the direct influence of North Atlantic climate or the ITCZ (Oster et al., 2009). We shall now turn our attention to the paleoclimate record in North America, in order to establish climatological trends that may have affected our site in SE Minnesota.

1.1.2 Records of abrupt climate change in North America

Continuous paleoclimate records from terrestrial North America during the last glacial period were sparse prior to the 1990s. An early record that indicated responses to rapid climatic oscillations in the North Atlantic came from Lake Tulane lake sediments. Grimm and colleagues found that there was a higher abundance of *Pinus*, indicating a wetter climate, during Heinrich stadials (Grimm et al., 1993). While many records have been released charting climate and paleo-vegetation across the late Pleistocene, speleothem records prove particularly useful in determining climatic changes on a millennial scale. While the use of speleothem records will be further discussed in section 1.2, the primary advantage is that the dating resolution is high enough to accurately track short term climate variability.

High resolution speleothem records from the last glacial period have been particularly well developed in western North America, but remain sparse throughout the rest of the continent.

This is illustrated in Figure 1.2. All sites shown contain speleothem records that predate 11.7 ky BP, the beginning of the Holocene (Broecker et al., 2010). The site for this study is indicated by the pin at Spring Valley Caverns, MN.

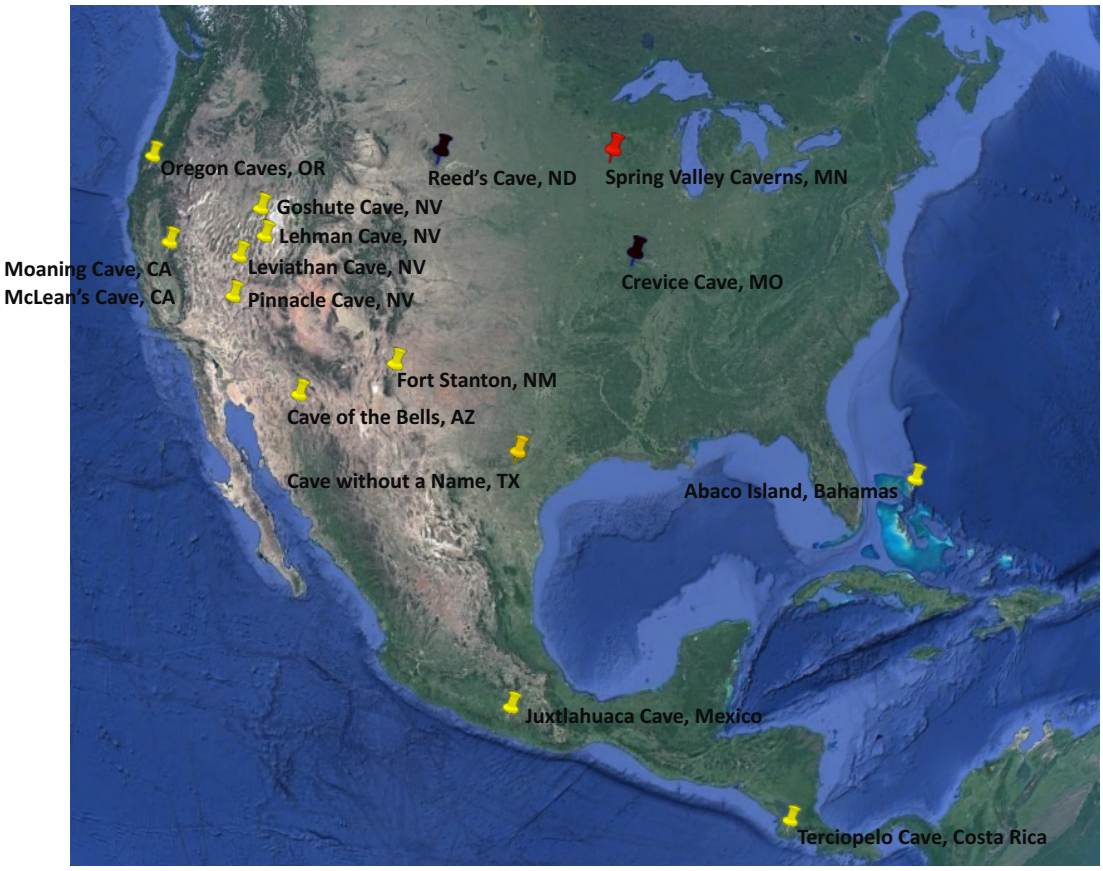

Figure 1.2: High resolution speleothem samples from the last glacial period. All pinned study sites are available at NOAA's National Centers for Environmental Information, except those at Reed's Cave, ND, and Crevice Cave, MO. This study will present data from Spring Valley Caverns, MN.

The study sites vary in their moisture sources, with locations in western North America dominated by Pacific-sourced winter precipitation - Oregon (Ersek et al., 2012), California (Oster et al., 2009, Oster et al., 2014), the Great Basin (Lachniet et al., 2014), Arizona (Wagner et al., 2010), and New Mexico (Asmerom et al., 2010). While study locations in the Southwest receive heavy precipitation during the summer monsoon, intense evaporation results in nearly all cave drip-water sourced from winter precipitation (Wagner et al., 2010). Western North American sites are acutely affected by the trajectory of winter storm tracks, dictated by the location of the polar jet-stream. Periods of weakened thermohaline circulation in the North Atlantic resulted in a strengthening of the Aleutian low, an atmospheric low-pressure system located in the Pacific's Bering Sea (Okumura et al., 2009). As the

Aleutian low strengthened, the polar jet stream moved southward, increasing the amount of winter precipitation in the region. This is illustrated not only in low δ^{18}O speleothem values during North Atlantic cold events in the speleothem records, but by paleolake highstands in the Great Basin region (Lachniet et al., 2014). While lake high-stands in the west do not appear to trend exactly latitudinally across deglaciation, their timing supports an influx in Pacific high latitude moisture during periods of reduced AMOC (Lyle et al., 2012, Lachniet et al., 2014). When proxy records from the Last Glacial Maximum (LGM) at 21 ky before present (BP) were compared to climate model simulations, a NW-SE trending precipitation dipole across Western North America appears to explain non-synchronous highstands, and supports the possibility that a stronger westerly-storm track was squeezed and steered along a NW-SE trend during the LGM rather than uniformly displaced southward (Oster et al., 2015).

The four sites farthest south - Texas (Feng et al., 2014), the Bahamas (Arienzo et al., 2017), Mexico (Lachniet et al., 2013), and Costa Rica (Lachniet et al., 2009) - are dominated by summer precipitation sourced from the tropical Atlantic. These sites show an increase in δ^{18}O speleothem values during North Atlantic cold events and a decrease during North Atlantic warm events at periods of high summer insolation. The Terciopelo Cave in Costa Rica currently lies within the boundaries of the ITCZ, and records increased aridity during Heinrich events as the ITCZ was displaced southward (Lachniet et al., 2009). The position of the ITCZ also influenced the strength of the North American Monsoon (NAM), as the site in Mexico saw a reduction in summer monsoon strength during Heinrich stadial 1 and the Younger Dryas (Lachniet et al., 2013). While the climate in the Bahamas is largely controlled by easterly trade winds, a southward shift in the ITCZ may be accompanied by an expansion in the Bermuda High, leading to higher δ^{18}O values at the site and an increase in aridity (Arienzo et al., 2015, Arienzo et al., 2017). The Texas record indicates not only drying during the Younger Dryas, but also records the δ^{18}O signature of seawater in the Gulf of Mexico. Additionally, this record suggests that Gulf of Mexico moisture may have encroached farther into the continental Southwest during North Atlantic warm events (Feng et al., 2014).

To summarize, North American regions dominated by Pacific-sourced winter precipitation appear to gain moisture during periods of low North Atlantic temperatures and reduced AMOC strength, whereas regions dominated by Atlantic-sourced summer precipitation appear to lose moisture. This is illustrated in a model simulation in Figure 1.3, which sees a higher amount of winter precipitation in the American southwest and a lower amount of summer precipitation in the continental interior at the LGM compared to the present (Kim et al., 2008).

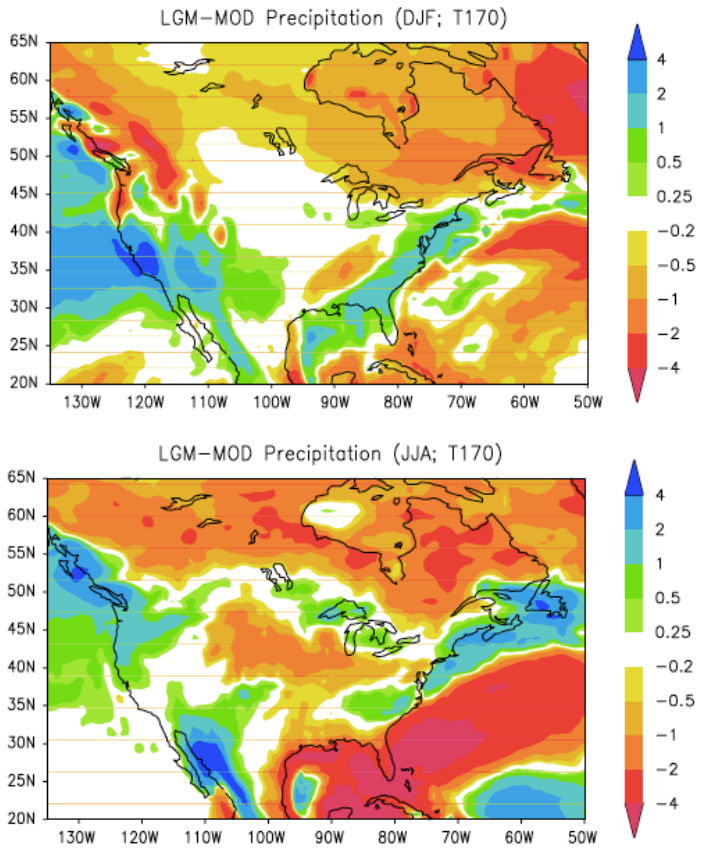

Figure 1.3: Model simulations of winter (DJF) and summer (JJA) precipitation of Last Glacial Maximum (LGM) compared to present (MOD). From Kim et al., 2008

Records in the mid-continent that receive summer and winter moisture are more difficult to interpret. Speleothem records from both Missouri and eastern North Dakota show evidence of millennial scale climate changes in their stable isotope signatures (Dorale et al., 1998, Serefiddin et al., 2004). A record from the Black Hills shows potential correlation to Greenland interstadial events, but a synchronous sample from the same cave shows differing trends (Serefiddin et al., 2004). The sampling resolution of records from Crevice Cave, Missouri, may not be high enough to correlate changes in the δ^{18}O record, but the record does show marked changes in ecotones (Dorale et al., 1998). The δ^{13}C record indicates a transition to a prairie dominated landscape between 59-55 ky BP across the Marine Interstadial (MIS) 4-3 boundary. This suggests there may be a connection between mid-continental aridity and solar insolation. Additionally, sharp ecotone boundaries have been shown to be influenced by the incursion of Pacific and Gulf of Mexico air masses in the region during the mid-Holocene (Denniston et al., 1999b). A pollen record from Illinois indicates that the last glacial period was marked by drier and colder conditions, and the last interglacial was potentially warmer and wetter than the Holocene (Teed, 2000).

While records from western North America are well developed, the effects of North Atlantic climate oscillations on the mid-continent remain inconclusive. With the record presented in this study, we hope to further elucidate the extent of abrupt climate change during the late Pleistocene in this area, aims which will be discussed further in Chapter 3. For now, we turn our attention to the details of using speleothems as paleoclimate recorders.

1.2 Methods of paleoclimate reconstruction

1.2.1 Carbonate series geochemistry in karst environments

Carbonates ($CaCO_3$), either aquatic or terrestrial, are widely used in paleoclimate research. While the use of calcium carbonate shells of marine organisms such foraminifera and coccolithophores has gained dominance in reconstructing changes in marine geochemistry, cave deposits (speleothems) have been shown to be reliable terrestrial paleoproxies. The presence or absence of speleothems in karst systems, as well as their growth rate, geochemical composition and crystallographic structure, can all provide clues as to paleo-environmental changes and regimes, and they can be dated at high resolution (Richards et al., 2003).

Speleothems form in caves through the degassing of percolating drip water. During this process, meteoric water first passes through a soil zone that is high in pCO_2 due to aerobic respiration. Gaseous carbon dioxide is converted into aqueous carbon dioxide, interacting with the percolating water to form carbonic acid. At a neutral pH, the majority of the carbonic acid formed dissociates to bicarbonate, with some amount fully dissociating to form carbonate. When the water reaches overlying limestone bedrock in the vadose zone, the reaction with this weakly acidic solution will result in carbonate dissolution until saturation is reached. The complete reaction is presented in Equation 1.1.

$$CaCO_{3(s)} + H_2O_{(l)} + CO_{2(g)} \Rightarrow Ca^{2+}_{(aq)} + 2HCO^{-}_{3(aq)} \tag{1.1}$$

This reaction over long time scales can result in the formation of epigenetic caves.

As caves are both high in relative humidity and lower in pCO_2 than the soil zone, secondary carbonate formation occurs through carbon dioxide degassing rather than through water evaporation (McDermott et al., 2005). Once the saturated drip water reaches the cave, the reaction reverses, resulting in the deposition of calcium carbonate.

$$Ca^{2+}_{(aq)} + 2HCO^{-}_{3(aq)} \Rightarrow CaCO_{3(s)} + H_2O_{(l)} + CO_{2(g)} \tag{1.2}$$

These carbonate deposits come in a variety of forms, dependent on location of drip, flow rate, and solute concentrations. Stalagmites are most commonly used as paleoproxies, but stalactites and flowstones can also be appropriate depending on growth behavior. The majority of stalagmites are slightly tapered, with some amount of calcite deposition occurring during flow down the sides (Ford et al., 2007). Carbonate is deposited as a thin film, resulting in growth layers along the stalagmite with oldest depositions at its base. Periods of inactive drip can result in a build up of detrital layers, and a noticeable hiatus in growth.

1.2.2 Uranium series disequilibrium dating in carbonates

Uranium series disequilibrium dating has been used for decades to determine the age of deposition for marine, lacustrine, and terrestrial carbonate deposits. After a flurry of early work on radioactivity and uranium decay series isotopes around the turn of the century, technical advancements over the following decades allowed for the determination of absolute concentrations of isotopes using alpha counting by the mid-century. In 1941, Urry developed a co-precipitation method using iron and aluminum carrier agents to form a uranium oxide film whose uranium concentration could be determined through alpha spectrometry (Urry, 1941). The determination of thorium concentration was complicated by natural isotopic variation, but by 1953 Isaac and Picciotto had developed a thorium separation method through ion exchange and an alpha radiation technique to determine ^{230}Th concentrations by differentiating alpha-tracks (Isaac et al., 1953). Much of this work was done to determine deposition rates of ocean sediment, but was adopted for use in corals soon thereafter. After determining that ^{230}Th concentrations vary with depth in corals and are lower than secular equilibrium values, Barnes and colleagues hypothesized that ^{230}Th/^{238}U ratios could be used to estimate age of formation (Barnes et al., 1956).

This assumption takes into account the chemical characteristics of ^{238}U and ^{230}Th specific to aqueous environments (marine, lacustrine, and meteoric). In these environments, uranium - typically in a +6 oxidation state at surface conditions - readily forms aqueous uranyl ions whereas thorium - in a +4 oxidation state - is insoluble and is typically precipitated or adsorbed. In karstic environments, meteoric water accumulates aqueous complexed uranyl ions - $UO_2(CO_3)_2^{2-}$ and $UO_2(CO_3)_3^{4-}$ - in the soil zone, which are then transported and incorporated into the lattice of the resulting carbonate deposit (Ford et al., 2007).

Carbonate deposits formed in aquatic surface conditions have minimal initial ^{230}Th (Barnes et al., 1956). Ingrowth of ^{230}Th is thus a result of radioactive decay from ^{238}U, via intermediate daughters ^{234}Th, ^{234}Pa, and ^{234}U, and can be measured as a function of time. Barnes and colleagues concluded that the activity ratio of ^{230}Th over ^{238}U would near unity

with increasing age - roughly within 5x the half-life of ^{230}Th (Barnes et al., 1956, Bourdon et al., 2003). Thus U-Th dating can be utilized to date samples that formed up to 600 ky before present (Cheng et al., 2016). The equation is as follows, where λ is the decay constant of ^{230}Th (9.1705E-6 yrs^{-1}) (Cheng et al., 2013):

$$(\frac{^{230}Th}{^{238}U})_A = 1 - e^{-\lambda_{230}t} \tag{1.3}$$

This equation, however, assumes that ^{234}U and ^{238}U are in unity (Edwards, 1988). In fact, uranium isotopes become fractionated during water-rock interactions due to preferential leaching of ^{234}U, oxidation of ^{234}U, and alpha-recoil of ^{234}Th, and most aqueous systems have an abundance of ^{234}U over ^{238}U (Richards et al., 2003). The age equation was improved to reflect this disequilibrium state, while continuing to assume negligible initial ^{230}Th (Broecker, 1963, Kaufman et al., 1965). The equation is as follows, where λ_{230} is the decay constant of ^{230}Th (9.1705E-6 yrs^{-1}) and λ_{234} is the decay constant of ^{234}U (1.82206E-6 yrs^{-1}) (Cheng et al., 2013):

$$(\frac{^{230}Th}{^{238}U})_A = 1 - e^{-\lambda_{230}t} + (\frac{\delta^{234}U_m}{100})(\frac{\lambda_{230}}{\lambda_{230} - \lambda_{234}})(1 - e^{(\lambda_{234}-\lambda_{230})t}) \tag{1.4}$$

$$\text{where } \delta^{234}U_i = \delta^{234}U_m e^{\lambda_{234}t}$$
$$\text{and } \delta^{234}U_m = ((\frac{(\frac{^{234}U}{^{238}U})_m}{(\frac{^{234}U}{^{238}U})_{eq}} - 1) * 1000$$

This equation was verified through comparison of U-Th and ^{14}C ages for young, near-surface carbonates (Thurber et al., 1965, Kaufman et al., 1965). If initial ^{230}Th cannot be assumed to be negligible such as in deep sea corals and many terrestrial carbonates, a correction can be made by measuring ^{232}Th and estimating an initial $\frac{^{230}Th}{^{232}Th}$ (Edwards et al., 2003, Cheng et al., 2000).

$$(\frac{^{230}Th}{^{238}U})_A - (\frac{^{232}Th}{^{238}U})_A(\frac{^{230}Th}{^{232}Th})_i(e^{-\lambda_{230}t}) = 1 - e^{-\lambda_{230}t} + (\frac{\delta^{234}U_m}{100})(\frac{\lambda_{230}}{\lambda_{230} - \lambda_{234}})(1 - e^{(\lambda_{234}-\lambda_{230})t}) \tag{1.5}$$

Estimating the contribution of initial ^{230}Th introduces additional time errors, thus high ^{232}Th concentrations limits the precision in determining ages of a sample. In determining the age of samples in this study, a bulk earth value of 4.4E-6 was used for the $(\frac{^{230}Th}{^{232}Th})_i$ ratio (Cheng et al., 2000).

In addition to errors introduced by initial ^{230}Th, uranium series disequilibrium dating was hindered due to the error constraints of alpha spectrometry. Errors using alpha counting were >5% and typically between 10-20% (2σ), which made millennial-scale climate signals

impossible to accurately identify in carbonate paleorecords. Errors of this magnitude are due to alpha-counting methods, whereby pulses are counted over multiple days of laboratory time. Thus, counting statistics limit errors below a certain threshold. To resolve this issue, methods were developed to measure U-Th ratios using isotope dilution mass spectrometry, in which errors based on counting statistics were reduced to a ‰ level (Edwards, 1988, Edwards et al., 1987). In this method, atoms in a separated solution are ionized and passed through a magnetic field which separates ion beams by mass. Counts per unit time are then recorded, either by passing a beam directly into a Faraday cup or by passing it first through a secondary electron multiplier (SEM). Recent work using a cup configuration has reduced counting errors to under 1‰ (Pythoud et al. *in prep*). These improvements to measurement methods not only greatly reduced age errors, but also reduced analysis time and sample size. Specifics of sample collection are discussed in Chapter 3 and Appendix A.2

Measured beam intensities of uranium and thorium on isotope mass spectrometers must undergo corrections for background levels, tailing, isotopic fractionation, and contamination during chemistry before calculating a sample's age. These corrections will be further discussed in Appendix B.

1.2.3 Use of confocal microscopy in speleothems

In addition to ^{230}Th dating, growth layer counting can confirm age estimates and improve estimations of growth periods. This can be done through fluorescence spectrophotometry, a non-destructive method whereby the presence of organic acids result in visible fluorescent banding in speleothems that can indicate annual layering. Speleothems are cut along the growth axis, polished, and imaged using a confocal laser scanning microscope. In this technique, a laser emits electromagnetic radiation within a specific excitation wavelength spectra. Exposure to a specific energy wavelength causes excitation in fluorophores - molecules with electrons able to move easily between energy levels. These electrons absorb and then re-emit the energy at a lower wavelength, resulting in measurable fluorescence (McGarry et al., 2000). The intensity of fluorescence increases with fluorophore concentration.

While fluorescent intensity can change due to pH, presence of metals, and soil properties, it has also been linked to changes in climate (McGarry et al., 2000). The organics causing fluorescence in speleothems are the result of humification processes in the soil zone, where decomposition of organic material results in the formation of humic substances. These consist of humic acids, which are mildly hydrophobic, and fulvic acids, which are hydrophilic (McGarry et al., 2000). These complexes accumulate in the soil zone, and are carried by

infiltrating water and co-precipitated or adsorbed onto speleothem surfaces. Depending on the characteristics of groundwater through the vadose zone, seasonal variation in the amount of incoming drip water can result in corresponding variability in fluorophore concentration in speleothem growth layers, causing visible annual lamina (Tan et al., 2006). A "light" layer of high intensity flourescence can indicate a period of enhanced surface water "flushing". Depending on the region this can indicate spring snowmelt, seasonal monsoons, or an autumn increase in soil moisture deficit (A. Baker et al., 2008). This is followed by a transition to a "dark" layer of low intensity fluorescence, until the following year's high infiltration period. Thus, a coupled light/dark layer will indicate a year of growth in speleothems that experience this type of lamination.

Determining whether a speleothem does in fact experience annual banding remains difficult. If band counts between two ^{230}Th dates exceed the age errors, annual layering can be confirmed, but this may not translate to all layering within the sample itself (Tan et al., 2006). Measuring dissolved organic carbon concentration of dripwaters or collecting calcite growth in situ can also confirm cyclicity of fluorescence. More recently, fluorescent lamination has been compared to stable isotope and trace element variation, which can help determine the timing and cause of changes in fluorophore concentration. For example, in Soreq cave, an increase in the δ^{18}O of precipitation correlates to a decrease in rainfall amount. The cave experiences a distinct dry and wet season, with 95% of precipitation occurring in boreal winter. Oxygen isotopes were compared to fluorescent banding, and showed that δ^{18}O values increase from light to dark growth. Light layers - periods of increased transport of organic material - corresponds to periods of low δ^{18}O, indicating that both of these signals are seasonal and correlate to the start of the wet season in early winter (Orland et al., 2009). Additionally, light layers in Soreq cave also demonstrate higher concentrations of particulates, indicating a "flushing" event that transports both organics and particulates into the cave seasonally (Orland et al., 2014).

1.2.4 Hydrological conditions and oxygen isotopes

Variations in stable isotope ratios provide essential evidence in reconstructing paleoclimate behavior. The abundance of ^{16}O to ^{18}O isotopes inherited from dripwater in speleothems can help determine changes in hydrological conditions during growth, but determining the primary drivers of oxygen isotopic variability can be problematic.

The ratio of heavy to light isotopes is a function of the energy state of each isotopologue. Heavier isotopes (e.g., ^{18}O) have a lower potential energy than lighter isotopes (e.g., ^{16}O) because they have a lower vibrational frequency. Additionally, phases of matter have

differences in vibrational frequency, with solid states having the lowest and gaseous states the highest. Thus, a phase change will result in isotopic fractionation even under equilibrium conditions. In the case of oxygen, ^{18}O will exist preferentially in phases with lower vibrational states. Figure 1.4 below illustrates the energetically favorable evaporation of $H_2^{16}O$ and condensation of $H_2^{18}O$.

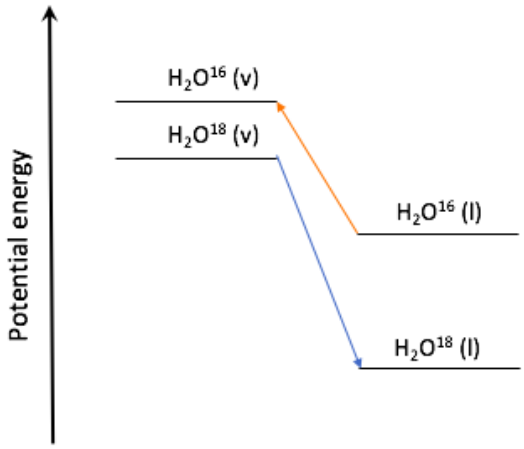

Figure 1.4: Potential energies for liquid and vapor water isotopologues. The arrows indicate the energetically favorable evaporation of $H_2^{16}O$ and condensation of $H_2^{18}O$. Based on Bigeleisen, 1965

Because of its energetic favorability, the ratio of ^{18}O/^{16}O is higher in liquid than in vapor for water, meaning the fractionation factor under both equilibrium and kinetic conditions is above 1 (Horita et al., 1994). The fractionation factor is inversely related to temperature, so that at higher temperatures there is a smaller amount of fractionation between phases. This fractionation is expressed through delta notation, where the ratio of a heavy to light isotope in a sample is related to that of a standard as shown in the Equation 1.6 (McKinney et al., 1950). Oxygen isotope ratios of water are recorded in reference to Vienna Standard Mean Ocean Water (VSMOW), where the δ^{18}O value is 0 ‰ (Sharp, 2007).

$$\delta = (\frac{R_{sample}}{R_{standard}} - 1) * 1000 \tag{1.6}$$

Meteoric water undergoes a series of fractionation events before being incorporated into speleothem growth. The moisture first begins as its oceanic source, the δ^{18}O of which is near the standard value. Upon evaporation, the water vapor is depleted in ^{18}O relative to ^{16}O, resulting in a δ^{18}O value of about -13‰ due to equilibrium and kinetic fractionation (Majoube, 1971). This fractionation effect is reversed upon immediate condensation, resulting in a δ^{18}O value of precipitation close to that of the oceanic moisture source.

However, as condensate continues to leave the system and restricts exchange between vapor and liquid phases, both the vapor and liquid water become more depleted in ^{18}O (Sharp, 2007). Additionally, condensation requires isobaric cooling, increasing the fractionation factor between vapor and liquid. This results in a process of isotopic depletion called open-system Rayleigh fractionation, described in the following equations (Dansgaard, 1964).

$$\delta_l = \frac{\alpha}{\alpha_o} F_v^{\alpha_m - 1} - 1 \tag{1.7}$$

$$\delta_v = \frac{1}{\alpha_o} F_v^{\alpha_m - 1} - 1 \tag{1.8}$$

In these equations, the $\delta^{18}O$ of liquid and vapor is dependent on the fraction of original vapor remaining (F) and the fractionation factors at the initial temperature (α_o), the temperature of momentary condensation (α), and the average of the two (α_m). Thus, the $\delta^{18}O$ of precipitation is inherently temperature dependent. Dansgaard found that in North Atlantic coastal sites, change in temperature is the primary driver of change in $\delta^{18}O$, with an average $d\delta^{18}O/dT$ of 0.70‰/°C (Dansgaard, 1964). This relationship holds for high-latitude coastal sites with mean annual temperature under -5°C where the slope of fractionation factor versus temperature remains linear for $\delta^{18}O$, but does not hold at higher mean annual temperatures due to the non-linearity of the fractionation curve.

The interpretation of $\delta^{18}O$ signatures is dependent on site locale, where temperature may not be the primary driver of the isotopic variability. At low-latitude coastal sites, convective monsoonal rainfall results in isotopic signals that are depleted in ^{18}O. Sites at altitude can experience isotopic depletion due to precipitation induced by change in elevation. Inland sites experience depletion due to their distance from moisture sources. Furthermore, moisture sources vary in their isotopic composition due to differences in evaporation and freshwater input, and mean oceanic water composition varies with global ice cover (Epstein et al., 1953). If a site receives contributions from multiple moisture sources, the dominance of the source can affect the isotopic signature of precipitation at the site.

Additionally, $\delta^{18}O$ values in speleothems are affected by phase change processes. If kinetic fractionation occurs during deposition, the resulting calcite will be enriched in heavy isotopes relative to the originating dripwater. However, this can be tested for by determining non-correlation between oxygen and carbon isotopic behavior within a growth layer, confirming precipitation under equilibrium conditions (Hendy, 1971, McDermott et al., 2005). If equilibrium conditions can be confirmed, variation in the $\delta^{18}O$ values of the sample will either be a result of changes in the isotopic signature of the drip water or changes in the cave air temperature. Changes in cave air temperature affect the fractionation during precipitation, where an increase in temperature will result in a decrease in the $\delta^{18}O$ of

calcite relative to dripwater of about - 0.24‰/°C, depending on site locale (Hendy et al., 1968). The $\delta^{18}O$ values can also be affected by fractionation processes within the soil or epikarst, such as increased evaporation, prior calcite precipitation, or changes in transit time.

Determining the primary drivers of oxygen isotopic variability in speleothems at a specific cave site remains integral in interpreting these records.

1.2.5 Environmental conditions and carbon isotopes

Carbon isotopic variability in speleothem samples can indicate changes in vegetation, although this relationship can be masked by prior calcite precipitation within the cave or epikarst or by kinetic fractionation (A. Baker et al., 1997). Additionally, interaction with atmospheric CO_2 within the soil zone and with the host rock in the epikarst influences the carbon isotopic signature of percolating water (Oster et al., 2010).

Large shifts in the $\delta^{13}C$ values of speleothem calcite, especially if replicated in multiple samples, have been interpreted to reflect changes in the ratio of C_3 to C_4 plants (Dorale et al., 1992, Dorale et al., 1998). C_3 plants represent the majority of terrestrial flora, where sugar is produced through the breakdown of CO_2 by the enzyme RuBisCo (ribulose -1,5-bisphosphate carboxylase/oxygenase). This process is the most energy efficient, however under times of heat stress C_3 plants can undergo a competing metabolic pathway called photorespiration. During this process RuBisCo converts O_2 rather than CO_2, which wastes energy and uses up fixed carbon. Some plants have evolved to minimize the harmful effects of photorespiration. C_4 plants, which largely consist of warm-weather grasses, have developed an additional pathway to carbon fixation to eliminate photorespiration. These different pathways result in differing fractionation of ^{13}C versus ^{12}C. The C_3 photosynthetic pathway only uses the metabolic enxyme RuBisCo, which has a strong preference for ^{12}C, whereas PEPC (phosphoenol pyruvate carboxylase), the carbon fixating enzyme of the C_4 pathway, is less discriminating (Alonso-Cantabrana et al., 2016). Thus C_3 plants have a carbon signature depleted in ^{13}C relative to C_4 plants, with averages of -27 ‰ versus -13 ‰ respectively (Cerling, 1984). While soil CO_2 is 3-7 ‰ higher than the $\delta^{13}C$ of soil organic matter due to respiration rates and diffusion of atmospheric CO_2, transitions in the relative proportion of C_3 to C_4 plants can be recorded in the isotopic signatures of speleothems (Cerling, 1984, Dreybrodt et al., 2011).

Fractionation can occur within the soil and epikarst that may complicate this signal. Soil zone processes that affect the isotopic composition of carbon include changes in plant respiration or decomposition, where an increase of either leads to an increase in soil pCO_2

and a decrease in δ^{13}C of soil CO_2 (Cruz et al., 2006). Thus dry periods would lead to lower respiration rates in soils, which would increase the δ^{13}C of soil CO_2 and decrease the proportion of depleted SOM-sourced versus enriched bedrock-sourced CO_2 in seepage water, ultimately increasing the δ^{13}C of calcite (Oster et al., 2009, Cruz et al., 2006). Periods of lower respiration and a decrease in depleted-SOM sourced CO_2 have also been interpreted as an increase in the relative proportion of enriched atmospheric CO_2, although the conclusions are the same (Genty et al., 2001, Genty et al., 2003). However, seepage water may also retain a higher proportion of enriched atmospheric CO_2 if water residence times are short enough that the water cannot equilibrate with soil CO_2 (A. Baker et al., 1997, Cosford et al., 2009).

Additionally, inorganic processes such as prior calcite precipitation and kinetic fractionation can influence the isotopic signal of seepage water (A. Baker et al., 1997). Degassing in the epikarst or in the cave prior to sample formation will result in the loss of ^{12}C, resulting in higher δ^{13}C values of the seepage water. If degassing of CO_2 during sample formation is rapid, kinetic fractionation can result in the enrichment of ^{13}C and higher δ^{13}C values (Hendy, 1971).

1.3 Conclusions

Speleothems are particularly useful paleorecorders due to their potential for high resolution ages. However, determining the drivers behind stable isotope variations can be difficult and site-specific. While paleoclimate records in western North America have been well established and largely monitor changes in winter precipitation, records in the mid-continent remain ambiguous. In order to determine how climate might have changed in south-eastern Minnesota during the last glacial period, we must establish current climatological trends in the area and how they affect temperature, precipitation, and stable isotopic variation. Chapter 2 will examine modern conditions in the area, and how changes in moisture delivery may affect the growth and stable isotopic signature of regional speleothem records. In Chapter 3 we will then present a high resolution record from Spring Valley Caverns which documents millennial-scale climate oscillations synchronous with North Atlantic events. This record illustrates that climate change prompted by AMOC reduction was felt in areas far from moisture sources, and provides clues as to how anthropogenic climate change may affect the North American mid-continent.

Chapter 2

Modern Hydrological Regime in SE Minnesota

2.1 Precipitation regimes in Minnesota

Minnesota experiences a continental climate with strong seasonality. The state receives much of its moisture during the summer months, with June, July, and August precipitation comprising on average 45% of the annual precipitation (D. Baker et al., 1978). This moisture originates from the Gulf of Mexico, and influx of this source creates a NW/SE annual precipitation gradient across the state. The December, January, February winter months only see 8% of annual precipitation, as Gulf of Mexico moisture is largely cut off and the state receives cold, dry air from Pacific and Arctic sources (D. Baker et al., 1978). Precipitation in the NE portion of the state is moderated by the effects of Lake Superior, and thus sees more moisture during the winter months than the rest of Minnesota.

Figure 2.1 shows the monthly averages for temperature and precipitation from December 2015 through November 2016, taken at the University of Minnesota St. Paul Climate Station by the MN Department of Natural Resources. Temperatures peak in July and August, as does total rainfall.

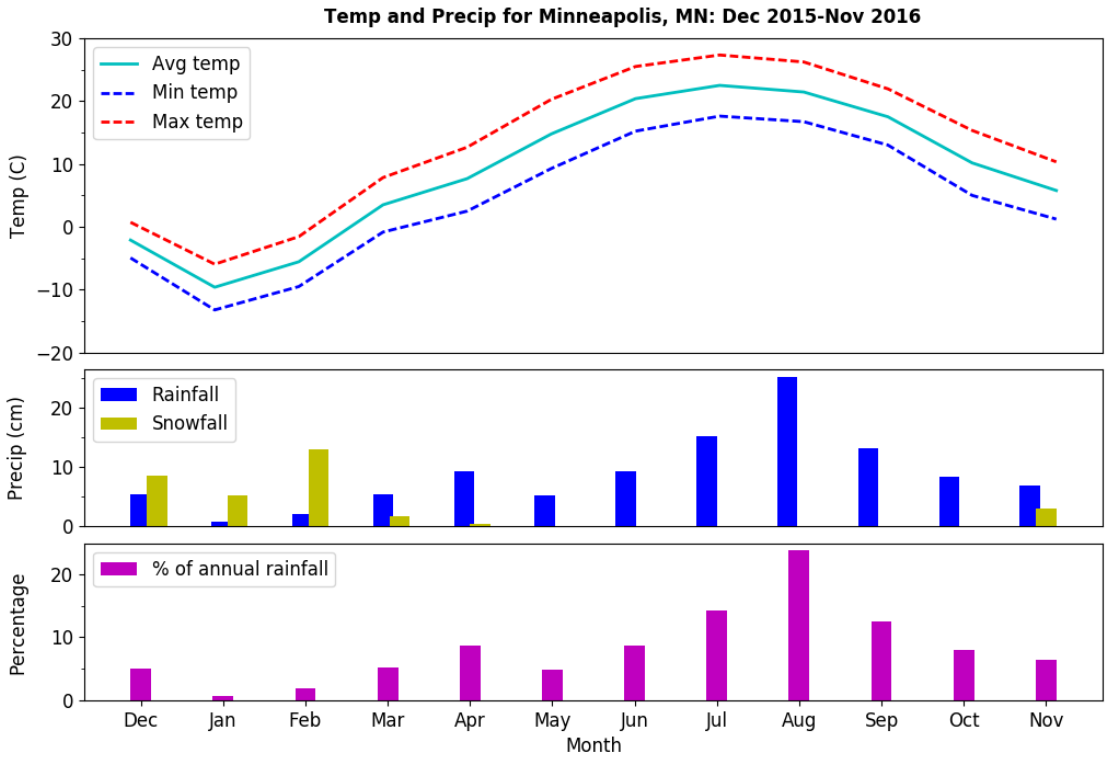

Figure 2.1: Monthly averages for temperature and precipitation from Dec 2015-Nov 2016. Measurements were taken at the UMN St. Paul campus by the MN Department of Natural Resources. Data available at the MN DNR website.

In addition to seasonal variability in precipitation amounts, Minnesota also experiences seasonal variability in moisture sources. Moisture-bearing back trajectories for the same period (Dec2015-Nov2016) were generated using National Oceanic and Atmospheric Administration's (NOAA) trajectory model, HySplit. Air masses that deposited precipitation at the University of Minnesota St. Paul campus were tracked over the previous 72 hours. The trajectories were grouped seasonally and plotted using the *Python* program *PySplit* (Cross, 2016). Wind roses were also generated seasonally using the *Python* program *Windrose*. Moisture flux in trajectory images is measured in $\frac{g}{\frac{kg}{\frac{m}{s}}}$ and plotted on a square root scale (Cross, 2016). Wind roses are plotted by cardinal direction, where radius indicates frequency and color indicates wind speed in $\frac{m}{s}$.

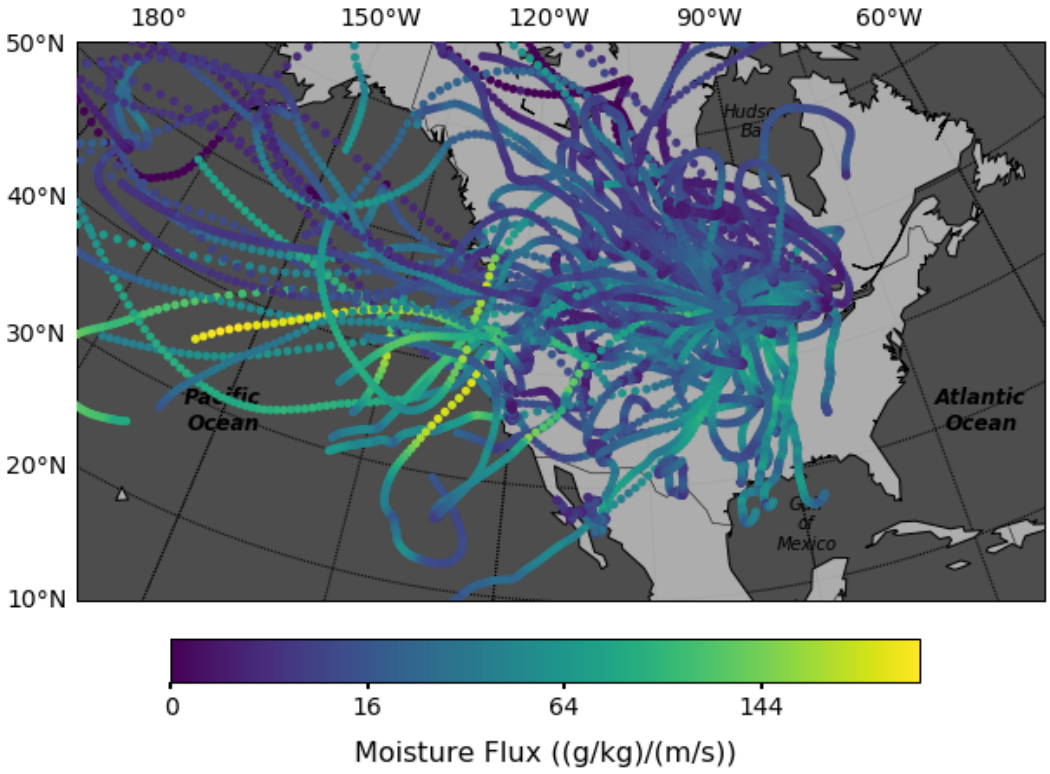

Figure 2.2: Moisture trajectories for Dec 2015, Jan, Feb 2016

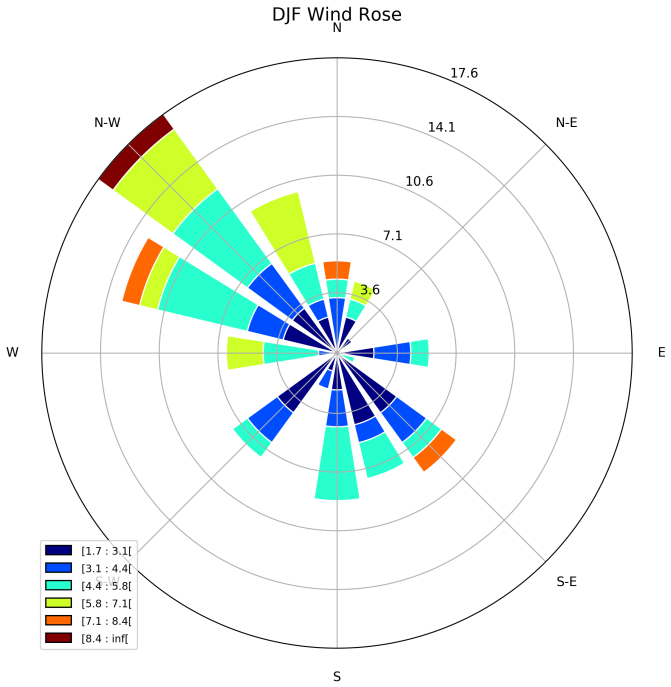

Figure 2.3: Wind rose for Dec 2015, Jan, Feb 2016

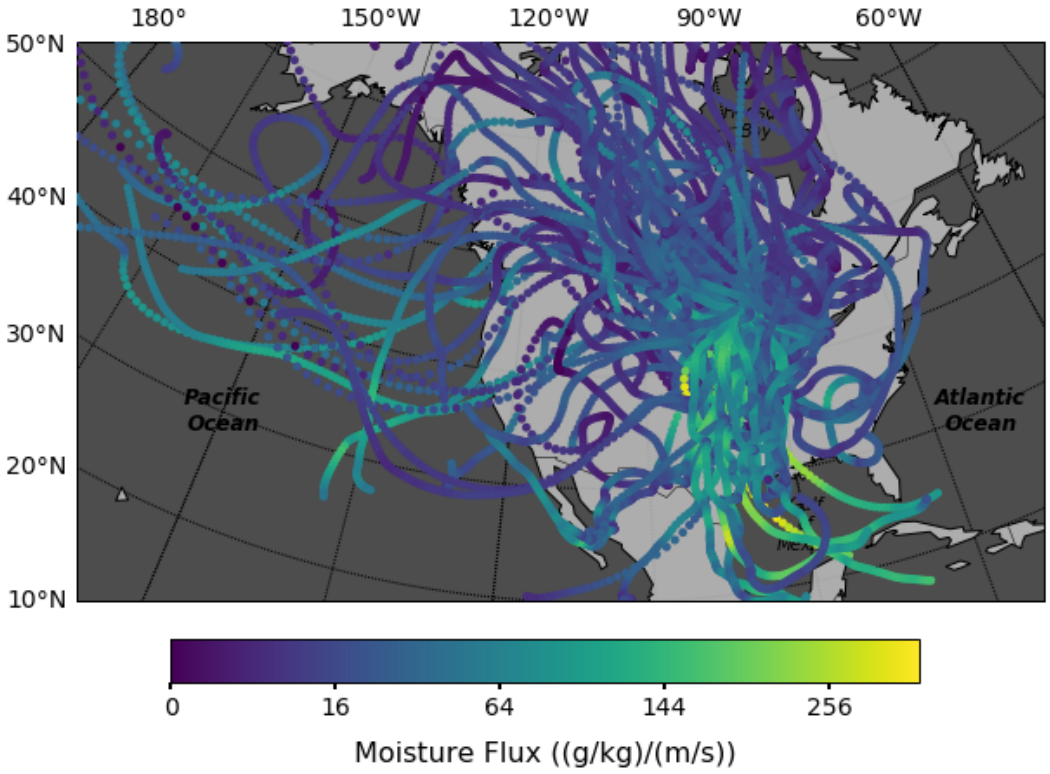

Figure 2.4: Moisture trajectories for Mar, Apr, May 2016

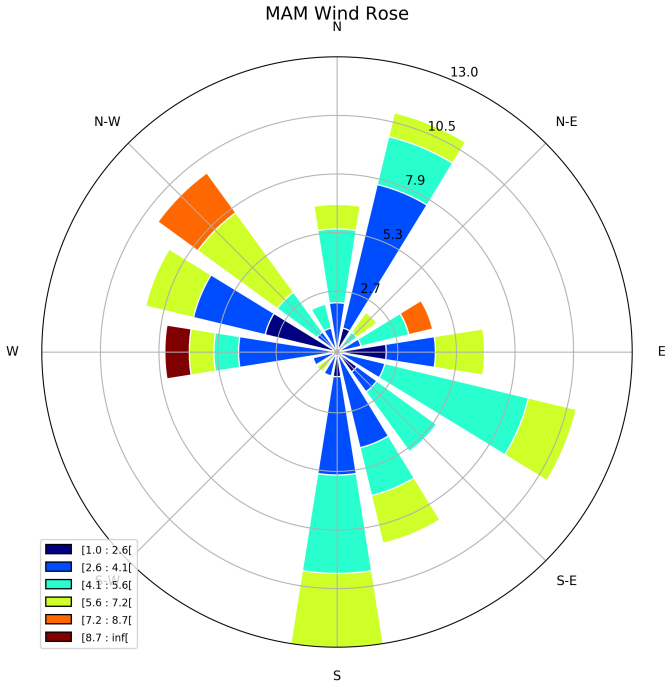

Figure 2.5: Wind rose for Mar, Apr, May 2016

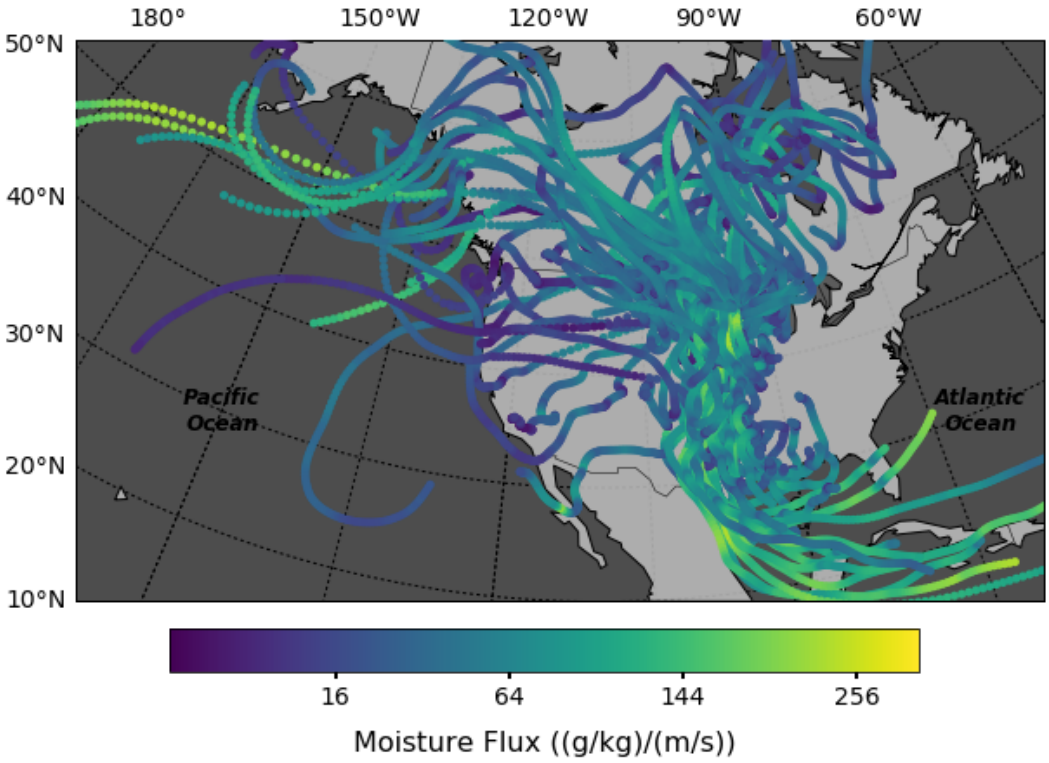

Figure 2.6: Moisture trajectories for Jun, Jul, Aug 2016

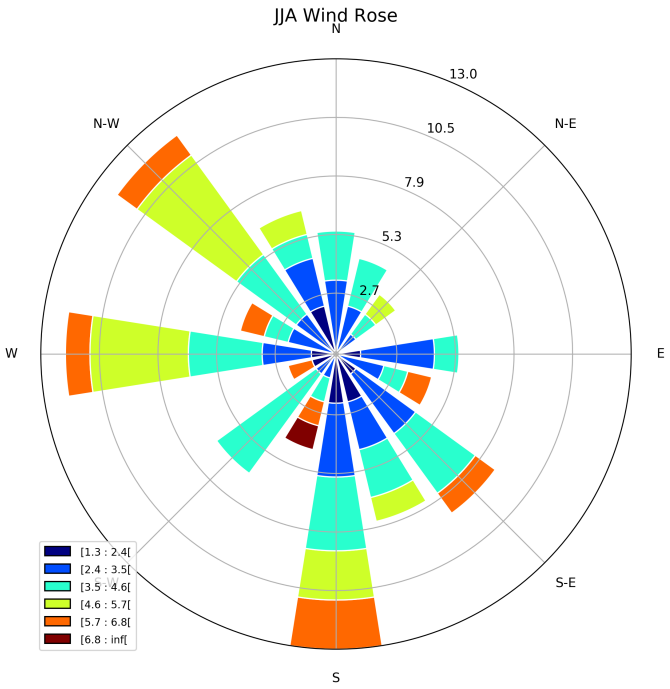

Figure 2.7: Wind rose for Jun, Jul, Aug 2016

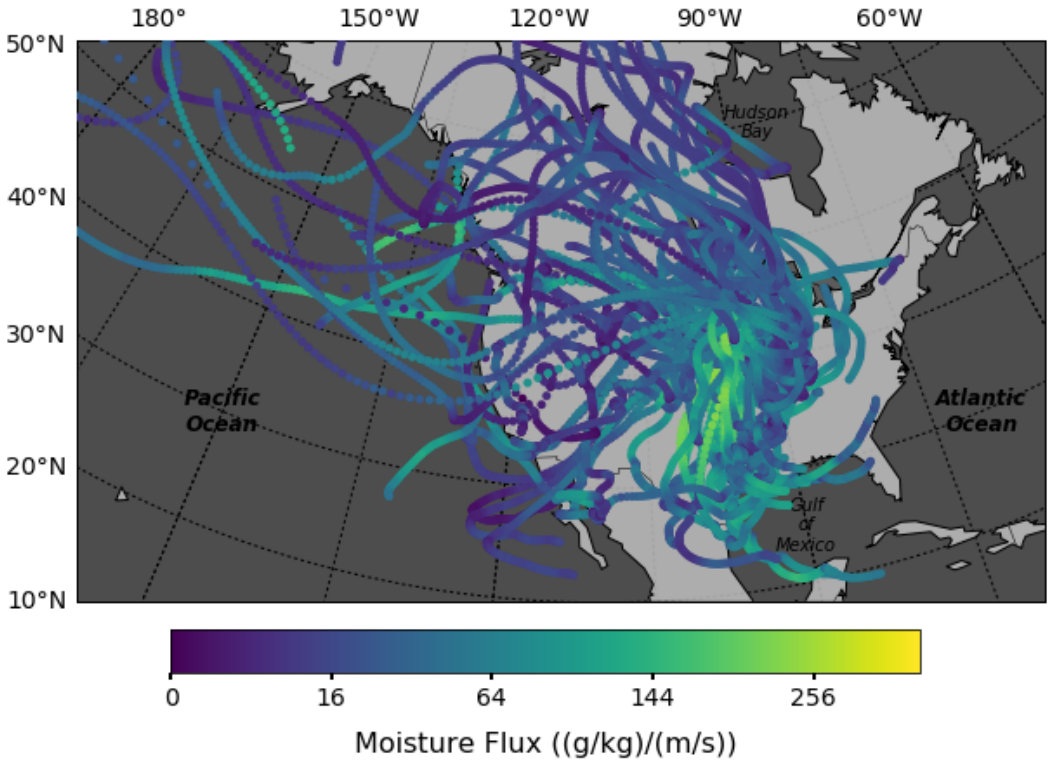

Figure 2.8: Moisture trajectories for Sep, Oct, Nov 2016

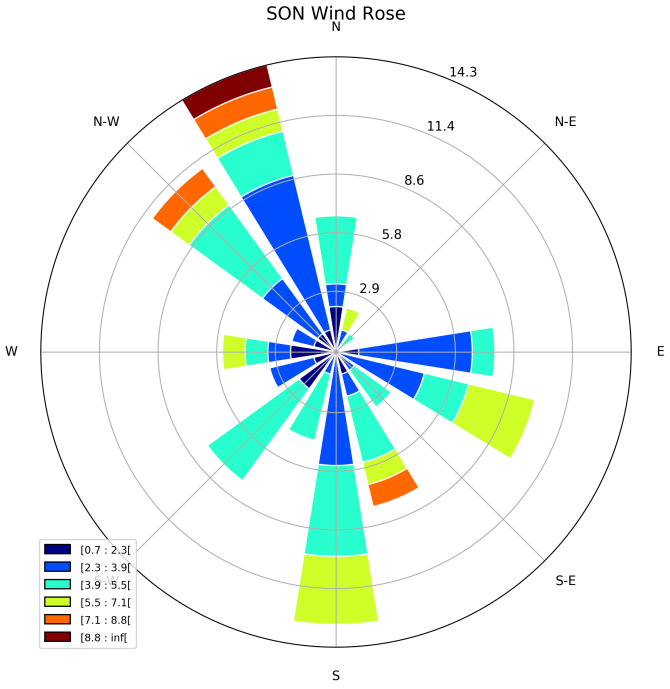

Figure 2.9: Wind rose for Sep, Oct, Nov 2016

The winter season (DJF) is marked by winds and precipitation primarily from the Northern Pacific, as illustrated in Figures 2.2 and 2.3. Moisture flux is significantly lower than other seasons, indicating lower moisture availability in Minnesota. Spring (MAM) season begins the southerly influx of Gulf of Mexico sourced moisture, shown in Figures 2.4 and 2.5 by an increase in a southerly moisture flux. This moisture source becomes dominant in the summer (JJA) season, when Minnesota experiences its highest moisture availability. This is seen in Figures 2.6 and 2.7 as a majority of moisture trajectories are southerly sourced from the Gulf of Mexico and tropical Atlantic. Gulf of Mexico moisture then decreases in the fall (SON), where dry, northwesterly winds encroach on the region. Moisture flux decreases during the fall, and winds become primarily northwesterly sourced, as shown in Figures 2.8 and 2.9.

Varying large-scale oceanic and atmospheric patterns have been shown to affect continental precipitation regions in the United States, such as the Atlantic Multidecadal Oscillation (AMO), Pacific Decadal Oscillation (PDO), North Atlantic Oscillation (NAO) and Pacific-North Atlantic (PNA) teleconnection. The AMO and PDO are driven by changes in the sea surface temperatures (SST) of the North Atlantic and Northeast-tropical Pacific, respectively (McCabe et al., 2004). Positive phases of the AMO, characterized by warm SSTs across the Northern Atlantic, have been shown to be correlated to multi-year droughts in North America (Sutton et al., 2005). However, interplay between AMO and PDO phases has been proposed to have more success in predicting drought frequency in the region (McCabe et al., 2004).

To evaluate AMO and PDO influence on Minnesota precipitation, seasonal precipitation data of the cumulative departure from normal for the Twin Cities from 1871-2017 was plotted against distinct AMO and PDO periods determined by McCabe and colleagues (McCabe et al., 2004). The results are shown in Figure 2.10. There is a slight correlation between below average precipitation during winter, spring, fall, and annual cumulative departure and positive AMO phases, and no discernible correlation between precipitation in any season and PDO phases. However, the 1930s drought is present in the spring, summer, and annual cumulative departure during the period with positive AMO and PDO indexes. This illustrates that while positive or negative phases of the AMO and PDO may not have considerable influence on the precipitation regime in Minnesota alone, the combination of warm anomalies in both may result in a significant decrease in annual, and particularly summer, precipitation.

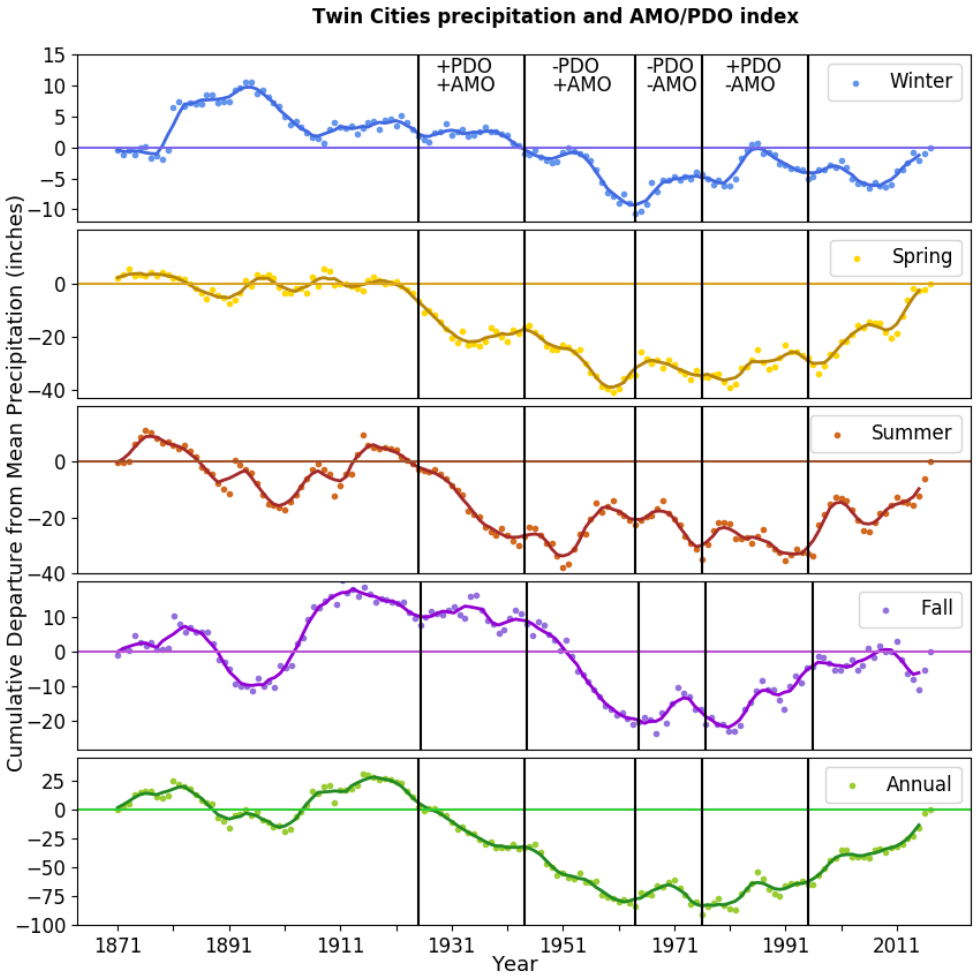

Figure 2.10: Raw and 5 year-smoothed precipitation record of cumulative departure from normal for the Twin Cities from 1871-2017 plotted with seasonal average. PDO and AMO periods defined by McCabe et al., 2004. Precipitation data available at the MN DNR website.

Of additional importance to Minnesota seasonal precipitation are the effects of large-scale atmospheric dynamics. The PNA is an atmospheric pattern defined by the amplification and damping of a mid-tropospheric ridge over the Rocky Mountains in the western US and a trough over the SE United States (Sheridan, 2003). A positive PNA refers to the amplification of this system, resulting in a dominance of meridional flow over North America, particularly in winter. A negative PNA results in a dominance of zonal flow due to a damping of the ridge-trough system (Leathers et al., 1991). Shifts in PNA index are quasi-periodic, occurring approximately every 40 months (Leathers et al., 1992).

The NAO refers to changes in high and low pressure atmospheric systems in the North Atlantic (Sheridan, 2003). An amplification of sea level pressure anomalies resulting in

a stronger Icelandic Low and Bermuda High are characteristic of a positive NAO index, whereas weaker pressure systems are characteristic of a negative NAO index. An extremely negative NAO index can sometimes entail the conversion of the Icelandic Low into a weak high pressure system (Sheridan, 2003).

To examine the effects of the PNA and NAO on precipitation in Minnesota, seasonal precipitation for the Twin Cites from 1950-2017 was plotted against annual PNA and NAO indexes. Figures 2.11 and 2.12 show the trends, where values above and below 0 for PNA and NAO indexes indicate positive or negative phases, respectively. Precipitation data was collected by the MN DNR, and PNA and NAO indexes are provided by NOAA's National Weather Service Climate Prediction Center. All data was smoothed over a 5-year period to better visualize trends.

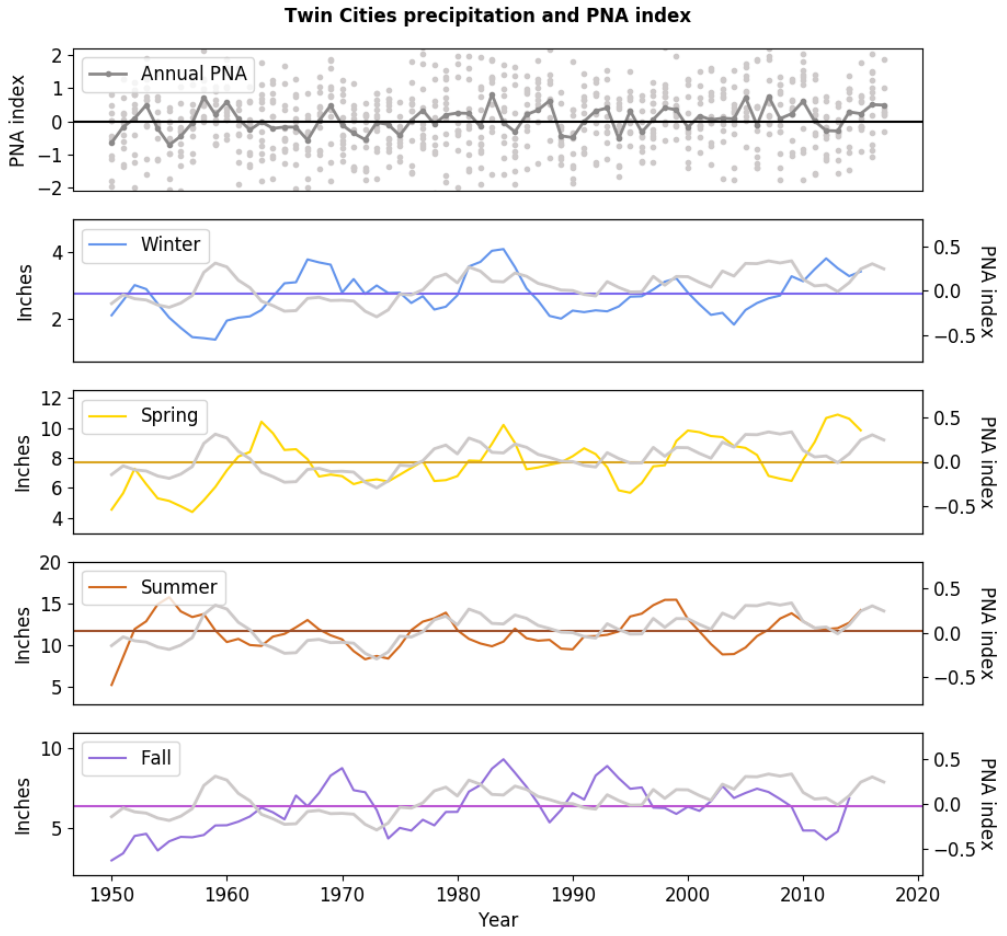

Figure 2.11: Annual PNA index and smoothed 5-year seasonal precipitation and PNA index

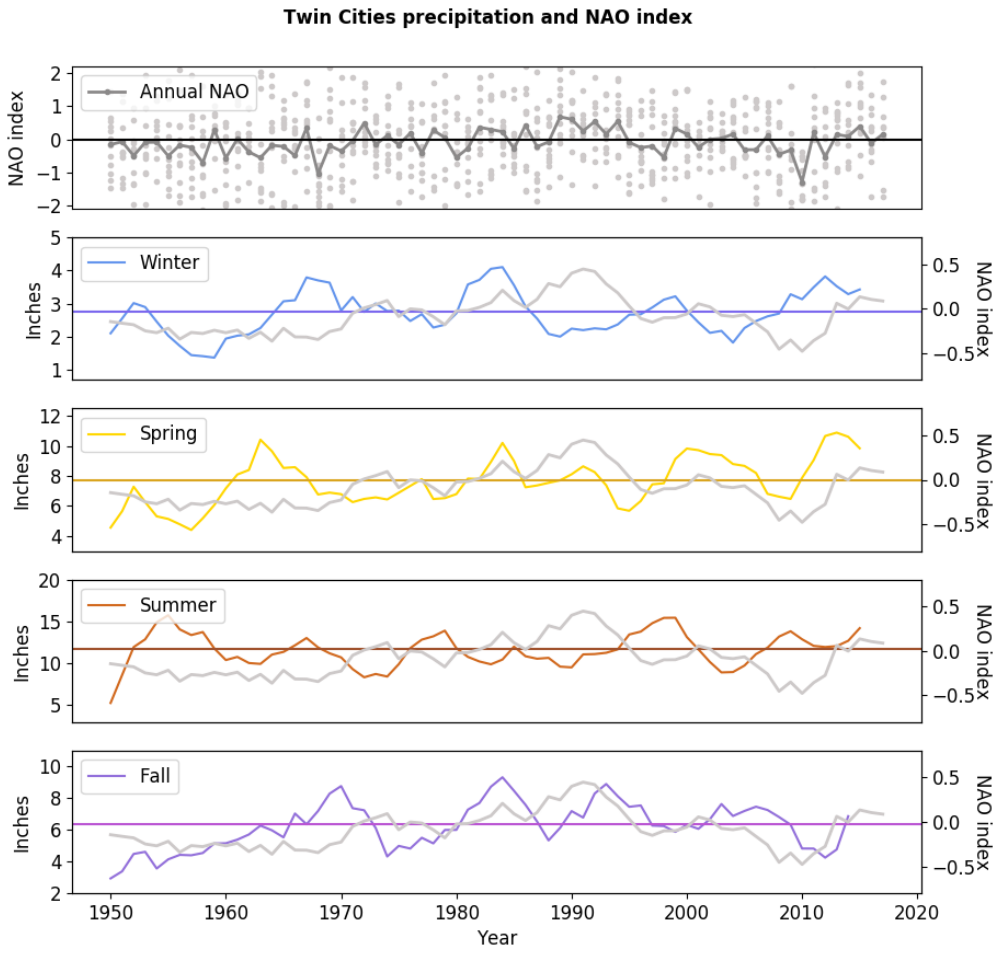

Figure 2.12: Annual NAO index and smoothed 5-year seasonal precipitation and NAO index

Summer precipitation in Minnesota appears to have the strongest correlation to PNA and NAO indexes, as shown in Figure 2.13. The highest values for summer precipitation occur during periods with negative NAO indexes and negative to mildly positive PNA indexes. Low summer precipitation occurs during periods with positive NAO indexes and positive to mildly negative PNA indexes. When summer precipitation is plotted with winter and summer PNA indexes, however, it appears that winter PNA local maxima correlate relatively well to low summer precipitation, and winter PNA local minima to high summer precipitation, as shown in Figure 2.14.

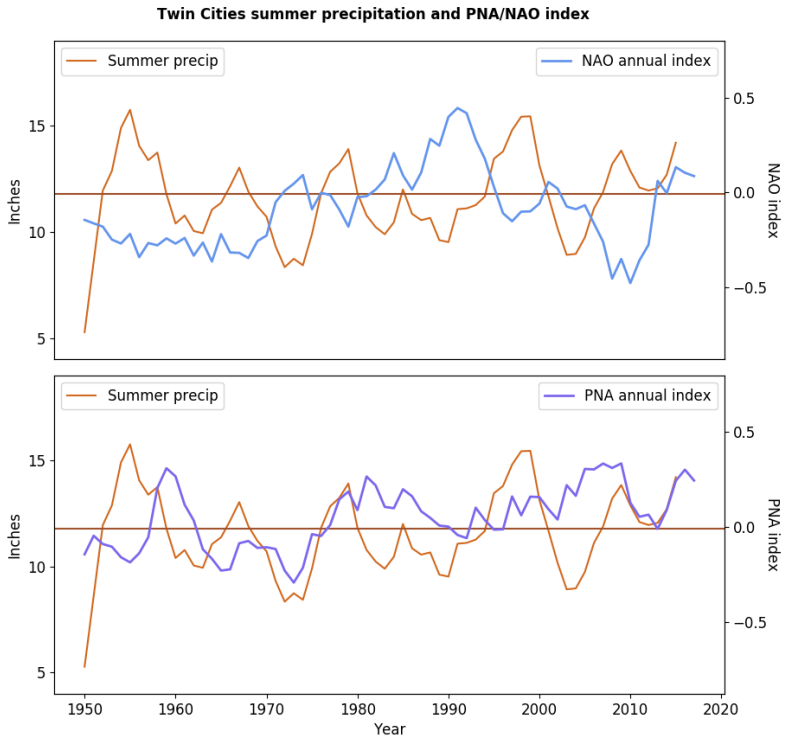

Figure 2.13: Smoothed 5-year summer precipitation, PNA and NAO indexes

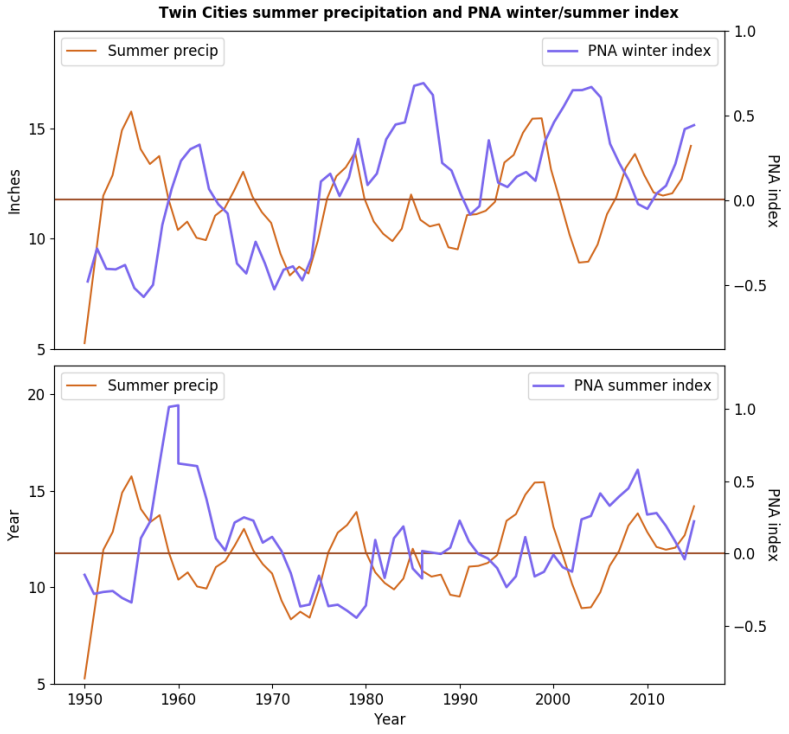

Figure 2.14: Smoothed 5-year summer precipitation, PNA winter and summer indexes

While a negative PNA results is strongly associated with an increase in zonal flow during winter months, it may have continued effects throughout the summer (Sheridan, 2003). A negative PNA index results in a strengthening in the Great Plains Low Level Jet (GPLLJ), which plays a key role in bringing Gulf of Mexico moisture into the mid-continent (Higgins et al., 1997). The GPLLJ is responsible for heavy rainfall events during summer months, which occur primarily nocturnally. Low level inflow from the Gulf of Mexico is up to 45% higher during GPLLJ events than average nocturnal rainfall (Harding et al., 2013). The PNA is responsible for over a third of total GPLLJ variance during the summer months (Harding et al., 2015). Additionally, PNA and NAO indexes are related, as changes in the intensity and location of the Bermuda High will result in alterations to the geopotential heights above PNA "centers of action" (Leathers et al., 1992, Harding et al., 2015). Thus changes to both PNA and NAO regimes should result in significant changes in source and amount of precipitation reaching Minnesota seasonally.

2.2 Modern stable isotopes in Minnesota precipitation

As discussed in Section 1.2.4, past changes to local hydroclimate are identified through variation in δ^{18}O isotopic values. However, interpretations are dependent upon a site's isotopic behavior towards hydroclimate variability. From 1996 to 1999, precipitation samples were collected by researchers at the UMN Stable Isotope Lab and analyzed for δ^{18}O and δD (Mohr, 2000). Stable isotopic signals were compared to temperature and precipitation data from the MN Department of Natural Resources. All samples and data were taken from St. Paul, MN.

As is seen in Figure 2.15, Minnesota experiences precipitation enriched in ^{18}O during the summer and depleted in ^{18}O during the winter. Significant snowfall occurs during winter months. The δ^{18}O value for precipitation is positively correlated to temperature. The relationship, shown in Figure 2.16, is significant (r^2 = 0.76) and has a slope of 0.466‰/ °C. This is lower than the global average of 0.7‰/ °C (Dansgaard, 1964).

Additionally, isotopic values for the Twin Cities plot extremely close to the Global Meteoric Water Line (GMWL), as shown in Figure 2.17b (Craig, 1961). This indicates minimal evaporative effects at the site. Even summer isotopic values, in which evaporative effects would be most expected, has a small associated change in slope.

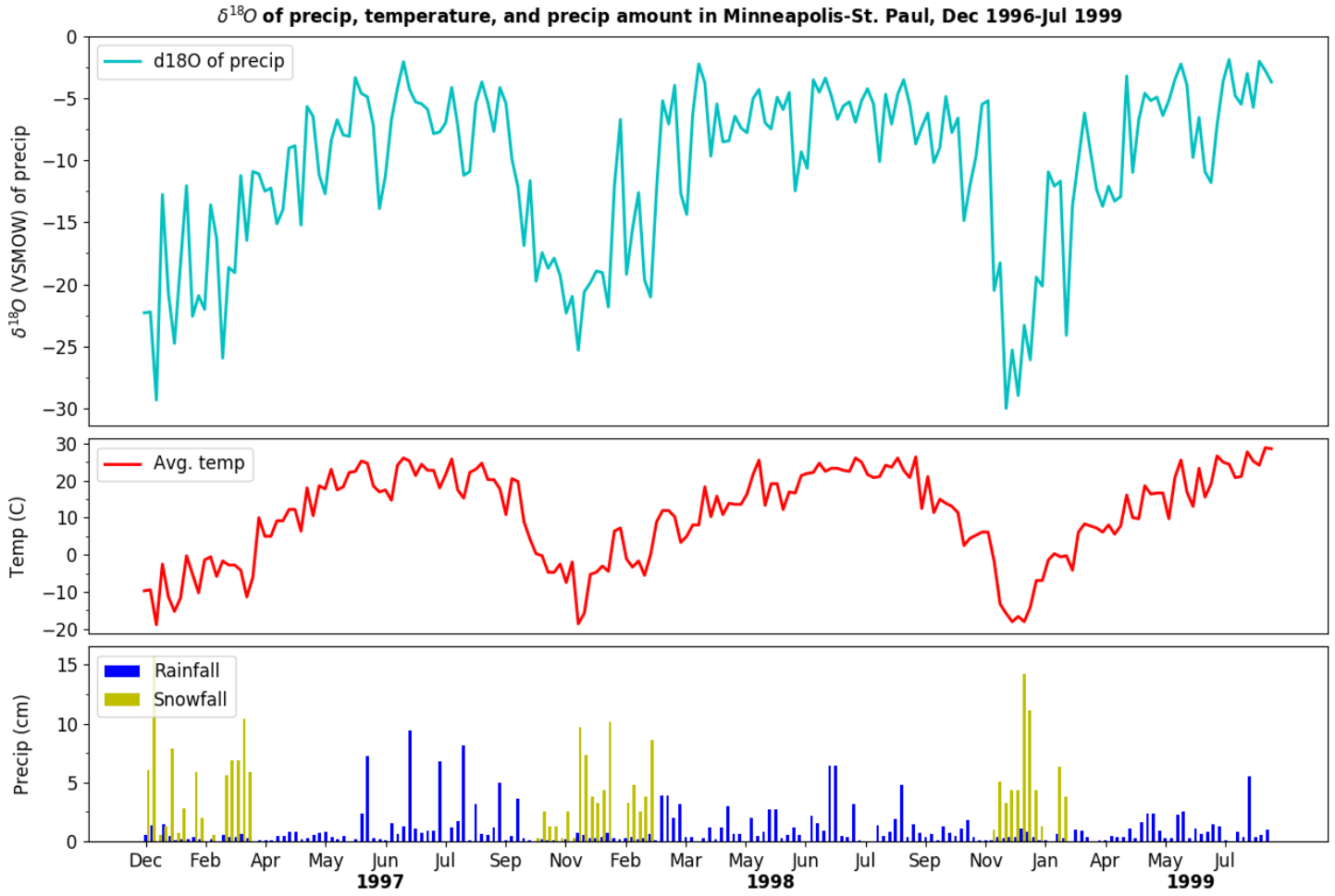

Figure 2.15: δ^{18}O, temperature, and precipitation trends from Dec 1996-Jul1999. δ^{18}O of precipitation for the Twin Cities collected by Mohr, 2000. Temperature and precipitation data from the MN DNR website.

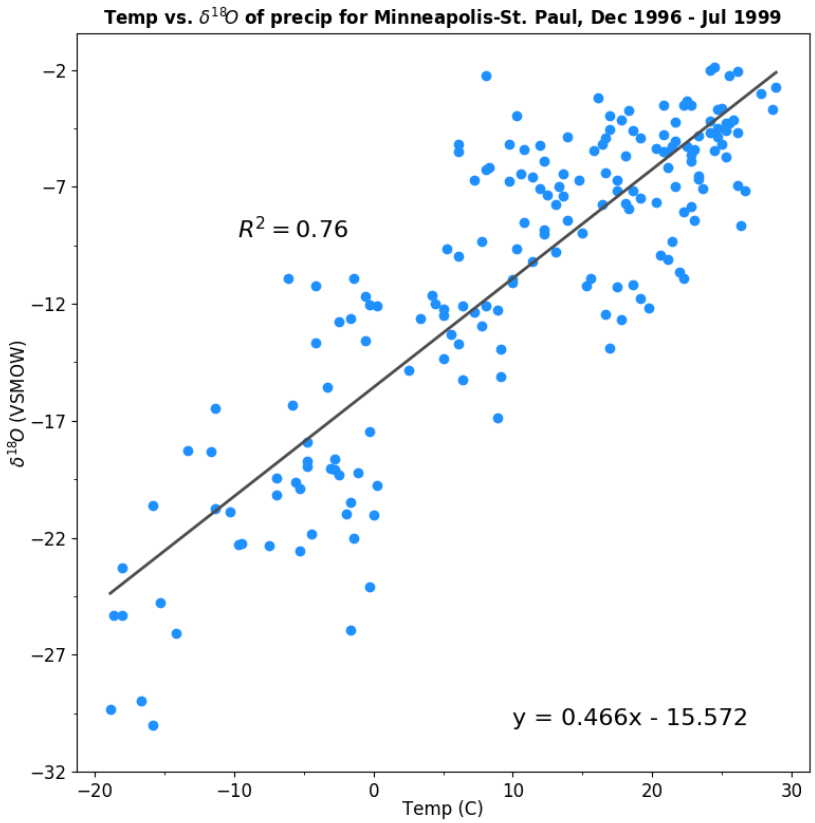

Figure 2.16: δ^{18}O of precipitation for the Twin Cities versus temperature in °C

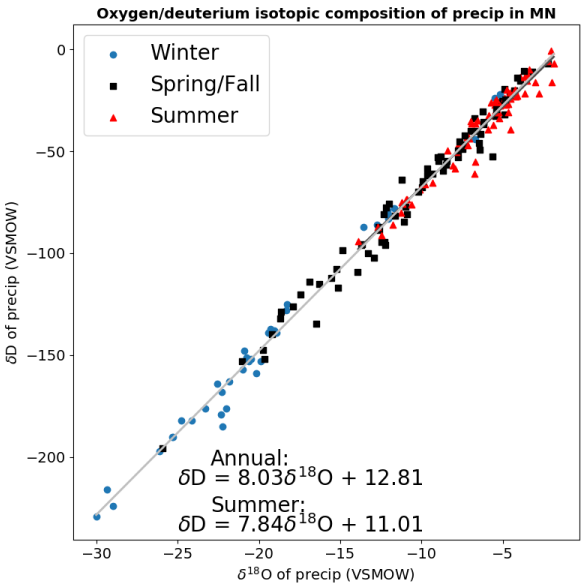

(a) Local annual and summer meteoric water line

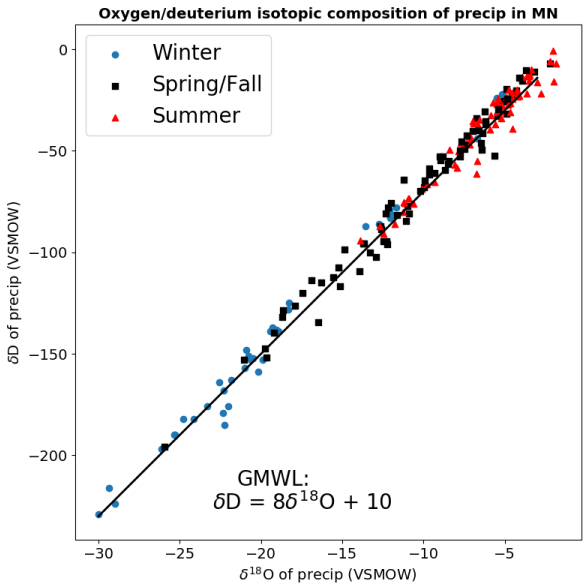

(b) Global meteoric water line

Figure 2.17: Meteoric water lines for the Twin Cities' isotopic data

Modern stable isotopic data from Minnesota shows a strong positive correlation between δ^{18}O of precipitation and temperature, and evaporation is not resulting in additional isotopic fractionation.

2.3 SE Minnesota Holocene record

Modern calcite collected at Spring Valley Caverns retains a positive correlation between δ^{18}O and mean annual temperature (r^2 = 0.43), and no significant correlation to annual precipitation (Dasgupta, 2008). The relationship between modern $\delta^{18}O_c$ and mean annual temperature (MAT) is 0.22‰/ °C. This slope matches well with predicted values: assuming the local $\delta^{18}O_{precip}$-MAT value found from modern precipitation of 0.466‰/ °C and a temperature-influenced fractionation effect between dripwater and calcite of -0.24‰/ °C, the local $\delta^{18}O_c$-MAT value should be ≈0.226‰/ °C. Thus as temperature increases one would expect an accompanying increase in $\delta^{18}O_c$.

A high resolution stable isotope record from Spring Valley Caverns has been previously compiled, and shows elevated δ^{13}C and δ^{18}O values during the mid-Holocene (Dasgupta, 2008). Assuming the $\delta^{18}O_c$-MAT relationship above, the change in $\delta^{18}O_c$ would result from a temperature increase of ≈4°C. This is significantly larger than the pollen-reconstructed 1-2°C change, thus it was determined additional factors must be present. The accompanying increase in δ^{13}C values indicates regional dry conditions may be causing elevated stable isotopic profiles.

Additionally, both δ^{13}C and δ^{18}O of calcite in Spring Valley Caverns show abrupt increases during the 8.2 ky cold event (Dasgupta, 2008). This cold event was a result of draining of glacial lakes into the North Atlantic, which created a freshwater cap and weakened the AMOC. Like abrupt climate events during the last glacial period, the 8.2 ky event was recorded in paleorecords across the Northern and Southern Hemispheres (Cheng et al., 2009). Figure 2.18 shows the δ^{13}C and δ^{18}O record of Spring Valley Caverns sample SVC983-2 (Dasgupta, 2008). The figure includes the composite Greenland NGRIP and GRIP record and the abundance of *N. Pachyderma*, indicating the abrupt decrease in North Atlantic temperatures (Vinther et al., 2006, Ellison et al., 2006). The shaded region shows the duration of the 8.2ky event.

The shift in Spring Valley Caverns stable isotope profiles during the event is corroborated by increasing aridity recorded in Moon Lake, ND and Kirchner Marsh, MN (Dasgupta, 2008 *and references therein*). These results were interpreted to indicate warm, dry conditions

in the region during Holocene North Atlantic cooling events. However, if the 0.22‰/°C relationship of calcite to MAT holds true, the 1‰ increase in δ^{18}O would indicate a 4.5° C increase in temperature. Such a localized temperature increase in mid-continental North America during a Northern Hemisphere cooling event seems improbable. Thus while elevated δ^{18}O values of calcite at Spring Valley Caverns may indicate aridity, it is questionable that they are also recording changes in temperature.

The drivers for isotopic variability at Spring Valley Caverns will be further explored in Chapter 3, where a new high resolution record will help clarify reasons for changes in δ^{18}O and δ^{13}C values of Spring Valley calcite.

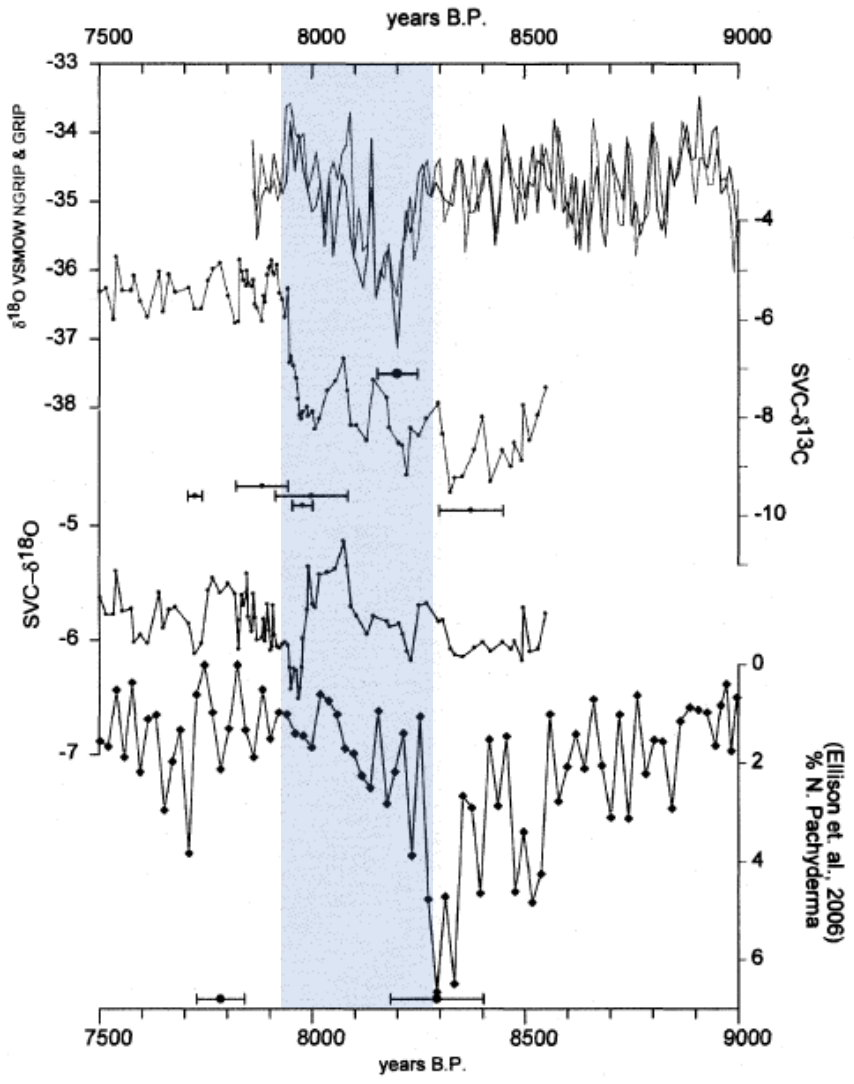

Figure 2.18: Evidence of 8.2 ky event in Spring Valley Caverns and North Atlantic from sample SVC983-2

Chapter 3

Climate Variability during the Late Pleistocene in SE Minnesota

3.1 Introduction

There is a current lack of high resolution paleoclimate records from the last glacial period in the upper mid-continent. Determining how long term and abrupt climate change affected this region is crucial in determining atmospheric teleconnections across North America.

Here we present growth histories of six speleothem samples from 114 - 29 ky BP, and high resolution stable isotope records from 104 - 29 ky BP. Previous studies presented low resolution records that showed potential correlation to global climatic events, but precluded robust interpretation (Shapiro, 2007, MacKinney et al., 2013). This study used high precision ^{230}Th dating and analysis of confocal fluorescence to determine well constrained growth histories, linking them to regional and global paleoclimatic trends. High resolution stable isotope analysis showed long term changes across the late Pleistocene suggesting changes in vegetation, temperature, and moisture availability. Higher frequency variability showed impressive synchroneity with records worldwide, illustrating the effects of abrupt North Atlantic climatic events on the mid-continent. We compare growth histories and stable isotopic records to global climate records to suggest possible oceanic and atmospheric dynamics that may have driven both short and long term climate variability in SE Minnesota.

3.2 Study Site

Samples used in this study were taken from Spring Valley Caverns, located in Fillmore County in SE Minnesota (43°44'N, 92°24'W). The caverns are developed within the upper Ordovician Galena group, within the Stewartville and Dubuque carbonate formations (Denniston et al., 1999b, Alexander et al., 2009). The cave was discovered in 1966, and after extensive work by John Ackerman following his acquisition of the caverns in 1989, over 9 km has been opened (Alexander et al., 2009). The system is currently active, and lies within the Root River watershed. Average atmospheric temperature and average cave temperature at Spring Valley are 6.5°C and 8.3°C, respectively (Dasgupta, 2008).

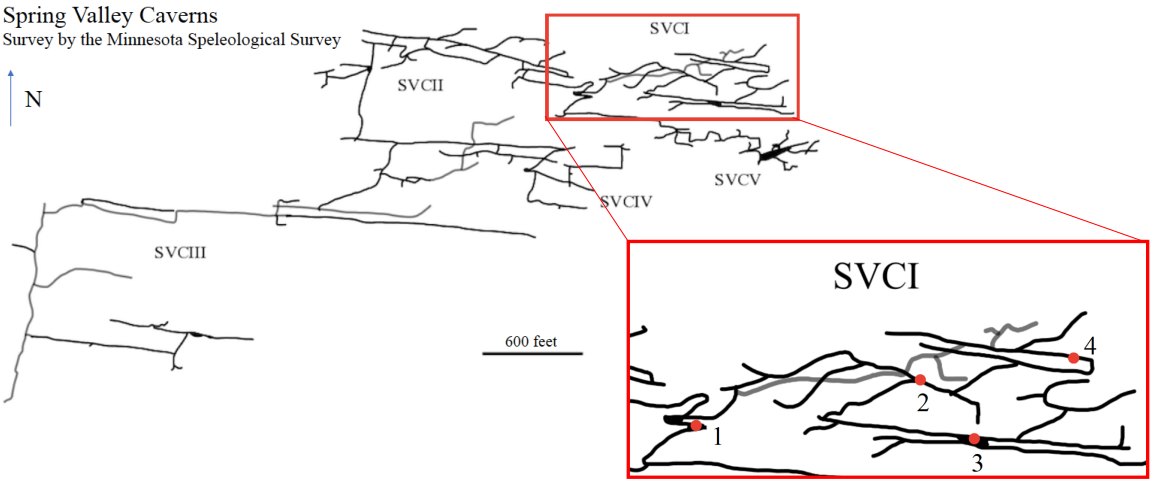

Figure 3.1: Map of Spring Valley Caverns. Modified from survey plot by David Gerboth, Minnesota Speleological Survey, 2010. Numbers refer to the location of samples used in this study. 1. Hoodoo Chamber, location of sample SVC05. 2. Medusa, location of sample SVC16-2A and SVC16-2B. 3. Resting Room, location of sample SVC16-1. 4. Location of sample SVC06, near entrance to SVCI. Sample SVC99-1d was a flowstone removed from the cave in 1999, from SVCI.

The cave consists of five sections, and passages lie along NW-SE joint lines (Alexander et al., 2009). Samples for this study came from chambers along SVCI, shown in the blow-up of Figure 3.1.

3.3 Previous work

Previous low resolution sampling has been done on both SVC06 and SVC05. In 2007, 16 ^{230}Th dates were determined at the UMN Isotope Lab for sample SVC06 using SEM measurements. Additionally, 103 stable isotope samples were analyzed at the Paleoenvironment and Neotectonics Labratory at the National University of Taiwan. The stable isotope record showed potential correlation to other paleorecords, but low sampling resolution precluded robust analysis (Shapiro, 2007, Dasgupta, 2008).

Additionally, a total of 12 ^{230}Th dates were analyzed at the UMN Isotope Lab for sample SVC05 using SEM measurements in 2008 and 2013. Eighty stable isotope samples were analyzed at the UMN Stable Isotope Lab. Various growth phases for the sample were imaged using confocal microscopy at the UMN Imaging Centers. Analyses showed an enrichment in δ^{18}O and a depletion in δ^{13}C throughout the sample growth, interpreted as a transition from warmer to cooler climate throughout the last glaciation (MacKinney et al., 2013). However, better constraint on short term growth phases of the sample could improve results and cast light on hydrological drivers of speleothem growth.

3.4 Methods

3.4.1 Sample collection

Sample SVC06 is a 615 mm sample taken in 2006 near the cave entrance of SVCI (Shapiro, 2007). The sample had been previously broken at the base. Sample SVC05 is 218 mm, and was collected in 2005 from the Hoodoo Chamber (MacKinney et al., 2013). To expand growth histories, four additional samples from Spring Valley Caverns were analyzed. SVC991d was part of a flowstone collected in the caverns in 1999. Samples SVC16-1, SVC16-2A and SVC16-2B were collected in 2016, and were all previously broken stalagmites. Samples SVC16-2A and SVC16-2B were connected at the base, and separated during sample preparation. Locations of samples in Spring Valley are shown in Figure 3.1.

In 2016, field work was conducted at Spring Valley Caverns with the support of John Ackerman to test for samples that would be of use in paleoclimate reconstruction. Four previously broken stalagmites were tested for bottom dates (SVC16-1, SVC16-2, SVC16-3 and SVC16-4). These samples were cored at the base along the growth axis using a battery-powered hand held drill and an Applied Diamond diamond tile drill with a water attachment. The diamond tile drill produced calcite cores approximately 8 mm in diameter.

Samples were tagged and left in place. Cores were returned to the UMN Isotope Lab, where they were sonicated to remove excess organics and processed to determine bottom dates. Samples SVC16-1 and SVC16-2 were deemed most promising due to growth periods and low detrital concentration, and removed from the cave. Both were located in SVCI. Each sample had an interior slab removed using a diamond saw, and the remaining speleothem was reformed and returned to Spring Valley. We believe this method of testing best ensures cave preservation.

All samples used for dating were cut along the growth axis using a diamond tile saw, and polished via a wet stone polisher to remove contaminants and prepare the surface for imaging. Slabbed samples were mounted in epoxy resin for stabilization.

3.4.2 ^{230}Th dating

Powdered calcite for ^{230}Th dating was collected perpendicularly to the growth axis of the sample using carbide dental burs. Sample size ranged from 20-250 mg, depending on the sample and the measurement method used. Sampling from layers with distinct color changes, often indicative of hiatuses in growth, were avoided. The collected powder was dissolved with weak acid, spiked, and processed to separate U and Th using the chemistry methods outlined in Edwards et al., 1987. U and Th solutions were analyzed on a Thermo Scientific Neptune or Neptune Plus multi-collector inductively-coupled plasma mass spectrometer (MC-ICP-MS) using either a secondary electron multiplier (SEM) or Faraday cups. Experimental methods are more fully described in Appendix A.2.

All U and Th data were reduced to produce ^{230}Th ages using new *Python* data reduction programs. These programs are discussed in Appendix B. Age models were made for sample SVC06 and the first growth phase of sample SVC05 using the *Python* package *Speleopy* (Cross, 2016). This program uses Monte Carlo modeling to produce acceptable age simulations. For short growth phases of sample SVC05, ages were constrained using ^{230}Th ages and confocal band counts. Example of stages in age modeling are shown in Figure 3.2 for sample SVC06 and the first growth phase of SVC05.

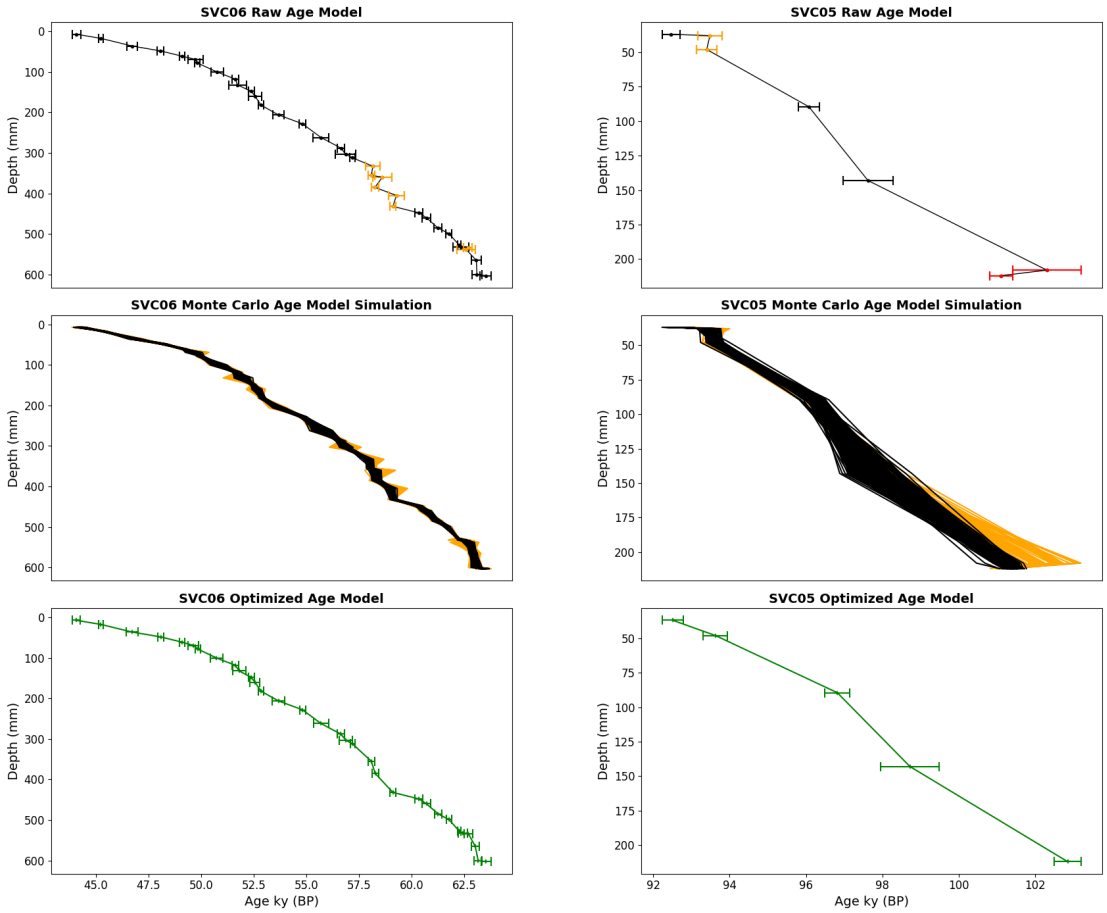

(a) Age modeling for SVC06

(b) Age modeling for SVC05

Figure 3.2: Speleopy age model results for SVC06 and first growth phase of SVC05

3.4.3 Confocal imaging

Growth phases for sample SVC05 were imaged using a Nikon A1RMP microscope at the University of Minnesota Imaging Center. To achieve maximum resolution at high efficiency, a 20x objective was used with excitation/emission wavelengths of 488/525 nm.

Confocal imaging and manual band counting had been done previously at lower resolution on three growth phases (MacKinney et al., 2013). For this study, high resolution confocal imaging was completed for all growth phases. Additionally, a previously unidentified growth hiatus was found at 182 mm above base, resulting in a total of 7 growth phases for sample SVC05.

To determine length of growth hiatuses, a new method of automatic band counting using

Python programs was tested against previous manual band counting. It was determined that filtering local maxima provided comparable results to band counting in growth phases 5 and 6, and better matched ^{230}Th ages in growth phase 3 than manual band counting. This method was used to estimate length of growth phases 2-6, which were then tied to the most accurate ^{230}Th age. This method is described fully in Appendix A.3, with accompanying images. Growth phase 7 did not contain banding, and only ^{230}Th ages were used.

3.4.4 X-ray Diffraction analysis

Powdered samples were analyzed via X-ray diffraction (XRD) to determine primary mineralogy for samples SVC06 and SVC05. As SVC06 shows continuous growth, two samples were taken at varying depths to confirm no change in mineralogy occurred. Samples were taken at each growth phase of sample SVC05. This resulted in a total of 9 samples of approximately 10-20 mg. These were analyzed at the University of Minnesota Characterization Facility.

3.4.5 Stable isotopes

Subsamples for stable isotopes were taken for SVC06 and SVC05. Subsamples weighing < 0.5 mg were hand-drilled along growth axis, at a sampling resolution of 0.75-3 mm for SVC06 and 0.5-5 mm for SVC05. Analyses were performed at Xi'an Jiatong University using a Thermo-Finnigan-MAT 253 mass spectrometer fitted with a Kiel IV Carbonate Device. Stable isotope results were compiled with previous analyses for sample SVC05. Values are reported in per mille relative to the Vienna Pee Dee Belemnite (VPDB) standard. Standard deviation for δ^{18}O and δ^{13}C were 0.02‰ and 0.03‰, respectively.

Stable isotope values were assigned ages in years BP using the University of Oxford's OxCal program. Optimized age models were submitted for all growth phases, with ages between dated points interpolated linearly. Stable isotope subsamples were then correlated to age models based on depths. After ages were determined, oxygen isotope values were corrected for historical changes in mean seawater composition using the *Python* package *Speleopy* (Cross, 2016).

3.5 Results

3.5.1 ^{230}Th dating

30 new dates were obtained for sample SVC06 using SEM measurements. ^{238}U concentrations range from 2.3 to 7.1 ppm, with ^{232}Th concentrations ranging from 46 to 2533 ppt. 2σ age uncertainties range from 2-5‰. Complete age data are available in Table A.1. Sixteen new dates were obtained for sample SVC05 using both SEM and cups measurements. Eight subsamples were run with both U and Th on SEM, and 8 were run with U on Faraday cups and Th on SEM. ^{238}U concentrations range from 0.4 to 1.4 ppm, with ^{232}Th concentrations ranging from 330 ppt to 128 ppb. The 2σ age uncertainties on SEM range from 2-4‰, with the sample with a ^{232}Th concentration of 128 ppb reaching an age error of 4% due to contamination. The 2σ age uncertainties range with U on cups and Th on SEM range from 2-8‰. Complete age data are available in Table A.2.

Additionally, 35 dates were completed for samples SVC16-1, SVC16-2A, SVC16-2B and SVC991d. Top-bottom dates were run on SEM, with 2σ age errors ranging from 2-9‰. All additional dates were analyzed with both U and Th on Faraday cups, and achieved 2σ age errors as low 0.6‰.

Age models were created for samples SVC06 and SVC05, for use in calculating stable isotope ages. Sample SVC06 shows continuous growth from 44 - 64 ky BP. Sample SVC05 shows continuous growth in its first growth phase, from 103 - 92.5 ky BP, and then experiences six short growth phases. Ages were constrained for short term growth phases using ^{230}Th ages and confocal results. Age-depth models are shown for both samples in Figure 3.3.

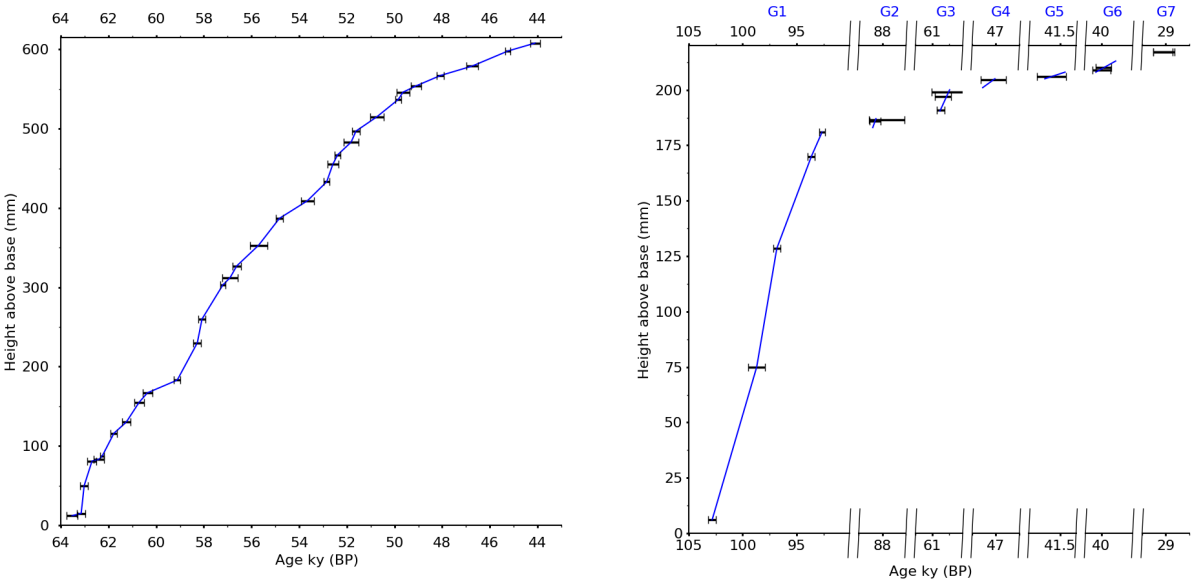

(a) Optimized age model for sample SVC06

(b) Optimized age model for sample SVC05

Figure 3.3: Age model results from ^{230}Th dating and confocal imaging for samples SVC06 and SVC05

3.5.2 Confocal imaging

Results from automatic band counting resulted in improved age estimates for SVC05 growth phases 2-6. Methods and results for automatic counting are presented in Appendix A.3. Banding is present but not well defined in growth phase 2. Maxima reduction analysis resulted in a band count of 135. If count is annual and anchored to the ^{230}Th age with the lowest error, this would result in an age range of 88.41 - 88.27 ky BP. Growth phase 3 shows prominent and well-defined banding, suggesting annual layering is present. Manual band counting had been done previously and resulted in a count of 460. However, maxima reduction analysis showed a significantly lower count of 283, which more closely matched the ^{230}Th ages. When tied to ^{230}Th ages, confocal banding suggests an age range of 60.77 - 60.49 ky BP. Growth phase 4 shows banding, though with significant scattering. Maxima reduction analysis resulted in a band count of 259. If anchored to the ^{230}Th age with the lowest error, this resulted in an age range of 47.28 - 47.02 ky BP. However, this range does not correlate to ^{230}Th ages near the base of the growth phase, suggesting banding is not annual or a hiatus is present. Growth phases 5 and 6 clearly show banding, and band counts through maxima reduction analysis and manual counting result in similar values. Growth phase 5 has an automatic count and manual count of 128 and 120, respectively, which if anchored to ^{230}Th ages results in an age range of 41.60 - 41.47 ky BP. Growth phase 6 has an automatic count and manual count of 251 and 250, respectively, and if anchored to ^{230}Th

ages 40.07 - 39.82 ky BP. Banding was not present in growth phase 7.

In addition to providing more accurate growth durations, this method suggests that automatic band counting with filtration may be a promising replacement for manual counting. For growth phases 5 and 6, automatic band counting produced almost the same results as manual band counting. Additionally, for growth phase 3 automatic band counting resulted in a band count that more closely matched ^{230}Th ages than manual band counting. As manual band counting is both tedious and time consuming, the use of automatic band counting should be considered in future studies.

3.5.3 X-ray Diffraction analysis

All subsamples from SVC06 and SVC05 showed calcite mineralogy. No change was determined for sample SVC06, or between growth phases in SVC05. Results of analysis are shown in Appendix A.4.

3.5.4 Stable isotopes

Through this study, stable isotope sampling resolution was significantly improved for SVC06 and SVC05. Stable isotope profiles for sample SVC06 show considerably more structure at higher sampling resolution, particularly in the the δ^{18}O record. This is apparent in Figures 3.4 and 3.5. Better constraint of SVC05 growth phases through additional ^{230}Th ages and improved confocal analysis resulted in changes to the sample's previous stable isotope data, as seen in Figures 3.6 and 3.7.

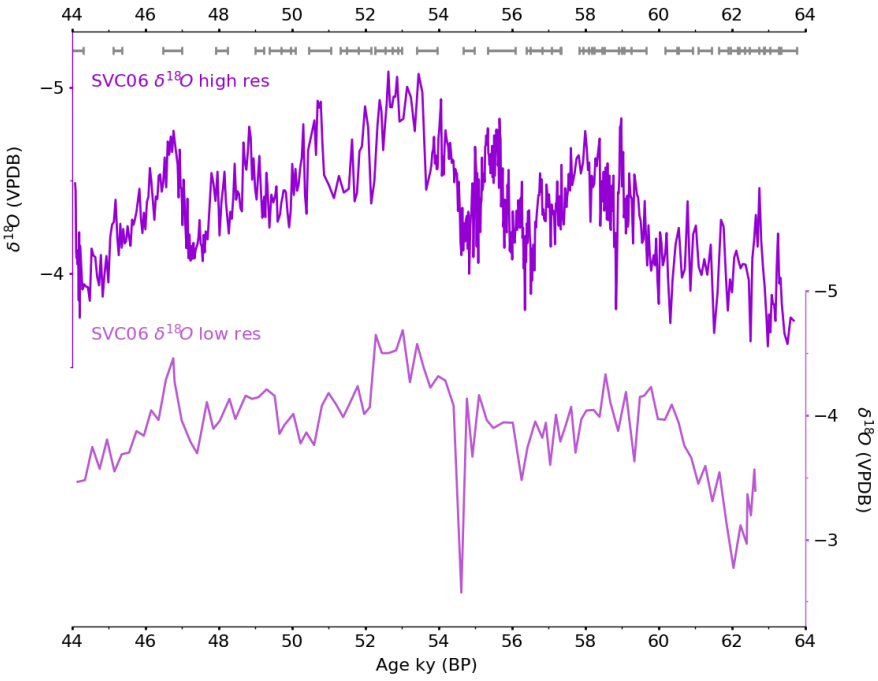

Figure 3.4: Improvement of δ^{18}O sampling resolution for SVC06. Previous low resolution sampling was completed by Shapiro, 2007.

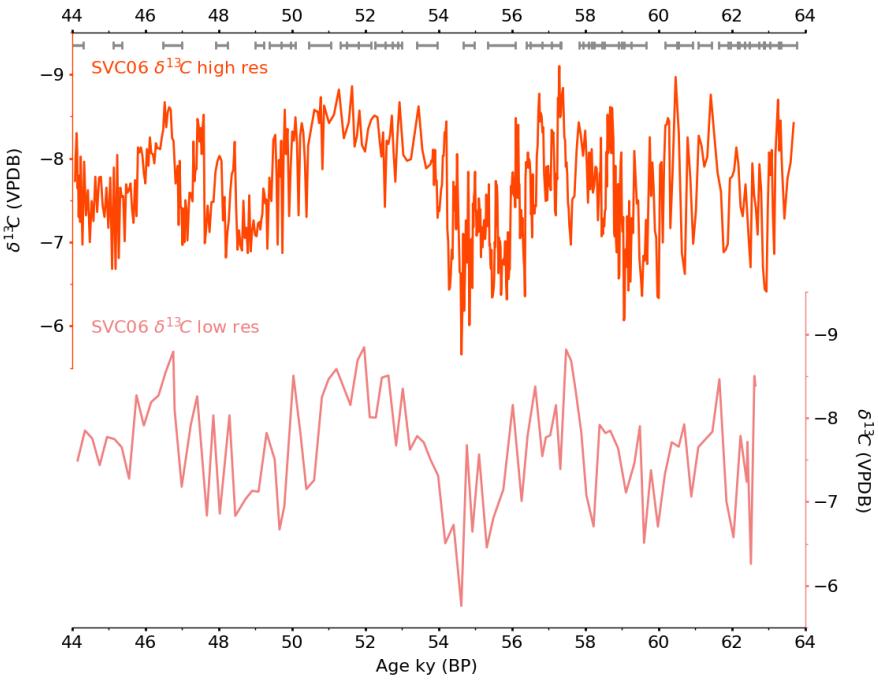

Figure 3.5: Improvement of δ^{13}C sampling resolution for SVC06. Previous low resolution sampling was completed by Shapiro, 2007.

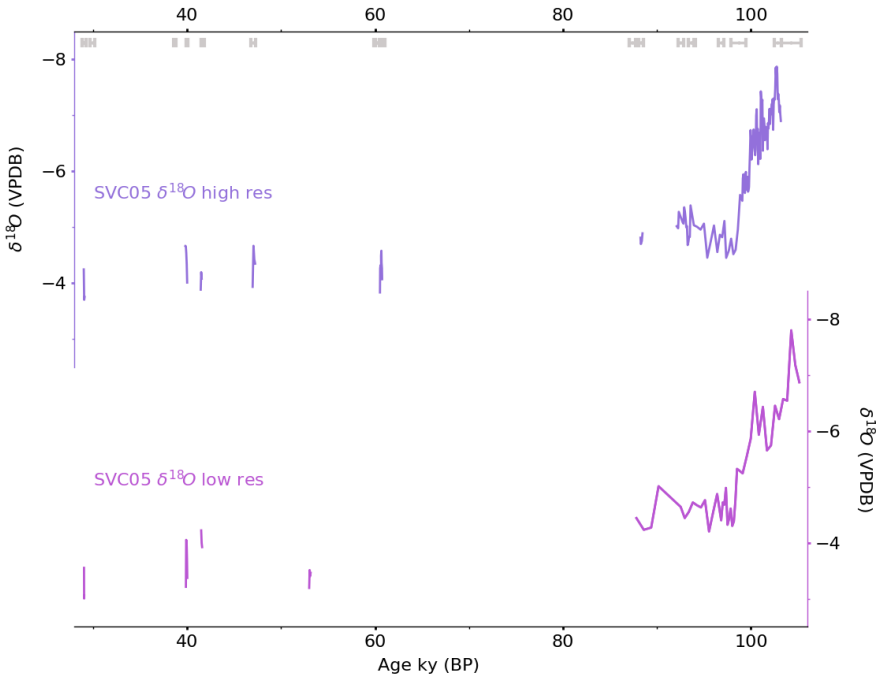

Figure 3.6: Improvement of δ^{18}O sampling resolution for SVC056. Previous low resolution sampling was completed by MacKinney et al., 2013.

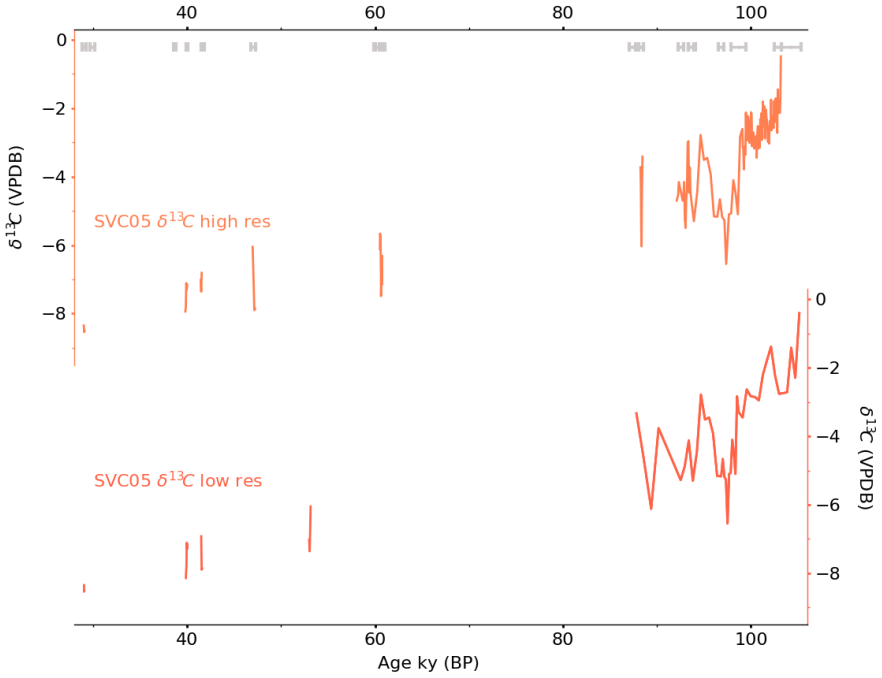

Figure 3.7: Improvement of δ^{13}C sampling resolution for SVC05. Previous low resolution sampling was completed by MacKinney et al., 2013.

The isotopic series from SVC06 extends from 63.68 - 44.08 ky BP. During this time, the δ^{18}O fluctuates between -5.08‰ and -3.61‰. The δ^{13}C ranges from -9.1‰ to -5.6‰. Sample SVC05 sees a large change in δ^{18}O and δ^{13}C during its first growth phase, with δ^{18}O values increasing from -7.9‰ to -4.4‰ and δ^{13}C values decreasing from -0.5‰ to -6.5‰. For the composite record, δ^{18}O values increase and δ^{13}C values decrease as the record nears the Last Glacial Maximum around 21 kyr BP. The composite stable isotope record for samples SVC06 and SVC05 are shown in Figure 3.8.

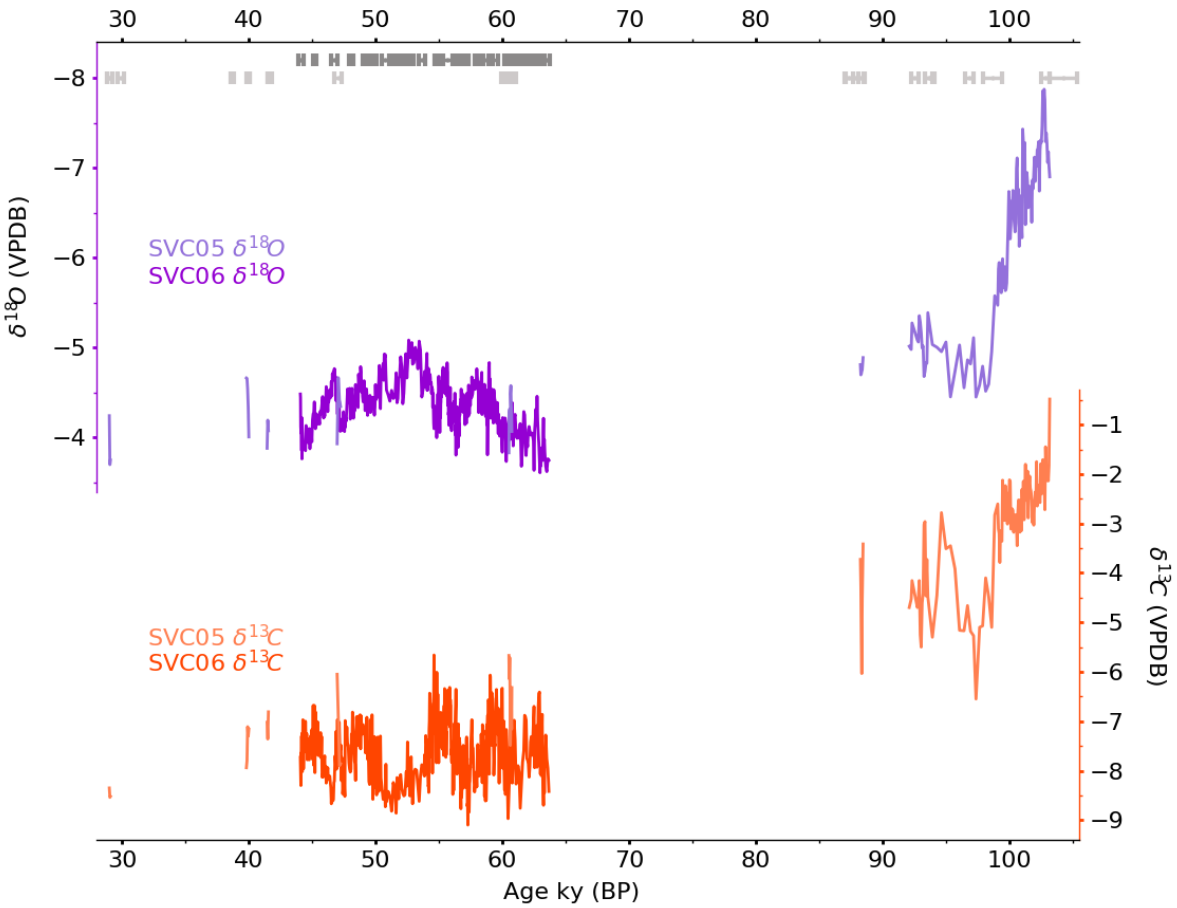

Figure 3.8: δ^{18}O and δ^{13}C records for samples SVC06 and SVC05. Note that the δ^{18}O axis is inverted, with values increasing as you move down the axis.

SVC06 and SVC05 do not appear to be affected by kinetic fractionation during deposition. Multiple subsamples from an individual growth layer in SVC05 were previously collected and analyzed for δ^{18}O and δ^{13}C variation (MacKinney et al., 2013). If kinetic fractionation occurred through rapid degassing of CO_2, the growth layer should show enrichment in both δ^{18}O and δ^{13}C values (Hendy, 1971). No positive correlation between stable isotope values was seen, indicating deposition under closed conditions. Sample SVC06 shows no positive

correlation between δ^{18}O and δ^{13}C values, negating the possibility of kinetic fractionation. The composite record, in particular the first growth phase of sample SVC05, actually shows a statistically significant negative correlation between δ^{18}O and δ^{13}C values. This is seen in Figure 3.9, where the r^2 value is minimal for SVC06 (0.03) but significant for SVC05 (0.71). This suggests that climatic conditions above the cave site were causing the increase in δ^{18}O values and the decrease in δ^{13}C values throughout the last glacial period.

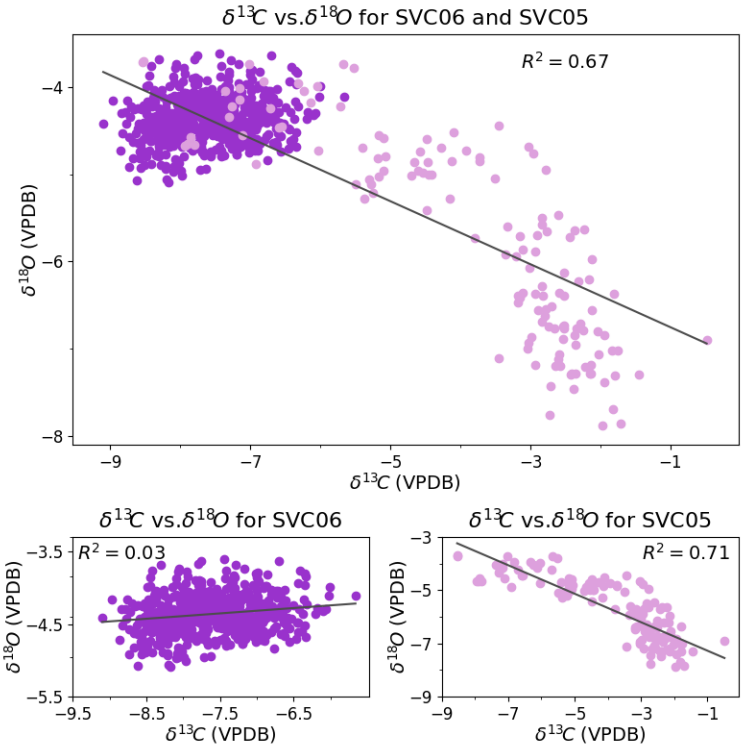

Figure 3.9: Correlation δ^{18}O and δ^{13}C for the composite record, SVC06, and SVC05.

The composite stable isotope record for SVC06 and SVC05 shows long-term changes in both δ^{18}O and δ^{13}C values. Additionally, sample SVC06 shows significant short term variability. Isotopic values for contemporaneous ages between SVC05 and SVC06 appear to correlate well, indicating that both samples record cave-wide isotopic variability, and are not drip specific.

3.6 Discussion

3.6.1 Growth phases

Growth in Spring Valley Caverns is largely constricted to periods of heightened summer monsoon intensity and increased Greenland temperatures. Composite records from Eastern

China have been shown to vary in $\delta^{18}O$ values with the strength of the East Asian summer monsoon (EASM), with depleted values indicating a strengthened monsoon regime (Cheng et al., 2012). Oxygen isotopic values in Greenland ice cores are determined by temperature of condensation, and thus elevated $\delta^{18}O$ values indicate warmer mean temperatures (Dansgaard et al., 1975). These growth phases appear to roughly correlate to periods of low global ice volume, as indicated by low benthic $\delta^{18}O$ values (Lisiecki et al., 2005).

The start of Spring Valley growth phases correlates extremely well to Greenland interstadials (GIS). Samples show growth commencement at times synchronous to GIS 25, 23, 22, 21, 12, 10, 9, 4, as defined by Rasmussen et al., 2014 and shown in Figure 3.10.

Interestingly, four of the six Spring Valley samples experienced beginning of growth in the middle of MIS4, which is the only time period within the record that is not well correlated to a Greenland interstadial event. Regional pollen and ostracode records from Raymond Basin, IL, indicate a transition to a more moist climate around 60 ky BP, suggesting an increase in precipitation may have spurred Spring Valley growth (Curry et al., 2000). Additionally, a pedothem record from Wind River Basin, WY, shows elevated $\delta^{18}O$ values from 70 - 55 ky BP. While Wind River Basin currently receives a majority of its moisture in the late spring from Pacific-based sources, the isotopically-enriched Pleistocene record was interpreted as an increase in Gulf of Mexico sourced summer precipitation (Amundson et al., 1996). This is thought to be due to increased anticyclonic activity over the heightened Laurentide ice sheet in the NE, which resulted in a dominance of southerly summer winds in the mid-continent (Oerter et al., 2016). An example of this scenario relative to present is shown in Figure 3.11.

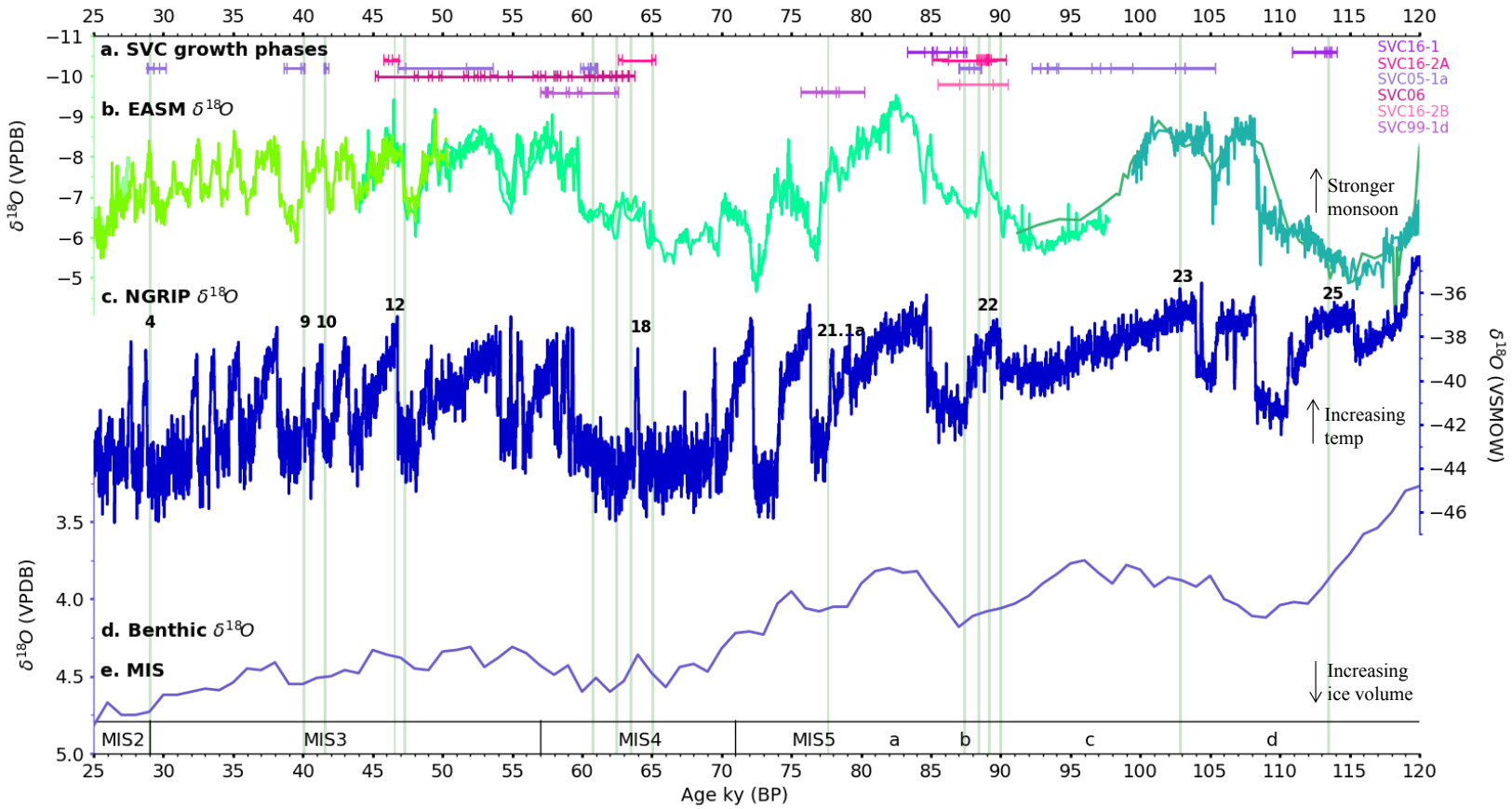

Figure 3.10: Growth history in Spring Valley of 6 speleothem samples compared to speleothem, ice core, and benthic δ^{18}O records. Vertical bars demarcate the beginning of sample growth. A) Growth periods of samples SVC16-1, SVC16-2A, SVC05, SVC06, SVC16-2B, and SVC99-1d. B) Composite record of East Asian Monsoon intensity (Y. Wang et al., 2001, Yuan et al., 2004, Kelly et al., 2006). C) NGRIP using GICC05modelext timescale (Rasmussen et al., 2014). Numbers of GIS that correspond to SVC growth phases are shown. D) LR04 stacked benthic record (Lisiecki et al., 2005). E. Marine Isotope Stages (MIS), defined by Lisiecki et al., 2005

.

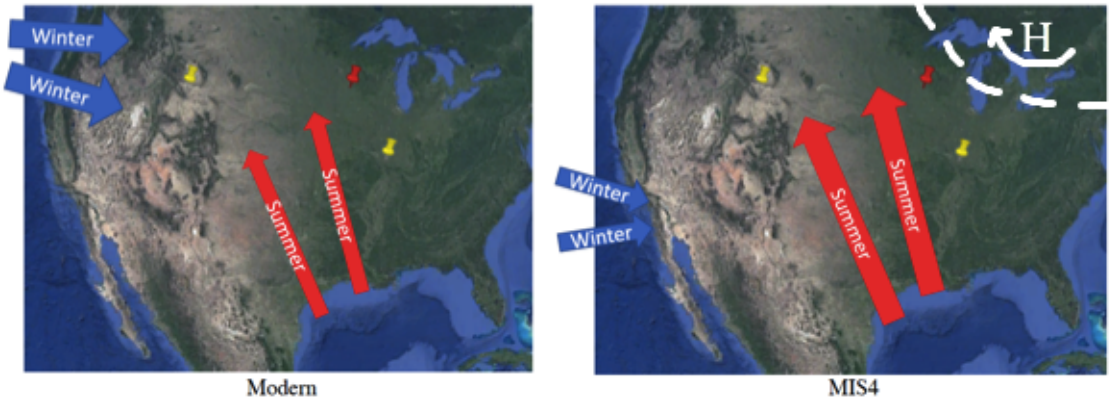

Figure 3.11: Atmospheric circulation scenarios for modern versus MIS4, adapted from Oerter et al., 2016. Pins show the locations of Wind River Basin, WY, Raymond Basin, IL and Spring Valley Caverns, MN. The MIS4 scenario includes the extent of the Laurentide ice sheet, and includes the high pressure anomaly and resulting anticylonic behavior.

Correlation between speleothem formation in Spring Valley Caverns and Greenland interstadial events suggests that above freezing temperatures and adequate moisture supply at Spring Valley allowed for drip water to enter the caves. The behavior of the Spring Valley system during MIS4 supports the idea that growth is correlated to heightened moisture delivery. As discussed in Chapter 2, SE Minnesota currently receives the majority of its moisture during the summer season. If this seasonality was maintained during the Pleistocene, warm events in the North Atlantic result in enhanced moisture delivery during the summer seasons. As global average temperatures were 2-5°C lower than modern during MIS4, and Greenland δ^{18}O values were markedly low, Spring Valley should have experienced reduced summer moisture delivery (Oerter et al., 2016). However, anticyclonic activity produced by the build up of the Laurentide in the NE throughout MIS4 resulted in anomalous intrusion of Gulf of Mexico moisture far into the mid-continent, prompting enhanced growth in Spring Valley Caverns.

3.6.2 Interpretation of Isotope Records

General trends for both δ^{18}O and δ^{13}C, shown in Figure 3.12, follow Northern Hemisphere summer insolation (NHSI) trends, with lower δ^{18}O and higher δ^{13}C corresponding to periods with elevated incoming solar radiation (Berger et al., 1991). This is particularly pronounced during the transition into MIS5-c, where both stable isotopic profiles mirror the change in NHSI. Average Holocene values for δ^{18}O and δ^{13}C were determined to be -5.36‰ and -6.70‰, respectively, based on two coeval speleothems that experienced growth from 6 ky BP to present (Dasgupta, 2008).

The δ^{13}C record experiences a decrease in values from -0.5‰ to -8.5‰ over the course of growth. Such a decrease implies a change in overlying vegetation, and a transition from C4 to C3 dominated ecosystems (Dorale et al., 1998). SE Minnesota has been shown to track ecotone borders during the Holocene, and sites farther south show ecotone transitions at the MIS 5/4 and MIS 4/3 boundaries (Denniston et al., 1999b, Dorale et al., 1998). The elevated δ^{13}C values at the start of growth at 104 ky BP indicate the presence of C4 grassland, correlating to peak NHSI and warm conditions in the Northern Hemisphere. By MIS4, δ^{13}C values in Spring Valley have dropped to ≈-7‰, indicating C3-dominated forest. This regime appears to have dominated the area until the present, with the exception of prairie encroachment during the mid-Holocene (Denniston et al., 1999b).

High resolution climate model simulations indicate that global mean annual temperatures (MAT) at the Last Glacial Maximum (LGM) were 5.9°C cooler than modern, with estimates for average temperature change in the north central United States reaching as high as 12°C (Kim et al., 2008). If the modern $\delta^{18}O_{calcite}$-MAT relationship in SE Minnesota discussed in Chapter 2 of 0.22‰/°C was unchanged during the last glacial period, one would expect a decrease in MAT of 5.9°C to be accompanied by a decrease in $\delta^{18}O$ of Spring Valley calcite of 1.3‰. If the temperature change was as large as 12°C, $\delta^{18}O$ would decrease by 2.64‰. Thus, if the oxygen isotopic record at Spring Valley were solely determined by temperature, $\delta^{18}O$ of calcite at LGM should be at least -6.6‰ and could be as low as -8‰. However, the $\delta^{18}O$ values for Spring Valley are actually higher during the last glacial period, and appear to be steadily increasing as they approach the LGM. This indicates that MAT was not the primary control over the oxygen isotopic signature at Spring Valley during the last glacial period.

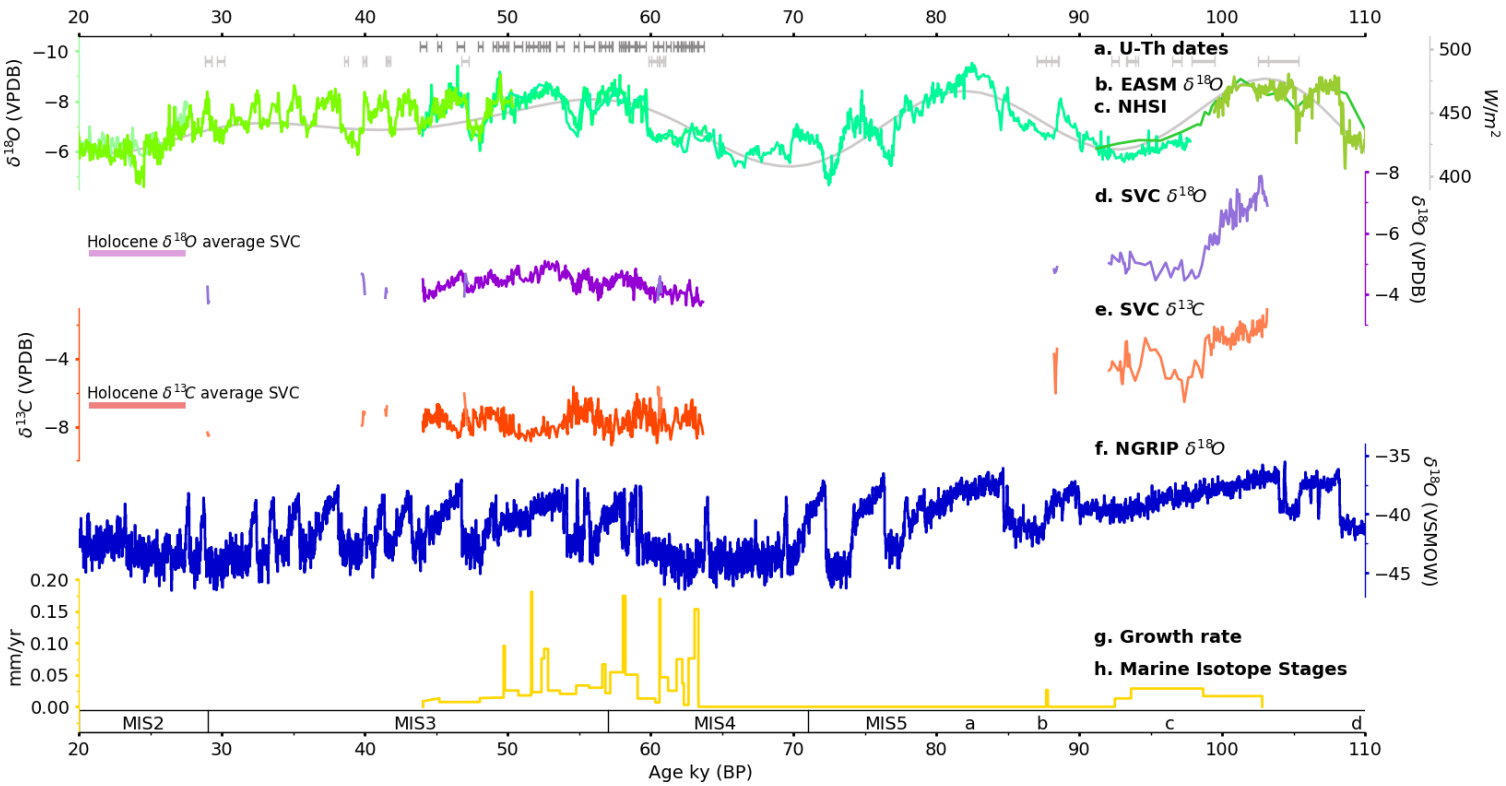

Figure 3.12: Stable isotope record for SVC05 and SVC06 compared to global paleorecords. A) ^{230}Th dates for SVC05 and SVC06. B) Composite record of East Asian Monsoon intensity (Y. Wang et al., 2001, Yuan et al., 2004, Kelly et al., 2006). C) Northern Hemisphere summer insolation (NHSI) record for Jul-65°N (Berger et al., 1991). D) Spring Valley δ^{18}O record for SVC05 and SVC06, including mean Holocene value (Dasgupta, 2008). Note that the record is inversed, with values increasing down the y-axis. E) Spring Valley δ^{13}C record for SVC05 and SVC06, including mean Holocene value (Dasgupta, 2008). F) NGRIP using GICC05modelext timescale (Rasmussen et al., 2014). G) Growth rate of SVC05 and SVC06, determined linearly. H) Marine Isotope Stages (MIS), defined by Lisiecki et al., 2005

Moisture availability and moisture source are both potential drivers for changes in $\delta^{18}O$ values. If there was a decrease in rain out during the air parcel's trajectory, this would result in higher $\delta^{18}O$ values of precipitation, as less ^{18}O has been preferentially removed. Additionally, if there was a transition to a more ^{18}O enriched moisture source, this would also lead to higher $\delta^{18}O$ values of precipitation. To explore these effects, various scenarios were modeled using *Python*. First, a general moisture source Rayleigh fractionation model was made with a $\delta^{18}O$ value of VSMOW for its moisture source signature (0.0‰). This model calculated the δ^{18}O of vapor and condensate with time by changing the fraction of original vapor remaining, using the Equations 3.1 and 3.2 where $\delta_{v,i}$ refers to the isotopic value of initial vapor and F_v is the fraction of vapor remaining (Dansgaard, 1964). As discussed in Chapter 1.2.4, α is the temperature specific fractionation factor at time of precipitation. This model has been simplified, and assumes a constant α value for each model run, rather than calculating α values throughout the moisture trajectory.

$$\delta_v = ((\delta_{v,i} + 1000) * F_v^{\alpha-1}) - 1000 \tag{3.1}$$

$$\delta_l = \alpha(\delta_v + 1000) - 1000 \tag{3.2}$$

Using these equations, the $\delta^{18}O$ values of vapor and condensate are calculated for each value of F from 1.0 to 0.0. Furthermore, the effect of temperature is modeled. For temperatures from 270 (-3.5°C) to 285K (11.85°C), the $\alpha_{l,v}$ value at time of evaporation was calculated using the relationship given by Majoube, 1971. The calculation used is shown in Equation 3.3.

$$\alpha_{evap} = e^{(1.137*\frac{10^3}{T^2})-(\frac{0.4156}{T})-(2.0667*10^{-3})} \tag{3.3}$$

From this value and the $\delta^{18}O$ of the moisture source, the $\delta^{18}O$ value of initial vapor was determined using Equation 3.4 (Rohling, 2013).

$$\delta_{v,i} = \delta_{source} - 10^3 * log(\alpha_{evap}) \tag{3.4}$$

Finally, the $\alpha_{l,v}$ at time of precipitation is calculated using the temperature given and equation found by Horita et al., 1994, shown in Equation 3.5. This fractionation factor is then used in Equations 3.1 and 3.2 to determine $\delta^{18}O$ of vapor and condensate at a specific temperature and fraction.

$$\alpha_{precip} = e^{\frac{(-7.685+6.7123*\frac{10^3}{T})-1.6664(\frac{10^6}{T^2})+0.35041(\frac{10^9}{T^3})}{1000}} \tag{3.5}$$

Additionally, models were made exploring moisture source variability. One used only Gulf of Mexico sourced moisture, with an initial $\delta^{18}O$ of 0.6‰, and one only Pacific sourced moisture, with an initial $\delta^{18}O$ of -0.5‰ (Schmidt, 1999). Again, temperature was varied

from 270 to 285K, and fraction remaining from 1.0 to 0.0. The last model looked at varying contributions of Gulf of Mexico versus Pacific sourced moisture, with varying temperature and the calculated F for average temperature and $\delta^{18}O$ in Minnesota. Contribution sources were varied from 100% Gulf of Mexico to 100% Pacific. All model runs are shown in Figure 3.13.

These simplified models illustrate that a reduction in temperature would decrease the average δ^{18}O value of precipitation considerably. However, higher δ^{18}O values can be attained relative to modern by increasing the fraction of moisture remaining regardless of moisture source, or by increasing the proportion of Gulf of Mexico moisture.

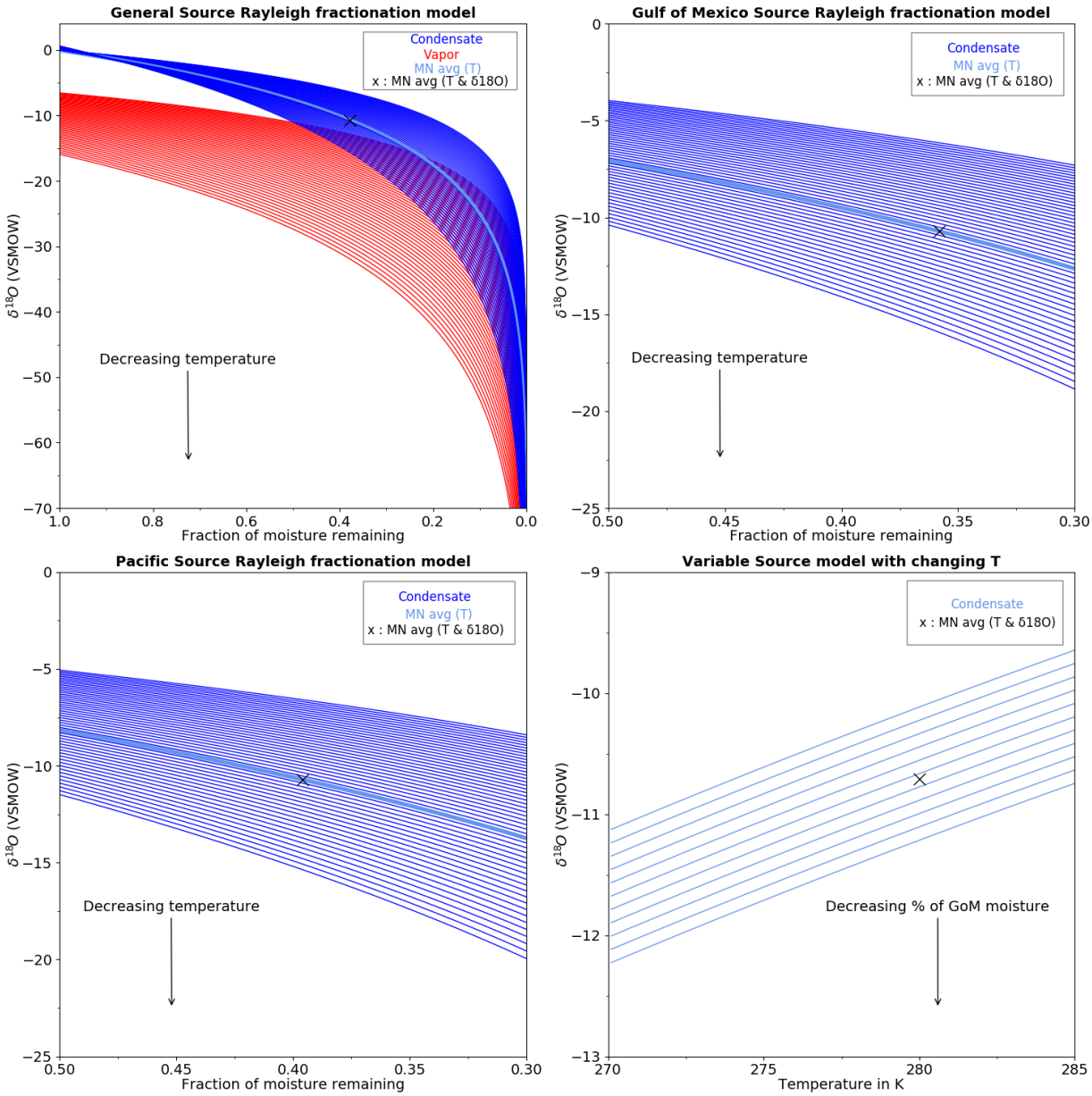

Figure 3.13: Simplified *Python* model of Rayleigh fractionation with: A) Changing temperature and general moisture source. B) Changing temperature and Gulf of Mexico moisture source. C) Changing temperature and Pacific moisture source. D) Changing contributions of Gulf of Mexico and Pacific moisture sources

Modern precipitation regimes in Minnesota indicate a predominance of Gulf of Mexico moisture. A multi-year study conducted in central Iowa that looked at isotopic composition of precipitation indicated that a majority of precipitation events involved moisture originating solely from the Gulf of Mexico, primarily occurring in the summer and autumn (Simpkins, 1995). However, over 30% of precipitation events involved a mixed Gulf-Pacific moisture source, primarily occurring in the winter and spring. The weighted average of Gulf of Mexico precipitation was -7.24‰, whereas the weighted average of Gulf-Pacific precipitation was significantly lower, at -10.80‰ (VSMOW). The modern weighted average δ^{18}O of precipitation in Minneapolis-St.Paul is -7.92‰ (Mohr, 2000). Assuming moisture characteristics are similar between central Iowa and southern Minnesota, this would indicate that about 80% of precipitation in Minnesota is derived from a Gulf of Mexico only source, whereas about 20% is from a mixed Gulf-Pacific source.

Modern calcite values averaged over the last fifty years at Spring Valley Caverns give an estimated δ^{18}O value of -5.78‰ (VPDB). With a modern cave temperature of 8.3°C, this would indicate a fractionation factor between drip water and calcite at equilibrium of 1.0387, and an estimated drip water value of -7.53‰ (VSMOW) (Fleitmann et al., 2004). With a modern weighted precipitation average of -7.92‰ (VSMOW), this suggests the cave system may be biased towards warm weather precipitation (Mohr, 2000). Modern drip water collection at Spring Valley Caverns supports this hypothesis (Dasgupta, 2008). However, for the remaining calculations we assume that drip water δ^{18}O values accurately reflect the average δ^{18}O of precipitation. The lowest seawater corrected calcite δ^{18}O value collected in this study was -3.7‰ (VPDB), achieved at 29 ky BP in sample SVC05. If temperatures remained at modern values during the glacial period, fractionation effects would remain the same, and one could predict a δ^{18}O drip water value of -5.45‰ (VSMOW). However, as temperature decreases, fractionation between phases of matter at equilibrium increases. If the cave were to mimic the global temperature average and achieve a temperature 5.9°C lower than modern nearing the last glacial maximum, the oxygen isotopic fractionation between drip water and calcite would measurably increase. At modern temperatures the equilibrium fractionation factor is about 1.0387, with a 1.75‰ difference between the δ^{18}O of calcite and the δ^{18}O of drip water. At 2.4°C it is 1.0403, with a 3.2‰ difference between the δ^{18}O of calcite and the δ^{18}O of drip water, and an estimated δ^{18}O drip water value of -6.96‰ (VSMOW).

In addition to the equilibrium fractionation factor between drip water and calcite, temperature also affects the equilibrium fractionation factor between water vapor and precipitation. Using modern calcite and temperature values at Spring Valley, the calculated fractionation factor of precipitation is 1.0115, giving a δ^{18}O vapor value of -18.815‰ (VSMOW). In

this scenario there is an 11.3‰ difference between the δ^{18}O of liquid and the δ^{18}O of vapor. With cooler conditions nearing the last glacial maximum, the calculated fractionation factor of precipitation is 1.0122 using a Spring Valley calcite value of -3.7‰ (VPDB) and local temperature of 2.4°C. This would give a δ^{18}O vapor value of -18.896‰ (VSMOW) and a 11.9‰ difference between the δ^{18}O of liquid and the δ^{18}O of vapor. Thus even at appreciably lower regional temperatures, the δ^{18}O vapor value does not significantly change between modern conditions and glacial conditions due to the combined effects of equilibrium fractionation between vapor, liquid, and calcite.

To explore how temperature, fraction of moisture remaining, and moisture source influence the calcite δ^{18}O values at Spring Valley Caverns, two additional models were created. One assumed that the modern precipitation regimes remained in place, and compared glacial precipitation regimes to a modern weighted precipitation average δ^{18}O value of -7.92‰ (VSMOW). This model is shown in Figure 3.14. The other assumed that nearing glacial conditions Pacific moisture contribution was completely eliminated, and compared glacial precipitation regimes to a Gulf of Mexico moisture only precipitation average δ^{18}O value of -7.24‰ (VSMOW). This model is shown in Figure 3.15. Both models used the lowest seawater corrected calcite δ^{18}O value from SVC05 of -3.7‰ (VPDB), achieved at 29 ky BP, and a modern weighted temperature average in Minneapolis-St. Paul of 8.3°C (Mohr, 2000). Additionally, models used a modern temperature and δ^{18}O for the Gulf of Mexico sea surface of 25.13°C and 1.25‰ (VSMOW), and to simplify the calculations used a constant relative humidity of 100% in the Gulf and 68% in Minnesota (Schmidt et al., 1999). The equilibrium fractionation factor of evaporation was calculated from Gulf of Mexico climate parameters, and tropical ocean temperature decreased by 1°C in each model run to simulate decreasing tropical temperature. The equilibrium fractionation factor of precipitation was calculated regionally using the local dew point temperature, and the regional δ^{18}O value of precipitation in VSMOW was calculated using the corrected calcite δ^{18}O value in VPDB and regional temperature. To simplify these models, the effects of kinetic fractionation were not included.

Using modern climate parameters, the model estimated the current annual average fraction of moisture remaining in Minneapolis-St. Paul was about 0.2. In both models, decreasing the sea surface temperature of the Gulf of Mexico results in a lower δ^{18}O value of initial vapor and more positive change in fraction of moisture remaining in order to achieve a δ^{18}O calcite value of -3.7‰ (VPDB). Both models indicate that with decreasing regional temperatures, there is a corresponding decrease in change of fraction of moisture remaining due to an increase in fractionation effects between dripwater and calcite within the cave. Due to this effect, a lower fraction of moisture remaining relative to modern is needed to

achieve a calcite value of -3.7‰ (VPDB) once temperatures decrease by -7 to -9°C if Pacific moisture is eliminated and by -9 to -11°C if moisture remains mixed, depending on Gulf of Mexico sea surface temperature. Assuming global temperatures decreased by 5.9°C nearing Last Glacial Maximum, a precipitation regime with Pacific moisture eliminated would see an increase in fraction of moisture remaining relative to modern of 0.0015 to 0.0159, and a precipitation regime with mixed Gulf-Pacific moisture would see an increase in fraction of moisture remaining relative to modern of 0.0153 to 0.0298, depending on Gulf of Mexico sea surface temperature (Kim et al., 2008).

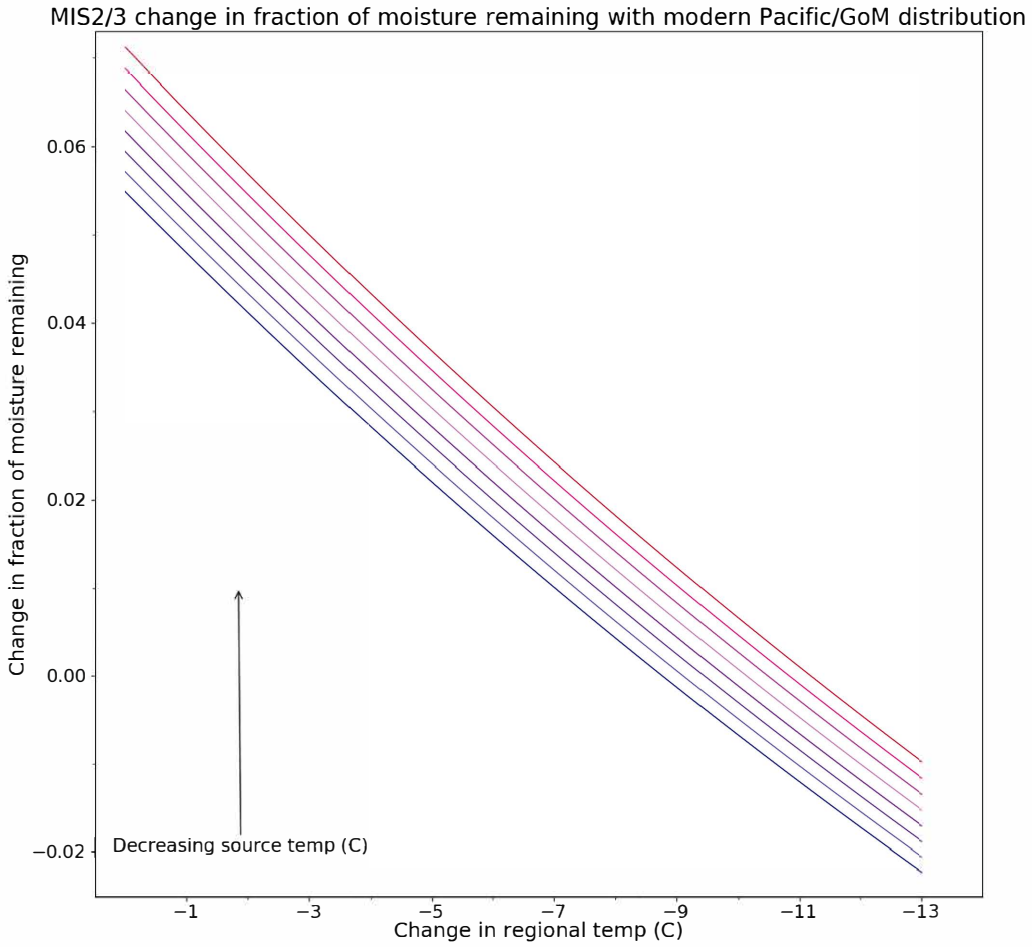

Figure 3.14: Python model of Rayleigh fractionation looking at change in fraction of moisture remaining to achieve calcite $\delta^{18}O$ value of -3.7‰(VPDB) at MIS2/3 boundary relative to modern with changing local and source temperatures assuming a modern Pacific/Gulf of Mexico moisture source distribution.

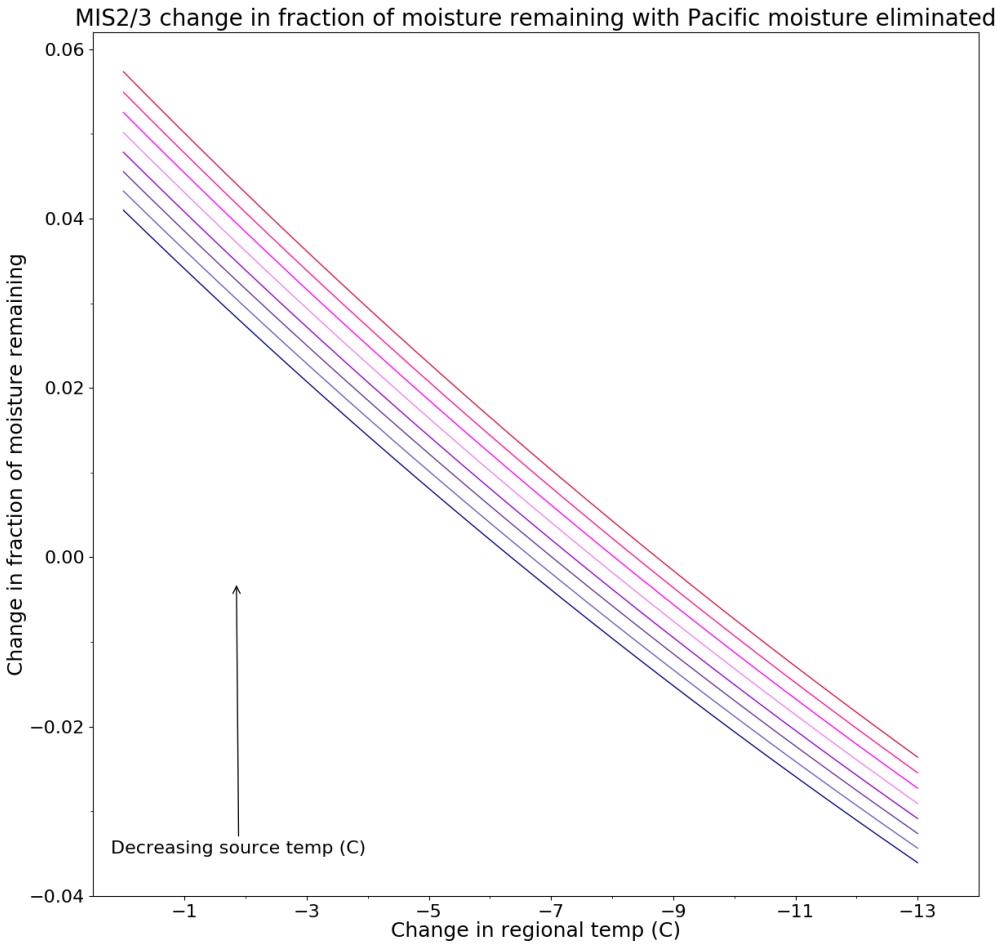

Figure 3.15: Python model of Rayleigh fractionation looking at change in fraction of moisture remaining to achieve calcite δ^{18}O value of -3.7‰(VPDB) at MIS2/3 boundary relative to modern with changing local and source temperatures assuming Pacific moisture has been eliminated.

There appears to be limited changes to fraction of moisture remaining relative to modern in both scenarios, indicating a similar percentage of rain out. However, integrated rain out between the Gulf of Mexico and Spring Valley would change depending on climate conditions in both locations. Assuming the modern annual average fraction of moisture remaining at Spring Valley is 0.2 and the modern Gulf of Mexico sea surface temperature and relative humidity is 25.13°C and 100%, respectively, the integrated rain out is 0.0184 kg/m^3. If temperature at Spring Valley decreased to 2.4°C nearing LGM and calcite values reached -3.7‰ (VPDB), integrated rain out would decrease dependent on Gulf of Mexico conditions. With 100% relative humidity and Gulf of Mexico sea surface temperatures the same as modern, -2.5°C lower than modern, and -5°C lower than modern, integrated rain out would be 0.0179, 0.0155, and 0.0131 kg/m^3, respectively. Thus we would expect to see

drier conditions throughout the mid-continent relative to modern.

Amundson and colleagues in the Wind River Basin of Wyoming found that oxygen isotopic ratios in pre-Holocene soils are significantly higher than modern and appear to increase steadily throughout the last glacial period (Amundson et al., 1996). This was interpreted as a more dominant summer precipitation component attributed to either a weakening of westerlies and/or an increase in the strength of summer monsoonal flow. This behavior is also seen in the Spring Valley record. While calcite values at Spring Valley nearing LGM are reasonably achieved in both models, it seems likely that the changes in precipitation regimes affecting Wind River may have also affected the upper mid-continent.

Additionally, a model run was completed using conditions following the last interglacial period, when seawater corrected calcite values for SVC05 reached -7.87‰ (VPDB), achieved at 103 ky BP. This model is shown in Figure 3.16. In this run, increasing Gulf of Mexico sea surface temperature resulted in a more negative change in fraction of moisture remaining in order to achieve calcite values, whereas increasing regional temperature resulted in a less negative change. This would indicate that closely following the last interglacial period, there was an increase in rain out along moisture trajectories, and potentially wetter conditions locally. This hypothesis is corroborated by pollen records from Illinois, which indicate that the last interglacial was warmer and potentially wetter than the Holocene (Teed, 2000, Curry et al., 2000).

However, low δ^{18}O values at the transition between MIS5d and MIS5c are accompanied by high δ^{13}C values, characteristic of a dry, prairie landscape. In the mid-Holocene, the prairie-forest sharp ecotone boundary was defined by a steep moisture gradient caused by incursions of Pacific air (Denniston et al., 1999b). This incursion was characterized by elevated growth rates, low δ^{18}O values, and high δ^{13}C values. As regional mid-Holocene conditions indicate dry conditions and the dominance of a prairie landscape, elevated growth rates may have been the result of increased infiltration outside of the growing season due to a higher proportion of cool-season precipitation (Denniston et al., 1999a). Following the last interglacial, it seems likely that while the mid-continent continued to receive ample precipitation, Minnesota experienced a higher proportion of winter Gulf-Pacific mixed precipitation than at present, resulting in a depleted δ^{18}O signal even while temperatures were elevated. Warm conditions in the North Atlantic due to high summer insolation would lead to a north position of the ITCZ and polar jet stream, which could lead to an increase in winter precipitation. Indeed, climate projections indicate higher than average winter precipitation in the Midwest with rising global temperatures (Wuebbles et al., 2004). It is also possible that due to higher temperatures, cave drip water was able to remain active

throughout the winter months.

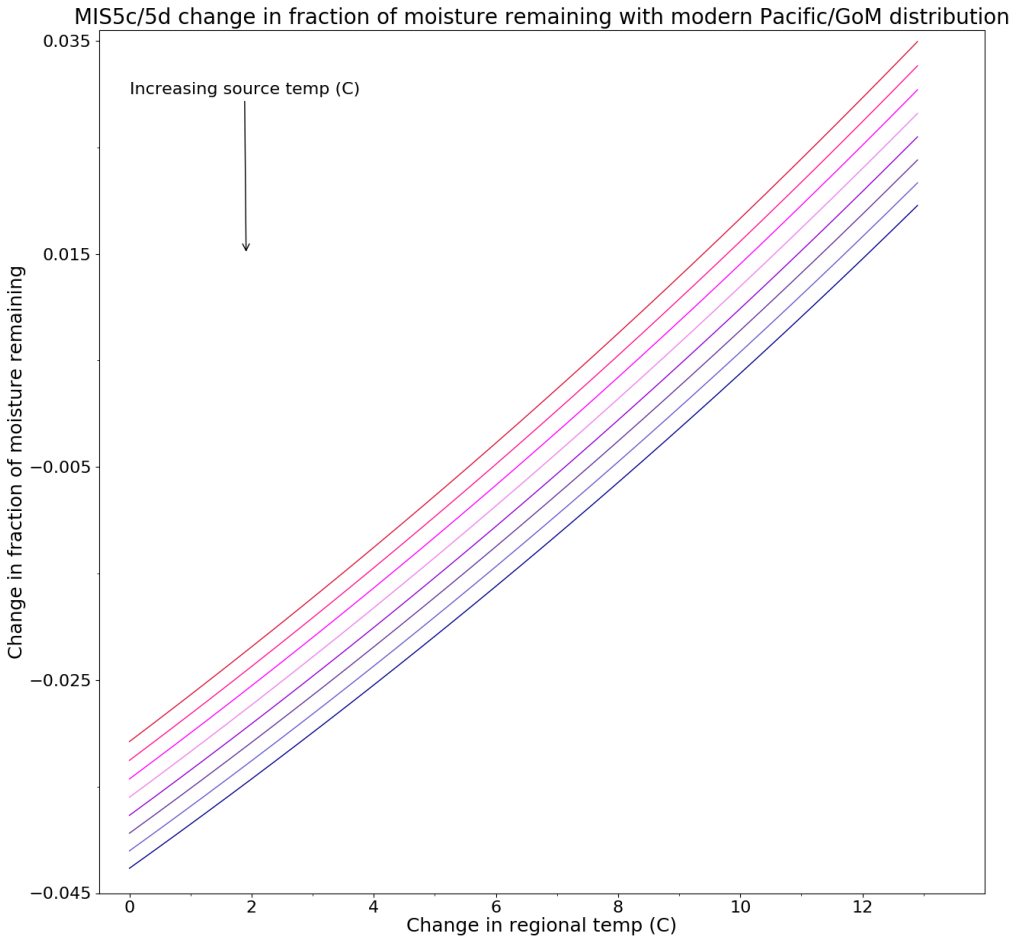

Figure 3.16: Python models of Rayleigh fractionation looking at change in fraction of moisture remaining to achieve calcite δ^{18}O value of -7.87‰ (VPDB) at MIS5c/5d boundary relative to modern with changing local and source temperatures, assuming modern Pacific/Gulf of Mexico moisture distribution.

In addition to long-term changes, sample SVC06 shows significant stable isotopic structure on a millennial scale. GIS events are identifiable and are exhibited as low δ^{18}O values. These correlate to periods with strong East Asian summer monsoons (EASM) and warm Greenland temperatures, as illustrated by the Hulu speleothem record and NGRIP ice core (Y. Wang et al., 2001, Rasmussen et al., 2014). Additionally, SVC06 shows similar structure to Gulf of Mexico δ^{18}O values and sea surface temperatures, indicating that Spring Valley was likely dominated by this moisture source during MIS4 and MIS3. These trends are shown in Figure 3.17.

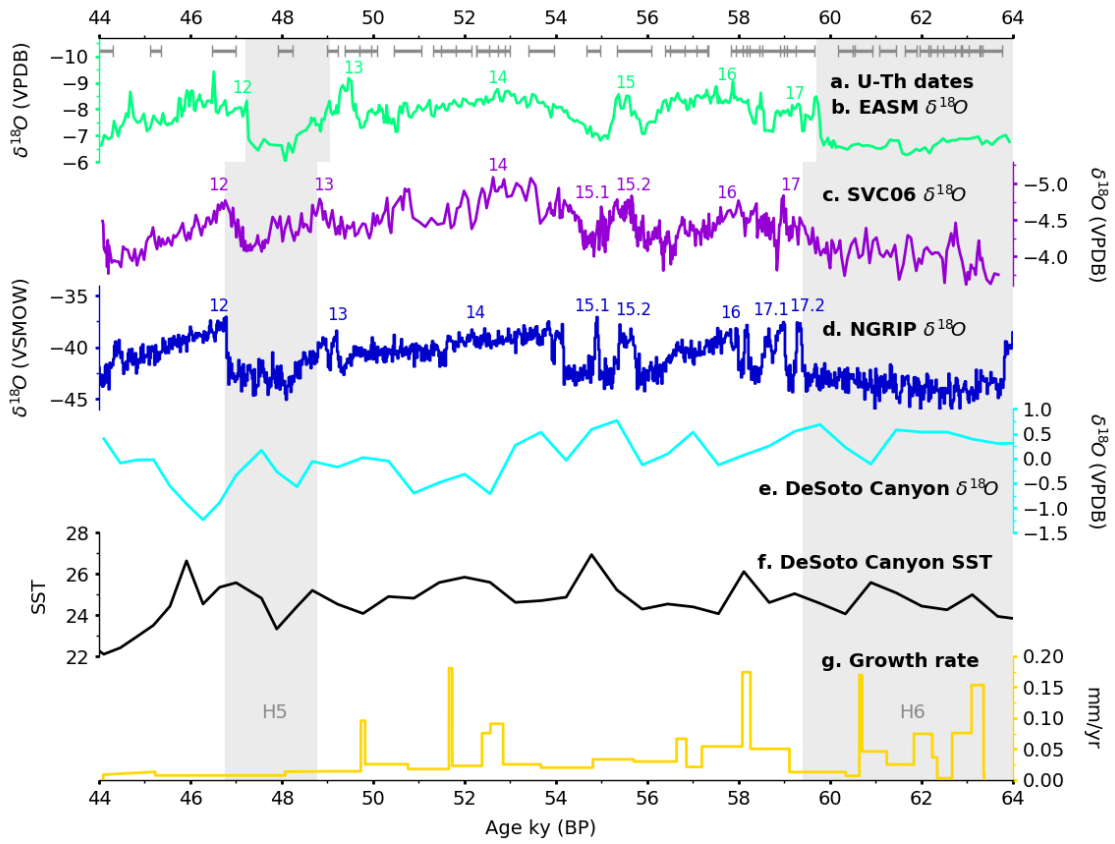

Figure 3.17: Correlation between SVC06 δ^{18}O record and GIS record in paleorecords. A) ^{230}Th dates for SVC06. B) SVC06 δ^{18}O record. C) Hulu δ^{18}O speleothem record (Y. Wang et al., 2001). D) NGRIP δ^{18}O ice core record (Rasmussen et al., 2014). E) DeSoto Canyon planktonic foraminfera δ^{18}O (Nurnberg et al., 2008). F) DeSoto Canyon reconstructed sea surface temperature (Nurnberg et al., 2008). G) SVC06 growth rate, computed linearly. Timing of GIS events and Heinrich stadials are indicated for all records.

With a dominant Gulf of Mexico moisture source throughout the period, changes in the δ^{18}O of the SVC06 record are controlled by the fraction of water vapor remaining in the air mass. Periods with a strong EASM and warm North Atlantic accompany depleted δ^{18}O values in Spring Valley, suggesting enhanced precipitation in the mid-continent. While δ^{18}O and δ^{13}C values have little temporal correlation in SVC06, as illustrated in Figure 3.9, smoothed trends indicate a positive correlation, shown in Figure 3.18. Elevated δ^{13}C values can be a result of a decrease in soil respiration and increase in infiltration time, indicating drier conditions. Thus periods with elevated δ^{18}O values are accompanied by an increase in soil aridity.

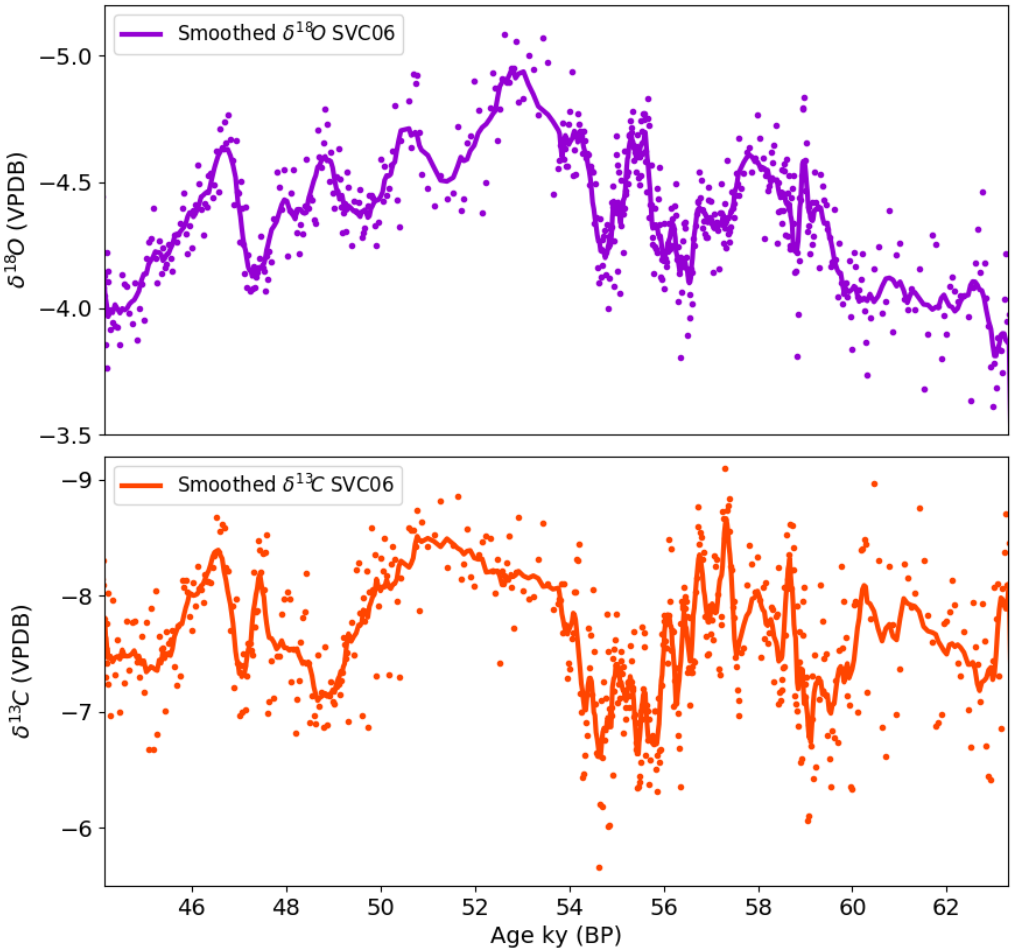

Figure 3.18: Smoothed 10-year records for δ^{18}O and δ^{13}C values for SVC06

Elevated δ^{18}O values at Spring Valley also correlate to a strengthening of the Icelandic Low pressure system, shown in Figure 3.19 and illustrated by an increase in calcium ions in the Greenland ice core (Rasmussen et al., 2014). The ions are derived from atmospheric dust, largely from low-latitude Asian deserts (Steffensen et al., 2008). Arid conditions intensify dust concentrations during North Atlantic cold events, and transport is increased due to a deepened Icelandic Low (Kang et al., 2003).

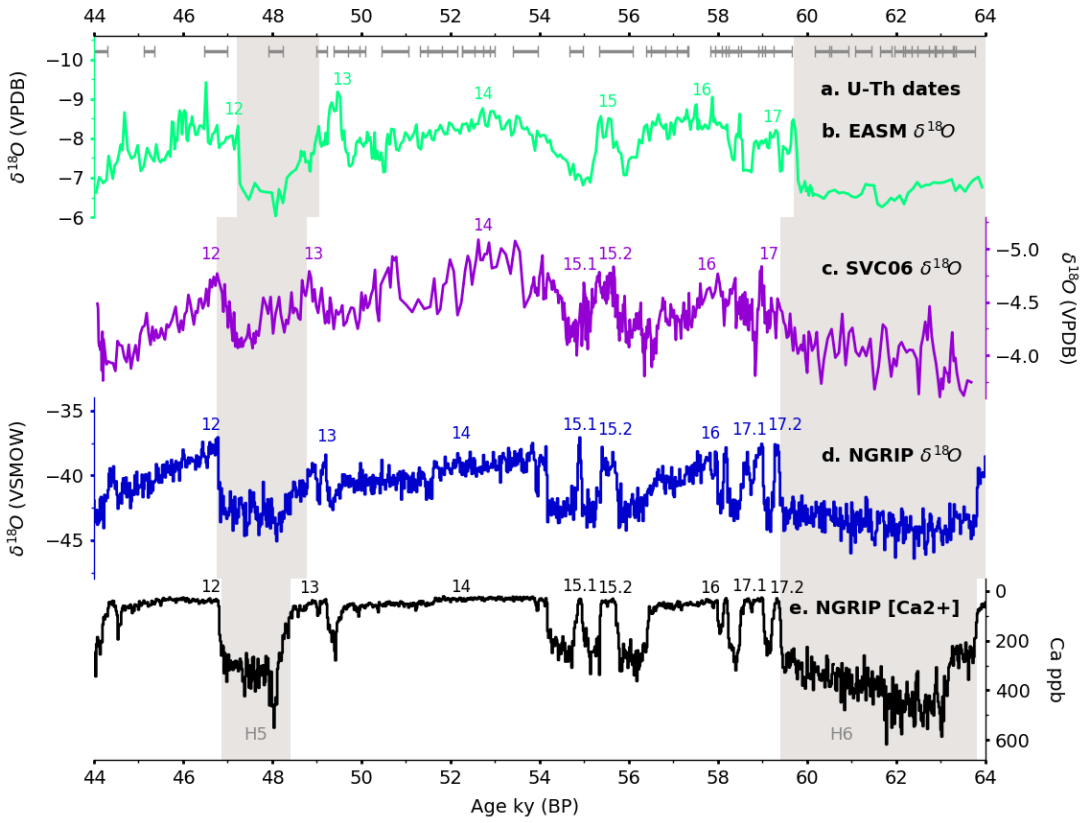

Figure 3.19: Correlation between SVC06 δ^{18}O record and GIS record in paleorecords. A) ^{230}Th dates for SVC06. B) SVC06 δ^{18}O record. C) Hulu δ^{18}O speleothem record(Y. Wang et al., 2001). D) NGRIP δ^{18}O ice core record (Rasmussen et al., 2014). E) NGRIP calcium concentration on log scale (Rasmussen et al., 2014). Timing of GIS events and Heinrich stadials are indicated for all records

During North Atlantic cold events, an anomalous dipole in SST due to cooling in the North Atlantic and warming in the South Atlantic results in an intensification of low and high pressure systems. This dipole also results in the reversal of equatorial heat-transfer and the southward displacement of the ITCZ (X. Wang et al., 2004). The increase in the sea level pressure (SLP) gradient is characteristic of the positive phase of the North Atlantic Oscillation (NAO). The intensification of the subtropical Atlantic high pressure system, the Bermuda High, causes an enhanced pressure gradient across the SE United States and induces an increase in summer precipitation in the region (Diem, 2013, Hardt et al., 2010). The stronger high pressure system also results in a drier conditions during the warm season in the upper Midwest (Patricola et al., 2013).

Inversely, North Atlantic warm events, like Greenland interstadials, are correlated to a

decrease in the SLP gradient across the North Atlantic characteristic of a negative NAO. During this time, the Bermuda High may shift towards the SW, resulting in an increase in SLP gradient between the Gulf of Mexico and southern Great Plains (Forman et al., 1995, Zhu et al., 2013). This increases the strength of the Great Plains Low Level Jet (GPLLJ), increasing summer precipitation into the mid-continent (Zhu et al., 2013). Modern flood records in Spring Valley support this hypothesis. Flood layers in the cave were associated with extreme rainfall events under warm and wet conditions, and flood frequency coincided with neutral or low NAO indexes (Dasgupta, 2008). Additionally, summer precipitation amounts show potential inverse correlation with NAO index, as illustrated in Chapter 2.

Paleorecords from North America discussed in Chapter 1 show indications of these trends. During Heinrich stadials, lake cores from Florida show wetter conditions during Heinrich stadials, whereas cave sites along the western Gulf Coast show increased aridity (Grimm et al., 1993, Feng et al., 2014). Sites in Central America record the southward displacement of the ITCZ, and sites in western North America illustrate the intensification of the Aleutian low and the resulting movement in the polar jet stream (Lachniet et al., 2009, Okumura et al., 2009, Wagner et al., 2010, Asmerom et al., 2010). Records in the Southwest indicate a significant increase in winter precipitation during Heinrich stadials, whereas Greenland interstadials show dry conditions, recorded as a decrease and increase in δ^{18}O, respectively. These records show a negative correlation to Spring Valley, as illustrated in Figure 3.20.

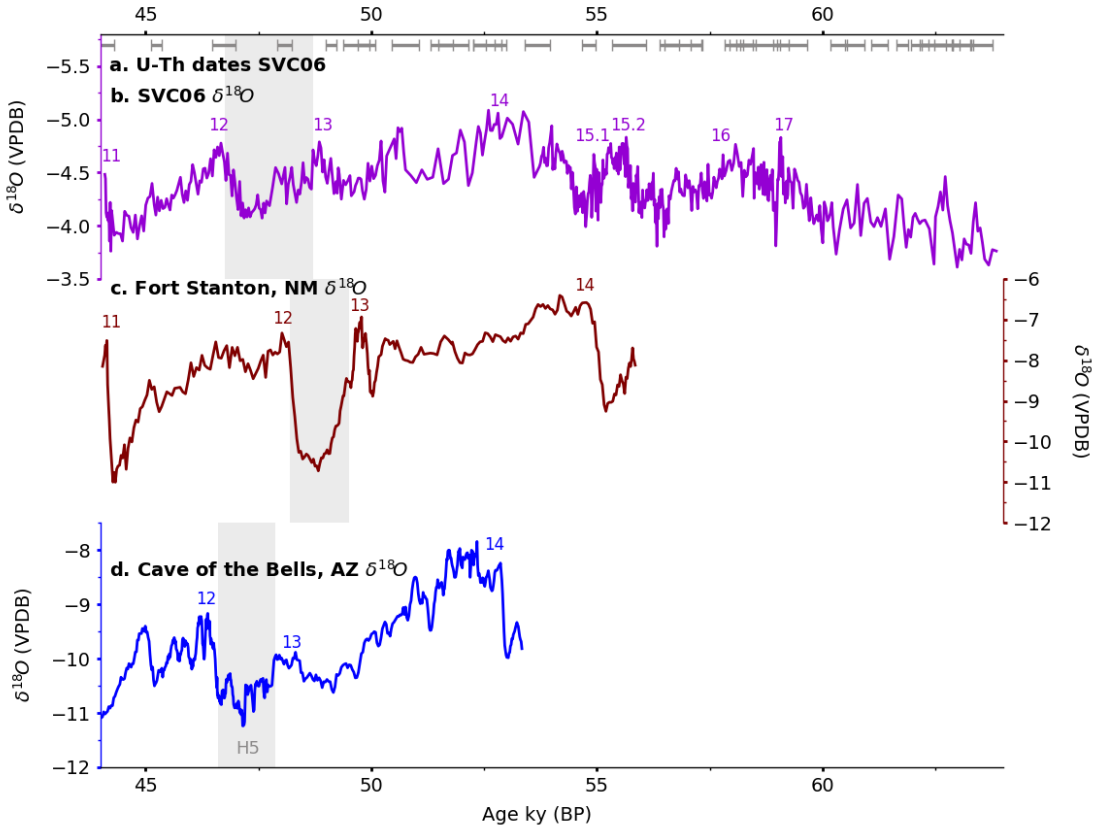

Figure 3.20: Correlation between SVC06 δ^{18}O record and records from SW North America. A) ^{230}Th dates for SVC06. B) SVC06 δ^{18}O record. C) δ^{18}O speleothem record from Fort Stanton, NM (Asmerom et al., 2010). D) δ^{18}O speleothem record from Cave of the Bells, AZ (Wagner et al., 2010). Timing of GIS events and Heinrich stadials is indicated for all records

Interestingly, an intensified Aleutian low is characteristic of a positive PNA phase, which would also reduce GPLLJ intrusion into the mid-continent. Thus it is likely that climatological responses at Spring Valley to North Atlantic anomalies are due to a variety of mediating atmospheric forces.

3.7 Conclusions

In this study, we investigated long and short term climate variability in SE Minnesota from 104 - 29 ky BP, using speleothem growth and stable isotope records from Spring Valley Caverns. We used high precision ^{230}Th dates, measured using SEM or Faraday cups and reduced using new *Python* programs, to determine growth periods for six speleothem samples. Additionally, confocal fluorescence microscopy allowed for improved constraint

on short term growth phases in sample SVC05. Growth in Spring Valley was shown to correlate to Greenland interstadial events, with anomalous growth during MIS4 potentially due to increased anticyclonic activity over the Laurentide. This indicates both warmer temperatures and adequate moisture supply during North Atlantic warm periods.

Stable isotope records from SVC05 and SVC06 showed impressive synchroneity with global paleorecords. δ^{13}C values implied a transition from C4 to C3 dominated landscapes between mid-MIS5 and mid-MIS4, most likely due to decreasing Northern Hemisphere temperatures. General trends in δ^{18}O values, however, were not controlled by temperature, as values increased during the last glacial period. Rayleigh fractionation models illustrated that higher δ^{18}O precipitation values could be reached even with decreasing temperature by varying the moisture source or increasing the fraction of vapor remaining. It is possible that the general trend in δ^{18}O throughout the period is due to a decrease in Pacific-sourced winter moisture in the region, or a reduction in winter-sourced moisture infiltrating the cave environment.

The oxygen stable isotopic values for sample SVC06 record millenial-scale climate change during MIS4 and MIS3. The relative correlation between δ^{18}O and δ^{13}C during growth indicates that increasing δ^{18}O values record increasing aridity. If the region remained strongly dependent on summer precipitation, Spring Valley saw an increase in summer precipitation during Greenland interstadials and a decrease during Heinrich stadials. This may be due to variation of the North Atlantic Oscillation (NAO) and position of the Bermuda High, whereby the Great Plains Low Level Jet is strengthened during negative NAO phases. However, effects from other large-scale atmospheric and oceanic regimes cannot be precluded.

Chapter 4

Conclusions

In this study, six late-Pleistocene speleothem samples from SE Minnesota were analyzed for growth, and two produced high resolution stable isotope records. Growth was determined using ^{230}Th dating, and short growth phases constrained through confocal fluorescence microscopy. Samples were run on a MC-ICP-MS, and U and Th data were reduced using new *Python* programs presented in Appendix B. These programs significantly reduce user time and expertise, ensuring quality control in the UMN Isotope Lab. A new form of automatic band counting was tested on confocal images, and appeared to perform as well as if not better than traditional manual band counting.

Sample growth showed correlation to Greenland interstadial events, with the exception of MIS4. Significant growth during this period may be due to anti-cyclonic activity over the Laurentide ice sheet, resulting in increased Gulf of Mexico precipitation into the region. Stable isotopic variation in both δ^{18}O and δ^{13}C during from 104 -29 ky BP track with Northern Hemisphere summer insolation, with periods of high insolation coinciding with high δ^{13}C and low δ^{18}O values. Decreases in the δ^{13}C record from mid-MIS5 to MIS4 indicate a transition from prairie to forest, and increasing δ^{18}O values may be due to a reduction in Pacific-sourced winter moisture and a drier moisture trajectory.

Millenial-scale oxygen isotopic variability in sample SVC06 showed a positive correlation to speleothem records of the East Asian summer monsoon intensity and marine temperature and isotopic records from the Gulf of Mexico and a negative correlation to Greenland ice core records of temperature and Icelandic low intensity (Y. Wang et al., 2001, Nurnberg et al., 2008, Rasmussen et al., 2014). Oxygen values were higher during North Atlantic cold events, and lower during Greenland interstadials. All interstadials during growth period were identifiable. Relative correlation between δ^{18}O and δ^{13}C values in sample SVC06 suggest that enriched δ^{18}O values are recording regional aridity, dominated by Gulf of

Mexico summer precipitation. North Atlantic cold events result in a decrease in moisture availability, whereas warm events cause a strengthening of southerly flow. This could be due to variability in the Bermuda High caused by changing sea level pressure gradients, but could also be influenced by sea surface temperature and sea level pressure patterns in the Atlantic and Pacific.

This study not only provides a record of late Pleistocene climatic variability in an area lacking high resolution paleorecords, but also indicates that precipitation in the region may have been more enriched in ^{18}O than previously assumed. This is counter to temperature effects on isotopic fractionation during precipitation and calcite formation, indicating the upper Midwest was highly influenced by moisture source and moisture availability. With modern calcite $\delta^{18}O$ values at Spring Valley ≈-5.7‰, calcite values nearing the Last Glacial Maximum were ≈2‰ higher, even with significantly lower temperatures. As the study samples show no indication of kinetic fractionation, these changes should mirror similar changes in the $\delta^{18}O$ of precipitation at the site.

Constraining isotopic values of meteoric precipitation in the upper mid continent during the Last Glacial Maximum is of particular importance in determining the amount of Mississippi-drained meltwater from the Laurentide during the last deglaciation. While sea levels rose significantly during deglaciation, a significant pulse in meltwater between 14.65 - 14.31 ky BP resulted in a sea level rise as high as 20m (Deschamps et al., 2012). The source of this meltwater pulse (MWP1a) has long been debated, but evidence exists suggesting contribution by both the Antarctic and Laurentide Ice Sheets. Additionally, contribution from Laurentide meltwater to the rise in sea level could have been routed through eastern, southern, or northern outlets (Flower et al., 2004, Carlson, 2009). Determining the timing, amount, and location of meltwater discharge is integral to understanding mechanisms of deglaciation.

Evidence for MWP1a - and of meltwater through 13 kyr BP - is present in marine cores from the Gulf of Mexico that illustrate a significant influx of fresh water. Sites on the Louisiana Slope and at Orca Basin show a decrease in sea surface temperature and in the $\delta^{18}O$ of planktonic and benthic foraminifera (Flower et al., 2004, Aharon, 2006). Oxygen signatures of foraminifera reflect changes in the ocean composition, and a decrease would correspond to an influx of meltwater depleted in ^{18}O either through surface runoff or hyperpycnal flow. While the rise in sea level at Bermuda appears to lag that at Tahiti, the $\delta^{18}O$ values for both marine and speleothem records surrounding the Gulf confirm that the Laurentide experienced a surge in meltwater through its southern-route at ≈14.6 ky BP (Deschamps et al., 2012, Williams et al., 2012, Feng et al., 2014.

Models estimating total freshwater runoff during MWP1a include the contributions of Laurentide meltwater, regional precipitation, and the Gulf of Mexico loop current. Most models use -25‰ and -35‰ (VSMOW) as end member estimates for melt composition, taken from ice reconstructions in the Lake Agassiz basin and on Baffin Island (Remenda et al., 1994, Hooke et al., 1982). Additionally, models use a modern seasonal precipitation value of -7.7‰ (VSMOW) and a loop current value between 1.1 and 1.7‰ (VSMOW) (Wickert et al., 2013, Aharon, 2006). Models can then estimate the increase in Laurentide melt volume that corresponds to a decrease in planktonic δ^{18}O of 0.8‰ and in benthic δ^{18}O of 2.30‰ (Aharon, 2006).

However, if climatic conditions during the Last Glacial Maximum resulted in a greater dominance of Gulf of Mexico sourced moisture and an increase in aridity throughout the Mississippi drainage basin, as evidenced at Spring Valley Caverns, isotopic values for both the Laurentide melt and regional precipitation may be higher. Ferguson and colleagues found significant spatial variability in fossil groundwater along the southern Laurentide, varying in value from -12.5 to -25.3‰ (VSMOW, Ferguson et al., 2015). The presented reconstruction from Spring Valley Caverns suggests that regional precipitation at the Last Glacial Maximum had a value between -6 and -7‰, assuming a drop in temperature of 5.9°C between modern and glacial maximum. In the model described below, a precipitation value of -6.3‰ was used as an estimate. This is an increase in value from the modern weighted average of -7.92‰ and contrary to temperature fractionation effects, which indicates the southern Laurentide may have been fed by moisture significantly higher in ^{18}O than previously thought.

To explore the effects of melt composition on discharge amount, the models created by Carlson and colleagues were replicated using *Python* with varying values for Laurentide melt and regional precipitation (Carlson, 2009). End member estimates for melt composition were taken from Ferguson and colleagues, from -12.5 to -25.5‰ (Ferguson et al., 2015). Results from the models are shown below in Figure 4.1. In both the benthic and planktonic records, an increase in the δ^{18}O of Laurentide melt results in a significant increase in discharge. In the benthic record, an increase in the δ^{18}O of precipitation results in an increase in discharge, as studies indicate an increase in precipitation-derived runoff experienced as hyperpycnal flow during MWP-1a (Carlson, 2009, Licciardi et al., 1999). However, in the planktonic record, an increase in the δ^{18}O of precipitation results in a decrease in precipitation-derived runoff experienced as hypopycnal flow during MWP-1a (Carlson, 2009, Licciardi et al., 1999). Thus, whereas changes in melt composition has a significant impact on both, changes in precipitation composition result in negligible changes to overall

discharge amount.

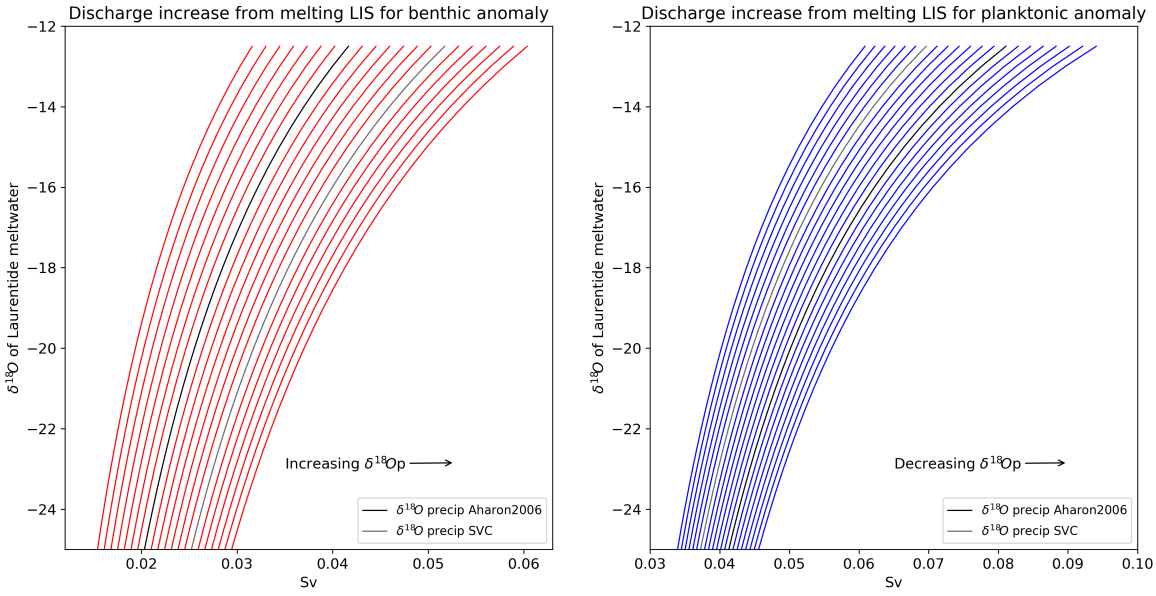

Figure 4.1: Results from discharge model, adapted from Carlson, 2009. Discharge increase is determined for varying melt compositions in order to result in a decrease of 2.30‰ in the benthic record and a decrease of 0.8‰ in the planktonic record. Results for a δ^{18}O value of precipitation of -7.7‰ and of -6.3‰ are plotted on both models.

Previous estimates of southern-routed discharge from the Laurentide using -25 and -35‰ as isotopic end members of melt ranged from 0.046-0.06 Sv, corresponding to a sea level rise of 2.0-2.7m over 500 years (Carlson, 2009). The updated model resulted in a minimum meltwater estimate of 0.0605 Sv and a maximum meltwater estimate of 0.1227 Sv. If the modern temperature sensitivity of the Greenland Ice Sheet is scaled to the size of the Laurentide's Mississippi drainage area, the highest drainage estimate would require only 17-30°C of warming or only a 17-30x increase in sensitivity (Clark et al., 1996). Temperature estimates in the Northern Hemisphere during the Bolling-Allerod suggest that annual temperatures may have increased by 16°C, and glaciological models of the Mississippi drainage basin suggest that from 14-13.5 ky BP meltwater discharge into the Gulf of Mexico was 0.098 Sv (Williams et al., 2012, Teller, 1990). Thus meltwater estimates between 0.0605-0.1227 Sv during MWP-1a are possible. As shown in Figure 4.2, this would correspond to a sea level rise of 2.6-5.3m, significantly higher than previous estimates.

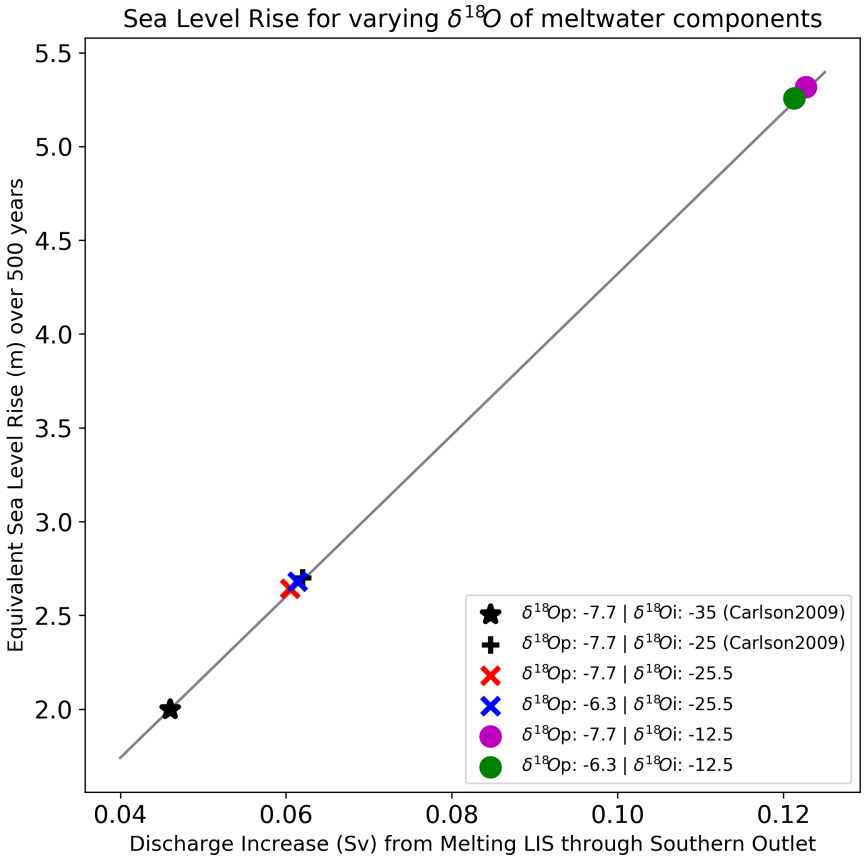

Figure 4.2: End member results from discharge model, plotted against equivalent sea level rise in meters over a 500 year period. Isotopic composition of precipitation results in minimal changes in overall discharge amount.

Current global climate models are able to accommodate up to 6m in sea level rise resulting from an increase in hyperpycnal flow in the Gulf of Mexico without reducing the strength of the AMOC, which actually increased in strength during MWP-1a (Carlson, 2009). Thus estimates in sea level rise from this model remain possible. If previous estimates of discharge from the northern and eastern outlets of the Laurentide do not change, the Laurentide as a whole would contribute between 5-8m of the ≈20m global sea level rise. Using these new model parameters, the Laurentide could plausibly account for up to 40% of the total rise in sea level during MWP-1a. Thus, the surprising δ^{18}O record in Spring Valley Caverns during the last glacial period raises the possibility that meltwater discharge into the Gulf of Mexico during the last glaciation has been underestimated.

Determining primary drivers for climatic variability in the mid continent is extremely important in predicting effects of climate change. The U.S. is currently the largest producer of both corn and soybeans according to the US Department of Agriculture. Primary agricultural belts for both crops are located in the Great Plains and Midwest regions. Being able to accurately predict effects of climate change in the region is crucial to mitigating changes to crop productivity. Current climate change projections indicate that the region will experience enhanced increases in temperature and most likely an increase in annual precipitation (Romero-Lankao et al., 2014). While this has contributed to improved crop yields, temperature increases will soon move past optimum temperature growth. Additionally, more frequent extreme events, like droughts and storms, will negatively affect production.

While climate change models have begun to incorporate paleoclimate simulations to improve predictability, simulated projections often underestimate observed changes in paleorecords (Braconnot et al., 2012). Additionally, records used in reconstructing paleoclimate for model testing are sparse in the mid continent. Reconstructing, expanding, and improving mid continental paleorecords are crucial in achieving accurate climate change predictions for the region.

To bolster the interpretation of the Spring Valley paleorecord, future work would benefit from high resolution trace element analysis. Trace elements often record changes in seasonality, which could confirm whether there is increase in dominance of summer precipitation during the last glacial period. It could also verify whether periods with high $\delta^{18}O$, synchronous with North Atlantic cold events, are in fact experiencing increased aridity. Additionally, producing high resolution stable isotope records for samples SVC16-1, SVC16-2A, SVC16-2B and SVC99-1d would confirm the long and short term trends suggested in samples SVC06 and SVC05.

Bibliography

Aharon, P. (2006). "Entrainment of meltwaters in hyperpycnal flows during deglaciation superfloods in the Gulf of Mexico". In: *Earth and Planetary Science Letters* 241.1-2, pp. 260–270.

Alexander, E.C., G.A. Brick, and A.N. Palmer (2009). "Minnesota". In: *Caves and Karst of the USA*. Ed. by Arthur N. Palmer and Margaret V. Palmer. National Speleological Society, Inc., pp. 146–150.

Alonso-Cantabrana, H. and S. von Caemmerer (2016). "Carbon isotope discrimination as a diagnostic tool for C4 photosynthesis in C3-C4 intermediate species". In: *Journal of Experimental Botany* 67.10, pp. 3109–3121.

Alvarez-Solas, J. and G. Ramstein (2011). "On the triggering mechanism of Heinrich events". In: *PNAS* 108.50, pp. 1359–1360.

Alvarez-Solas, J. et al. (2013). "Iceberg discharges of the last glacial period driven by oceanic circulation changes". In: *PNAS* 110.41, pp. 16350–16354.

Amundson, R et al. (1996). "Isotopic evidence for shifts in atmospheric circulation patterns during the late Quaternary in mid- . . . " In: *Geology* 1969, pp. 23–26.

Arienzo, M.M. et al. (2015). "Bahamian speleothem reveals temperature decrease associated with Heinrich stadials". In: *Earth and Planetary Science Letters* 430, pp. 377–386.

Arienzo, M.M. et al. (2017). "Multi-proxy evidence of millennial climate variability from multiple Bahamian speleothems". In: *Quaternary Science Reviews* 161, pp. 18–29.

Asmerom, Y., V.J. Polyak, and S.J. Burns (2010). "Variable winter moisture in the southwestern United States linked to rapid glacial climate shifts". In: *Nature Geoscience* 3.2, pp. 114–117.

Baker, A. et al. (1997). "Elevated and variable values of 13C in speleothems in a British cave system". In: *Chemical Geology* 136, pp. 263–270.

Baker, A. et al. (2008). "Annually Laminated Speleothems : a Review". In: *International Journal of Speleology* 37.October, pp. 193–206.

Baker, D.G. and E.L. Kuehnast (1978). “Part X: Precipitation Normals for Minnesota 1941-1970”. In: *Climate of Minnesota*.

Barnes, J.W., E.J. Lang, and H.A. Potratz (1956). “Ratio of Ionium to Uranium in Coral Limestone”. In: *Science* 124.3213, pp. 175–176.

Bender, M. et al. (1985). “Isotopic composition of atmospheric O2 in ice linked with deglaciation and global primary productivity”. In: *Nature* 318, pp. 349–353.

Berger, A. and M. F. Loutre (1991). “Insolation values for the climate of the last 10 million years”. In: *Quaternary Science Reviews* 10.4, pp. 297–317.

Bigeleisen, J. (1965). “Chemistry of Isotopes”. In: *Science* 147.3657, pp. 463–471.

Blunier, T. and E.J. Brook (2001). “Timing of Millennial-Scale climate change in Antartica and Greenland during the last glacial period”. In: *Science* 291.2001, pp. 109–112.

Bond, G. and R. Lotti (1995). “Iceberg discharges into the North Atlantic on millenial time scales during the last glaciation”. In: *Science1* 267.5200, pp. 1005–1010.

Bond, G. et al. (1992). “Evidence for massive discharges of icebergs into the North-Atlantic ocean during the last glacial period”. In: *Nature* 360, pp. 245–249.

Bond, G. et al. (1993). “Correlations between climate records from North Atlantic sediments and Greenland ice”. In: *Nature* 365, pp. 143–147.

Bourdon, B. et al. (2003). “Introduction to U-series Geochemistry”. In: *Reviews in Mineralogy & Geochemistry* 52.1, pp. 1–24.

Braconnot, P. et al. (2012). “Evaluation of climate models using palaeoclimatic data”. In: *Nature Climate Change* 2.6, pp. 417–424.

Broecker, W.S. (1963). “A prelimary evaluation of uranium series inequilibrium as a tool for absolute age measurement of marine carbonates”. In: *Journal of Geophysical Research* 68.9, pp. 2817–2834.

— (2006). “Abrupt climate change revisited”. In: *Global and Planetary Change* 54, pp. 211–215.

Broecker, W.S. et al. (2010). “Putting the Younger Dryas cold event into context”. In: *Quaternary Science Reviews* 29.9-10, pp. 1078–1081.

Carlson, A.E. (2009). “Geochemical constraints on the Laurentide Ice Sheet contribution to Meltwater Pulse 1A”. In: *Quaternary Science Reviews* 28.17-18, pp. 1625–1630.

Cerling, T.E. (1984). “The stable isotopic composition of modern soil carbonate and its relationship to climate”. In: *Earth and Planetary Science Letters* 71, pp. 229–240.

Chappell, J. and N.J. Shackleton (1986). “Oxygen isotopes and sea level”. In: *Nature* 324.6093, pp. 137–140.

Chappellaz, J. et al. (1993). “Synchronous changes in atmospheric CH4 and Greenland climate between 40 and 8 kyr BP”. In: *Nature* 366, pp. 443–445.

Cheng, H. et al. (2000). “U-Th dating of deep-sea corals”. In: *Geochimica et Cosmochimica Acta* 64.14, pp. 2401–2416.

Cheng, H. et al. (2009). “Timing and structure of the 8.2 kyr B.P. event inferred from δ18O records of stalagmites from China, Oman, and Brazil”. In: *Geology* 37.11, pp. 1007–1010.

Cheng, H. et al. (2012). “The Global Paleomonsoon as seen through speleothem records from Asia and the Americas”. In: *Climate Dynamics* 39.5, pp. 1045–1062.

Cheng, H. et al. (2013). “Improvements in 230Th dating, 230Th and 234U half-life values, and U-Th isotopic measurements by multi-collector inductively coupled plasma mass spectrometry”. In: *Earth and Planetary Science Letters* 371-372, pp. 82–91.

Cheng, H. et al. (2016). “The Asian monsoon over the past 640,000 years and ice age terminations”. In: *Nature* 534.7609, pp. 640–646.

Chiang, J.C.H., M. Biasutti, and D.S. Battisti (2003). “Sensitivity of the Atlantic Intertropical Convergence Zone to Last Glacial Maximum boundary conditions”. In: *Paleo* 18.4, pp. 1–18.

Clark, P.U. (1999). “Northern Hemisphere Ice-Sheet Influences on Global Climate Change”. In: *Science* 286.5442, pp. 1104–1111.

Clark, P.U. et al. (1996). “Numerical reconstruction of the Laurentide Ice Sheet during the last glacial maximum”. In: *Geology* 24, pp. 679–682.

Cosford, J. et al. (2009). “Climatic and local effects on stalagmite δ 13 C values at Lianhua Cave , China”. In: *Palaeogeography, Palaeoclimatology, Palaeoecology* 280.1-2, pp. 235–244.

Craig, H. (1961). “Isotopic Variations in Meteoric Waters”. In: *Science* 133.3465, pp. 1702–1703.

Cross, M.S. (2016). “New insights into Great Basin hydroclimate: Past and Present”. Ph.D. thesis. University of Minnesota.

Cruz, F.W. et al. (2006). “A stalagmite record of changes in atmospheric circulation and soil processes in the Brazilian subtropics during the Late Pleistocene”. In: *Quaternary Science Reviews* 25, pp. 2749–2761.

Curry, B.B. and R.G. Baker (2000). “Palaeohydrology, vegetation, and climate since the late Illinois Episode (˜130 ka) in south-central Illinois”. In: *Palaeogeography, Palaeoclimatology, Palaeoecology* 155.1-2, pp. 59–81.

Dansgaard, W. (1964). “Stable isotopes in precipitation”. In: *Tellus* 16.4, pp. 436–468.

Dansgaard, W. et al. (1975). “Climatic changes, Norsemen and modern man”. In: *Nature* 255.5503, pp. 24–28.

Dansgaard, W. et al. (1993). “Evidence for general instability of past climate from a 250-kyr ice-core record”. In: *Nature* 364.6434, pp. 218–220.

Dasgupta, S. (2008). “High-resolution speleothem record of late Quaternary climate change from the Upper Midwest, USA”. Ph.D. thesis. University of Minnesota.

Denniston, R.F. et al. (1999a). “Evidence for increased cool season moisture during the middle-Holocene”. In: *Geology* 27.September, pp. 815–818.

Denniston, R.F. et al. (1999b). “Speleothem evidence for Holocene fluctuations of the prairie-forest ecotone, north-central USA”. In: *The Holocene* 9.6, pp. 671–676.

Denton, G.H. et al. (2005). “The role of seasonality in abrupt climate change”. In: *Quaternary Science Reviews* 24, pp. 1159–1182.

Deschamps, P. et al. (2012). “Ice-sheet collapse and sea-level rise at the Bølling warming 14,600 years ago”. In: *Nature* 483.7391, pp. 559–564.

Diem, J.E. (2013). “Influences of the Bermuda High and atmospheric moistening on changes in summer rainfall in the Atlanta, Georgia region, the United States”. In: *International Journal of Climatology* 33, pp. 160–172.

Dorale, J.A. et al. (1992). “A High-Resolution Record of Holocene Climate Change in Speleothem Calcite from Cold Water Cave, Northeast lowa”. In: *Science* 258.December, pp. 1626–1630.

Dorale, J.A. et al. (1998). “Climate and Vegetation History of the Midcontinent from 75 to 25 ka: A Speleothem Record from Crevice Cave, Missouri, USA”. In: *Science* 282.1998, pp. 1871–1874.

Dreybrodt, W. and D. Scholz (2011). “Climatic dependence of stable carbon and oxygen isotope signals recorded in speleothems: From soil water to speleothem calcite”. In: *Geochimica et Cosmochimica Acta* 75.3, pp. 734–752.

Edwards, R.L. (1988). “High precision thorium-230 ages of corals and the timing of sea level fluctuations in the late Quarternary”. PhD thesis. California Institute of Technology.

Edwards, R.L., J. H. Chen, and G. J. Wasserburg (1987). “238U-234U-230Th-232Th systematics and the precise measurement of time over the past 500,000 years”. In: *Earth and Planetary Science Letters* 81.2-3, pp. 175–192.

Edwards, R.L., C.D. Gallup, and H. Cheng (2003). “Uranium-series Dating of Marine and Lacustrine Carbonates”. In: *Reviews in Mineralogy and Geochemistry* 52.1, pp. 363–405.

Ellison, C.R.W., M.R. Chapman, and I.R. Hall (2006). “Surface and Deep Ocean Interactions during the Cold Climate Event 8200 Years Ago”. In: *Science* 312.5782, pp. 1929–1932.

Emiliani, C. (1955). “Pleistocene Temperatures”. In: *The Journal of Geology* 63.6, pp. 538–578.

Epstein, S. and T. Mayeda (1953). “Variation of O18 content of waters from natural sources”. In: *Geochimica et Cosmochimica Acta* 4.5, pp. 213–224.

Ersek, V. et al. (2012). “Holocene winter climate variability in mid-latitude western North America”. In: *Nature Communications* 3, pp. 1218–1219.

Feng, W. et al. (2014). “Changing amounts and sources of moisture in the U.S. southwest since the Last Glacial Maximum in response to global climate change”. In: *Earth and Planetary Science Letters* 401, pp. 47–56.

Ferguson, G. and S. Jasechko (2015). “The isotopic composition of the Laurentide Ice Sheet and fossil groundwater”. In: *Geophysical Research Letters* 42.12, pp. 4856–4861.

Fleitmann, D. et al. (2004). “The Speleothem Record of Climate change in Saudi Arabia”. In: *Saudi Geological Survey Open-File Report Sgs-Of-2004-8* January.

Flower, B.P. et al. (2004). “Phasing of deglacial warming and Laurentide Ice Sheet meltwater in the Gulf of Mexico”. In: *Geology* 32.7, pp. 597–600.

Ford, D. and P. Williams (2007). *Karst Hydrogeology and Geomorphology*. Chicester, England: John Wiley & Sons, pp. 1–562.

Forman, S.L. et al. (1995). “Paleoclimatic significance of Late Quaternary eolian deposition on the Piedmont and High Plains, Central United States”. In: *Global and Planetary Change* 11.1-2, pp. 35–55.

Genty, D. et al. (2001). “Dead carbon in stalagmites : Carbonate bedrock paleodissolution vs . ageing of soil organic matter . Implications for 13 C variations in speleothems”. In: *Geochimica et Cosmochimica Acta* 65.20, pp. 3443–3457.

Genty, D. et al. (2003). “Precise dating of Dansgaard-Oeschger climate oscillations in western Europe from stalagmite data”. In: *Nature* 421.6925, pp. 833–837.

Gourgiotis, A. et al. (2014). “Method for isotope ratio drift correction by internal amplifier signal synchronization in MC-ICPMS transient signals”. In: *Journal of Analytical Atomic Spectrometry* 29.9, p. 1607.

Grimm, E.C. et al. (1993). “A 50,000-year record of climate oscillations from Florida and its temporal correlation with the heinrich events.” In: *Science* 261.5118, pp. 198–200.

Gutjahr, M. et al. (2010). “Changes in North Atlantic Deep Water strength and bottom water masses during Marine Isotope Stage 3 (45 -35 ka BP)”. In: *Quaternary Science Reviews* 29.19-20, pp. 2451–2461.

Hall, I.R. et al. (2006). “Accelerated drawdown of meridional overturning in the late-glacial Atlantic triggered by transient pre-H event freshwater perturbation”. In: *Geophysical Research Letters* 33, pp. 1–5.

Harding, K.J. and P.K. Snyder (2015). “The relationship between the Pacific-North American teleconnection pattern, the great plains low-level jet, and north central U.S. heavy rainfall events”. In: *Journal of Climate* 28.17, pp. 6729–6742.

Harding, K.J., P.K. Snyder, and S. Liess (2013). “Use of dynamical downscaling to improve the simulation of Central U.S. warm season precipitation in CMIP5 models”. In: *Journal of Geophysical Research Atmospheres* 118.22, pp. 12522–12536.

Hardt, B. et al. (2010). “The seasonality of east central North American precipitation based on three coeval Holocene speleothems from southern West Virginia”. In: *Earth and Planetary Science Letters* 295.3-4, pp. 342–348.

Hastings, D.W., A.D. Russell, and S.R. Emerson (1998). “Foraminiferal magnesium in Globeriginoides sacculifer as a paleotemperature proxy”. In: *Paleoceanography* 13.2, pp. 161–169.

Heinrich, H. (1988). “Origin and consequences of cyclic ice rafting in the Northeast Atlantic Ocean during the past 130,000 years”. In: *Quaternary Research* 29.2, pp. 142–152.

Hemming, S.R. et al. (1998). “Provenance of Heinrich layers in core V28-82, northeastern Atlantic: 40Ar/39Ar ages of ice-rafted hornblend, Pb isotopes in feldspar grains, and Nd-Sr-Pb isotopes in the fine sediment fraction”. In: *Earth and Planetary Science Letters* 164, pp. 317–333.

Hendy, C.H. (1971). “The isotopic geochemistry of speleothems-I. The calculation of the effects of different modes of formation on the isotopic composition of speleothems and their applicability as palaeoclimatic indicators”. In: *Geochimica et Cosmochimica Acta* 35.8, pp. 801–824.

Hendy, C.H. and A.T. Wilson (1968). “Palaeoclimatic data from speleothems”. In: *Nature* 219, pp. 48–51.

Higgins, R.W. et al. (1997). “Influence of the great plains low-level jet on summertime precipitation and moisture transport over the central United States”. In: *Journal of Climate* 10.3, pp. 481–507.

Hooke, R.L. and H.B. Clausen (1982). “Wiconsin and Holocene d18O variations, Barnes Ice Cap, Canada”. In: *Geological Society of America Bulletin* 93, pp. 784–7889.

Horita, J. and D.J. Wesolowski (1994). “Liquid-vapor fractionation of oxygen and hydrogen isotopes of water from the freezing to the critical temperature”. In: *Geochimica et Cosmochimica Acta* 58.16, pp. 3425–3437.

Imbrie, J. et al. (1984). “The orbital theory of Pleistocene climate: support from a revised chronology of d18O record”. In: *Milankovitch and Climate, Part 1*. Ed. by A. Berger et al., pp. 269–305.

Isaac, N. and E. Picciotto (1953). “Ionium Determination of Deep-Sea Sediments”. In: *Nature* 171.4356, pp. 742–743.

Kageyama, M. et al. (2010). “Modelling glacial climatic millennial-scale variability related to changes in the Atlantic meridional overturning circulation : a review”. In: *Quaternary Science Reviews* 29.21-22, pp. 2931–2956.

Kang, S. et al. (2003). “Dust records from three ice cores: Relationships to spring atmospheric circulation over the Northern Hemisphere”. In: *Atmospheric Environment* 37.34, pp. 4823–4835.

Kaufman, A. and W.S. Broecker (1965). “Comparison of Th-230 and C-14 Ages for Carbonate Materials from Lake Lahontan and Bonneville”. In: *Journal of Geophysical Research* 70.16, pp. 4039–4054.

Kelly, M.J. et al. (2006). “High resolution characterization of the Asian Monsoon between 146,000 and 99,000 years B.P. from Dongge Cave, China and global correlation of events surrounding Termination II”. In: *Palaeogeography, Palaeoclimatology, Palaeoecology* 236.1-2, pp. 20–38.

Kim, S.J. et al. (2008). “High-resolution climate simulation of the last glacial maximum”. In: *Climate Dynamics* 31, pp. 1–16.

Lachniet, M.S. et al. (2009). “Late Quaternary moisture export across Central America and to Greenland : evidence for tropical rainfall variability from Costa Rican stalagmites”. In: *Quaternary Science Reviews* 28.27-28, pp. 3348–3360.

Lachniet, M.S. et al. (2013). “Orbital pacing and ocean circulation-induced collapses of the Mesoamerican monsoon over the past 22,000 y”. In: *PNAS* 110.23, pp. 9255–9260.

Lachniet, M.S. et al. (2014). “Orbital control of western North America atmospheric circulation and climate over two glacial cycles”. In: *Nature Communications* 5.May, pp. 1–8.

Leathers, D.J. and M.A. Palecki (1992). *The Pacific/North American teleconnection pattern and United States climate. Part II: temporal characteristics and index specification*.

Leathers, D.J. et al. (1991). *The Pacific/North American Teleconnection Pattern and United States Climate. Part I: Regional Temperature and Precipitation Associations*.

Licciardi, J.M., J.T. Teller, and P.U. Clark (1999). “Freshwater routing by the Laurentide ice sheet during the last deglaciation”. In: *Mechanisms of Global Climate Change at Millennial Time Scales*. Ed. by P.U. Clark, R.S. Webb, and L.D. Keigwin. American Geophysical Union, pp. 177–201.

Lisiecki, L.E. and M.E. Raymo (2005). “A Pliocene-Pleistocene stack of 57 globally distrubted benthic d18O records”. In: *Paleoceanography* 20.1, pp. 1–17.

Lorius, C. et al. (1985). “A 150,000-year climatic record from Antarctic ice”. In: *Nature* 316, pp. 591–596.

Lorius, C. et al. (1988). “Antarctic Ice Core : CO2 and Climatic Change Over the Last Climatic Cycle”. In: *Eos* 69.26, pp. 681, 683–684.

Lyle, M. et al. (2012). “Out of the Tropics : The Pacific, Great Basin Lakes , and Late Pleistocene Water Cycle in the Western United States”. In: *Science* 337.September, pp. 1629–1634.

MacAyeal, D.R. (1993). “Binge/Purge oscillations of the Laurentide ice sheet as a cause of the North Atlantic’s Heinrich Events”. In: *Paleoceanography* 8.6, pp. 775–784.

MacKinney, J.S. et al. (2013). “Northern Midwest climate changes leading up to the Wisconsinan glacial maximum”. In: *Geological Society of America Abstracts with Programs*.

Majoube, M. (1971). “Fractionnement en oxygene 18 et en deuterium entre l’eau et sa vapeur”. In: *Journal de Chemie et Physique* 68, pp. 1423–1436.

Marcott, S.A. et al. (2011). “Ice-shelf collapse from subsurface warming as a trigger for Heinrich events”. In: *PNAS* 108.33, pp. 13415–13419.

McCabe, G.J., M.A. Palecki, and J.L. Betancourt (2004). “Pacific and Atlantic Ocean influences on multidecadal drought frequency in the United States”. In: *PNAS* 101.12, pp. 4136–4141.

McDermott, F., H.P. Schwarcz, and P.J. Rowe (2005). “Isotopes in Speleothems”. In: *Isotopes in Palaeoenvironmental Research*. Springer, pp. 185–225.

McGarry, S.F. and A. Baker (2000). “Organic acid fluorescence: Applications to speleothem palaeoenvironmental reconstruction”. In: *Quaternary Science Reviews* 19.11, pp. 1087–1101.

McKinney, C.R. et al. (1950). “Improvements in mass spectrometers for the measurement of small differences in isotope abundance ratios”. In: *Review of Scientific Instruments* 21.8, pp. 724–730.

Mesolella, K.J. et al. (1969). “The Astronomical Theory of Climatic Change : Barbados Data”. In: *The Journal of Geology* 77.3, pp. 250–274.

Milankovitch, M. (1930). “Mathematische Klimalehre und Astronomische Theorie der Kilmaschwankungen”. In: *Handbuch der Kilmatologie*.

Mohr, J. (2000). *H and O isotope values of Twin Cities precipitation*. Tech. rep. University of Minnesota.

Nurnberg, D. et al. (2008). “Interacting Loop Current variability and Mississippi River discharge over the past 400 kyr”. In: *Earth and Planetary Science Letters* 272.1-2, pp. 278–289.

Oerter, E.J. et al. (2016). “Pedothem carbonates reveal anomalous North American atmospheric circulation 70,000 - 55,000 years ago”. In: *PNAS* 113.4, pp. 919–924.

Okumura, Y.M. et al. (2009). “North Pacific climate response to freshwater forcing in the subarctic North Atlantic: Oceanic and atmospheric pathways”. In: *Journal of Climate* 22, pp. 1424–1445.

Orland, I.J. et al. (2009). “Climate deterioration in the Eastern Mediterranean as revealed by ion microprobe analysis of a speleothem that grew from 2.2 to 0.9 ka in Soreq Cave, Israel”. In: *Quaternary Research* 71.1, pp. 27–35.

Orland, I.J. et al. (2014). “Seasonal climate signals (1990-2008) in a modern Soreq Cave stalagmite as revealed by high-resolution geochemical analysis”. In: *Chemical Geology* 363, pp. 322–333.

Oster, J.L. et al. (2009). “Late Pleistocene California droughts during deglaciation and Arctic warming”. In: *Earth and Planetary Science Letters* 288.3-4, pp. 434–443.

Oster, J.L. et al. (2010). “Modeling speleothem d13C variability in a central Sierra Nevada cave using 14C and 87Sr / 86Sr”. In: *Geochimica et Cosmochimica Acta* 74, pp. 5228–5242.

Oster, J.L. et al. (2014). “Millennial-scale variations in western Sierra Nevada precipitation during the last glacial cycle MIS 4/3 transition”. In: *Quaternary Research* 82, pp. 236–248.

Oster, J.L. et al. (2015). “Steering of westerly storms over western North America at the Last Glacial Maximum”. In: *Nature Geoscience* 8.March, pp. 201–205.

Patricola, C.M. and K.H. Cook (2013). “Mid-twenty-first century climate change in the Central United States. Part II: Climate change processes”. In: *Climate Dynamics* 40.3-4, pp. 569–583.

Rasmussen, S.O. et al. (2014). “A stratigraphic framework for abrupt climatic changes during the Last Glacial period based on three synchronized Greenland ice-core records : refining and extending the INTIMATE event stratigraphy”. In: *Quaternary Science Reviews* 106, pp. 14–28.

Remenda, V.H., J.A. Cherry, and T.W.D. Edwards (1994). “Isotopic Composition of Old Ground Water from Lake Agassiz : Implications for Late Pleistocene Climate”. In: *Science* 266.5193, pp. 1975–1978.

Richards, D.A. and J.A. Dorale (2003). “Uranium-series Chronology and Environmental Applications of Speleothems”. In: *Reviews in Mineralogy and Geochemistry* 52.1, pp. 407–460.

Rohling, E.J. (2013). “Oxygen Isotope Composition of Seawater”. In: *Encyclopedia of Quaternary Science* 2, pp. 915–922.

Romero-Lankao, P. et al. (2014). “Climate Change 2014: Impacts, Adaptation, and Vulnerability. Part B: Regional Aspects. Contribution of Working Group II to the Fifth Assessment Report of the Intergovernmental Panel on Climate Change”. In: *Fifth Assessment Report*, pp. 1439–1498.

Ruddiman, W.F. (2010). “A Paleoclimatic Enigma?” In: *Science* 328, pp. 838–839.

Schmidt, G.A. (1999). “Forward modeling of carbonate proxy data from planktonic foraminifera using oxygen isotope tracers in a global ocean model”. In: *Paleoceanography* 14.4, pp. 482–497.

Schmidt, G.A., G.R. Bigg, and E.J. Rohling (1999). *Global Seawater Oxygen-18 Database -v1.22*.

Serefiddin, F. et al. (2004). “Late Pleistocene paleoclimate in the Black Hills of South Dakota from isotope records in speleothems”. In: *Palaeogeography, Palaeoclimatology, Palaeoecology* 203.1-2, pp. 1–17.

Severinghaus, J.P. et al. (1998). “Timing of abrupt climate change at the end of the Younger Dryas interval from thermally fractionated gases in polar ice”. In: *Nature* 391, pp. 141–146.

Shackleton, N.J. (2000). “The 100,000-year ice-age cycle identified and found to lag temperature, carbon dioxide, and orbital eccentricity”. In: *Science* 289.5486, pp. 1897–1902.

Shapiro, D. (2007). “Evidence for wide scale climate forcing in the late Pleistocene from a speleothem stable isotope record from Spring Valley Caverns, Fillmore County, Minnesota”. Senior Thesis. Carleton College.

Sharp, Z. (2007). *Principles of Stable Isotope Geochemistry*. New Jersey: Pearson/Prentice Hall.

Shen, C. et al. (2002). “Uranium and thorium isotopic and concentration measurements by magnetic sector inductively coupled plasma mass spectrometry”. In: *Chemical Geology* 185.3-4, pp. 165–178.

Sheridan, S.C. (2003). “North American weather-type frequency and teleconnection indices”. In: *International Journal of Climatology* 23.1, pp. 27–45.

Simpkins, W.W. (1995). “Isotopic composition of precipitation in central Iowa”. In: *Journal of Hydrology* 172.1-4, pp. 185–207.

Steffensen, J.P. et al. (2008). “High-resolution Greenland ice core data show abrupt climate change happens in a few years”. In: *Science* 321, pp. 680–684.

Stocker, T.F. (2000). “Past and future reorganizations in the climate system”. In: *Quaternary Science Reviews* 19, pp. 301–319.

Sutton, R.T. and D.L.R. Hodson (2005). “Atlantic Ocean Forcing of North American and European Summer Climate”. In: *Science* 309.5731, pp. 115–118.

Tan, M. et al. (2006). “Applications of stalagmite laminae to paleoclimate reconstructions : Comparison with dendrochronology/climatology”. In: *Quaternary Science Reviews* 25, pp. 2103–2117.

Teed, R. (2000). “A >130,000-Year-Long Pollen Record from Pittsburg Basin, Illinois”. In: *Quaternary Research* 54, pp. 264–274.

Teller, James T. (1990). “Volume and routing of late-glacial runoff from the southern Laurentide Ice Sheet”. In: *Quaternary Research* 34.1, pp. 12–23.

Thurber, D.L. et al. (1965). “Uranium-series ages of Pacific Atoll coral”. In: *Science* 149.3679, pp. 55–58.

Urry, W.D. (1941). “The Radioactive Determination of Small Amounts of Uranium”. In: *American Journal of Science* 239.3, pp. 191–203.

Vinther, B.M. et al. (2006). “A synchronized dating of three Greenland ice cores throughout the Holocene”. In: *Journal of Geophysical Research Atmospheres* 111.13, pp. 1–11.

Wagner, J.D.M. et al. (2010). “Moisture variability in the southwestern United States linked to abrupt glacial climate change”. In: *Nature Geoscience* 3.2, pp. 110–113.

Wang, X. et al. (2004). “Wet periods in northeastern Brazil over the past 210 kyr linked to distant climate anomalies”. In: *Nature* 432, pp. 740–743.

Wang, Y. et al. (2001). “A High-Resolution Absolute-Dated Late Pleistocene Monsoon Record from Hulu Cave, China”. In: *Science* 294.5550, pp. 2345–2348.

Wickert, A.D. et al. (2013). “Gradual demise of a thin southern Laurentide ice sheet recorded by Mississippi drainage”. In: *Nature* 502.7473, pp. 668–671.

Williams, C., B.P. Flower, and D.W. Hastings (2012). “Seasonal Laurentide Ice Sheet melting during the "Mystery Interval" (17.5-14.5 ka)”. In: *Geology* 40.10, pp. 955–958.

Wuebbles, D.J. and K. Hayhoe (2004). “Climate change projections for the United States Midwest”. In: *Mitigation and Adaptation Strategies for Global Change* 9, pp. 335–363.

Yuan, D. et al. (2004). “Timing , Duration , and Transitions of the Last Interglacial Asian Monsoon”. In: *Science* 304.5670, pp. 575–578.

Zhu, J. and X.Z. Liang (2013). “Impacts of the Bermuda High on regional climate and ozone over the United States”. In: *Journal of Climate* 26.3, pp. 1018–1032.

Appendix A

Supplementary data

A.1 Formatting and Programming Languages

This thesis was written in LaTeX, and converted to PDF using PDFLaTeX, BibLaTeXand Biber.

All figures were made using *Python* plotting programs, including *Matplotlib*, *TrendVis* and *PySplit*. The author used *Python* version 2.7 and publicly available *Python* modules to create the data reduction methods described in Appendix B. These programs were made specifically for the UMN Isotope Lab and are available for public use at https://github.com/junissen.

A.2 ^{230}Th dates

All ^{230}Th dates were analyzed at the University of Minnesota Isotope Lab. If analyzing top-bottoms, samples were assumed to have a ^{238}U concentration of 300 parts per billion (ppb) and 50-100 mg of powder was drilled from surface layer. If rough estimates for ^{238}U concentration and $\frac{^{230}Th}{^{238}U}$ activity ratio were known, sample size could be calculated to gain the desired counting statistics error. For example, under SEM conditions, you would need 4 million counts of ^{230}Th ions to achieve a counting statistics error of 1‰. You can then calculate the sample size you would need under basic machine and chemistry yields. For SVC06 and SVC05, samples run on SEM had a typical sample size between 20-50 mg. Top bottom samples for SVC162A, SVC162B, SVC161 and SVC991d had a sample size of 50-100 mg. Non-top bottom SVC162A samples run on SEM had a sample size ≈50 mg.

For measurements using Faraday cups, beam intensities of the minor isotope must be greater than the $10^{13}\Omega$ amplifier noise. For a 2 minute measurement, the amplifier noise is $\approx 2.5\mu$V

(Pythoud et al. *in prep*). The number of counts of minor isotope can be calculated for the measurement time and desired signal-to-noise ratio. From the minor isotope count, sample size can then be calculated. SVC05 samples run on cups had a typical sample size between 60-150 mg. Non-top bottom SVC162A samples samples run on cups had a sample size ≈100 mg. SVC161 samples run on cups had a sample size ≈100 mg. SVC991d samples run on cups had a sample size between 100-250 mg.

Samples were spiked using a ^{229}Th and ^{233}U-^{236}U double spiked tracer, after first dissolving them in 1% HNO_3 (Edwards et al., 1987, Shen et al., 2002). If conducting top-bottom runs, ^{238}U concentrations of 300 ppb were used and samples were spiked at a 1:1 sample to spike ratio. If ^{238}U concentration was known, samples were spiked such that the $\frac{^{233}U}{^{234}U}$ was ≈10. After the removal of organics by the use of perchloric, U and Th underwent Fe co-precipitation and removed from solution. The Fe, U, and Th fractions were separated using an anion exchange column. The Fe fraction was discarded, and U and Th fractions were purified through multiple dry downs with perchloric and nitric acid, and then prepared for analysis by a dilution of water, 1% nitric acid, and a minimal amount of hydrofluoric acid. Chemical procedures follow those outlined in Edwards et al., 1987, Edwards, 1988, and Shen et al., 2002. Two spiked blanks were made for each batch, to determine the amount of contamination occurring during chemistry. While chemistry blank values as low as < 1 ag ^{230}Th and < 5 ag ^{234}U were achieved, average chemistry blank values used in age calculation are shown in Table A.7. Perchloric was the largest source of contamination, as shown in the reagent blank values in Table A.8.

All samples were run on a Thermo Scientific Neptune Plus or Neptune multi-collector inductively-coupled plasma mass spectrometer (MC-ICP-MS) with an Aridus II desolvating nebulizer system. Both SEM and Faraday cups were used for varying measurements. In a SEM configuration, beam intensities are collected via peak jumping, whereby the magnetic intensity changes to direct isotopes into the SEM for a set measurement time. The SEM is preceded by a retarding potential quadrupole (RPQ) to improve abundance sensitivity (Cheng et al., 2013). The SEM amplifies the electron count and is thus ideal for low beam intensities, but introduces additional errors. Additionally, beams must be kept low, and thus counting statistics restricts yield errors to 1‰ or greater (2σ) and results in long measurement times. Results are measured in ion counts per second. For measurements using Faraday cups, beam intensities are collected statically. For this type of collection, the magnetic intensity remains constant and isotopes are collected in Faraday cups placed specifically for the radius of curvature of each mass. Results are measured in voltage, and measurement capabilities are dependent on the resistance of the detector. The Neptune Plus MC-ICP-MS used in this study has been equipped with $10^{13}\Omega$ resistors, which allows for

beams of different magnitudes to be measured (Pythoud et al. *in prep*). Due to the beam capabilities of Faraday cups, measurement times and counting statistics are greatly reduced, resulting in yield errors <1‰ (2σ). However, tailing effects of ^{238}U, ^{232}Th, and ^{229}Th must be corrected for in cups measurements. Both SEM and cups measurements need to be preceded by running a standard of known concentrations, to ensure machine parameters are correct.

After collection on the MC-ICP-MS, data must then be analyzed to determine ^{230}Th ages using the age equation discussed in Chapter 1.2.2. Corrections must be made for background machine levels, isotopic fractionation, contamination during chemistry, and in the case of cups measurements, tailing. These corrections are discussed in Appendix B. All isotopic data for this study was reduced using the *Python* programs created by the author, as introduced in Appendix B.

A.2.1 Samples used for SVC stable isotope and growth record

(a) Full image of sample SVC06.

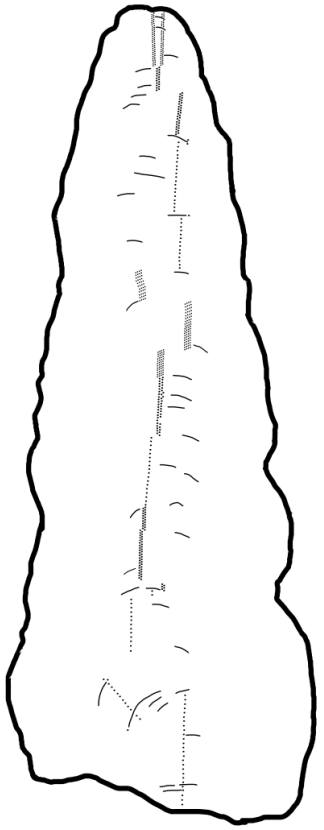

(b) Sampling of sample SVC06.

Figure A.1: Images of sample SVC06

^{230}Th dates and Uranium/Thorium isotopic composition of 30 subsamples from SVC06.

230Th dating results for SVC06. The error is 2s error.

Sample Number	Height from bottom (mm)	238U (ppb)		232Th (ppt)		230Th / 232Th (atomic x 10-6)		d234U* (measured)		230Th / 238U (activity)		230Th Age (yr) (uncorrected)		230Th Age (yr) (corrected)		d234U initial*** (corrected)		230Th Age (yr BP)*** (corrected)	
SVC06-19	598	2275.7	± 5.5	68	± 0	335968.7	± 2049.2	740.8	± 2.2	0.60742	± 0.00096	45304	± 112	45303	± 112	841.8	± 2.5	**45236**	**± 112**
SVC06-30	567	2657.8	± 8.1	293	± 2	95680.3	± 523.8	742.6	± 2.3	0.63941	± 0.00141	48143	± 151	48142	± 151	850.6	± 2.6	**48075**	**± 151**
SVC06-20	554	2820.7	± 9.7	2533	± 15	11580.9	± 61.1	690.7	± 2.1	0.63062	± 0.00098	49182	± 121	49168	± 122	793.5	± 2.4	**49101**	**± 122**
SVC06-21	537	3019.8	± 10.4	962	± 6	33694.3	± 178.3	724.0	± 2.1	0.65119	± 0.00100	49901	± 122	49896	± 122	833.5	± 2.4	**49829**	**± 122**
SVC06-31	497	3617.9	± 12.1	1189	± 7	31641.9	± 167.6	625.8	± 2.6	0.63059	± 0.00119	51709	± 162	51704	± 162	724.1	± 3.1	**51637**	**± 162**
SVC06-22	467	3255.0	± 7.4	318	± 2	110611.8	± 584.7	669.7	± 2.0	0.65592	± 0.00109	52462	± 135	52461	± 135	776.5	± 2.3	**52394**	**± 135**
SVC06-23	433	4500.7	± 17.0	351	± 2	134766.5	± 725.2	613.5	± 1.9	0.63738	± 0.00095	52919	± 128	52918	± 128	712.4	± 2.3	**52851**	**± 128**
SVC06-32	409	4132.9	± 14.9	511	± 3	84197.7	± 495.6	578.8	± 4.0	0.63086	± 0.00195	53747	± 275	53745	± 275	673.6	± 4.7	**53678**	**± 275**
SVC06-24	387	3540.3	± 11.5	170	± 1	226037.6	± 1281.2	618.6	± 2.0	0.65836	± 0.00107	54884	± 144	54883	± 144	722.2	± 2.4	**54816**	**± 144**
SVC06-33	327	4735.6	± 14.5	66	± 1	805510.4	± 8728.3	637.0	± 2.1	0.68377	± 0.00124	56714	± 163	56714	± 163	747.6	± 2.5	**56647**	**± 163**
SVC06-34-1	312	4969.3	± 19.2	376	± 2	144375.8	± 775.5	577.1	± 2.1	0.66275	± 0.00123	57280	± 170	57279	± 170	678.3	± 2.5	**57212**	**± 170**
SVC06-34-2	303	5229.5	± 18.3	392	± 2	145566.5	± 785.2	573.9	± 2.3	0.66105	± 0.00123	57246	± 175	57244	± 175	674.6	± 2.7	**57177**	**± 175**
SVC06-35	260	4196.7	± 10.5	148	± 1	322073.2	± 1735.6	620.5	± 2.2	0.69002	± 0.00104	58153	± 153	58153	± 153	731.1	± 2.6	**58086**	**± 153**
SVC06-10-2	230	5218.3	± 18.1	85	± 1	676585.5	± 4325.3	569.6	± 2.1	0.66894	± 0.00136	58331	± 184	58331	± 184	671.5	± 2.5	**58264**	**± 184**
SVC06-25	183	4950.0	± 13.6	65	± 0	851099.5	± 5759.3	571.7	± 1.7	0.67751	± 0.00097	59185	± 139	59185	± 139	675.6	± 2.1	**59118**	**± 139**
SVC06-36	167	3030.1	± 7.6	62	± 0	593058.0	± 3287.2	678.1	± 2.5	0.73747	± 0.00139	60422	± 189	60421	± 189	804.2	± 3.0	**60354**	**± 189**
SVC06-26	155	3492.1	± 12.1	189	± 1	218624.3	± 1221.2	631.7	± 2.3	0.71933	± 0.00161	60773	± 209	60772	± 209	749.8	± 2.7	**60705**	**± 209**
SVC06-37	130	3097.7	± 8.2	237	± 1	162728.0	± 867.9	699.3	± 2.4	0.75580	± 0.00136	61316	± 183	61315	± 183	831.4	± 2.9	**61248**	**± 183**
SVC06-29-1	116	2853.9	± 8.3	118	± 2	306591.8	± 5989.3	719.8	± 1.6	0.76950	± 0.00117	61742	± 143	61741	± 143	856.8	± 1.9	**61674**	**± 143**
SVC06-29-2	116	2843.2	± 10.4	176	± 1	205723.5	± 1210.2	717.9	± 5.1	0.77205	± 0.00245	62101	± 357	62100	± 357	855.4	± 6.2	**62033**	**± 357**
SVC06-29-4	116	2838.9	± 8.1	179	± 1	201156.6	± 1329.4	720.8	± 1.5	0.76920	± 0.00104	61664	± 128	61663	± 128	857.8	± 1.8	**61596**	**± 128**
SVC06-18-1	87	3721.1	± 10.1	139	± 6	327768.7	± 14076.3	643.4	± 1.7	0.74122	± 0.00079	62561	± 122	62561	± 122	767.7	± 2.0	**62494**	**± 122**
SVC06-18-2	87	4729.7	± 23.3	130	± 2	441486.7	± 5242.6	643.6	± 1.7	0.73846	± 0.00112	62250	± 150	62249	± 150	767.2	± 2.0	**62182**	**± 150**
SVC06-18-3	87	4848.6	± 25.3	198	± 2	300119.3	± 2878.2	532.3	± 1.8	0.74268	± 0.00292	69130	± 382	69129	± 382	647.0	± 2.3	**69062**	**± 382**
SVC06-18-4	87	4654.0	± 18.4	196	± 2	289649.2	± 2287.1	642.9	± 1.7	0.73959	± 0.00099	62411	± 139	62410	± 139	766.7	± 2.0	**62343**	**± 139**
SVC06-18-5	87	7115.9	± 29.7	269	± 2	322528.7	± 2275.4	646.0	± 1.9	0.73861	± 0.00116	62142	± 159	62141	± 159	769.9	± 2.3	**62074**	**± 159**
SVC06-38	81	2783.5	± 7.8	196	± 1	178687.9	± 962.6	689.4	± 2.7	0.76472	± 0.00144	62746	± 206	62745	± 206	822.9	± 3.3	**62678**	**± 206**
SVC06-27	50	5206.6	± 23.3	46	± 1	1277646.3	± 22170.8	502.4	± 2.3	0.67922	± 0.00148	63141	± 223	63141	± 223	600.3	± 2.7	**63074**	**± 223**
SVC06-39	15	5893.4	± 18.9	137	± 1	474690.0	± 2667.3	480.6	± 2.1	0.66910	± 0.00150	63175	± 224	63174	± 224	574.4	± 2.6	**63107**	**± 224**
SVC06-28	12	5853.3	± 21.5	568	± 4	115677.5	± 652.8	497.1	± 2.4	0.68034	± 0.00171	63584	± 253	63582	± 253	594.8	± 2.9	**63515**	**± 253**

All dates run with both U and Th on SEM

U decay constants: l238 = 1.55125x10-10 (Jaffey et al., 1971) and l234 = 2.82206x10-6 (Cheng et al., 2013). Th decay constant: l230 = 9.1705x10-6 (Cheng et al., 2013).

238U and 232Th errors include sample and spike weight errors

* d234U = ([234U/238U]activity – 1)x1000.

** d234U initial was calculated based on 230Th age (d234Uinitial = d234Umeasured * e^234T).

Corrected 230Th ages assume the initial 230Th/232Th atomic ratio of 4.4 ±2.2 x10-6. Those are the values for a material at secular equilibrium, with the bulk earth 232Th/238U value of 3.8. The errors are arbitrarily assumed to be 50%.

*** B.P. stands for "Before Present" where the "Present" is defined as the year 1950 A.D.

Table A.1: ^{230}Th dates for sample SVC06. Ages in gray are replicates. All subsamples were completed for this study by author and run on SEM.

(a) Full image of sample SVC05.

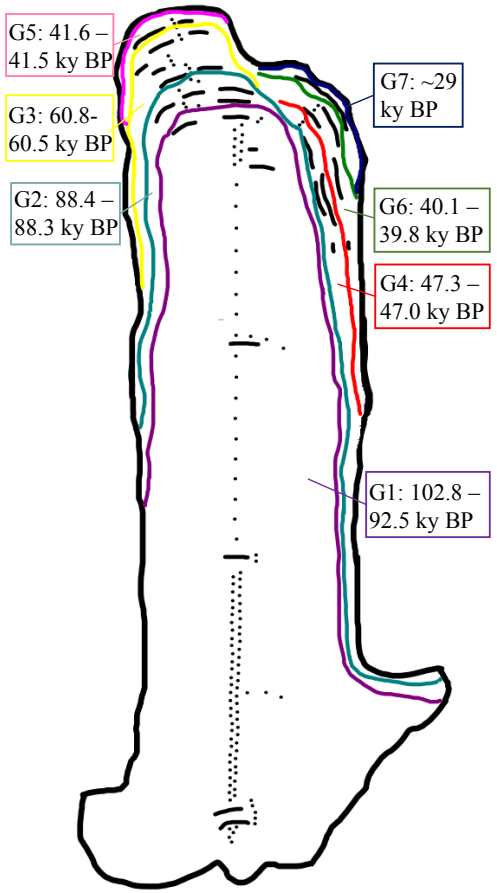

(b) Growth phases and approximate durations for SVC05.

Figure A.2: Images of sample SVC05

^{230}Th dates and Uranium/Thorium isotopic composition of 28 subsamples from SVC05.

230Th dating results for composite SVC05 record. The error is 2s error.

Growth phase	Sample Number	Height from bottom (mm)	238U (ppb)		232Th (ppt)		230Th / 232Th (atomic x 10-6)		d234U* (measured)		230Th / 238U (activity)		230Th Age (yr) (uncorrected)		230Th Age (yr) (corrected)		d234U initial*** (corrected)		230Th Age (yr BP)*** (corrected)	
G7	SVC051a-6	217	1200.0	±3.0	1310	±105	6380.0	±510.0	766.0	±4.0	0.421	±0.00200	29130	±200	29120	±200	832.0	±4.0	**29062**	**±200**
	SVC051a-7	217	1270.0	±3.0	330	±110	26900.0	±8770.0	796.0	±3.0	0.428	±0.00300	29110	±230	29100	±230	865.0	±4.0	**29042**	**±230**
	SVC051a-27	215	1210.9	± 1.1	27214	± 138	321.6	± 1.7	771.4	± 0.9	0.43831	± 0.00062	30356	± 51	30000	± 257	839.6	± 1.2	**29933**	**± 257**
G6	SVC051a-26	213	919.4	± 1.0	7326	± 38	1260.7	± 6.5	978.7	± 1.1	0.60926	± 0.00086	38889	± 69	38778	± 104	1091.9	± 1.2	**38711**	**± 104**
	SVC051a-21.1	210	944	±1	4161	±83	2334.9	±46.9	975.1	±2.0	0.6242	±0.0010	40093	±88	40031	±98	1092	±2	**39968**	**±98**
	SVC051a-25	209	1006.0	± 1.4	4511	± 23	2286.9	± 12.4	967.2	± 1.3	0.62202	± 0.00133	40123	± 106	40060	± 114	1083.0	± 1.5	**39993**	**± 114**
G5	SVC051a-20.2	206	1118.7	±1.2	2499	±50	4387	±88	824.7	±1.8	0.5943	±0.0009	41653	±89	41619	±92	927	±2	**41556**	**±92**
	SVC051a-24	206	1216.4	± 1.9	5197	± 27	2274.3	± 13.0	804.5	± 1.6	0.58928	± 0.00163	41801	± 144	41736	± 151	905.1	± 1.8	**41669**	**± 151**
G4	SVC051a-23	204.5	770.7	± 1.1	14733	± 77	542.9	± 3.0	737.2	± 1.4	0.62946	± 0.00156	47419	± 151	47117	± 261	842.0	± 1.7	**47050**	**± 261**
	SVC051a-20.6	202	857.6	±2.3	68206	±1375	149	±3	773.6	±4.0	0.7190	±0.0024	54384	±279	53159	±909	899	±5	**53096**	**±909**
	SVC051a-22	202	883.7	± 1.4	77047	± 402	135.2	± 0.7	771.2	± 1.2	0.71479	± 0.00119	54087	± 123	52741	± 960	894.9	± 2.8	**52674**	**± 960**
G3	*SVC051a-19-1*	*200*	*2234.5*	*±2.4*	*26869*	*±538*	*726*	*±15*	*684.7*	*±1.6*	*0.5296*	*±0.0008*	*40068*	*±84*	*39870*	*±163*	*766*	*±2*	***39804***	***±163***
	SVC051a-1	199	1650.0	±4.0	14310	±80	1390	±10	661.0	±3.0	0.7320	±0.0040	60740	±470	60600	±470	784	±4	**60542**	**±470**
	SVC051a-19-2	199	1620.6	± 3.9	26881	± 149	725.9	± 3.7	647.1	± 1.4	0.73030	± 0.00066	61184	± 101	60910	± 218	768.5	± 1.8	**60843**	**± 218**
	SVC051a-21	197	1831.9	± 3.5	28580	± 152	770.1	± 4.1	647.2	± 1.2	0.72868	± 0.00140	61005	± 162	60748	± 243	768.2	± 1.5	**60681**	**± 243**
	SVC051a-3	191	1270.0	±3.0	1520	±60	10160	±430	680.0	±3.0	0.7370	±0.0030	60300	±340	60280	±340	807	±4	**60222**	**±340**
	SVC051a-18	191	1689.9	± 4.2	1680	± 9	12345.9	± 63.1	684.1	± 1.6	0.74424	± 0.00083	60840	± 116	60824	± 116	812.2	± 1.9	**60757**	**± 116**
G2	SVC051a-4	186.5	1000.0	±2.0	16990	±90	920	±7	645.0	±3.0	0.9530	±0.0050	88140	±750	87870	±760	827	±5	**87812**	**±760**
	SVC051a-17	186.5	426.0	± 1.6	127561	± 793	54.5	± 0.3	633.0	± 1.3	0.98897	± 0.00102	94046	± 188	89150	± 3481	814.1	± 8.2	**89083**	**± 3481**
	SVC051a-20	186	1128.6	± 2.3	4930	± 27	3582.1	± 18.5	633.9	± 1.7	0.94905	± 0.00131	88444	± 227	88374	± 232	813.5	± 2.2	**88307**	**± 232**
	SVC051a-13	183	1240.7	± 3.2	30952	± 174	625.9	± 3.2	638.1	± 1.5	0.94699	± 0.00121	87821	± 205	87421	± 349	816.6	± 2.1	**87354**	**± 349**
G1	SVC051a-18.0	181	1202	±2	4621	±93	4494.1	±90.2	740.9	±1.9	1.0483	±0.0017	92640	±276	92583	±278	962	±3	**92520**	**±278**
	SVC051a-14	180	1042.8	± 2.9	32320	± 184	561.8	± 2.9	733.6	± 1.5	1.05589	± 0.00118	94263	± 202	93801	± 384	955.9	± 2.2	**93734**	**± 384**
	SVC051a-15	170	961.4	± 2.5	7638	± 43	2041.4	± 10.7	627.2	± 2.1	0.98361	± 0.00167	93828	± 308	93700	± 320	817.0	± 2.9	**93633**	**± 320**
	SVC051a-12.8	128.5	1470.4	±2.1	1198	±24	19814	±400	587.8	±1.9	0.9789	±0.0017	96905	±323	96891	±323	773	±3	**96828**	**±323**
	SVC051a-5	75	1185.0	±3.0	15250	±85	1270	±9	589.0	±3.0	0.9920	±0.0050	98950	±770	98735	±780	778	±5	**98677**	**±780**
	SVC051a-2	10	1265.0	±3.0	6910	±60	2860	±30	472.0	±3.0	0.9460	±0.0060	104430	±1065	104330	±1065	634	±4	**104272**	**±1065**
	SVC051a-16	6	1122.5	±3.0	4905	±28	3552.8	±18.6	476.9	±2.0	0.94153	±0.00153	102949	±353	102871	±357	637.6	±2.7	**102804**	**±357**

U decay constants: l238 = 1.55125x10-10 (Jaffey et al., 1971) and l234 = 2.82206x10-6 (Cheng et al., 2013). Th decay constant: l230 = 9.1705x10-6 (Cheng et al., 2013).
238U and 232Th errors include sample and spike weight errors
* d234U = ([234U/238U]activity – 1)x1000.
** d234U initial was calculated based on 230Th age (d234Uinitial = d234Umeasured * e^234T).
Corrected 230Th ages assume the initial 230Th/232Th atomic ratio of 4.4 ±2.2 x10-6. Those are the values for a material at secular equilibrium, with the bulk earth 232Th/238U value of 3.8. The errors are arbitrarily assumed to be 50%.
*** B.P. stands for "Before Present" where the "Present" is defined as the year 1950 A.D.

Table A.2: ^{230}Th dates for sample SVC05. Age in gray out of stratigraphic order due to contamination from neighboring hiatus. Subsamples 1-7 were completed by Sushmita Dasgupta in 2008 on SEM (Dasgupta, 2008). Subsamples 12.8, 20.6, 18.0, 20.2 and 21.2 were completed by Joel MacKinney in 2013 on SEM (MacKinney et al., 2013). Subsamples 13-27 were completed for this study by author. Subsamples 13-19 were run on SEM. Subsamples 20-27 were run with U on cups and Th on SEM.

A.2.2 Samples used for SVC growth record

(a) Full image of sample SVC162A.

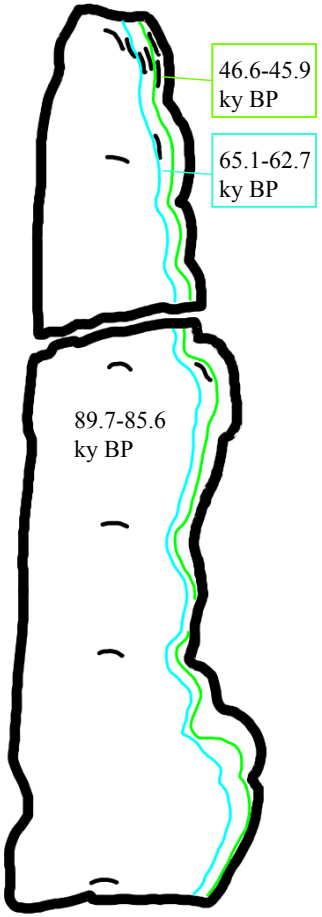

(b) Growth phases and approximate durations of sample SVC162A.

Figure A.3: Images of sample SVC162A

^{230}Th dates and Uranium/Thorium isotopic composition of 14 subsamples from SVC162A.

230Th dating results for SVC16-2A . The error is 2s error.

Sample Number	Height from bottom (mm)	238U (ppb)		232Th (ppt)		230Th / 232Th (atomic x 10-6)		d234U* (measured)		230Th / 238U (activity)		230Th Age (yr) (uncorrected)		230Th Age (yr) (corrected)		d234U initial*** (corrected)		230Th Age (yr BP)*** (corrected)	
Top-Bottoms																			
SVC162A-2	395	3836.8	± 22.0	10502	± 80	4958.5	± 32.1	459.4	± 2.8	0.82316	± 0.00341	85759	± 575	85708	± 576	585.1	± 3.7	**85641**	**± 576**
SVC162A-1	2	4051.4	± 26.8	1662	± 14	34641.2	± 239.5	479.5	± 2.8	0.86210	± 0.00402	89807	± 676	89799	± 676	617.7	± 3.8	**89732**	**± 676**
Additional samples																			
SVC162A-3	5	4333.8	± 4.6	1153	± 1	53251.0	± 25.4	480.0	± 0.5	0.85903	± 0.00027	89287	± 65	89282	± 65	617.5	± 0.7	**89215**	**± 65**
SVC162A-4	105	3930.0	± 2.4	8086	± 5	6966.2	± 18.0	497.8	± 0.5	0.86922	± 0.00030	89143	± 62	89107	± 67	640.1	± 0.6	**89040**	**± 67**
SVC162A-5	165	4691.3	± 3.7	4305	± 3	15533.2	± 8.2	490.6	± 0.5	0.86447	± 0.00030	89104	± 64	89087	± 65	630.8	± 0.6	**89020**	**± 65**
SVC162A-6	235	3671.3	± 1.9	7151	± 4	7288.4	± 4.2	486.0	± 0.5	0.86096	± 0.00036	89009	± 71	88974	± 75	624.7	± 0.6	**88907**	**± 75**
SVC162A-7	330	4566.3	± 3.3	1315	± 1	49215.0	± 19.4	486.7	± 0.4	0.85933	± 0.00027	88696	± 58	88691	± 58	625.1	± 0.6	**88624**	**± 58**
SVC162A-8	388	4061.4	± 3.5	6575	± 6	8677.8	± 28.9	477.4	± 0.4	0.85199	± 0.00035	88456	± 64	88426	± 67	612.7	± 0.5	**88359**	**± 67**
Top-Bottoms on growth phases																			
SVC162A-9	396	1619.5	± 8.9	111524	± 845	202.4	± 1.4	686.7	± 4.1	0.84518	± 0.00372	71767	± 491	70673	± 912	838.3	± 5.4	**70606**	**± 912**
SVC162A-10	399	1476.3	± 7.9	98	± 1	17390027 968.2	± 1759835	840.3	± 4.3	69957.31 784	± 611.0064	25550	± 0	25550	± 0	903.1	± 4.6	**25483**	**± 0**
SVC162A-11	402	1068.6	± 5.1	9371	± 65	1399.3	± 8.4	1063.8	± 3.5	0.74421	± 0.00243	46820	± 209	46704	± 224	1213.7	± 4.1	**46637**	**± 224**
SVC162A-12	404	1114.3	± 5.1	5153	± 35	2634.2	± 15.3	1076.4	± 3.3	0.73880	± 0.00216	46065	± 185	46004	± 190	1225.6	± 3.8	**45937**	**± 190**
Improved top-Bottoms on growth phases																			
SVC162A-9-2	396	1536.6	± 4.2	2977	± 17	7018.2	± 35.7	765.2	± 1.9	0.82466	± 0.00079	65194	± 126	65165	± 128	919.7	± 2.3	**65098**	**± 128**
SVC162A-10-2	399	1329.9	± 2.4	2457	± 13	7551.0	± 38.6	858.8	± 2.0	0.84599	± 0.00089	62828	± 123	62801	± 125	1025.3	± 2.4	**62734**	**± 125**

U decay constants: l238 = 1.55125x10-10 (Jaffey et al., 1971) and l234 = 2.82206x10-6 (Cheng et al., 2013). Th decay constant: l230 = 9.1705x10-6 (Cheng et al., 2013).
238U and 232Th errors include sample and spike weight errors
* d234U = ([234U/238U]activity – 1)x1000.
** d234U initial was calculated based on 230Th age (d234Uinitial = d234Umeasured * e^234T).
Corrected 230Th ages assume the initial 230Th/232Th atomic ratio of 4.4 ±2.2 x10-6. Those are the values for a material at secular equilibrium, with the bulk earth 232Th/238U value of 3.8. The errors are arbitrarily assumed to be 50%.
*** B.P. stands for "Before Present" where the "Present" is defined as the year 1950 A.D.

Table A.3: ^{230}Th dates for sample SVC162A. Age in gray has some error during run, potentially from nearby hiatus. Samples SVC162A-9 and SVC162A-10 were replicated to improve top-bottom ages on growth phase. All subsamples were completed for this study by author. Subsamples 1-2, 9-12 were run on SEM. Subsamples 3-8 were run on cups.

(a) Full image of sample SVC162B.

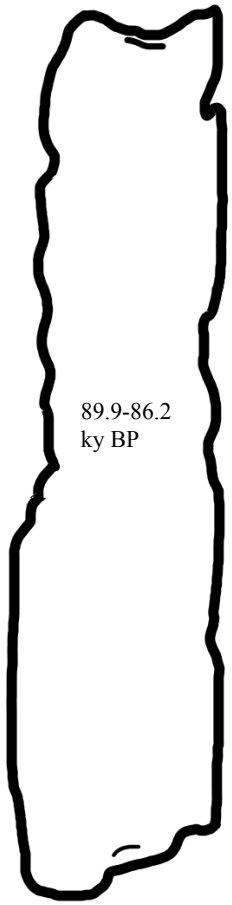

(b) Sampling of sample SVC162B.

Figure A.4: Images of sample SVC162B

^{230}Th dates and Uranium/Thorium isotopic composition of 2 subsamples from SVC162B.

230Th dating results for SVC162B. The error is 2s error.

Sample Number	238U (ppb)		232Th (ppt)		230Th / 232Th (atomic x 10-6)		d234U* (measured)		230Th / 238U (activity)		230Th Age (yr) (uncorrected)		230Th Age (yr) (corrected)		d234U initial*** (corrected)		230Th Age (yr BP)*** (corrected)	
Top-Bottoms																		
SVC162B-2	4251.5	± 26.7	996	± 8	57382.0	± 441.2	440.4	± 3.4	0.81521	± 0.00460	86313	± 779	86309	± 779	561.8	± 4.6	**86242**	**± 779**
SVC162B-1	3617.6	± 16.6	23175	± 159	2244.1	± 14.1	491.4	± 2.5	0.87190	± 0.00320	90156	± 546	90042	± 551	633.6	± 3.4	**89975**	**± 551**

U decay constants: l238 = 1.55125x10-10 (Jaffey et al., 1971) and l234 = 2.82206x10-6 (Cheng et al., 2013). Th decay constant: l230 = 9.1705x10-6 (Cheng et al., 2013).
238U and 232Th errors include sample and spike weight errors
* d234U = ([234U/238U]activity – 1)x1000.
** d234U initial was calculated based on 230Th age (d234Uinitial = d234Umeasured * e^234T).
Corrected 230Th ages assume the initial 230Th/232Th atomic ratio of 4.4 ±2.2 x10-6. Those are the values for a material at secular equilibrium, with the bulk earth 232Th/238U value of 3.8. The errors are arbitrarily assumed to be 50%.
*** B.P. stands for "Before Present" where the "Present" is defined as the year 1950 A.D.

Table A.4: ^{230}Th dates for sample SVC162B. Sample SVC162B is a conjoined stalagmite of SVC162A. All subsamples were completed for this study by author and run on SEM.

(a) Full image of sample SVC161.

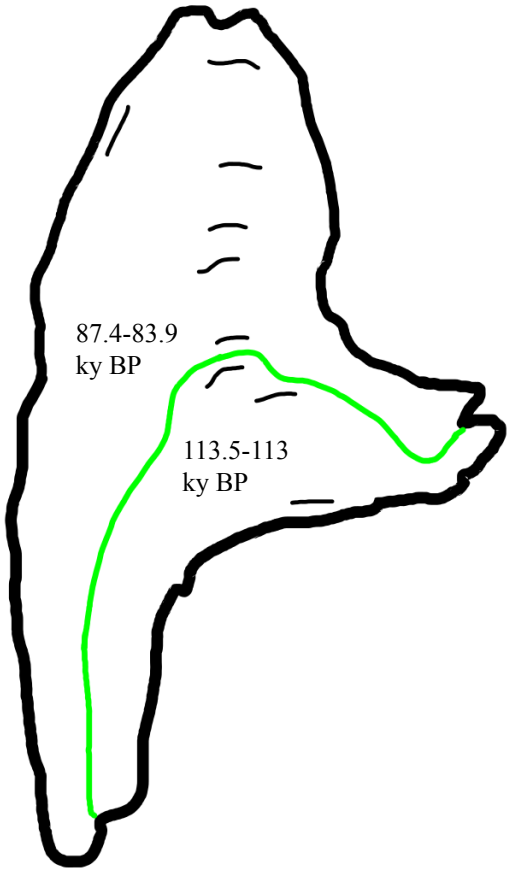

(b) Growth phases and approximate durations of sample SVC161.

Figure A.5: Images of sample SVC161

^{230}Th dates and Uranium/Thorium isotopic composition of 10 subsamples from SVC161.

230Th dating results for SVC161. The error is 2s error.

Sample Number	Height from bottom (mm)	238U (ppb)		232Th (ppt)		230Th / 232Th (atomic x 10-6)		d234U* (measured)		230Th / 238U (activity)		230Th Age (yr) (uncorrected)		230Th Age (yr) (corrected)		d234U initial*** (corrected)		230Th Age (yr BP)*** (corrected)	
Top-Bottoms																			
SVC161-2	111	1627.9	± 8.5	48170	± 355	503.0	± 3.2	606.4	± 3.0	0.90264	± 0.00332	84461	± 506	83973	± 609	768.5	± 4.0	**83906**	**± 609**
SVC161-1	2.5	1897.4	± 10.7	48908	± 371	650.1	± 3.9	495.9	± 2.7	1.01632	± 0.00339	113792	± 724	113345	± 786	682.9	± 4.0	**113278**	**± 786**
Additional samples																			
SVC161-3	102	1781.8	± 1.7	247148	± 263	110.9	± 13.3	601.5	± 0.6	0.93003	± 0.00285	88599	± 398	86295	± 1678	767.3	± 3.7	**86228**	**± 1678**
SVC161-4	80	1769.1	± 1.1	6030	± 4	4450.8	± 43.8	624.3	± 0.6	0.92003	± 0.00108	85344	± 150	85289	± 155	794.2	± 0.8	**85222**	**± 155**
SVC161-5	66	1690.5	± 1.7	1777	± 2	14645.1	± 40.3	646.6	± 0.8	0.93365	± 0.00106	85362	± 152	85345	± 153	822.7	± 1.1	**85278**	**± 153**
SVC161-6	58	1316.3	± 1.4	10459	± 11	2010.6	± 18.1	686.0	± 0.7	0.96856	± 0.00139	86786	± 188	86662	± 207	876.0	± 1.0	**86595**	**± 207**
SVC161-7	41	1813.8	± 1.5	4298	± 4	6292.9	± 17.5	572.0	± 0.7	0.90421	± 0.00062	87543	± 106	87503	± 110	732.2	± 0.9	**87436**	**± 110**
SVC161-8	35	1659.4	± 1.3	181041	± 148	153.3	± 7.9	484.6	± 0.7	1.01039	± 0.00210	114253	± 403	112332	± 1417	665.4	± 2.8	**112265**	**± 1417**
SVC161-9	25	2203.9	± 1.8	7921	± 7	4576.8	± 42.4	472.7	± 0.7	0.99759	± 0.00075	113516	± 171	113452	± 177	651.1	± 1.0	**113385**	**± 177**
SVC161-10	5.5	2124.8	± 2.0	3110	± 3	11459.9	± 33.9	498.9	± 0.8	1.01739	± 0.00071	113584	± 166	113559	± 167	687.4	± 1.1	**113492**	**± 167**

U decay constants: l238 = 1.55125x10-10 (Jaffey et al., 1971) and l234 = 2.82206x10-6 (Cheng et al., 2013). Th decay constant: l230 = 9.1705x10-6 (Cheng et al., 2013).
238U and 232Th errors include sample and spike weight errors
* d234U = ([234U/238U]activity – 1)x1000.
** d234U initial was calculated based on 230Th age (d234Uinitial = d234Umeasured * e^234T).
Corrected 230Th ages assume the initial 230Th/232Th atomic ratio of 4.4 ±2.2 x10-6. Those are the values for a material at secular equilibrium, with the bulk earth 232Th/238U value of 3.8. The errors are arbitrarily assumed to be 50%.
*** B.P. stands for "Before Present" where the "Present" is defined as the year 1950 A.D.

Table A.5: ^{230}Th dates for sample SVC161. Sample has two primary growth phases, with hiatus separating growth around 35 mm from base. All subsamples were completed for this study by author. Subsamples 1-2 were run on SEM. Subsamples 3-10 were run on cups.

(a) Full image of sample SVC991d.

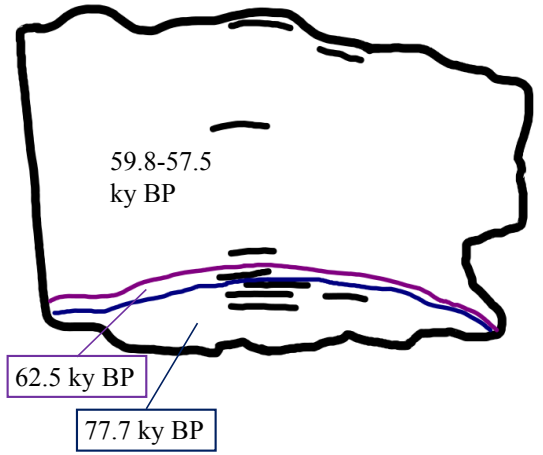

(b) Growth phases and approximate durations of sample SVC991d.

Figure A.6: Images of sample SVC991d

^{230}Th dates and Uranium/Thorium isotopic composition of 9 subsamples from SVC991d.

230Th dating results for SVC991d. The error is 2s error.

Sample Number	Height from bottom (mm)	238U (ppb)		232Th (ppt)		230Th / 232Th (atomic x 10-6)		d234U* (measured)		230Th / 238U (activity)		230Th Age (yr) (uncorrected)		230Th Age (yr) (corrected)		d234U initial*** (corrected)		230Th Age (yr BP)*** (corrected)	
Top-Bottoms																			
SVC991d-2b		1150.4	± 6.9	6783	± 54	2377.2	± 17.7	994.0	± 6.0	0.85011	± 0.00455	57599	± 449	57520	± 452	1169.2	± 7.2	**57453**	**± 452**
SVC991d-1b		718.0	± 3.7	10364	± 74	1253.1	± 7.8	1040.0	± 4.7	1.09695	± 0.00411	77928	± 474	77745	± 490	1295.2	± 6.1	**77678**	**± 490**
Additional samples	***Run by Zongyi Wang***																		
SVC991d-8 Duplicat	93	1624.6	±7.5	6799	±32	3386.4	±9.8	1015.4	±0.5	0.8594	±0.0005	57584	±48	57528	±62	1194	±1	**57461**	**±62**
SVC991d-8	93	1626.4	±6.5	7233	±29	3183.7	±8.9	1014.7	±0.5	0.8586	±0.0005	57543	±45	57484	±61	1193	±1	**57417**	**±61**
SVC991d-7	60	1492.3	±4.4	13855	±40	1524.6	±1.2	972.6	±0.5	0.8582	±0.0005	59122	±47	58997	±101	1149	±1	**58930**	**±101**
SVC991d-6	19	1091.6	±4.0	12381	±45	1257.9	±7.2	965.1	±0.4	0.8650	±0.0005	60016	±52	59862	±121	1143	±1	**59795**	**±121**
SVC991d-5	12	873.9	±3.2	9720	±42	1221.7	±3.1	815.5	±0.7	0.8241	±0.0007	62699	±76	62535	±138	973	±1	**62468**	**±138**
SVC991d-4	9	1410.9	±5.6	264688	±1102	100.0	±0.5	1044.7	±0.5	1.1307	±0.0036	80975	±358	78584	±1730	1304	±6	**78517**	**±1730**
SVC991d-3	6	577.8	±1.8	84489	±262	124.2	±0.4	1020.3	±0.6	1.0965	±0.0025	78982	±247	77093	±1360	1268	±5	**77026**	**±1360**

U decay constants: l238 = 1.55125x10-10 (Jaffey et al., 1971) and l234 = 2.82206x10-6 (Cheng et al., 2013). Th decay constant: l230 = 9.1705x10-6 (Cheng et al., 2013).
* d234U = ([234U/238U]activity – 1)x1000.
** d234U initial was calculated based on 230Th age (d234Uinitial = d234Umeasured * e^234T).
Corrected 230Th ages assume the initial 230Th/232Th atomic ratio of 4.4 ±2.2 x10-6. Those are the values for a material at secular equilibrium, with the bulk earth 232Th/238U value of 3.8. The errors are arbitrarily assumed to be 50%.
*** B.P. stands for "Before Present" where the "Present" is defined as the year 1950 A.D.

Table A.6: ^{230}Th dates for sample SVC991d. Sample is a flowstone, with potential hiatuses during later growth. Subsamples for top-bottom dates were completed for this study by author, and subsamples 3-8 were completed for this study by Zongyi Wang. Subsamples 8-2 is a duplicate. Subsamples 1-2 were run on SEM. Subsamples 3-8 were run on cups.

Average values for chemistry blanks used in age calculation using perchloric before 7/20/15

	230Th	232Th	234U	235U	238U
Chemistry blank weight	306.9	3778.5	3416.9	19.2	3052.3
2σ Abs. error	± 109.8	± 233.6	± 2852.1	± 222.4	± 825.2
	ag	fg	ag	fg	fg

Average values for chemistry blanks used in age calculation using 7/20/15 perchloric

	230Th	232Th	234U	235U	238U
Chemistry blank weight	109.23	124.2	251.9	28	1584.9
2σ Abs. error	± 15.8	± 2.2	± 38.7	± 4.8	± 98.3
	ag	fg	ag	fg	fg

Average values for chemistry blanks used in age calculation using 10/29/15 perchloric

	230Th	232Th	234U	235U	238U
Chemistry blank weight	37.6	121	361.7	37.4	1544.1
2σ Abs. error	± 15.9	± 3.9	± 96.8	± 8.7	± 89.6
	ag	fg	ag	fg	fg

Table A.7: Average chemistry blank values for chemistry batches used in age calculation. Values are divided into perchloric used, as perchloric was the largest source of contamination.

Average values for reagent blanks without perchloric

	230Th	232Th	234U	235U	238U
Reagent blank weight	17.4	51.4	20.3	2.3	257.3
2σ Abs. error	± 7.4	± 0.4	± 8.9	± 0.6	± 22.2
	ag	fg	ag	fg	fg

Average values for perchloric used before 7/20/15

	230Th	232Th	234U	235U	238U
Reagent blank weight	44.7	7.7	311.2	31.9	4125.7
2σ Abs. error	± 12.5	± 0.2	± 27.4	± 0.3	± 3.1
	ag	fg	ag	fg	fg

Average values for 7/20/15 perchloric

	230Th	232Th	234U	235U	238U
Reagent blank weight	76.5	118.3	908.9	111.4	3627.4
2σ Abs. error	± 20.1	± 2.8	± 69.0	± 8.1	± 337.9
	ag	fg	ag	fg	fg

Average values for 10/29/15 perchloric

	230Th	232Th	234U	235U	238U
Reagent blank weight	94	-2	3873	668	21546
2σ Abs. error	± 94	± 9	± 180	± 24	± 1243
	ag	fg	ag	fg	fg

Average values for reagent blanks w/ perchloric before 7/20/15

	230Th	232Th	234U	235U	238U
Reagent blank weight	75.2	305.3	241.5	23.6	2434.3
2σ Abs. error	± 12.2	± 0.8	± 24.9	± 0.2	± 2.5
	ag	fg	ag	fg	fg

Average values for reagent blanks w/ 7/20/15 perchloric

	230Th	232Th	234U	235U	238U
Reagent blank weight	3.3	112.8	414.7	60.3	2959.7
2σ Abs. error	± 8.9	± 6.5	± 36.3	± 4.3	± 167.3
	ag	fg	ag	fg	fg

Average values for reagents blanks w/ 10/29/15 perchloric

	230Th	232Th	234U	235U	238U
Reagent blank weight	15	125	2479	415	10564
2σ Abs. error	± 17.8	± 3.8	± 183.2	± 21.25	± 414.6
	ag	fg	ag	fg	fg

Table A.8: Average reagent blank values. Reagent blank values are extremely low for all reagents except perchloric. Three different perchloric batches were used during chemistry, and results from both separate perchloric and reagents with perchloric analysis are shown.

A.3 Confocal analysis

The following includes confocal analyses of growth phases for sample SVC05. All confocal images were taken on a Nikon A1RMP microscope at the University Imaging Centers of University of Minnesota. We used a Plan Fluor ELWD 20x DIC L objective, with an excitation wavelength of 488 nm and an emission wavelength of 525 nm. This provides high resolution resolution images without needing to use immersion oil with your objective. Scans were made of each growth phase at these settings, imaging between hiatuses with at least 2 frames in width and manually focusing at every frame to ensure best quality. Resulting Nikon .nd2 files were converted into JPEG and enhanced using the *skimage Python* package submodule *exposure.equalize_adapt_hist*. This sub-module uses a contrast limited adaptive histogram equalization (CLAHE) function to perform local contrast enhancement. The image was then de-noised using the *scipy Python* package submodule *ndimage* by applying a medium filter to the image.

Confocal band counting has traditionally been done manually, but this method can be error-prone and incredibly time consuming. Previous band counting had been completed on growth phases 3, 5 and 6 on SVC05 by Joel MacKinney (MacKinney et al., 2013). In this study, we attempted to test methods of automatic band counting to see if they provided comparable results to previously completed manual band-counting. Intensity profiles were generated for contrast enhanced and de-noised images using the *skimage Python* package submodule *ImageViewer* and *viewer* plug-in *LineProfile*. Local maxima were then calculated for the resulting intensity profile using the *numpy Python* package. This resulted in a much larger number of maxima then high-intensity bands. To filter the results, two methods were tried. The first only counted maxima above a specified intensity threshold, which would eliminate low-intensity maxima which likely did not correlate to fluorescent banding. The second only counted maxima that were higher in intensity than the following five local maxima, which would eliminate noise within high intensity fluorescent bands.

The maxima reduction method provided results comparable to manual band counting in SVC05 growth phases 5 and 6, with manual counting identifying 120 and 250 annual bands and automatic maxima reduction identifying 128 and 251 annual bands, respectively. Additionally, automatic maxima reduction provided an annual band count that most closely replicated U/Th ages in growth phase 3, whereas manual band counting seemed to greatly overestimate the number of annual bands. Where U/Th ages are far from the bounds placed by confocal annual band counts, either ages could be contaminated by the neighboring haitus, or annual banding may not be occurring within the growth phase. This appears to be contributing to ages with growth phase 2, 4, and 6. For example, as growth phase

6 does appear to have strong banding present and appears largely annual between ages SVC051a-25 and SVC051a-21.1, it seems likely that the younger age for SVC051a-26 was due to contamination by the neighboring hiatus between growth phase 6 and 7.

Below are the results of confocal analysis, both manual and automatic. We are hopeful that these results can not only provide higher resolution in determining the timing of short term growth within Spring Valley Caverns, but may provide support for adopting automatic methods for confocal analysis in the future.

SVC05 Growth Phase 2 (183-187 mm above base)

Original image

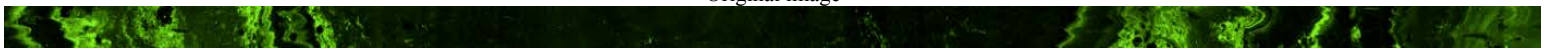

Adaptive equalization and de-noised

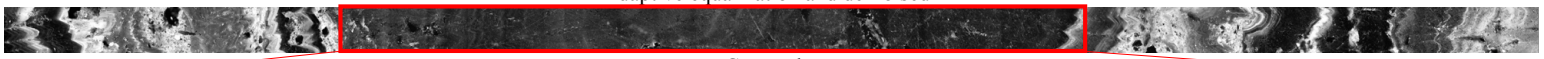

Cropped

Repeated adaptive equalization and de-noise to improve contrast

Intensity profile generated through skimage plugin LineProfile

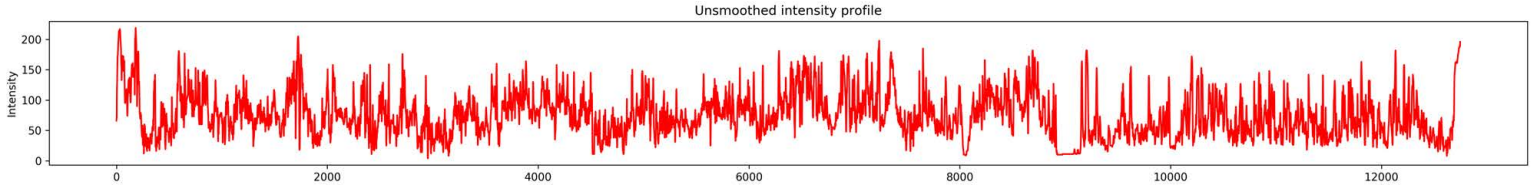

Profile smoothed and 624 local maxima found

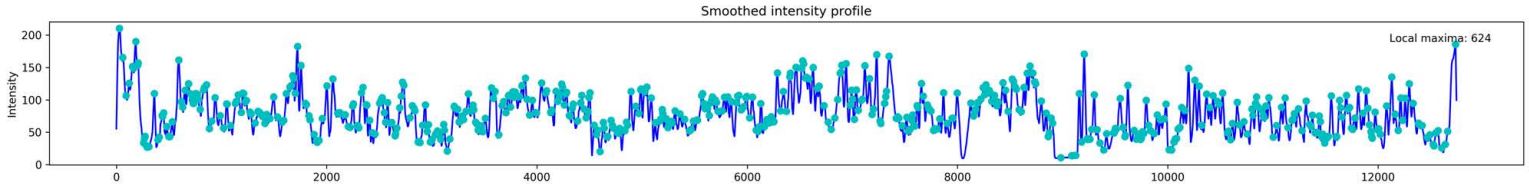

Only maxima above specified (100) threshold intensity: 169 local maxima

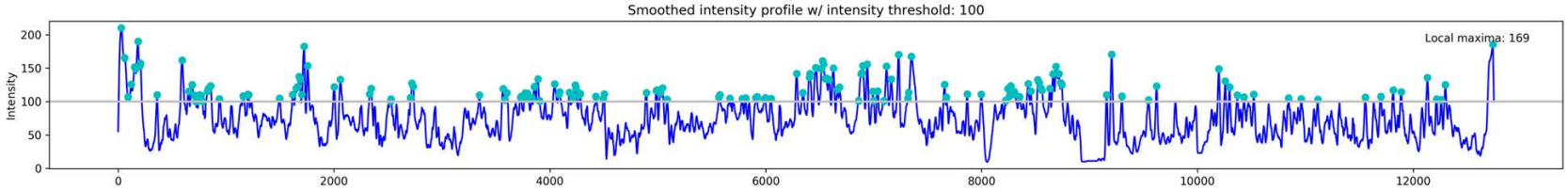

Only maxima that were greater than the next 5: 135 local maxima

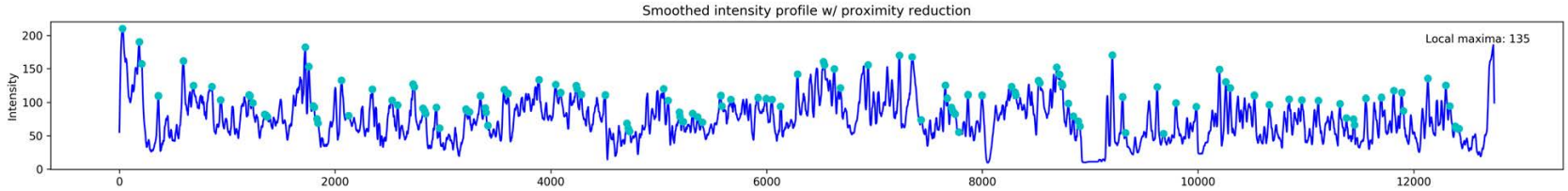

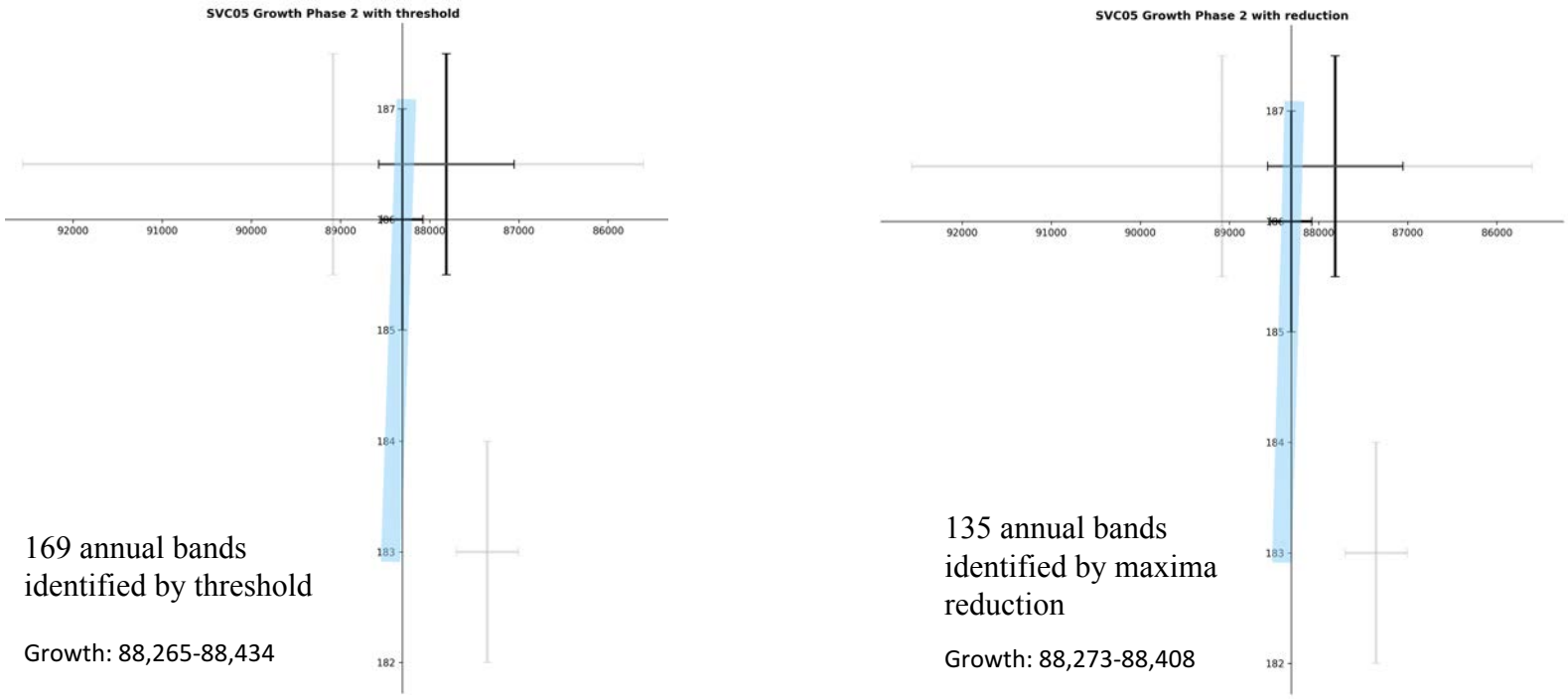

Figure A.7: Confocal analysis for SVC05 Growth Phase 2, 183-187 mm above base. Growth phase shows indication of banding. Applied threshold and maxima reduction filters to improve band count. Confocal ages anchored at U/Th age 88,307 yr BP at 186mm, which had lowest age error and was clearly within growth phase.

SVC05 Growth Phase 3 (190.5 – 200 mm above base)

Original image

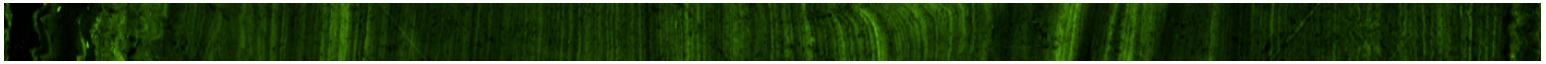

Adaptive equalization and de-noised

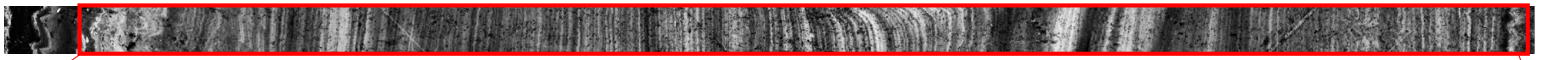

Cropped

Intensity profile generated through skimage plugin LineProfile

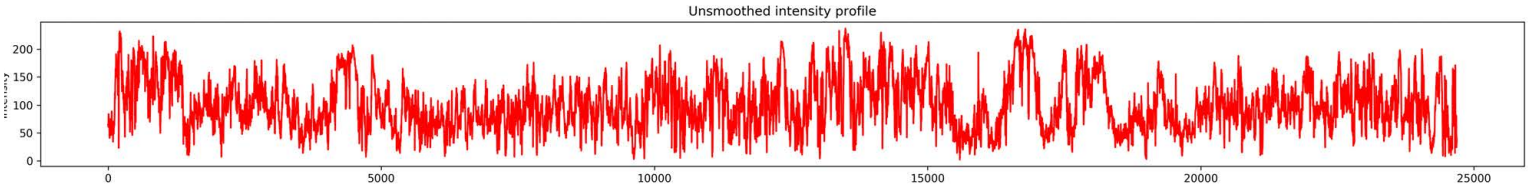

Profile smoothed and 1258 local maxima found

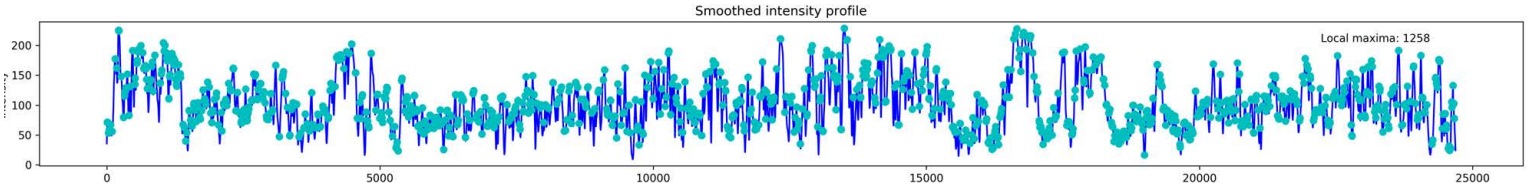

Only maxima above specified (125) threshold intensity: 357 local maxima

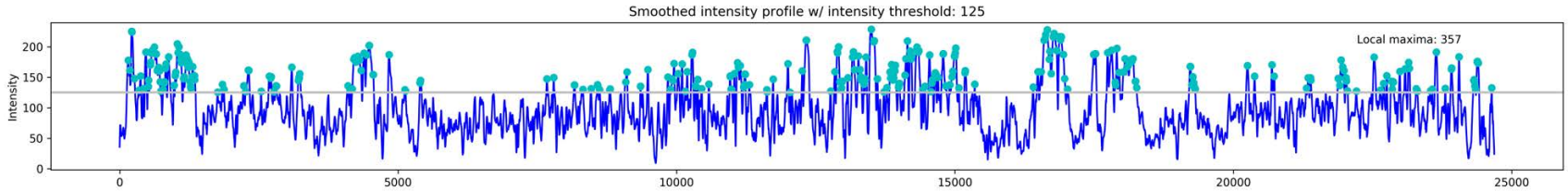

Only maxima that were greater than the next 5: 283 local maxima

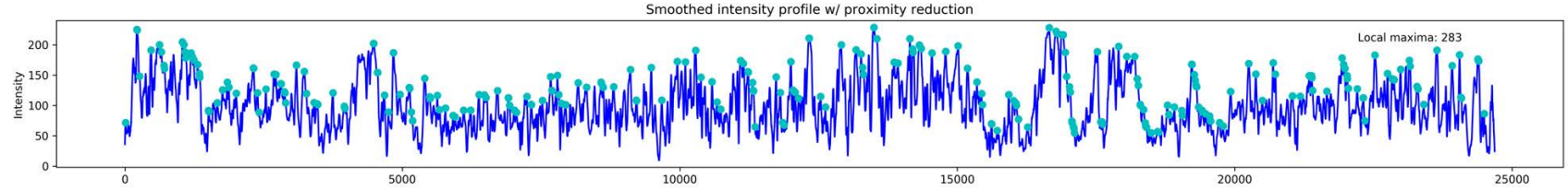

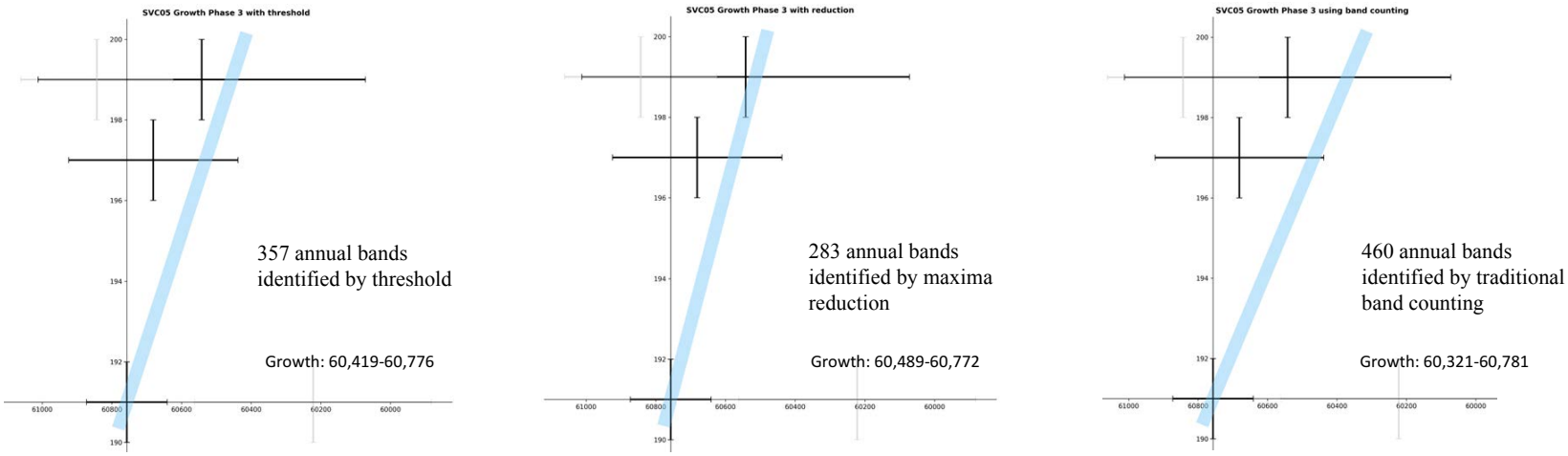

Figure A.8: Confocal analysis for SVC05 Growth Phase 3, 190.5-200 mm above base. Growth phase shows strong banding. Applied threshold and maxima reduction filters to improve band count. Confocal ages anchored at U/Th age 60,757 yr BP at 191 mm, which had lowest age error and was clearly within growth phase. Maxima reduction filter correlated best to U/Th ages, with both threshold filter and manual band counting overestimating growth. Previous band counting completed by Joel MacKinney in 2013.

SVC05 Growth Phase 4 (201-205 mm above base)

Original image

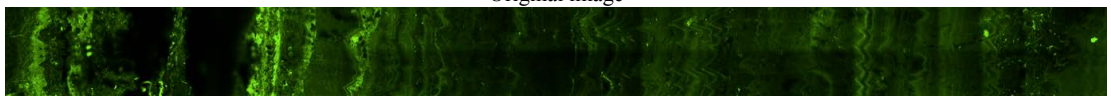

Adaptive equalization and de-noised

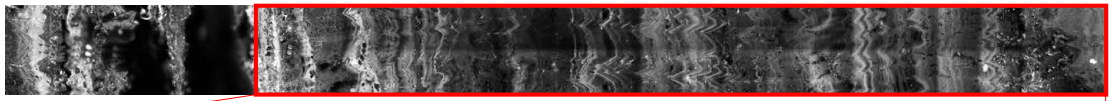

Cropped

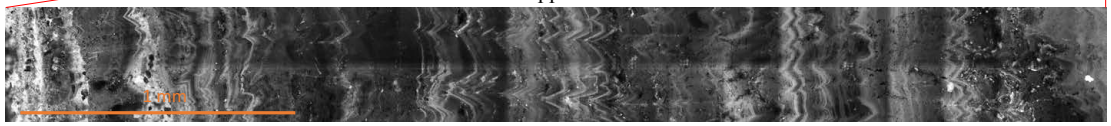

Intensity profile generated through skimage plugin LineProfile

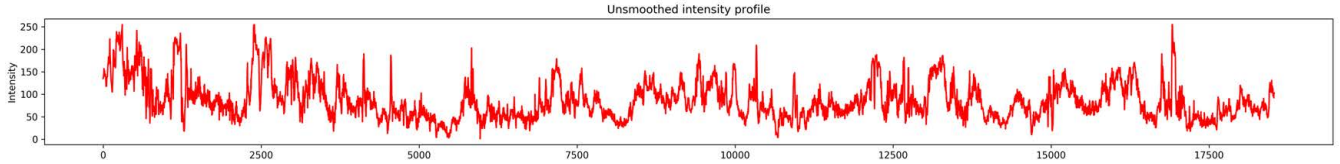

Profile smoothed and 1004 local maxima found

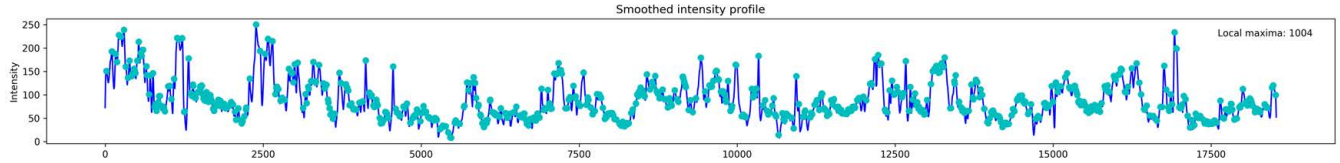

Only maxima above specified (100) threshold intensity: 292 local maxima

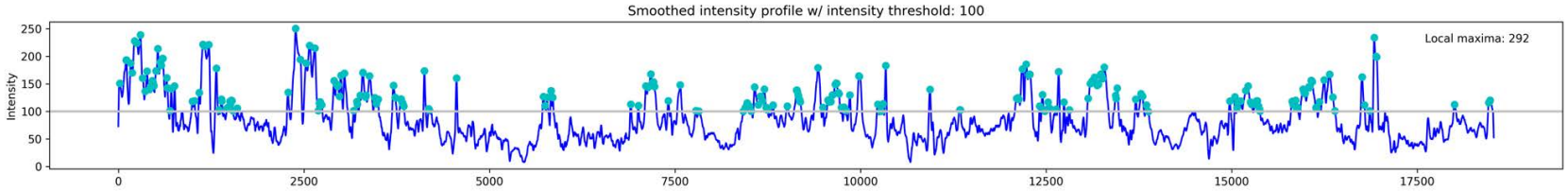

Only maxima that were greater than the next 5: 259 local maxima

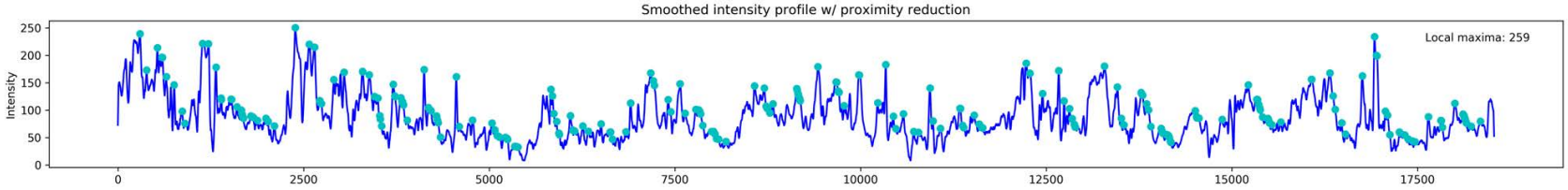

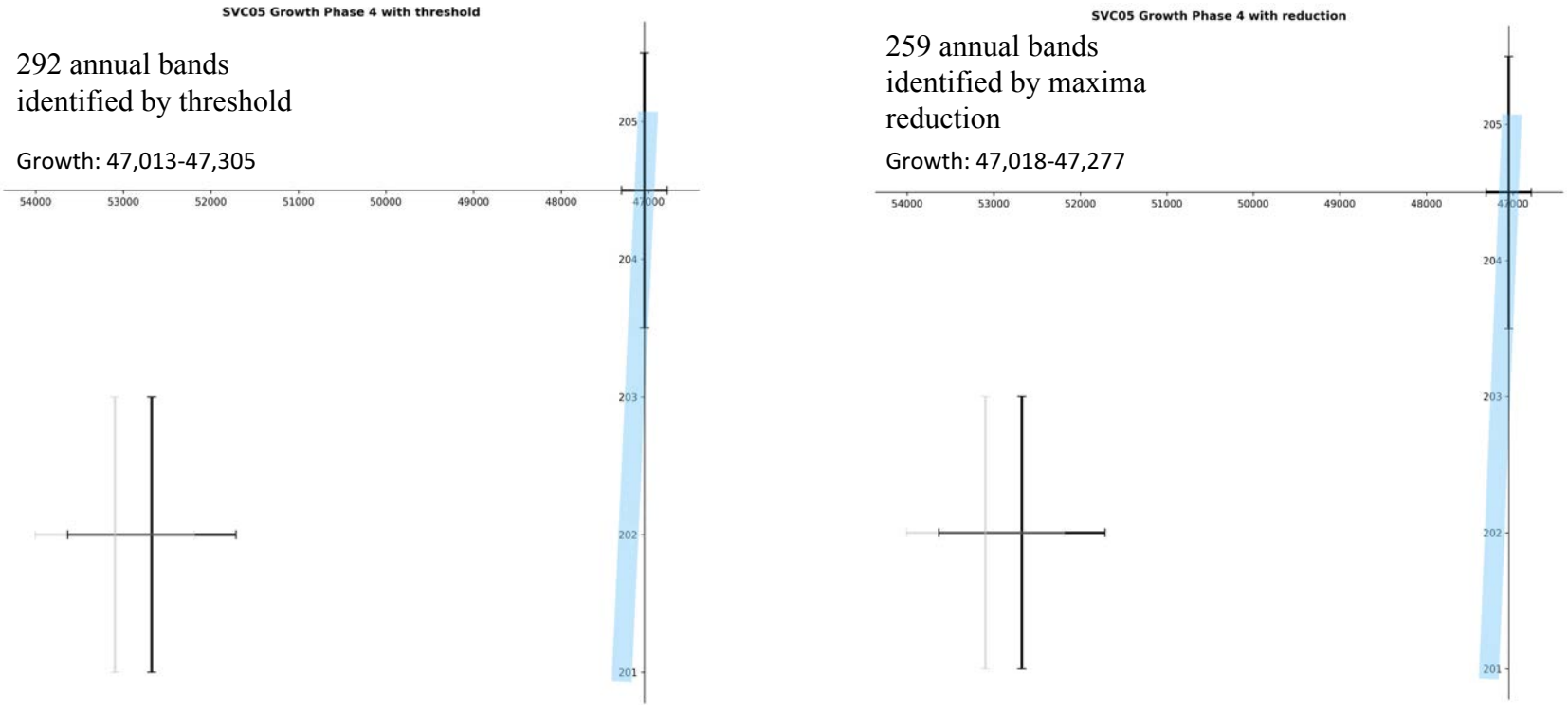

Figure A.9: Confocal analysis for SVC05 Growth Phase 4, 201-205 mm above base. Growth phase shows indication of banding. Applied threshold and maxima reduction filters to improve band count. Confocal ages anchored at U/Th age 47,050 yr BP at 204.5 mm, which had lowest age error and was clearly within growth phase. Ages at 202 mm show potential contamination from hiatus.

SVC05 Growth Phase 5 (205-208 mm above base)

Original image

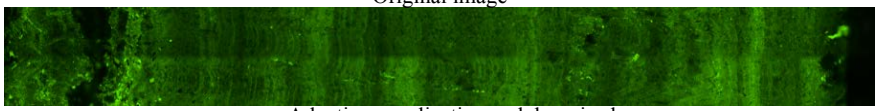

Adaptive equalization and de-noised

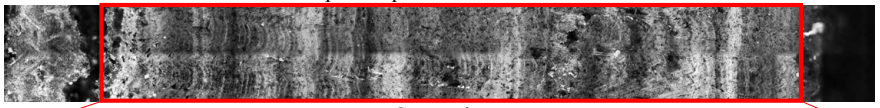

Cropped

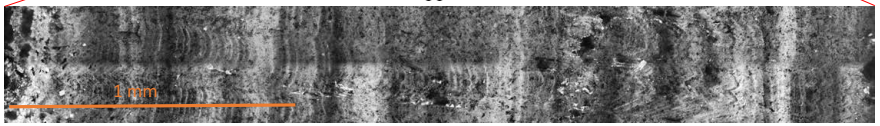

Intensity profile generated through skimage plugin LineProfile

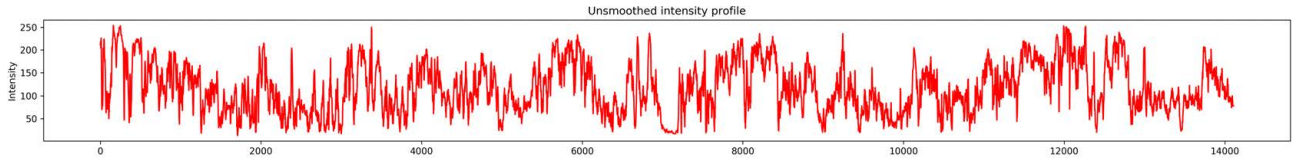

Profile smoothed and 552 local maxima found

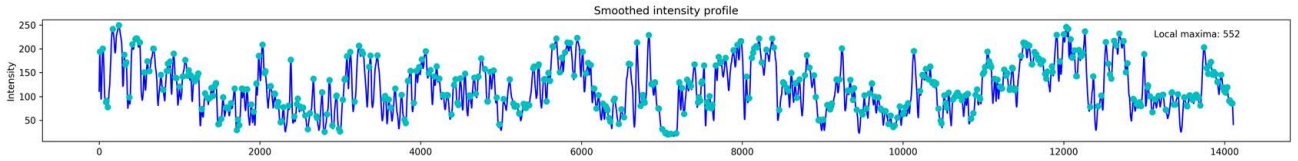

Only maxima above specified (125) threshold intensity: 253 local maxima

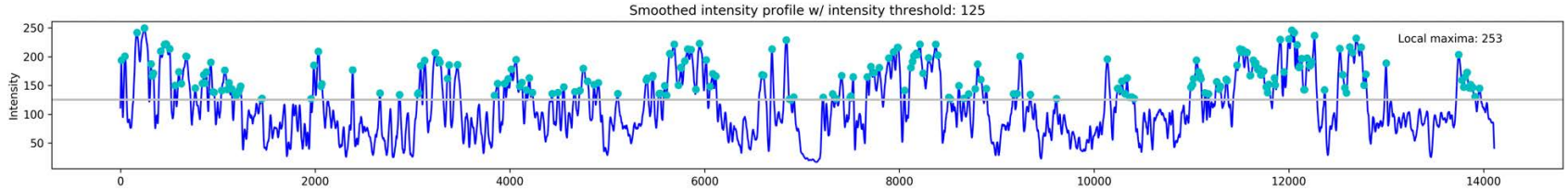

Only maxima that were greater than the next 5: 128 local maxima

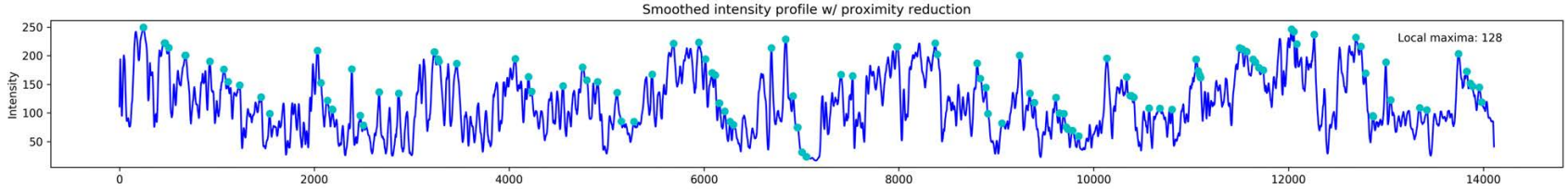

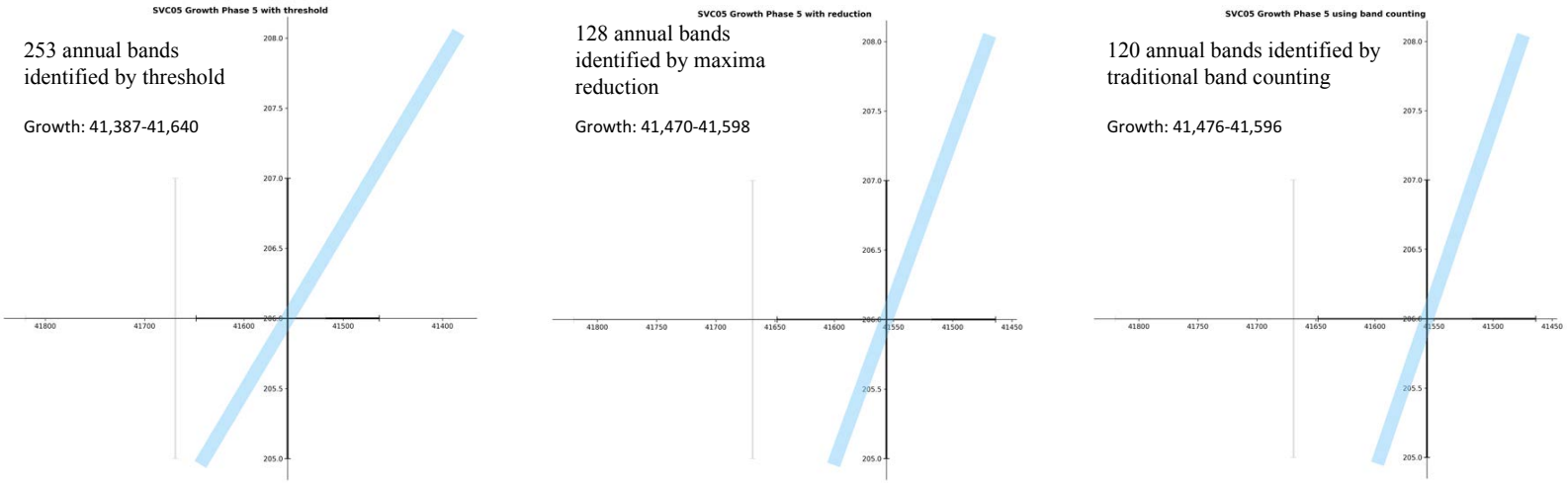

Figure A.10: Confocal analysis for SVC05 Growth Phase 5, 205-208 mm above base. Growth phase shows good banding. Applied threshold and maxima reduction filters to improve band count. Confocal ages anchored at U/Th age 41,556 yr BP at 206 mm, which had lowest age error and was clearly within growth phase. Maxima reduction filter and band counting provide same band count. Previous band counting completed by Joel MacKinney in 2013.

SVC05 Growth Phase 6 (208-213 mm above base)

Original image

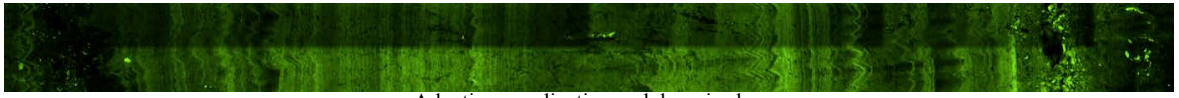

Adaptive equalization and de-noised

Cropped

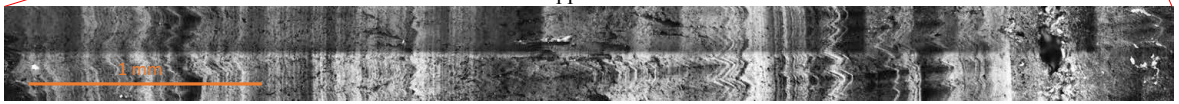

Intensity profile generated through skimage plugin LineProfile

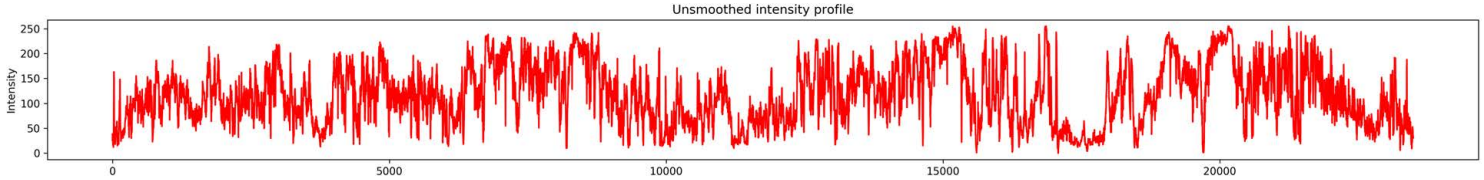

Profile smoothed and 1199 local maxima found

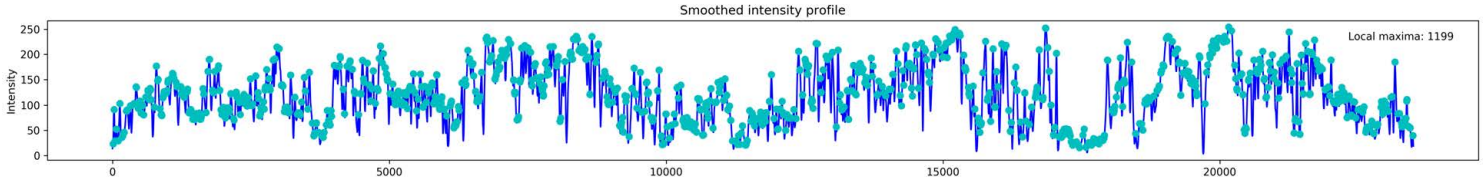

Only maxima above specified (125) threshold intensity: 554 local maxima

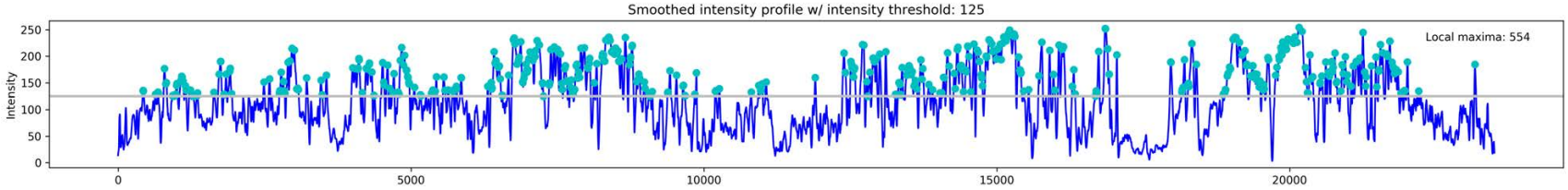

Only maxima that were greater than the next 5: 251 local maxima

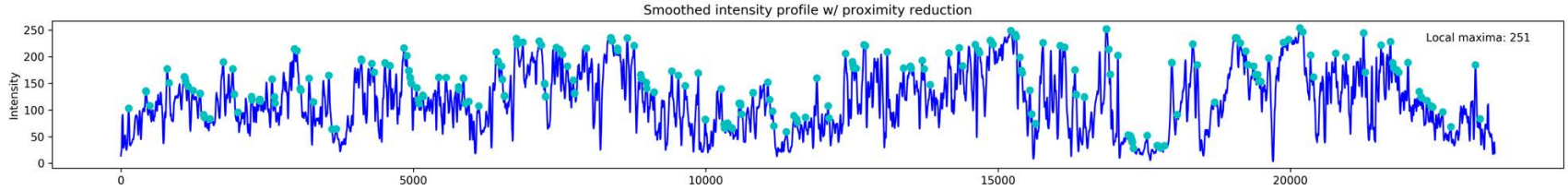

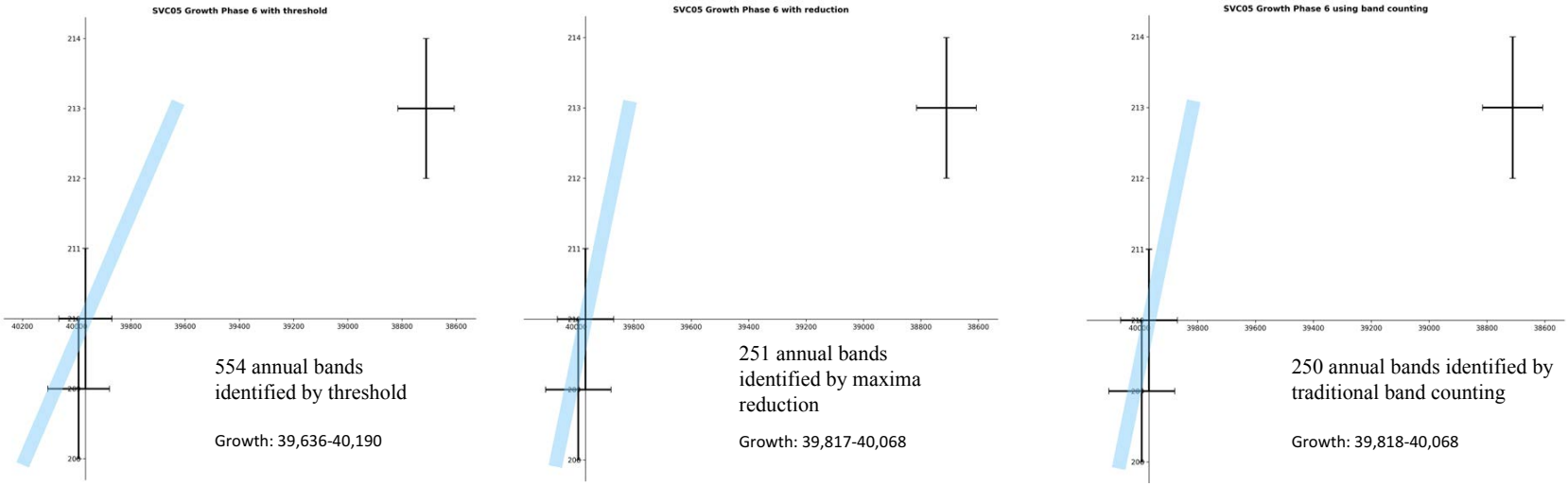

Figure A.11: Confocal analysis for SVC05 Growth Phase 6, 208-213 mm above base. Growth phase shows good banding. Applied threshold and maxima reduction filters to improve band count. Confocal ages anchored at U/Th age 39,968 yr BP at 210 mm, which had lowest age error and was clearly within growth phase. Maxima reduction filter and band counting provide same band count. Previous band counting completed by Joel MacKinney in 2013.

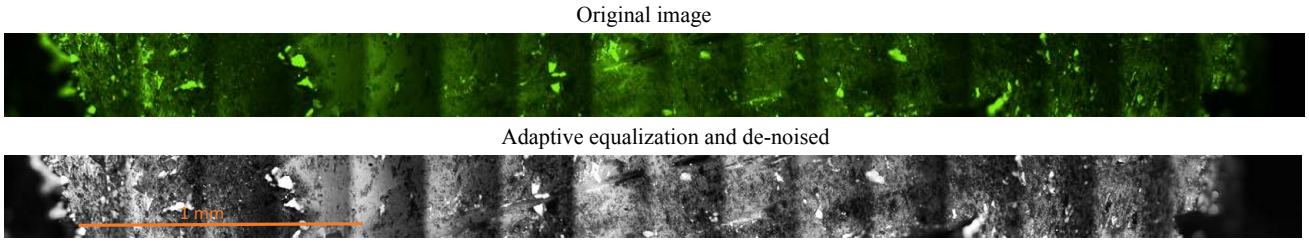

Figure A.12: Confocal analysis for SVC05 Growth Phase 7, 213-217 mm above base. Growth phase shows no banding present. Differences in light intensity due to imaging errors on uneven sample surface. Unable to improve growth estimate through confocal analysis.

A.4 X-ray Diffraction analysis

X-ray Diffraction (XRD) was completed on samples SVC06 and SVC05 by Javier Garcia Barriocanal at the University of Minnesota Characterization Facility. 9 samples of 10-20 mg of power were taken in total. 2 samples were taken from SVC06 at 155 and 574 mm above base, as the sample appears continuous with no noticeable hiatuses. 7 samples were taken from SVC05, one from each growth phase, to test for changes in mineralogy between hiatuses (at 174, 185, 195, 203, 207, 210 and 217 mm above base). XRD analysis works by measuring the angle of deflection produced by a crystallographic surface reflecting incoming electromagnetic radiation. Different crystal structures result in a specific pattern of reflected angles, and can be identified by their spectrum.

Figure A.10 shows the results of all 9 samples from SVC06 and SVC05. All powder samples show a calcite crystal structure, indicating that neither sample experienced changes in mine

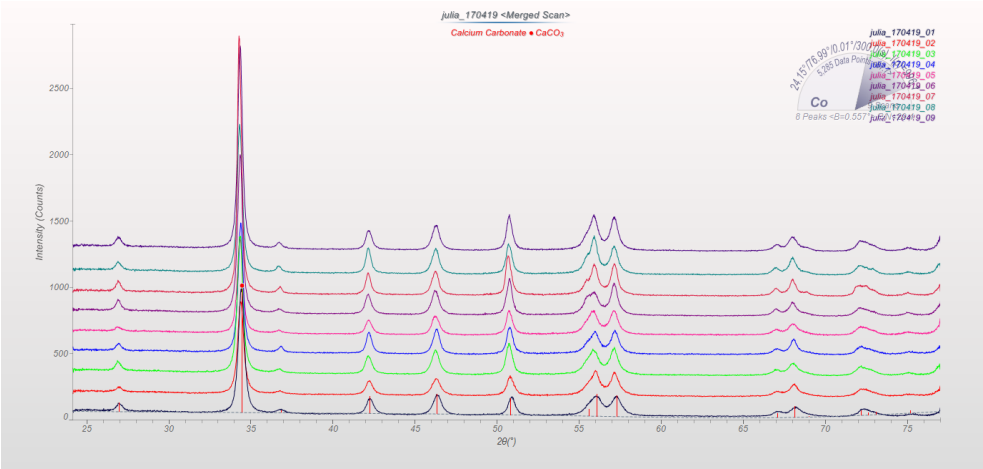

Figure A.13: XRD results for samples SVC05 and SVC06. 2 samples were taken from SVC06, and 7 from SVC05 (one from each growth phase). All samples show calcite mineralogy.

A.5 Stable isotope analysis

Oxygen (δ^{18}O) and carbon (δ^{13}C) isotopic analysis of speleothem samples SVC06 (568 subsamples) and SVC05 (96 subsamples) were analyzed at Xi'an Jiaotong University. 45 additional subsamples of SVC05 completed in 2013 at the University of Minnesota were used in the stable isotope SVC05 compilation. Results are reported in per mil (‰) relative to Vienna PeeDee Belemnite (VPDB) standard. Stable isotope subsamples were drilled by hand using a 0.9 mm carbide dental burr, as sample parameters did not allow for micro-milling. Drilling was conducted every 0.75-3 mm along growth axis on sample SVC06, and every 0.5-5 mm along growth axis on sample SVC05, dependent on growth rate and desired resolution. Analysis conducted at Xi'an Jiatong University were completed on a Thermo-Finnigan MAT-253 mass spectrometer fitted with a Kiel Carbonate Device IV (Cheng et al., 2016). Long-term reproducibility of standards indicates 0.1‰ or better (1σ). Analysis conducted at the University of Minnesota stable isotope laboratory were conducted on a Finnigan MAT-252 mass spectrometer fitted with a Kiel Carbonate Device III.

Stable isotope data for SVC06

Age yrs BP	Height above base (mm)	d13C (VPDB)	d18O (VDPB)	d18O sw corr (VPDB)
63680	3	-8.42	-3.1	-3.75
63596	6	-7.95	-3.12	-3.77
63512	9	-7.76	-2.98	-3.62
63428	12	-7.28	-3.04	-3.68
63356	15	-7.94	-3.2	-3.84
63322	18	-8.45	-3.34	-3.98
63287	21	-8.09	-3.31	-3.95
63253	24	-8.7	-3.58	-4.22
63218	27	-8.37	-3.4	-4.04
63184	30	-8.06	-3.1	-3.75
63149	33	-6.86	-3.18	-3.83
63115	36	-7.31	-3.18	-3.84
63081	39	-8.1	-3.22	-3.89
63046	42	-7.8	-3.01	-3.69
63011	45	-8.07	-3.1	-3.78
62976	48	-7.44	-2.92	-3.61
62937	51	-6.41	-3.07	-3.77
62889	54	-6.44	-3.22	-3.93
62842	57	-6.71	-3.32	-4.04
62794	60	-7.61	-3.45	-4.18
62745	63	-7.93	-3.72	-4.46
62697	66	-7.09	-3.4	-4.15
62649	69	-7.41	-3.57	-4.32
62601	72	-7.56	-3.43	-4.18
62553	75	-7.94	-3.33	-4.08
62504	78	-6.7	-2.88	-3.64
62457	81	-7.02	-3.21	-3.97
62367	84	-7.69	-3.29	-4.05
62290	87	-7.31	-3.29	-4.05
62232	90	-7.42	-3.27	-4.03
62173	93	-7.92	-3.32	-4.07
62116	96	-8.13	-3.38	-4.12
62057	99	-7.86	-3.35	-4.09
62000	102	-7.78	-3.17	-3.90
61942	105	-7.76	-3.25	-3.97
61884	108	-6.98	-3.09	-3.80
61826	111	-6.91	-3.31	-4.01

Age yrs BP	Height above base (mm)	d13C (VPDB)	d18O (VDPB)	d18O sw corr (VPDB)
61768	114	-6.88	-3.56	-4.25
61698	117	-7.6	-3.6	-4.29
61604	120	-7.83	-3.21	-3.90
61510	123	-8.3	-2.99	-3.68
61418	126	-8.76	-3.46	-4.16
61324	129	-8.02	-3.29	-3.99
61242	132	-7.9	-3.38	-4.08
61166	135	-8.15	-3.3	-3.99
61090	138	-8.27	-3.35	-4.04
61013	141	-7.37	-3.58	-4.26
60939	144	-6.98	-3.54	-4.21
60862	147	-7.75	-3.24	-3.91
60786	150	-8.25	-3.73	-4.39
60712	153	-6.62	-3.37	-4.03
60632	156	-6.87	-3.33	-3.98
60547	159	-8.3	-3.62	-4.25
60459	162	-8.97	-3.56	-4.16
60374	165	-7.8	-3.39	-3.96
60316	167	-7.167	-3.172	-3.74
60283	167.5	-8.442	-3.308	-3.86
60249	168	-8.48	-3.44	-3.99
60215	168.5	-8.402	-3.676	-4.22
60180	169	-8.393	-3.579	-4.12
60145	169.5	-7.93	-3.54	-4.07
60110	170	-6.995	-3.514	-4.05
60073	170.5	-7.955	-3.634	-4.17
60036	171	-7.92	-3.69	-4.22
60000	171.5	-6.333	-3.301	-3.84
59965	172	-6.35	-3.428	-3.97
59930	172.5	-7.059	-3.651	-4.19
59895	173	-7.139	-3.505	-4.05
59861	173.5	-7.639	-3.564	-4.10
59827	174	-7.95	-3.53	-4.06
59791	174.5	-7.551	-3.489	-4.02
59754	175	-8.252	-3.58	-4.10
59719	175.5	-7.527	-3.743	-4.26
59684	176	-6.74	-3.53	-4.04

Continued stable isotope data for SVC06

Age yrs BP	Height above base (mm)	d13C (VPDB)	d18O (VDPB)	d18O sw corr (VPDB)
59650	176.5	-7.266	-3.682	-4.19
59617	177	-6.78	-3.88	-4.39
59581	177.5	-6.837	-3.669	-4.18
59545	178	-6.358	-3.649	-4.17
59509	178.5	-6.593	-3.765	-4.28
59474	179	-6.797	-3.793	-4.31
59438	179.5	-7.497	-3.891	-4.41
59402	180	-7.46	-3.91	-4.43
59368	180.5	-7.784	-3.969	-4.49
59333	181	-8.088	-4.016	-4.53
59298	181.5	-7.109	-3.644	-4.16
59264	182	-7.288	-3.888	-4.40
59228	182.5	-6.528	-3.908	-4.42
59192	183	-7.49	-4.03	-4.54
59174	184	-6.423	-3.777	-4.29
59156	185	-6.932	-3.743	-4.25
59139	186	-7.31	-3.91	-4.42
59120	187	-6.707	-3.853	-4.36
59102	188	-6.919	-3.703	-4.22
59085	189	-6.89	-3.89	-4.40
59067	190	-6.103	-3.814	-4.33
59049	191	-6.067	-3.787	-4.30
59030	192	-7.3	-4.14	-4.65
59012	193	-7.124	-4.073	-4.59
58995	194	-7.239	-3.951	-4.47
58978	195	-8.07	-4.32	-4.83
58960	196	-7.955	-4.278	-4.79
58942	197	-7.663	-4.274	-4.79
58924	198	-6.6	-4.01	-4.53
58906	199	-6.566	-3.913	-4.43
58888	200	-7.693	-3.92	-4.44
58871	201	-7.43	-3.67	-4.19
58853	202	-6.878	-3.457	-3.98
58835	203	-7.008	-3.287	-3.81
58817	204	-7.91	-3.7	-4.22
58799	205	-7.067	-3.627	-4.15
58781	206	-7.136	-3.624	-4.14

Age yrs BP	Height above base (mm)	d13C (VPDB)	d18O (VDPB)	d18O sw corr (VPDB)
58763	207	-8.22	-4.01	-4.53
58745	208	-8.415	-3.82	-4.34
58727	209	-8.602	-3.957	-4.47
58709	210	-8.06	-3.92	-4.44
58692	211	-8.215	-3.716	-4.24
58674	212	-8.612	-3.728	-4.25
58656	213	-8.35	-4.01	-4.53
58638	214	-8.147	-3.943	-4.46
58621	215	-8.06	-3.771	-4.29
58603	216	-8.52	-4.08	-4.59
58584	217	-7.661	-3.777	-4.29
58567	218	-8.073	-4.032	-4.54
58549	219	-7.39	-4.06	-4.57
58530	220	-7.374	-3.879	-4.39
58513	221	-7.188	-3.829	-4.34
58495	222	-7.28	-4.04	-4.55
58477	223	-7.097	-3.88	-4.39
58459	224	-7.164	-3.947	-4.45
58442	225	-7.07	-3.99	-4.50
58424	226	-8.244	-3.875	-4.38
58406	227	-7.84	-3.748	-4.26
58389	228	-7.82	-4.22	-4.73
58341	231	-7.26	-4.14	-4.65
58307	234	-7.88	-4.07	-4.58
58273	237	-7.9	-4.11	-4.62
58239	240	-7.68	-3.97	-4.48
58205	243	-7.59	-3.95	-4.46
58171	246	-8.11	-4.01	-4.53
58137	249	-7.63	-3.76	-4.28
58103	252	-8.07	-4.08	-4.60
58069	255	-7.47	-4.04	-4.56
58035	258	-7.96	-4.16	-4.68
57993	261	-8.33	-4.25	-4.77
57935	264	-8.03	-4.07	-4.60
57876	267	-8.27	-4	-4.54
57817	270	-8.43	-4.09	-4.64
57758	273	-8.09	-4.07	-4.62

Continued stable isotope data for SVC06

Age yrs BP	Height above base (mm)	d13C (VPDB)	d18O (VDPB)	d18O sw corr (VPDB)
57699	276	-7.55	-3.98	-4.53
57641	279	-7.51	-3.92	-4.48
57602	281	-6.97	-4.12	-4.67
57582	282	-7.1	-3.89	-4.45
57562	283	-7.19	-3.94	-4.50
57543	284	-7.39	-3.98	-4.54
57523	285	-7.47	-3.89	-4.45
57503	286	-7.81	-3.86	-4.42
57484	287	-7.95	-3.8	-4.36
57464	288	-7.9	-3.84	-4.40
57444	289	-8.22	-3.9	-4.46
57424	290	-8.25	-3.76	-4.32
57405	291	-8.55	-3.7	-4.26
57386	292	-8.84	-3.74	-4.30
57367	293	-8.78	-3.73	-4.30
57347	294	-8.73	-4.02	-4.58
57327	295	-8.51	-3.67	-4.24
57308	296	-8.49	-3.75	-4.32
57288	297	-9.1	-3.85	-4.42
57268	298	-8.66	-3.69	-4.26
57249	299	-8.72	-3.77	-4.34
57229	300	-7.75	-3.93	-4.50
57210	301	-7.82	-3.81	-4.38
57191	302	-7.32	-3.81	-4.38
57169	303	-7.37	-3.59	-4.16
57146	304	-8.01	-3.74	-4.31
57123	305	-8.31	-3.77	-4.34
57100	306	-8.25	-3.75	-4.32
57077	307	-8.34	-3.8	-4.37
57054	308	-7.62	-3.57	-4.15
57030	309	-7.79	-3.76	-4.34
57007	310	-7.67	-3.85	-4.43
56983	311	-7.91	-3.78	-4.36
56960	312	-7.5	-3.85	-4.43
56938	313	-7.9	-3.9	-4.48
56916	314	-7.49	-3.7	-4.28
56894	315	-7.65	-3.7	-4.28

Age yrs BP	Height above base (mm)	d13C (VPDB)	d18O (VDPB)	d18O sw corr (VPDB)
56872	316	-7.82	-3.71	-4.29
56849	317	-8.37	-3.76	-4.35
56827	318	-8.31	-3.73	-4.32
56805	319	-8.5	-3.92	-4.51
56783	320	-8.54	-3.85	-4.44
56761	321	-8.44	-3.95	-4.54
56739	322	-8.77	-3.83	-4.42
56717	323	-8.59	-3.83	-4.42
56695	324	-8.15	-3.78	-4.37
56673	325	-8.03	-3.73	-4.33
56651	326	-7.43	-3.65	-4.25
56628	327	-7.44	-3.68	-4.28
56612	327.5	-7.341	-3.416	-4.02
56595	328	-7.39	-3.54	-4.14
56578	328.5	-7.339	-3.553	-4.16
56562	329	-7.81	-3.45	-4.05
56546	329.5	-7.056	-3.357	-3.96
56529	330	-7.38	-3.53	-4.14
56513	330.5	-7.335	-3.283	-3.89
56497	331	-7.82	-3.55	-4.16
56481	331.5	-7.954	-3.595	-4.20
56464	332	-7.99	-3.73	-4.34
56447	332.5	-7.888	-3.706	-4.32
56431	333	-8.07	-3.72	-4.33
56414	333.5	-7.914	-3.547	-4.16
56398	334	-7.89	-3.65	-4.27
56381	334.5	-7.955	-3.44	-4.06
56365	335	-7.76	-3.58	-4.20
56348	335.5	-6.354	-3.177	-3.81
56332	336	-6.69	-3.51	-4.14
56315	336.5	-6.801	-3.401	-4.03
56298	337	-6.99	-3.62	-4.25
56281	337.5	-7.287	-3.566	-4.19
56265	338	-7.08	-3.87	-4.49
56249	338.5	-7.382	-3.745	-4.37
56232	339	-7.27	-3.78	-4.40
56216	339.5	-7.047	-3.621	-4.25

Continued stable isotope data for SVC06

Age yrs BP	Height above base (mm)	d13C (VPDB)	d18O (VDPB)	d18O sw corr (VPDB)
56200	340	-7.69	-3.69	-4.32
56183	340.5	-7.702	-3.732	-4.36
56167	341	-8.4	-3.77	-4.39
56150	341.5	-7.527	-3.619	-4.24
56134	342	-7.95	-3.61	-4.24
56117	342.5	-7.833	-3.713	-4.34
56101	343	-8.48	-3.63	-4.26
56085	343.5	-7.416	-3.602	-4.23
56069	344	-7.76	-3.54	-4.17
56053	344.5	-7.548	-3.56	-4.19
56036	345	-7.61	-3.57	-4.20
56019	345.5	-7.834	-3.71	-4.34
56002	346	-7.78	-3.45	-4.08
55985	346.5	-7.575	-3.599	-4.22
55969	347	-7.67	-3.49	-4.11
55952	347.5	-7.225	-3.571	-4.19
55936	348	-6.68	-3.5	-4.12
55920	348.5	-6.662	-3.713	-4.33
55904	349	-6.56	-3.94	-4.56
55887	349.5	-7.119	-3.818	-4.44
55870	350	-6.63	-3.86	-4.48
55854	350.5	-6.316	-3.605	-4.22
55837	351	-6.5	-3.62	-4.24
55820	351.5	-7.01	-3.633	-4.25
55804	352	-7.01	-3.79	-4.40
55787	352.5	-6.73	-3.532	-4.14
55771	353	-6.8	-3.68	-4.28
55757	353.5	-6.789	-3.652	-4.25
55742	354	-6.77	-3.97	-4.57
55727	354.5	-6.765	-3.818	-4.41
55713	355	-6.58	-3.82	-4.41
55698	355.5	-6.37	-3.771	-4.36
55684	356	-6.94	-4.14	-4.72
55670	356.5	-7.011	-4.168	-4.75
55655	357	-6.76	-4.25	-4.83
55641	357.5	-7.054	-3.876	-4.46
55626	358	-6.63	-4.04	-4.62

Age yrs BP	Height above base (mm)	d13C (VPDB)	d18O (VDPB)	d18O sw corr (VPDB)
55612	358.5	-7.038	-3.996	-4.58
55597	359	-7.56	-4.19	-4.77
55583	359.5	-7.682	-4.163	-4.75
55568	360	-7.2	-4.19	-4.77
55553	360.5	-7.729	-4.119	-4.70
55539	361	-6.94	-4.03	-4.61
55525	361.5	-7.002	-3.94	-4.52
55510	362	-6.56	-4.16	-4.74
55495	362.5	-6.444	-3.904	-4.49
55481	363	-6.39	-4.02	-4.60
55466	363.5	-6.35	-3.938	-4.52
55452	364	-6.34	-4.11	-4.69
55437	364.5	-6.907	-4.034	-4.61
55423	365	-6.68	-4.07	-4.64
55409	365.5	-6.739	-3.967	-4.54
55394	366	-6.98	-4.05	-4.62
55380	366.5	-6.96	-4.017	-4.59
55365	367	-7.69	-4.07	-4.64
55351	367.5	-7.207	-4.083	-4.65
55336	368	-7.19	-4.22	-4.78
55322	368.5	-7.438	-4.137	-4.70
55307	369	-7.26	-4.16	-4.71
55293	369.5	-7.568	-4.191	-4.74
55278	370	-7.14	-4.14	-4.69
55264	370.5	-7.038	-4.137	-4.68
55250	371	-7.25	-3.95	-4.49
55235	371.5	-7.263	-3.999	-4.54
55220	372	-7.15	-3.99	-4.53
55206	372.5	-7.033	-3.934	-4.47
55192	373	-6.94	-3.92	-4.45
55178	373.5	-7.124	-4.098	-4.62
55163	374	-7.18	-3.87	-4.40
55148	374.5	-6.821	-3.851	-4.38
55134	375	-7.39	-3.7	-4.22
55120	375.5	-7.325	-3.881	-4.40
55105	376	-7.44	-3.81	-4.33
55091	376.5	-7.522	-3.99	-4.51

Continued stable isotope data for SVC06

Age yrs BP	Height above base (mm)	d13C (VPDB)	d18O (VDPB)	d18O sw corr (VPDB)
55076	377	-7.12	-3.54	-4.06
55061	377.5	-7.368	-3.858	-4.37
55047	378	-7.24	-4.03	-4.54
55032	378.5	-7.076	-3.634	-4.15
55018	379	-7.36	-4.06	-4.57
55004	379.5	-7.402	-4.104	-4.61
54989	380	-7.84	-4.18	-4.68
54974	380.5	-7.615	-3.903	-4.40
54959	381	-7.54	-3.77	-4.27
54944	381.5	-7.178	-3.591	-4.09
54930	382	-7.46	-3.91	-4.40
54916	382.5	-6.453	-3.995	-4.49
54902	383	-7.04	-3.93	-4.42
54888	383.5	-6.969	-3.838	-4.32
54873	384	-6.99	-3.83	-4.31
54859	384.5	-7.028	-3.771	-4.25
54844	385	-6.02	-3.64	-4.12
54830	385.5	-6.009	-3.52	-4.00
54815	386	-7.52	-3.77	-4.25
54801	386.5	-7.839	-3.859	-4.33
54786	387	-7.12	-3.66	-4.13
54762	387.5	-6.754	-3.841	-4.31
54737	388	-7.26	-3.82	-4.29
54713	388.5	-6.608	-3.708	-4.17
54689	389	-6.18	-3.81	-4.27
54666	389.5	-7.1	-3.661	-4.12
54643	390	-6.2	-3.89	-4.35
54618	390.5	-5.66	-3.631	-4.10
54594	391	-6.63	-3.69	-4.16
54569	391.5	-6.641	-3.887	-4.36
54545	392	-7.07	-4.02	-4.49
54522	392.5	-7.519	-3.86	-4.34
54497	393	-8.05	-4.06	-4.54
54473	393.5	-7.152	-4.063	-4.54
54449	394	-7.66	-4.08	-4.56
54424	394.5	-7.378	-4.005	-4.49
54399	395	-7.72	-4.12	-4.61

Age yrs BP	Height above base (mm)	d13C (VPDB)	d18O (VDPB)	d18O sw corr (VPDB)
54374	395.5	-6.8	-4.127	-4.61
54351	396	-6.91	-4.11	-4.60
54328	396.5	-6.624	-4.182	-4.67
54303	397	-6.46	-4.22	-4.70
54279	397.5	-6.433	-4.133	-4.62
54256	398	-7	-4.2	-4.68
54232	398.5	-7.162	-4.221	-4.70
54207	399	-8.44	-4.25	-4.73
54182	399.5	-8.298	-4.292	-4.77
54157	400	-8.31	-4.21	-4.69
54133	400.5	-8.033	-4.054	-4.53
54110	401	-8.03	-4.15	-4.63
54086	401.5	-7.678	-4.046	-4.53
54062	402	-7.63	-4.46	-4.94
54015	403	-7.37	-4.3	-4.78
53990	403.5	-7.414	-4.248	-4.73
53966	404	-7.29	-4.08	-4.56
53942	404.5	-7.731	-4.077	-4.56
53918	405	-7.75	-4.15	-4.63
53895	405.5	-8.101	-4.106	-4.59
53870	406	-7.68	-4.25	-4.74
53846	406.5	-8.104	-4.182	-4.67
53822	407	-7.96	-4.16	-4.65
53797	407.5	-7.974	-4.094	-4.58
53773	408	-7.93	-4.06	-4.55
53655	411	-7.88	-3.95	-4.45
53551	414	-8.1	-4.47	-4.97
53447	417	-8.62	-4.57	-5.07
53344	420	-8.31	-4.26	-4.77
53240	423	-7.99	-4.44	-4.95
53135	426	-7.97	-4.49	-5.00
53032	429	-8.04	-4.31	-4.83
52927	432	-8.67	-4.29	-4.82
52862	435	-8.2	-4.53	-5.06
52814	438	-7.72	-4.42	-4.95
52766	441	-8.07	-4.42	-4.95
52719	444	-8.51	-4.36	-4.89

Continued stable isotope data for SVC06

Age yrs BP	Height above base (mm)	d13C (VPDB)	d18O (VDPB)	d18O sw corr (VPDB)
52671	447	-8.28	-4.36	-4.89
52624	450	-8.17	-4.55	-5.09
52577	453	-8.21	-4.37	-4.91
52529	456	-7.42	-4.25	-4.79
52481	459	-8.31	-4.12	-4.66
52434	462	-8.02	-4.33	-4.87
52386	465	-8.21	-4.39	-4.93
52326	468	-8.49	-4.25	-4.79
52241	471	-8.51	-3.95	-4.50
52156	474	-8.46	-3.83	-4.38
52072	477	-8.35	-4.24	-4.79
51987	480	-8.08	-4.35	-4.90
51903	483	-8.16	-4.13	-4.68
51835	486	-8.57	-4.1	-4.66
51768	489	-8.27	-3.87	-4.43
51702	492	-8.14	-3.82	-4.39
51633	495	-8.86	-4.15	-4.72
51544	498	-8.43	-3.88	-4.46
51409	501	-8.24	-3.86	-4.44
51275	504	-8.82	-3.95	-4.53
51139	507	-8.52	-3.83	-4.41
51004	510	-8.42	-3.9	-4.47
50870	513	-8.63	-3.96	-4.53
50825	514	-7.87	-4.13	-4.70
50779	515	-8.73	-4.36	-4.92
50736	516	-8.42	-4.33	-4.89
50693	517	-8.56	-4.37	-4.93
50649	518	-8.56	-4.08	-4.64
50606	519	-8.58	-4.27	-4.82
50435	523	-8.15	-4.12	-4.66
50390	524	-7.3	-3.78	-4.32
50347	525	-7.95	-3.89	-4.43
50304	526	-8.31	-4.27	-4.80
50261	527	-8.42	-4.09	-4.62
50218	528	-8.27	-4.04	-4.57
50174	529	-7.32	-3.95	-4.48
50132	530	-8.17	-3.92	-4.45

Age yrs BP	Height above base (mm)	d13C (VPDB)	d18O (VDPB)	d18O sw corr (VPDB)
50089	531	-8.49	-4.04	-4.56
50045	532	-8.21	-3.9	-4.42
50002	533	-8.32	-4.07	-4.59
49960	534	-7.91	-3.82	-4.34
49917	535	-7.31	-3.73	-4.25
49873	536	-8.35	-3.81	-4.33
49829	537	-8.05	-3.92	-4.44
49797	538	-8.58	-3.93	-4.45
49765	539	-8.03	-3.93	-4.45
49733	540	-6.87	-3.89	-4.41
49700	541	-8.21	-3.86	-4.38
49668	542	-7.78	-3.8	-4.32
49637	543	-7.98	-3.78	-4.30
49603	544	-6.97	-3.76	-4.28
49570	545	-7.85	-3.95	-4.47
49539	546	-8.28	-3.9	-4.42
49486	547	-8.22	-3.86	-4.38
49432	548	-7.49	-3.9	-4.42
49379	549	-7.77	-3.72	-4.25
49322	550	-6.92	-3.95	-4.48
49295	550.5	-7.509	-4.012	-4.54
49267	551	-7.46	-3.77	-4.30
49240	551.5	-7.58	-3.879	-4.41
49213	552	-7.64	-3.84	-4.38
49186	552.5	-7.335	-3.761	-4.30
49159	553	-7.27	-3.86	-4.40
49132	553.5	-7.15	-3.97	-4.51
49105	554	-7.24	-4.09	-4.63
49068	554.5	-7.222	-3.976	-4.52
49029	555	-7.07	-3.85	-4.40
48988	555.5	-7.084	-3.908	-4.46
48947	556	-7.26	-4.07	-4.62
48907	556.5	-7.136	-3.953	-4.50
48867	557	-6.89	-4.18	-4.73
48828	557.5	-7.559	-4.237	-4.79
48790	558	-6.87	-4.1	-4.65
48749	558.5	-7.172	-4.01	-4.56

Continued stable isotope data for SVC06

Age yrs BP	Height above base (mm)	d13C (VPDB)	d18O (VDPB)	d18O sw corr (VPDB)
48709	559	-7.05	-4.06	-4.60
48669	559.5	-7.494	-4.174	-4.70
48629	560	-6.9	-3.81	-4.34
48589	560.5	-6.963	-3.835	-4.35
48550	561	-7.14	-3.92	-4.43
48510	561.5	-6.91	-3.943	-4.44
48470	562	-7.42	-3.9	-4.40
48431	562.5	-8.197	-4.096	-4.59
48392	563	-7.86	-3.91	-4.40
48351	563.5	-7.81	-3.801	-4.30
48311	564	-7.6	-3.84	-4.33
48271	564.5	-7.269	-3.724	-4.22
48232	565	-7.11	-3.81	-4.30
48192	565.5	-6.816	-3.896	-4.38
48153	566	-7.54	-4.06	-4.55
48112	566.5	-7.259	-3.969	-4.46
48071	567	-7.97	-3.9	-4.39
48018	567.5	-8.029	-3.715	-4.21
47963	568	-7.97	-4.06	-4.55
47907	568.5	-7.838	-3.904	-4.39
47853	569	-7.48	-4	-4.48
47799	569.5	-7.479	-4.063	-4.54
47745	570	-7.12	-3.88	-4.36
47694	570.5	-7.435	-3.711	-4.18
47641	571	-7.09	-3.76	-4.23
47614	571.25	-6.987	-3.651	-4.11
47587	571.5	-8.52	-3.75	-4.21
47558	571.75	-8.378	-3.613	-4.07
47530	572	-8.05	-3.7	-4.15
47501	572.25	-8.362	-3.719	-4.16
47473	572.5	-8.2	-3.85	-4.29
47445	572.75	-8.393	-3.763	-4.20
47416	573	-8.47	-3.73	-4.16
47389	573.25	-7.87	-3.716	-4.14
47362	573.5	-7.86	-3.7	-4.12
47335	573.75	-7.727	-3.657	-4.08
47309	574	-8.2	-3.74	-4.17

Age yrs BP	Height above base (mm)	d13C (VPDB)	d18O (VDPB)	d18O sw corr (VPDB)
47282	574.25	-7.487	-3.653	-4.08
47256	574.5	-7.53	-3.72	-4.15
47227	574.75	-7.585	-3.64	-4.07
47198	575	-7.59	-3.78	-4.21
47169	575.25	-7.305	-3.651	-4.08
47142	575.5	-7.02	-3.97	-4.40
47114	575.75	-7.396	-3.696	-4.14
47087	576	-7.5	-3.81	-4.26
47061	576.25	-7	-3.948	-4.40
47035	576.5	-7.4	-4.05	-4.51
47008	576.75	-6.966	-3.798	-4.26
46982	577	-7.41	-3.99	-4.46
46956	577.25	-7.417	-3.991	-4.46
46930	577.5	-7.97	-4.19	-4.67
46903	577.75	-7.205	-3.927	-4.41
46876	578	-7.91	-4.1	-4.58
46820	578.5	-7.7	-4.18	-4.67
46762	579	-8.21	-4.27	-4.77
46725	579.5	-8.24	-4.15	-4.65
46687	580	-8.58	-4.23	-4.74
46646	580.5	-8.61	-4.13	-4.64
46605	581	-8.55	-4.2	-4.71
46563	581.5	-8.37	-3.95	-4.46
46522	582	-8.67	-4.11	-4.62
46482	582.5	-8.34	-3.97	-4.49
46440	583	-8.24	-3.92	-4.44
46399	583.5	-8.11	-4.01	-4.53
46359	584	-8.12	-4	-4.53
46321	584.5	-8.12	-3.87	-4.40
46281	585	-8.18	-3.88	-4.41
46241	585.5	-7.94	-3.75	-4.29
46199	586	-8.05	-3.85	-4.39
46158	586.5	-8.06	-3.95	-4.49
46118	587	-8.25	-4.02	-4.57
46078	587.5	-7.91	-3.86	-4.41
46036	588	-8.11	-3.83	-4.39
45995	588.5	-7.7	-3.68	-4.24

Continued stable isotope data for SVC06

Age yrs BP	Height above base (mm)	d13C (VPDB)	d18O (VDPB)	d18O sw corr (VPDB)
45954	589	-7.82	-3.77	-4.33
45914	589.5	-8.03	-3.66	-4.22
45873	590	-8.13	-3.74	-4.30
45833	590.5	-8.07	-3.9	-4.46
45793	591	-8.13	-3.84	-4.40
45754	591.5	-7.31	-3.78	-4.34
45712	592	-7.74	-3.74	-4.29
45673	592.5	-7.23	-3.71	-4.26
45632	593	-7.39	-3.74	-4.29
45590	593.5	-7.7	-3.6	-4.15
45549	594	-7.62	-3.65	-4.20
45509	594.5	-7.59	-3.71	-4.26
45469	595	-7.69	-3.63	-4.17
45430	595.5	-7.01	-3.62	-4.16
45390	596	-7.55	-3.7	-4.24
45351	596.5	-7.54	-3.6	-4.14
45310	597	-7.65	-3.73	-4.27
45269	597.5	-6.81	-3.56	-4.10
45228	598	-8.04	-3.66	-4.20
45182	598.5	-6.68	-3.86	-4.40
45135	599	-7.89	-3.74	-4.28
45087	599.5	-6.68	-3.73	-4.26
45038	600	-7.77	-3.67	-4.20
44985	600.5	-7.17	-3.43	-3.95
44933	601	-7.65	-3.58	-4.10
44881	601.5	-7.3	-3.49	-4.00
44830	602	-7.43	-3.37	-3.88
44781	602.5	-7.78	-3.6	-4.10
44732	603	-7.77	-3.44	-3.94
44680	603.5	-7.36	-3.49	-3.98
44629	604	-7.78	-3.6	-4.09
44578	604.5	-7.25	-3.61	-4.10
44528	605	-7.49	-3.65	-4.13
44479	605.5	-7	-3.37	-3.85
44427	606	-7.62	-3.44	-3.93
44374	606.5	-7.32	-3.43	-3.93
44325	607	-7.96	-3.43	-3.94

Age yrs BP	Height above base (mm)	d13C (VPDB)	d18O (VDPB)	d18O sw corr (VPDB)
44278	607.5	-6.97	-3.39	-3.92
44230	608	-8.02	-3.57	-4.11
44217	608.5	-7.24	-3.61	-4.15
44203	609	-7.42	-3.22	-3.76
44189	609.5	-7.76	-3.68	-4.22
44175	610	-7.3	-3.31	-3.86
44161	610.5	-7.8	-3.58	-4.13
44148	611	-7.64	-3.5	-4.05
44134	611.5	-8.09	-3.55	-4.10
44120	612	-8.3	-3.53	-4.08
44106	612.5	-8.14	-3.57	-4.12
44092	613	-8.02	-3.89	-4.44
44077	613.5	-7.73	-3.93	-4.48

Table A.9: Stable isotope data for SVC06. Ages were determined using University of Oxford's OxCal program. Oxygen isotopes have also been corrected for mean seawater δ^{18}O through *Python* submodule *SpeleoPy*.

Stable isotope data for SVC05

Growth Phase 1				
Age yrs BP	Height above base (mm)	d13C (VPDB)	d18O (VPDB)	d18O sw corr (VPDB)
103175	0	-0.48	-6.79	-6.90
103120	1	-1.83	-6.90	-7.01
103066	2	-2.14	-7.07	-7.18
103012	3	-2.03	-6.95	-7.06
102957	4	-2.13	-7.17	-7.27
102903	5	-1.94	-7.28	-7.38
102847	6	-1.45	-7.19	-7.29
102793	7	-2.72	-7.66	-7.75
102737	8	-1.97	-7.78	-7.87
102683	9	-1.82	-7.60	-7.69
102628	10	-1.71	-7.76	-7.86
102574	11	-2.39	-7.37	-7.46
102518	12	-2.40	-7.19	-7.28
102465	13	-1.79	-7.22	-7.31
102411	14	-2.58	-7.10	-7.20
102357	15	-2.53	-6.64	-6.74
102303	16	-2.43	-7.20	-7.29
102245	17	-2.22	-7.12	-7.21
102191	18	-2.65	-7.11	-7.20
102138	19	-1.75	-6.93	-7.02
102083	20	-2.59	-6.98	-7.07
102028	21	-2.36	-6.75	-6.85
101973	22	-2.60	-7.03	-7.12
101917	23	-3.03	-6.84	-6.93
101863	24	-2.66	-6.67	-6.77
101808	25	-2.98	-6.77	-6.86
101754	26	-2.52	-6.30	-6.39
101699	27	-2.35	-6.68	-6.77
101644	28	-2.28	-6.62	-6.71
101591	29	-2.04	-6.71	-6.79
101536	30	-2.24	-6.70	-6.79
101481	31	-2.89	-6.47	-6.56
101427	32	-1.94	-6.76	-6.84
101372	33	-2.35	-6.87	-6.95
101317	34	-2.53	-6.80	-6.88
101263	35	-1.80	-6.29	-6.37

Growth Phase 1 (cont.)				
Age yrs BP	Height above base (mm)	d13C (VPDB)	d18O (VPDB)	d18O sw corr (VPDB)
101208	36	-2.36	-7.21	-7.28
101153	37	-2.93	-7.11	-7.19
101099	38	-2.15	-7.21	-7.28
101044	39	-2.72	-7.36	-7.43
100990	40	-2.31	-6.14	-6.22
100934	41	-3.15	-6.33	-6.41
100879	42	-2.83	-6.61	-6.69
100824	43	-3.18	-6.32	-6.39
100770	44	-2.53	-6.05	-6.13
100715	45	-2.52	-6.69	-6.76
100661	46	-2.79	-6.48	-6.54
100607	47	-3.45	-7.05	-7.11
100552	48	-3.04	-6.93	-6.99
100497	49	-2.82	-6.32	-6.39
100442	50	-2.84	-6.22	-6.29
100387	51	-2.93	-6.31	-6.38
100332	52	-3.18	-6.40	-6.48
100278	53	-2.74	-6.68	-6.75
100223	54	-2.70	-6.44	-6.52
100168	55	-2.80	-6.55	-6.63
100113	56	-3.11	-6.28	-6.36
100059	57	-2.16	-6.13	-6.21
100005	58	-2.12	-6.48	-6.56
99951	59	-2.52	-6.65	-6.74
99896	60	-2.59	-6.28	-6.37
99841	61	-3.01	-5.99	-6.08
99787	62	-2.44	-5.62	-5.72
99732	63	-2.37	-5.55	-5.65
99678	64	-2.23	-5.53	-5.63
99624	65	-2.94	-5.79	-5.90
99569	66	-2.77	-5.55	-5.67
99515	67	-2.91	-5.59	-5.71
99459	68	-2.12	-5.87	-5.99
99406	69	-3.36	-5.80	-5.93
99351	70	-3.32	-5.48	-5.61
99296	71	-3.15	-5.58	-5.72

Continued stable isotope data for SVC05

Growth Phase 1 (cont.)				
Age yrs BP	Height above base (mm)	d13C (VPDB)	d18O (VPDB)	d18O sw corr (VPDB)
99241	72	-3.79	-5.60	-5.74
99187	73	-3.20	-5.80	-5.95
99131	74	-3.11	-5.72	-5.88
99077	75	-2.60	-5.31	-5.47
98839	80	-2.83	-5.40	-5.58
98600	85	-5.10	-4.76	-4.96
98363	90	-4.48	-4.38	-4.59
98124	95	-4.10	-4.30	-4.52
97885	100	-5.07	-4.61	-4.79
97647	105	-5.10	-4.43	-4.59
97362	111	-6.55	-4.32	-4.45
97171	115	-5.27	-4.98	-5.11
96932	120	-5.18	-4.68	-4.82
96693	125	-4.66	-4.72	-4.87
96418	130	-5.17	-4.40	-4.55
96062	135	-5.16	-4.87	-5.03
95706	140	-3.92	-4.54	-4.74
95349	145	-3.45	-4.20	-4.45
94993	150	-3.51	-4.76	-5.06
94636	155	-2.78	-4.63	-4.96
94279	160	-4.45	-4.67	-5.00
93922	165	-5.30	-4.72	-5.03
93565	170	-4.48	-5.12	-5.39
93491	171	-3.73	-4.56	-4.83
93415	172	-4.46	-4.57	-4.83
93339	173	-2.96	-4.48	-4.73
93263	174	-3.02	-4.41	-4.68
93189	175	-4.41	-4.73	-5.02
93114	176	-4.61	-4.70	-5.00
93040	177	-5.50	-4.86	-5.17
92964	178	-5.25	-4.96	-5.28
92890	179	-4.16	-5.02	-5.36
92814	180	-4.53	-4.71	-5.06
92739	181	-4.70	-4.71	-5.08

Growth Phase 2				
Age yrs BP	Height above base (mm)	d13C (VPDB)	d18O (VPDB)	d18O sw corr (VPDB)
88456	183.5	-3.41	-4.71	-4.89
88387	184.5	-4.57	-4.57	-4.75
88352	185	-6.04	-4.56	-4.74
88317	185.5	-5.40	-4.53	-4.71
88281	186	-4.28	-4.52	-4.70
88245	186.5	-3.73	-4.64	-4.81

Growth Phase 3				
Age yrs BP	Height above base (mm)	d13C (VPDB)	d18O (VPDB)	d18O sw corr (VPDB)
60758	191	-6.32	-3.41	-4.07
60738	192	-7.16	-3.61	-4.27
60697	193	-6.72	-3.71	-4.36
60677	194	-6.59	-3.93	-4.58
60637	195	-7.49	-3.84	-4.49
60647	195	-7.26	-3.69	-4.34
60606	196	-6.24	-3.5	-4.15
60586	197	-5.71	-3.68	-4.32
60545	198	-6.14	-3.64	-4.27
60525	199	-5.67	-3.21	-3.83

Growth Phase 3				
Age yrs BP	Height above base (mm)	d13C (VPDB)	d18O (VPDB)	d18O sw corr (VPDB)
60758	191	-6.32	-3.41	-4.07
60738	192	-7.16	-3.61	-4.27
60697	193	-6.72	-3.71	-4.36
60677	194	-6.59	-3.93	-4.58
60637	195	-7.49	-3.84	-4.49
60647	195	-7.26	-3.69	-4.34
60606	196	-6.24	-3.5	-4.15
60586	197	-5.71	-3.68	-4.32
60545	198	-6.14	-3.64	-4.27
60525	199	-5.67	-3.21	-3.83

Continued stable isotope data for SVC05

Growth Phase 4				
Age yrs BP	Height above base (mm)	d13C (VPDB)	d18O (VPDB)	d18O sw corr (VPDB)
47247.6	202	-7.86	-3.92	-4.35
47158.8	203	-7.9	-3.99	-4.42
47070.1	204	-6.92	-4.22	-4.67
46977.9	205	-6.05	-3.46	-3.93

Growth Phase 5				
Age yrs BP	Height above base (mm)	d13C (VPDB)	d18O (VPDB)	d18O sw corr (VPDB)
41557	206	-6.81	-3.4	-4.08
41507	207	-7.36	-3.51	-4.19
41455	208	-7.02	-3.19	-3.88

Growth Phase 6				
Age yrs BP	Height above base (mm)	d13C (VPDB)	d18O (VPDB)	d18O sw corr (VPDB)
40014	209	-7.16	-3.37	-4.01
39966	210	-7.3	-3.71	-4.34
39918	211	-7.11	-3.92	-4.54
39871	212	-7.8	-4.04	-4.66
39821	213	-7.94	-4.05	-4.66

Growth Phase 7				
Age yrs BP	Height above base (mm)	d13C (VPDB)	d18O (VPDB)	d18O sw corr (VPDB)
29102	215	-8.52	-3.05	-3.75
29057	216	-8.54	-3	-3.70
29012	217	-8.35	-3.55	-4.24

Table A.10: Stable isotope data for SVC05. Ages were determined using University of Oxford's OxCal program. Oxygen isotopes have also been corrected for mean seawater δ^{18}O through *Python* submodule *SpeleoPy*.

Appendix B

Python programs for data reduction

B.1 Advantages of *Python* for MC-ICP-MS data reduction

Isotopic data collection using MC-ICP-MS entails significant data reduction. The Neptune Plus and Neptune MC-ICP-MS used in the University of Minnesota (UMN) Isotope Lab export run data as DAT, EXP, and TDT files. The data files contain beam counts per cycle of major isotopes and isotopic ratio, collected on either SEM or cups depending on method used. Current protocol involves reducing EXP run data via a series of Excel spreadsheets, most of which contain Excel Macros programs for data filtration. Excel spreadsheets must be customized for your sample information, machine parameters, and spike used. Data import consists of copy-pasting EXP run data into the Excel spreadsheet body, increasing data reduction time. Additionally, Macros programs need to be in an Excel Macro-Enabled Workbook (.xlsm) file, or linked to a working .xlsm file.

The complexities of working with data reduction spreadsheets in the UMN Isotope Lab has led to error introduction and a lack of process monitoring. The UMN Isotope Lab receives over 20 scientific visitors each year, who complete sample preparation, chemistry procedures, and machine analysis on their own after limited staff instruction. Often Excel spreadsheets are used by visitors with little knowledge regarding the process of data reduction, which can lead to errors importing data and changing spreadsheet parameters. Additionally, visitors often run a large amount of samples in a limited amount of time. The use of Excel spreadsheets not only increases reduction time but requires personal data management tactics to keep track of spreadsheets during and after data reduction.

Furthermore, a new method of using Faraday cups to measure high intensity beams at low counting errors has been developed for the UMN Isotope Lab (Pythoud et al. *in prep*).

This method greatly reduces machine run time, but involves a new set of Excel spreadsheets for data reduction. Teaching visitors not only this new machine method, but this new data reduction procedure, impinges upon limited Isotope Lab staff time.

The lab's current system for data reduction via Excel spreadsheets has not been monitored. Visitors often receive access to spreadsheets through a staff member, who may or may not have the most current or applicable version. This may lead to continuation or propagation of errors, and could result in the publication of inaccurate data processed at the UMN Isotope Lab.

In order to consolidate and validate data reduction methods for the UMN Isotope Lab, we transformed all ^{230}Th dating functions into user-friendly *Python* programs. *Python* is an object-oriented, high-level programming language developed in the early 1990s. This interpreted language was created with an emphasis on readability, and thus is ideal for a lab environment where source code data processing functions may need to be periodically edited. Stand alone data reduction programs have been developed for analyzing data on either the SEM or Faraday cups. SEM measurements include reagent blanks, chemistry blanks, SEM spiked standards and samples. Cups measurements include cups unspiked and spiked standards and samples. All programs use a *Tkinter* graphical user interface (GUI) for data upload, completely separating the user from the program scripts. Programs can be run either as *Python* files or system-specific executable files, and are available via GitHub repositories at https://github.com/junissen.

This chapter will discuss the processes involved in data reduction and how each Python program functions. We believe these programs significantly improve work flow for users and quality control of lab results. Further work involves converting ^{230}Th- ^{231}Pa data reduction methods into Python programs, thus retiring all Excel spreadsheets used by the UMN Isotope Lab.

B.2 Reagent Blank Calculation

Blanks are periodically run by lab individuals to ensure minimal contamination is coming from chemistry reagents. These are most important when reagents are refilled or lab equipment is cleaned. Reagents blanks can either be separated to test each individual reagent, or combined to test reagents as a whole. All reagent blanks consist of combining a typical amount of each reagent used in a chemistry batch, drying down with nitric acid, and diluting with water, 1% nitric acid, and a minimal amount of hydrofluoric acid. This sample is then run on the MC-ICP-MS using the SEM configuration on the background method.

Calculating reagent blanks is the simplest data reduction done in the UMN Isotope Lab. The signal measured while the sampler is in wash solution is subtracted from the total signal measured while the sample is in the reagent blank. This provides the reagent blank signal in counts per second (cps). The signal in cps is then converted into a reagent blank weight using the total solution weight, ionization efficiency, and uptake rate. Blanks are measured on the ag (10^{-18}g) and fg (10^{-15}g) level.

Current methods for reducing reagent blanks involve a single Excel spreadsheet with tabs for the wash signal, total signal, and data reduction. Wash measurements and signal measurements for both U and Th must be copied and pasted from EXP data files. To streamline this process, the *Python* program uploads each file needed and reduces the data internally, exporting an Excel table with reagent blank weights after calculation is complete.

To begin, a GUI is generated and prompts the user for data input. The user must input the blank name, solution weight, uptake rate (mg/sec), ionization efficiency (%) and include an export file name for the resulting Excel table. The file type (.xlsx) must be included as a part of the file name. The user then has the option of altering their Th method. During a method run on the MC-ICP-MS, it is possible to continue running after the solution is spent, resulting in a sharp spike followed by a decay of the ion beam. An example of this is shown in Figure B.1. Additionally, peak spikes can occur on occasion during the sample run. For this reason, it is possible for the user to edit the data file to delete anomalies, save as a .xlsx file, and upload into the program.

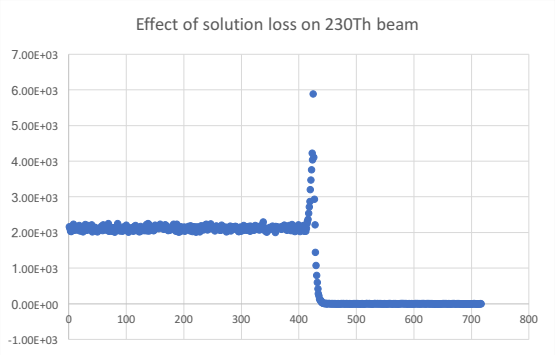

Figure B.1: Example of the effect of solution loss on ^{230}Th ion beam. The solution is completely used up by ≈400 cycles, resulting in a sharp spike and decay of ion beam intensity.

To correct for this with minimal effort, the program allows you to specify the last cycle number you would like analyzed. The program will then only reduce the specified cycles. The user is also given this option for the U method. An example of the GUI windows which result from choosing to alter or not to alter methods are show in Figure B.2.

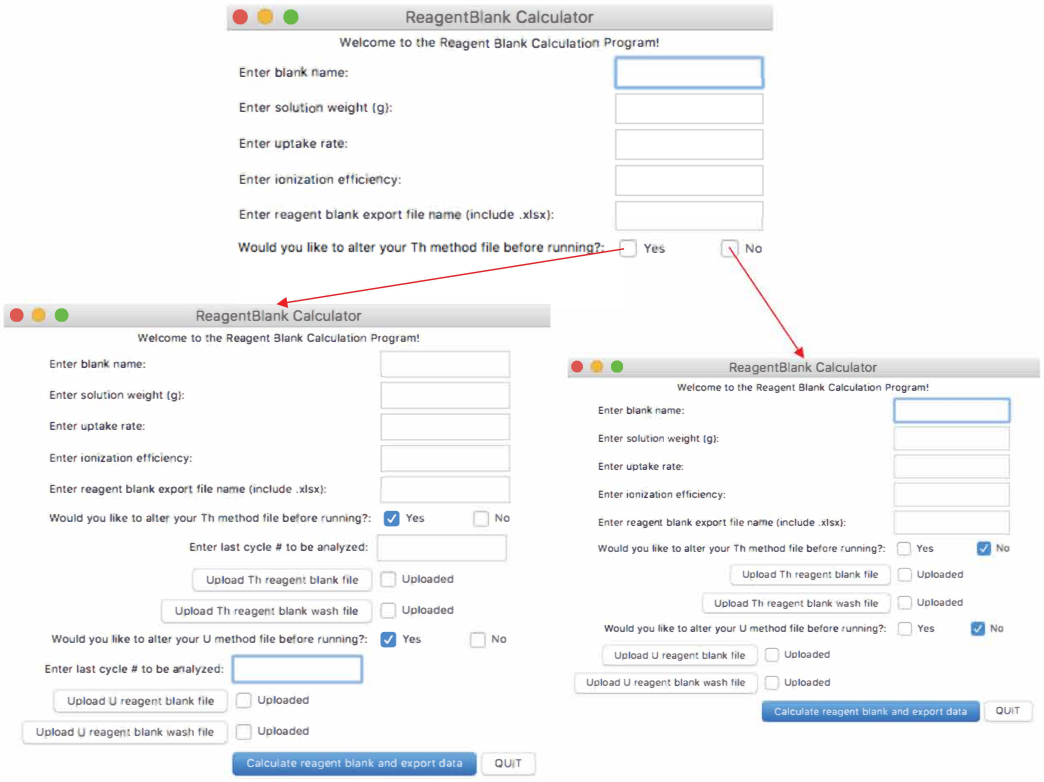

Figure B.2: Example of GUI windows for altering or not altering reagent blanks

The user can upload the wash and method files by clicking on the "Upload" button and choosing the file via a drop-down directory. Once the file has been chosen, the uploaded button will show a check mark. Once all the files have been uploaded, the user clicks on "Calculate reagent blank and export data" to begin the program. An example of the complete program with data input is shown in Figure B.3.

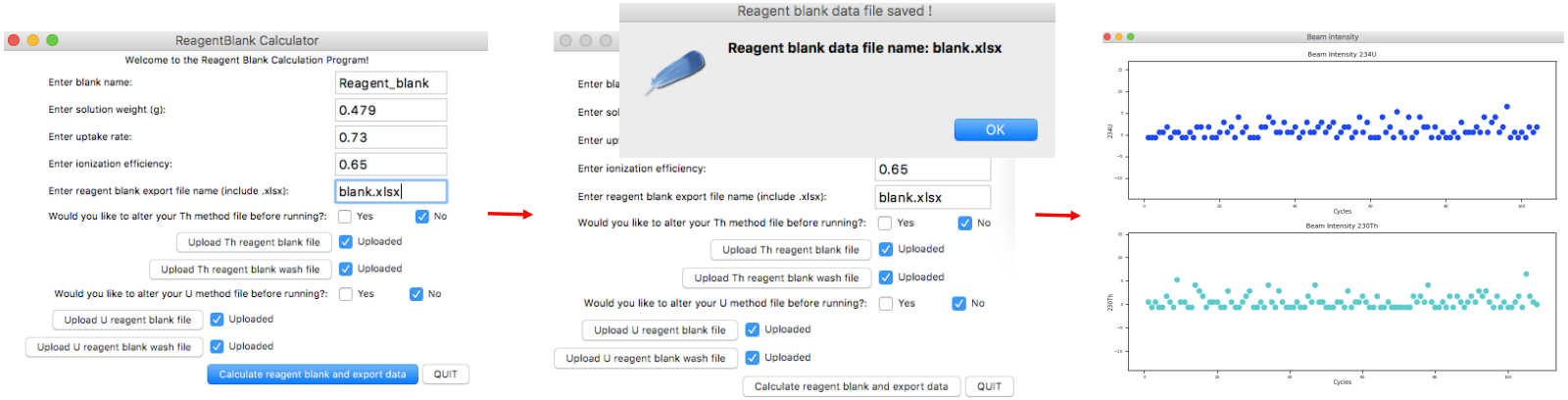

Figure B.3: Example of steps for reagent blank calculation using program

The program results in an Excel spreadsheet export under the filename chosen, and plots the ^{234}U and ^{230}Th beam to ensure beam stability. The Excel export is located in the same directory as the *Python* programs. Figures B.4 and B.5 show the results of the *Python* reagent blank program and the traditional Excel data reduction method. Figure B.4 shows the formatting of the program's Excel export.

	1_Reagent_blank	229Th	230Th	232Th	233U	234U	235U	236U	238U
1_fileinfo	Reagent_blank								
2_regblank		11.95735	3.55648	17.66556	150.8113	17.46626	2.464434	139.965	360.7554
3_2s err		74.6386	17.89997	10.64751	99.52776	21.03001	0.94897	73.97839	59.98159
4_units		ag	ag	fg	ag	ag	fg	ag	fg
5_param	Run info	Sln wt	U.R.	I.E					
6_param		0.479	0.73	0.65					
7_param		g	mg/sec	%					

Figure B.4: Results of *Python* reagent blank data reduction

Reagent blank for all reagents calculated by Excel

	229Th	230Th	232Th	233U	234U	235U	236U	238U
Reagent blank weight	11.96	3.56	17.67	150.81	17.47	2.46	139.96	360.76
2σ Abs. error	± 74.64	± 17.90	± 10.65	± 99.53	± 21.03	± 0.95	± 73.98	± 59.98
	ag	ag	fg	ag	ag	fg	ag	fg

Figure B.5: Results of Excel reagent blank data reduction

Reagent blank data reduction provides the same results for the *Python* program as the traditional Excel spreadsheet, with minimal effort. The Excel spreadsheet created by the program can then be stored for later reference if needed. The *Python* Reagent Blank Calculation is the simplest of the *Python* programs created for the UMN Isotope lab, and contains 745 lines of code and documentation. At 25 lines of code per page, this is approximately 30 pages.

B.3 Chemistry Blank Calculation

Chemistry blanks are run with each sample batch to determine the amount of contamination that may have occurred during chemistry procedures. These blanks are minimally spiked (< 2μg) and run identically to samples with the same amount of reagents. U and Th fractions are run as blank methods on the SEM, after ensuring backgrounds are low enough to run. Signal isotopic ratios of the measured isotope versus spike isotope are calculated by subtracting the machine wash values from the total signal. The ratios must then be corrected for isotopic fractionation that occurs in the sample during ionization by the plasma source. The ion beam is originally disproportionately enriched in light isotopes, and only with time does the ratio of light to heavy isotopes decrease. The amount of mass fractionation occurring can be determined by comparing the known spike $\frac{236}{233}$ ratio and the measured $\frac{236}{233}$ ratio. These should be equal, and any deviation is a result of mass fractionation.

As the amount of fractionation occurring is dependent upon isotope mass, we can correct for fractionation at other masses. The exponential law provides the most accurate correction, and is show in Equation B.1 below, using the $\frac{230}{229}$ ratio as an example. The variables in the exponent are atomic masses of isotopes.

$$\frac{230}{229}_{(corrected)} = \frac{230}{229}_{(measured)} * \left(\frac{spike\frac{236}{233}}{signal\frac{236}{233}}\right)^{\frac{ln\frac{230}{229}}{ln\frac{236}{233}}} \tag{B.1}$$

The blank isotopic ratios are finalized by subtracting the spike isotopic ratios from the resulting fractionation corrected ratios, and converted into chemistry blank weights using the atomic weight and amount of spike isotope in the blank. Chemistry blanks for the UMN Isotope Lab are ideally under 20 ag ^{230}Th, 500 fg ^{232}Th, 60 ag ^{234}U, 5 fg ^{235}U and 500 fg ^{238}U, but are typically significantly higher due to reagent contamination or contamination during chemistry.

Current data reduction for chemistry blanks involves an Excel spreadsheet that must be customized for spike used and raw data must be copied and pasted into the spreadsheet. The *Python* data reduction program for chemistry blank uses a GUI and begins with a prompt for changing spike concentration. Over time, evaporation can occur as spike bottles are opened and spike dispensed, resulting in a change in absolute spike concentrations. Lab users must monitor spike evaporation with time, and recalculate absolute spike concentrations in pmol/g. Evaporation results in little to no change in spike isotopic ratios. The program allows you to manually change the ^{233}U spike concentration, and calculates the resulting change in ^{229}Th based off of isotopic ratios of spike used. This option is shown in Figure B.6, where clicking "yes" to changing preset spike values results in a second GUI window

where you are prompted to manually change the concentration. Once changed, pressing the "submit" button will save the new ^{233}U spike concentration, update the ^{229}Th spike concentration, and return the user to the main GUI window to continue.

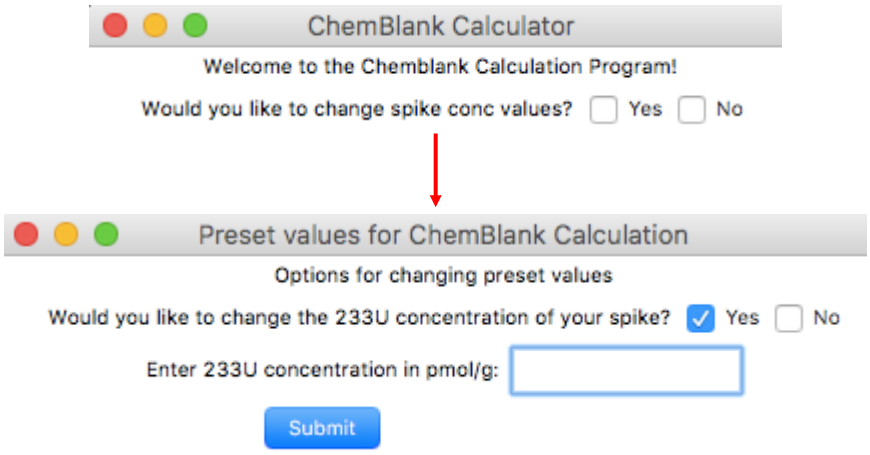

Figure B.6: Option to change spike concentration for chemistry blank program

The chemistry blank program allows you to alter Th and U methods to correct for beam spiking if the solution runs out. Additionally, it allows for an edited .xlsx file to be uploaded. The chemistry blank program requires the user to input the blank name, spike used, spike weight (g), weight of U solution (g), weight of Th solution (g), uptake rate (mg/sec), ionization efficiency (%) and filename for the resulting Excel export with .xlsx extension. An example of the program is show in Figure B.7 for chemistry blank B28.

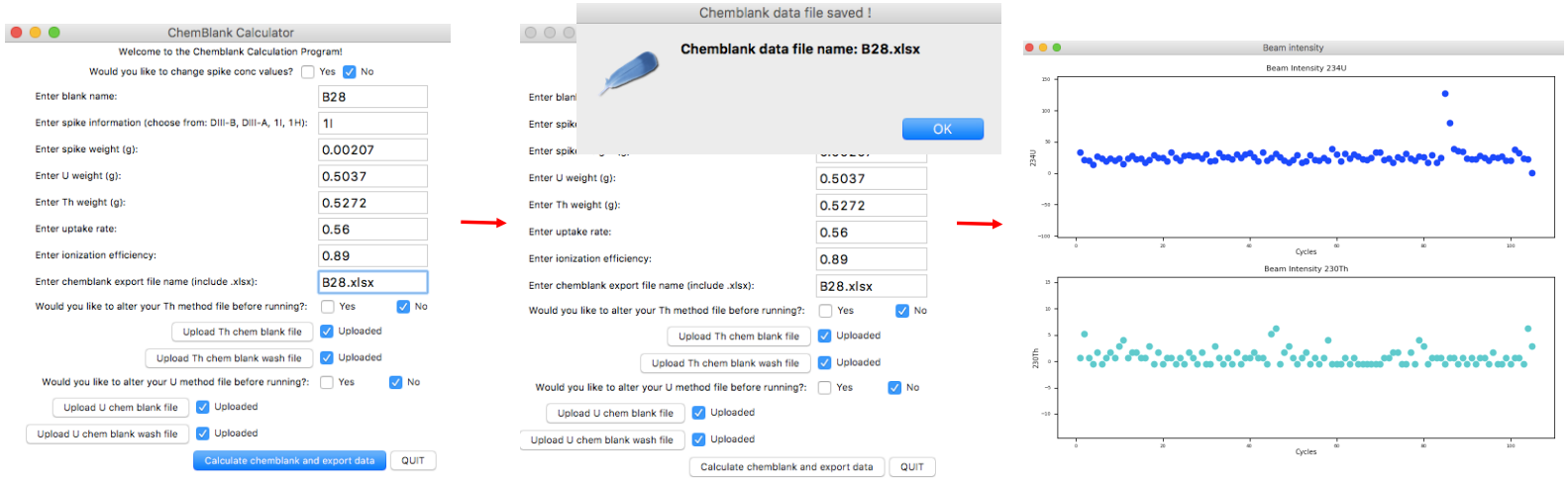

Figure B.7: Example of steps for chemistry blank calculation using program

The program exports an Excel spreadsheet of results under the filename provided in the same directory as the *Python* chemistry blank program. The results of data reduction for chemistry blank B28 using both the *Python* program and traditional Excel spreadsheets are show in Figures B.8 and B.9. Figure B.8 shows the formatting of the program's Excel export. The chemistry blank data will be required for the *Python* age calculation program, which will pull chemistry blank weights from specified cells. Thus, the formatting of this spreadsheet must be maintained if the user wishes to use it while reducing age data.

	1_Chemblank	229Th	230Th	232Th	233U	234U	235U	238U
1_fileinfo	B28							
2_yields		66.21122			79.9601			
3_chemblank			22.92755	186.1442		316.2409	41.36938	2692.519
4_2s err			26.57541	15.25279		124.0121	12.87434	219.3719
5_units		%	ag	fg	%	ag	fg	fg
6_param	Run info							
7_param		Spike used	Spike wt	Th wt	U.R.	U wt	I.E.	
8_param		1l	0.00207	0.5272	0.56	0.5037	0.89	
9_param			g	g	mg/sec	g	%	

Figure B.8: Results of *Python* chemistry blank data reduction

Chemistry blank values for B28 calculated by Excel

	230Th	232Th	234U	235U	238U
Chemistry blank weight	22.93	186.14	316.24	41.37	2692.52
2σ Abs. error	± 26.58	± 15.25	± 124.01	± 12.87	± 219.37
	ag	fg	ag	fg	fg

	Th	U
Chemistry yield	66.21%	79.96%

Figure B.9: Results of Excel chemistry blank data reduction

Chemistry blank data reduction provides the same results for the *Python* program as the traditional Excel spreadsheet, with minimal effort. The Excel spreadsheet created by the program can be stored by the user, and can be used in reducing age data later on. The *Python* Chemistry Blank Calculation contains 1123 lines of code and documentation. At 25 lines of code per page, this is approximately 45 pages.

B.4 Standard Calculation

Standards need to be run for both SEM and cups configuration before running samples to ensure the machine is correctly measuring isotopes. These standards are made to have set isotopic ratios and absolute concentrations, thus machine runs of the standards should always produce these values within error. If they do not, machine parameters may need to be adjusted. Sections B.4.1 and B.4.2 discuss the procedures for running standards on an MC-ICP-MS in SEM and cups configurations and the *Python* programs created for standard data reduction. The *Python* standard program can reduce both SEM and cups standard data, thus combining the functions of multiple Excel spreadsheets.

The *Python* standard program GUI menu allows you the option of choosing which method was used. The user merely needs to mark the checkbox of the method used, and the GUI will provide the necessary input and upload options, which will be discussed in Sections B.4.1 and B.4.2.

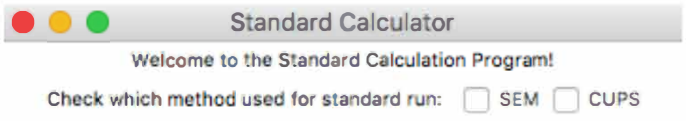

Figure B.10: Option to run SEM or cups standard

The *Python* standard data reduction program consists of 1926 lines of code. At 25 lines per page, this is approximately 77 pages.

B.4.1 Standard on SEM

Current procedure for SEM configuration involves running a dilute 112A standard. Concentrated 112A standard (at 1.6194 pmol/g ^{235}U) is diluted with ICP solution (water, 1% nitric acid, and trace hydrofluoric acid). Approximate ^{234}U background value of wash should be measured, as it used in calculating the δ^{234}U standard value. Abundance sensitivity ($\frac{^{237}U}{^{238}U}$) and ion counter yield ($\frac{^{235}U}{^{235}U}$) of the standard must be measured before standard method run, and should be < 0.7 ppm and 100% ± 0.2% , respectively.

The dilute standard is run under U method parameters, and should be run for 600-1000 cycles to reduce errors. The run data can be exported for data reduction as an EXP file. Current data reduction involves an Excel spreadsheet equipped with a Macros program which filters data and deletes anomalous values. Thus the spreadsheet must either be a .xlsm file or linked to a working .xlsm file, which can make spreadsheet sharing among lab users difficult.

Through SEM standard data reduction, the user should end up with the standard $\frac{^{236}U}{^{233}U}$ ratio, $\frac{^{235}U}{^{233}U}$ ratio, and δ^{234}U value. The $\frac{^{236}U}{^{233}U}$ ratio is the measured ratio value after filtering out anomalous values. To determine the $\frac{^{235}U}{^{233}U}$ ratio, the $\frac{^{236}U}{^{233}U}$ measured ratio must be corrected for ^{238}U tail. The $\frac{^{236}U}{^{238}U}$ ratio is assumed to be $\frac{1}{5}$ the value of the abundance sensitivity, and the $\frac{^{238}U}{^{235}U}$ is a constant (137.83). The correction for tailing at 236 is shown in Equation B.2.

$$\frac{^{236}U}{^{233}U}_{corr} = \frac{^{236}U}{^{233}U}_{meas} * (1 - \frac{(\frac{^{236}U}{^{238}U})_{AS}(\frac{^{235}U}{^{233}U})_{meas}(\frac{^{238}U}{^{235}U})}{(\frac{^{236}U}{^{233}U})_{spike})} \tag{B.2}$$

The measured $\frac{^{235}U}{^{233}U}$ can then be corrected for fractionation using the tail corrected $\frac{^{236}U}{^{233}U}$ value, as discussed in Appendix B.3.

The δ^{234}U value is in parts per mille (‰), and is $[\frac{^{234}U}{^{238}U}_{activity} - 1] * 1000$. The activity ratio of $\frac{^{234}U}{^{238}U}$ is the atomic ratio of $\frac{^{234}U}{^{238}U}$ multiplied by $\frac{\lambda_{234}}{\lambda_{238}}$. Determining the atomic ratio of $\frac{^{234}U}{^{238}U}$ in the standard involves correcting the measured $\frac{^{235}U}{^{233}U}$, $\frac{^{234}U}{^{233}U}$, and $\frac{^{234}U}{^{235}U}$ ratios for tailing and fractionation. First the measured $\frac{^{236}U}{^{233}U}$ ratio is corrected for tailing, as shown in Equation B.2, and the resulting $\frac{^{236}U}{^{233}U}$ is used to correct for isotopic fractionation for each ratio.

After correcting for tail and fractionation, the wash signal of ^{234}U is subtracted from the corrected $\frac{^{234}U}{^{235}U}$ ratio through the following conversion:

$$\frac{^{234}U}{^{235}U}_{corr,signal} = \frac{^{234}U}{^{235}U}_{corr,total} * (1 - \frac{^{234}U_{wash}}{(^{233}U_{meas}) * (\frac{^{235}U}{^{233}U}_{corr,total}) * (\frac{^{234}U}{^{235}U}_{corr,total})}) \tag{B.3}$$

This ratio must then be corrected for spike contribution to ^{234}U and ^{235}U.

$$\frac{^{234}U}{^{235}U}_{corr,final} = \frac{^{234}U}{^{235}U}_{corr,signal} * \frac{(1 - \frac{\frac{^{234}U}{^{235}U}_{spike}}{\frac{^{234}U}{^{235}U}_{corr,total}})}{(1 - \frac{\frac{^{235}U}{^{233}U}_{spike}}{\frac{^{235}U}{^{233}U}_{corr,total}})} \tag{B.4}$$

The resulting $\frac{^{234}U}{^{235}U}_{corr,final}$ ratio is converted into the atomic ratio of $\frac{^{234}U}{^{238}U}$ using the natural ratio of $\frac{^{235}U}{^{238}U}$, and reported as a δ^{234}U value, as discussed above.

Finalized results must be within error of the standard. The 112A standard used in the UMN Isotope Lab has a $\frac{^{235}U}{^{233}U}$ ratio of 14.63 and a δ^{234}U of -38.5 ‰. The $\frac{^{236}U}{^{233}U}$ ratio should be between 1.018 and 1.030.

The calculation of the SEM standard takes greater data reduction capabilities than reagent and chemistry blanks, as the method results must be filtered and significantly corrected. This can currently be done in Excel Macros-enabled spreadsheets, which can be cumbersome for users. Additionally, results of SEM standard data reduction do not need to be saved as a data file. The *Python* SEM standard program reduces user effort and does not produce an export file.

Figure B.11 shows the process for reducing 112A standard data on SEM configuration, with minimal user input. The program again allows the user to alter 112A method in case the solution runs out during the run. *Python* SEM standard data reduction program provides the same results as traditional Excel spreadsheets, as shown in Figure B.12.

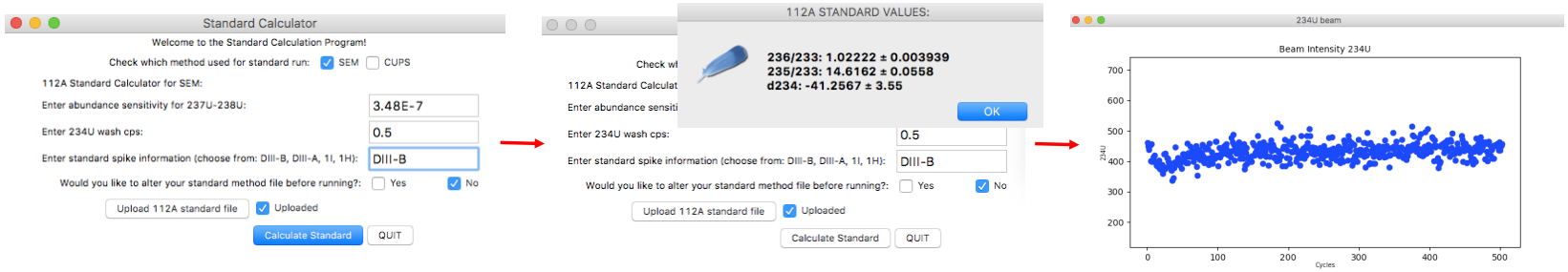

Figure B.11: Example of steps for SEM standard calculation using program

SEM standard results for Excel and Python

Excel 112A SEM standard results	
236/233	1.0222 ± 0.003939
235/233	14.6162 ± 0.0558
d234U	-41.2567 ± 3.55

Python 112A SEM standard results	
236/233	1.02222 ± 0.003939
235/233	14.6162 ± 0.0558
d234U	-41.2567 ± 3.55

Figure B.12: Results of *Python* and Excel SEM standard data reduction

B.4.2 Standard on cups

As cups methods are run at much higher beam intensities than are run on SEM, the effect of tails from higher beams becomes significant. The cups standard method not only verifies correct machine parameters, but also characterizes the ^{238}U tail correction factors. ^{237}U is measured to correct for ^{238}U tail, as any signal present at this mass is due to tailing.

To correct for tail, an unspiked 112A standard is run, and compared against a background wash method to determine the tail/237 correction factor at each isotope. Machine blank corrected tail/237 ratios are calculated for $\frac{233}{237}$, $\frac{233.5}{237}$, $\frac{234.5}{237}$, and $\frac{236}{237}$. Using the 2σ error for measured ratios, maximum and minimum tail ratios are calculated and a logarithmic line of best fit is calculated for each. A logarithmic equation best characterizes the decay of tail intensity per mass unit. Minimum and maximum tail ratios are calculated using both equations at masses ^{233}U, $^{233.5}$U, ^{234}U, $^{234.5}$U, ^{235}U and ^{236}U. The offset between the calculated ratio and measured ratio is determined for ratios $\frac{233}{237}$, $\frac{233.5}{237}$, $\frac{234.5}{237}$, and $\frac{236}{237}$. Based off these values, offset is determined for ratios $\frac{234}{237}$ and $\frac{235}{237}$ and tail/237 ratios are calculated for both. The user is left with finalized $\frac{233}{237}$, $\frac{234}{237}$, $\frac{235}{237}$ and $\frac{236}{237}$ ratios and 2σ errors. 2σ errors for tail are either the measured or calculated 2σ error based off run data, or 5% of tail ratio, depending on which is greater. Unspiked standard tail ratios are not only used in calculating the 112A spiked standard for cups, but are also used to correct for tails in sample method runs.

112A standard is also run for cups configuration to verify machine parameters. However, a concentrated rather than dilute 112A spike solution is run to ensure high beam intensities. A background wash method is first collected, and current lab protocol is in transition from running backgrounds on SEM to running backgrounds on cups. The *Python* standard cups program allows for either. The concentrated 112A data undergoes a series of corrections, beginning with correction for isotope ratio drift that occurs due to a slow response time to changes in signal intensity from the amplifier system (Gourgiotis et al., 2014). Drift offset is calculated element-wise for the ^{234}U signal using the ^{234}U method integration time (1.049 seconds) and amplifier time constant (0.65 sec). The drift offset calculated in B.5 is then used to correct the measured $\frac{234}{233}$ ratio for drift in B.6.

$$^{234}U(i)_{drift} = ^{234}U(i)_{meas} + \left(\frac{^{234}U(i+1)_{meas} - ^{234}U(i-1)_{meas}}{2 * int\_time}\right) * amp\_time\_constant \tag{B.5}$$

$$\frac{234}{233}(i)_{drift\_corr} = ^{234}U(i)_{drift} * \frac{234}{233}(i)_{meas} \tag{B.6}$$

The drift corrected $\frac{234}{233}$ ratio and measured $\frac{235}{233}$, $\frac{236}{233}$, $\frac{238}{233}$ and $\frac{237}{238}$ ratios must then be corrected

for background machine values. This is done element-wise, using the machine blank values in counts per sec for both isotopes (mb), and the mean measured beam intensity in counts per second for the isotope on the bottom of the isotopic ratio (meas). For example, Equation B.7 illustrates what the correction would look like for the $\frac{234}{233}$ ratio.

$$\frac{234}{233}(i)_{mb\_corr} = \left(\frac{\frac{234}{233}(i)_{drift\_corr} - \frac{^{234}U_{mb}}{^{233}U_{meas}}}{1 - \frac{^{233}U_{mb}}{^{233}U_{meas}}}\right) \tag{B.7}$$

The machine blank corrected $\frac{237}{238}$ ratio is the abundance sensitivity and will be reported in data reduction for the standard cups measurement. Additionally, this value is used to convert tail/237 values into tail/238 values, which will be used in tail corrections.

Ratios are corrected for tailing using the tail/238 values calculated from the unspiked standard and spiked standard abundance sensitivity. This is done element-wise for machine blank corrected ratios $\frac{234}{233}$, $\frac{235}{233}$, $\frac{236}{233}$, and $\frac{238}{233}$. This is shown in Equations B.8 and B.9 using the $\frac{234}{233}$ ratio as an example, where first the isotope on the top of the ratio is corrected and then the isotope on the bottom of the ratio is corrected. The machine blank corrected mean $\frac{238}{233}$ ratio is used to convert the tail/238 ratio. As ^{238}U does not need to be corrected, the tail correction for $\frac{238}{233}$ only involves Equation B.9.

$$\frac{234}{233}(i)_{tail\_corr\_top} = \frac{234}{233}(i)_{mb\_corr} - \frac{234}{238}_{tail} * \frac{238}{233}_{mb\_corr\_mean} \tag{B.8}$$

$$\frac{234}{233}(i)_{tail\_corr\_final} = \frac{234}{233}(i)_{tail\_corr\_top} * \left(\frac{1}{1 - \frac{233}{238}_{tail} * \frac{238}{233}_{mb\_corr\_mean}}\right) \tag{B.9}$$

Additionally, tail corrected $\frac{238}{235}$ and $\frac{234}{238}$ ratios are calculated by dividing element-wise the tail corrected $\frac{238}{233}$ and $\frac{235}{233}$, and $\frac{238}{233}$ and $\frac{234}{233}$ ratios, respectively.

Tail corrected ratios $\frac{234}{233}$, $\frac{235}{233}$, $\frac{238}{233}$, $\frac{238}{235}$ and $\frac{234}{238}$ are corrected element-wise for isotopic fractionation using the correction discussed in Appendix B.3. These fractionation corrected ratios are then corrected for spike by subtracting isotope-specific spike ratios.

Desired values at the end of data reduction for cups spiked standard runs includes $\frac{234}{238}$ spike corrected ratio in ppm, the $\frac{237}{238}$ machine blank corrected ratio, the $\frac{236}{233}$ machine blank corrected ratio, the $\frac{238}{235}$ spike corrected ratio, and the $\delta^{234}U$ value. This is calculated using the $\frac{234}{238}$ spike corrected ratio as discussed in Appendix B.4.1. The reported $\frac{234}{238}$ ratio and 2σ absolute error will be used in standardization of U-measurements for samples run on cups, and the remaining values are to ensure proper machine calibration.

Calculation of standards using cups measurements entails extensive data reduction for both unspiked and spiked standards. The *Python* program for reducing cups standard data is packaged with the *Python* SEM standard program. *Python* is particularly useful for element-wise data reduction calculations, as data can be placed into a *Numpy* array, corrected element-wise using loops, and bundled into a new corrected array. The program first calculates the tail/237 values and errors of the unspiked standard, and then imports these values into the spiked standard data correction function.

The *Python* cups standard program results in a GUI window that provides data reduced values. The program provides the option of altering both the unspiked and spiked method runs, in case the solution is spent during run. Additionally, the data for the spiked standard wash can be run on either a cups or SEM configuration. As the program involves element-wise corrections, the data processing time is significantly greater than that for the *Python* SEM standard reduction. Figure B.13 provides an example of a cups standard run on the Neptune Plus MC-ICP-MS at the UMN Isotope Lab.

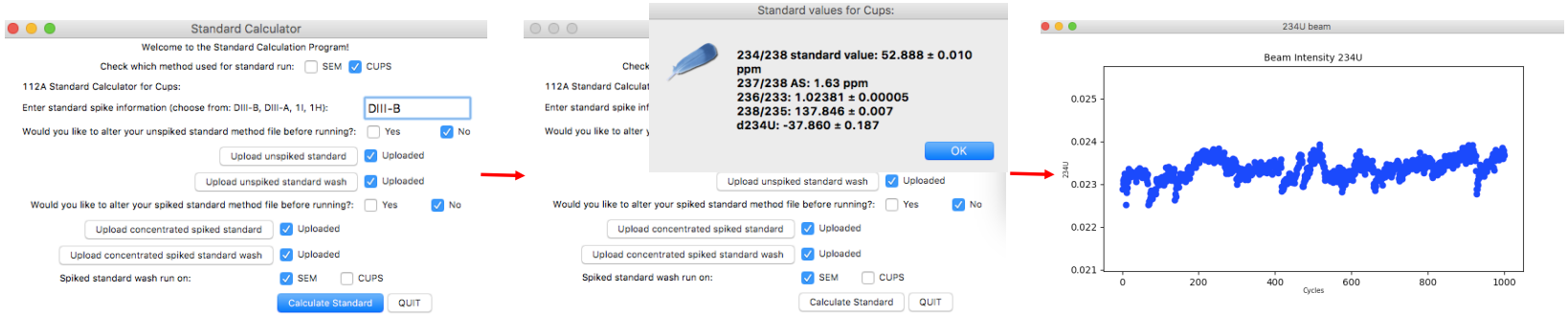

Figure B.13: Example of steps for Cups standard calculation using program

As is shown in Figure B.14, the *Python* program and Excel spreadsheet provide the same results for standards run on cups. Typically a user will run a spiked standard method a number of times throughout the day and recalculate the $\frac{234}{238}$ spike corrected ratio in ppm, to ensure the best normalization for their U samples. Thus the use of an automated data reduction program will greatly reduce user time and effort.

Cups standard results for Excel and Python

Excel Cups standard results	
234/238	52.888 ± 0.010 ppm
237/238	1.63 ppm
236/233	1.02381 ± 0.00005
238/235	137.846 ± 0.007
d234U	-37.860 ± 0.187

Python Cups standard results	
234/238	52.888 ± 0.010 ppm
237/238	1.63 ppm
236/233	1.02381 ± 0.00005
238/235	137.846 ± 0.007
d234U	-37.860 ± 0.187

Figure B.14: Results of *Python* and Excel Cups standard data reduction

B.5 Age Calculation

Determining the ages of carbonate formations through ^{230}Th dating requires users to collect powder along growth layers, run powder through chemical separation, and analyze U and Th isotopic ratios and concentrations on a mass spectrometer. These steps are described in full in Appendix A.2. The data reduction for converting U and Th isotopic ratios and concentrations into usable ages is extensive, and current methods require a series of Macros-enabled Excel spreadsheets. As measurements on Faraday cups become more common in the UMN Isotope Lab, the number of spreadsheets with which lab users will need to be literate will only grow. These spreadsheets require extensive user manipulation, which will be discussed in Appendix B.5.1, B.5.2, and B.5.3, and are prone to errors either by individual users or propagated between users. The conversion of age reduction functions into user-friendly *Python* is an important step in improving the quality and efficiency of the UMN Isotope Lab.

The *Python* Age Calculation program allows for data reduction using SEM or cups configurations. Additionally, the program allows you to manually change a number of preset values. These values include the ^{233}U and ^{229}Th concentrations of spike, the sample and spike weight errors, and the $\frac{230}{232}$ initial ratio and error. The program uses values that work for typical samples, thus reducing user input, but may not be appropriate for all scenarios.

^{233}U and ^{229}Th concentrations in $\frac{pmol}{g}$ have been set for each individual spike, but may change due to evaporative effects. Lab users must monitor their spike and change these values if needed. Sample weight error has been set to 0.1 mg and spike weight error to 0.3 mg, which is appropriate for weighted measurements using current balances. However, errors may be altered dependent on sample and spike weights used, and should be larger if spikes are measured volumetrically. Initial $\frac{230}{232}$ ratios are assumed to be bulk earth value (4.4E-6) with a 50% error, but can be adjusted if more accurate initial ratios are known.

Programs have been slightly altered for speleothems and corals. Speleothem spikes always have set isotopic ratios, thus any evaporative effects will result in constant changes in ^{233}U and ^{229}Th concentrations. To reduce user error, if the ^{233}U concentration preset value is manually changed, the ^{229}Th concentration is automatically calculated based off the spike used. However, for corals it may be necessary to use different spike concentrations. Thus ^{233}U and ^{229}Th concentrations can be entered separately. Speleothem and coral age reduction programs are otherwise identical.

Figures B.15a and B.15b show the options for changing preset values for speleothems and corals, respectively. If the user chooses to change preset values, a secondary GUI window

will appear. The user can input whichever parameters they would like change. By clicking "Submit" those parameters will be updated and the user will be returned to the primary GUI window and be prompted for U-method.

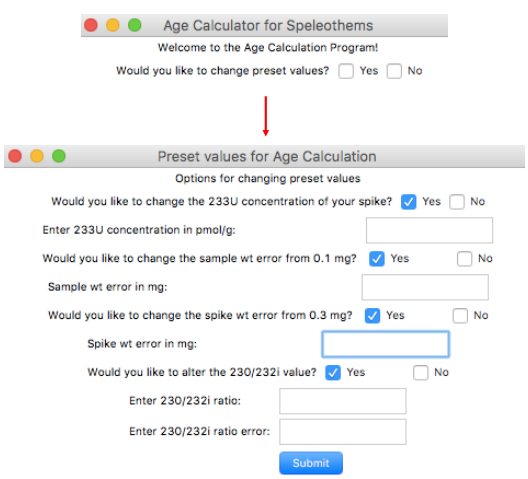

(a) Preset options for speleothems

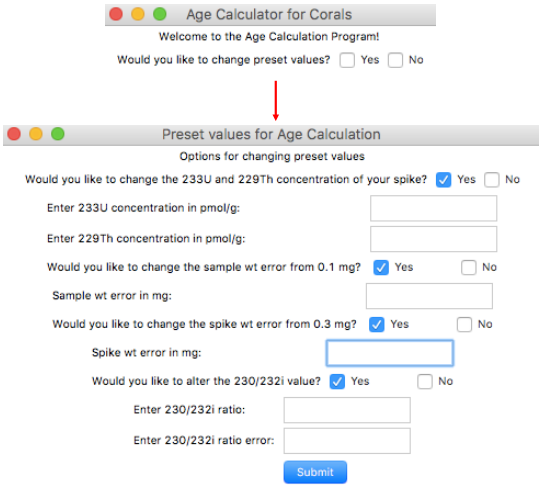

(b) Preset options for corals

Figure B.15: Options for changing preset values for speleothem and coral age data reduction

If the user does not wish to change preset values, clicking the "No" checkbox will take them directly to the U-method prompt. The user has a number of data reduction options. If U is run on SEM, it is assumed that Th is as well, as the ^{230}Th beam will not be high enough to run on cups. If U is run on cups, the ^{230}Th beam may or may not be high enough to run on cups as well. Thus, the Th may be run on SEM or on cups. The *Python* Age Calculation program provides all the above options, combining the functions of multiple Excel Macros-enabled spreadsheets. Examples of the GUI windows of these options are shown in Figure B.16, and the data reduction involved in all three are discussed in the following sections.

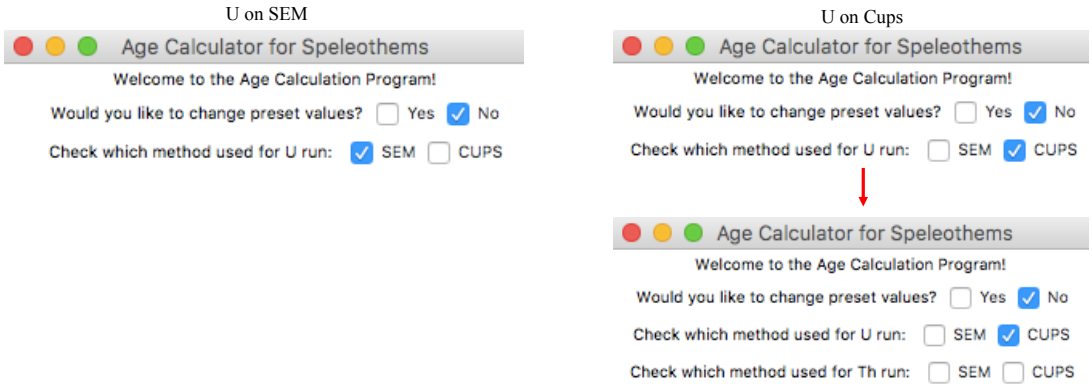

Figure B.16: Method options for U and Th for *Python* age data reduction

All method options require a number of input files. First, a chemistry blank Excel file must be uploaded in order to correct for chemistry blanks. The format of this file must match that of the Excel spreadsheet generated through the *Python* Chemistry Blank program. Additionally, an Excel spreadsheet must be uploaded into which the reduced data will be entered. The program will prompt the user for the row in which the data should be entered, thus the user can continue to compile data within the same spreadsheet, reducing files generated. An example of the Excel formats are shown in Figures B.17 and B.18 below, and a blank age file and default chemistry blank file are available for users on the GitHub repository.

	A	B	C	D	E	F	G	H	I
1		**1_Chemblank**	**229Th**	**230Th**	**232Th**	**233U**	**234U**	**235U**	**238U**
2	**1_fileinfo**	B28							
3	**2_yields**		66.21122			79.9601			
4	**i_chemblank**			22.92755	186.1442		316.2409	41.36938	2692.519
5	**4_2s err**			26.57541	15.25279		124.0121	12.87434	219.3719
6	**5_units**		%	ag	fg	%	ag	fg	fg
7	**6_param**	Run info							
8	**7_param**		Spike used	Spike wt	Th wt	U.R.	U wt	I.E.	
9	**8_param**		1I	0.00207	0.5272	0.56	0.5037	0.89	
10	**9_param**			g	g	mg/sec	g	%	

Figure B.17: Example of chemistry blank Excel format for upload

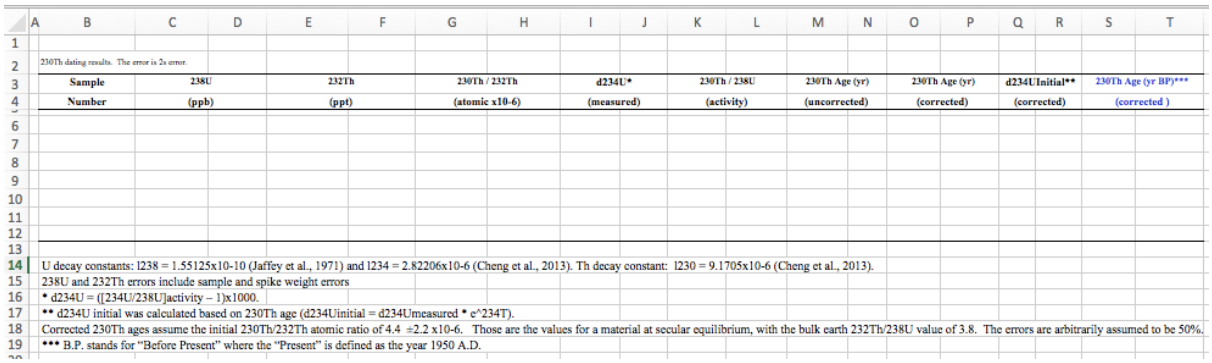

Sample Number	238U (ppb)	232Th (ppt)	230Th / 232Th (atomic x10-6)	d234U* (measured)	230Th / 238U (activity)	230Th Age (yr) (uncorrected)	230Th Age (yr) (corrected)	d234UInitial** (corrected)	230Th Age (yr BP)*** (corrected)

230Th dating results. The error is 2σ error.

U decay constants: l238 = 1.55125x10-10 (Jaffey et al., 1971) and l234 = 2.82206x10-6 (Cheng et al., 2013). Th decay constant: l230 = 9.1705x10-6 (Cheng et al., 2013).
238U and 232Th errors include sample and spike weight errors
* d234U = ([234U/238U]activity – 1)x1000.
** d234U initial was calculated based on 230Th age (d234Uinitial = d234Umeasured * e^234T).
Corrected 230Th ages assume the initial 230Th/232Th atomic ratio of 4.4 ±2.2 x10-6. Those are the values for a material at secular equilibrium, with the bulk earth 232Th/238U value of 3.8. The errors are arbitrarily assumed to be 50%.
*** B.P. stands for "Before Present" where the "Present" is defined as the year 1950 A.D.

Figure B.18: Example of age spreadsheet Excel format for upload

For all collection methods, the data is inserted into the uploaded age file. All errors are 2σ. The data reduction for ^{230}Th age calculation results in the following values:

- ^{238}U in parts per billion (ppb) and error. Error includes the effect of spike and sample weight errors.
- ^{232}Th in parts per trillion (ppt) and error. Error includes the effect of spike and sample weight errors.
- $\frac{^{230}Th}{^{232}Th}$ atomic ratio in parts per million (ppm) and error.
- Measured δ^{234}U after corrections and error.
- $\frac{^{230}Th}{^{238}U}$ activity ratio and error.
- ^{230}Th age and error, before correction for initial ^{230}Th.
- ^{230}Th age and error, after correction for initial ^{230}Th.
- Initial δ^{234}U and error using corrected ^{230}Th age.
- Final ^{230}Th age and error in years before present (BP), where present is defined as 1950.

The *Python* Age Calculation program significantly reduces time needed for data reduction and improves user data management. Additionally, it consolidates age data reduction functions for all measurement methods at the UMN Isotope Lab. During the process of creating this program, data reduction calculations for all methods were reviewed and revised, providing the most accurate program for users and ensuring further improvements are centrally distributed. The *Python* Age Calculation program entails 5281 lines of code. At 25 lines per page, this approximately 211 pages.

B.5.1 Age Calculation for U and Th on SEM

Current data reduction for U and Th on SEM consists of a Macros-enabled Excel spreadsheet, modified for spike used, and requires data to be copied and pasted into separate sheets and reduced. First, the U method data is pasted into a U data reduction sheet. The method data is filtered by the Macros U-program to eliminate anomalous values. The U data is then reduced to provide the $\frac{^{235}U}{^{233}U}$ and $\frac{^{234}U}{^{235}U}$ ratios and 2σ errors corrected for tail and isotopic fractionation, as discussed in Appendix B.4.1. Additionally, the ^{233}U filtered counts, unfiltered counts, and mean intensity (in cps) are also generated. These 7 values are copied and pasted into the age data reduction sheet. The tail corrected $\frac{^{236}U}{^{233}U}$ and 2σ error are copied and pasted into the Th data reduction sheet, as they will be used to correct for isotopic fractionation in the Th isotopes. Additionally, the $\frac{^{237}U}{^{238}U}$ abundance sensitivity must be manually entered into both the U and Th data reduction sheets.

For Th data reduction, the Th method data is pasted into the sheet and filtered by the Macros Th-program to eliminate anomalous values. The mean intensity (in cps) of the $\frac{^{230}Th}{^{229}Th}$, $\frac{^{232}Th}{^{229}Th}$ and $\frac{^{230}Th}{^{232}Th}$ ratios are determined. The $\frac{^{230}Th}{^{229}Th}$ and $\frac{^{232}Th}{^{229}Th}$ ratios are then corrected for ^{232}Th and ^{229}Th tails. The $\frac{^{230}Th}{^{229}Th}$ ratio must be corrected for both tail effects, whereas the $\frac{^{232}Th}{^{229}Th}$ must only be corrected for the effect of ^{232}Th at ^{229}Th. The abundance sensitivity ratios for $\frac{^{230}Th}{^{232}Th}$ and $\frac{^{229}Th}{^{232}Th}$ are $\frac{1}{5}$ and $\frac{1}{15}$ of the $\frac{^{237}U}{^{238}U}$ ratio. The tail correction calculations are shown in Equations B.10 and B.11.

$$\frac{^{230}Th}{^{229}Th}_{tailcorr} = \frac{^{230}Th}{^{229}Th}_{meas} * \left(1 - \frac{\frac{^{230}Th}{^{232}Th}_{AS}}{\frac{^{230}Th}{^{232}Th}_{meas}}\right) * \left(1 - \frac{^{230}Th}{^{229}Th}_{AS}\right) \tag{B.10}$$

$$\frac{^{232}Th}{^{229}Th}_{tailcorr} = \frac{^{232}Th}{^{229}Th}_{meas} * \left(1 - \frac{1}{1 - \frac{\frac{^{229}Th}{^{232}Th}_{AS}}{\frac{^{229}Th}{^{232}Th}_{meas}}}\right) \tag{B.11}$$

The resulting tail corrected $\frac{^{230}Th}{^{229}Th}$ and $\frac{^{232}Th}{^{229}Th}$ is then corrected for isotopic fractionation using the tail corrected $\frac{^{236}U}{^{233}U}$ ratio imported from the U data reduction sheet. The Th data reduction sheet provides the $\frac{^{230}Th}{^{229}Th}$ and $\frac{^{232}Th}{^{229}Th}$ ratios and 2σ errors corrected for tail and isotopic fractionation, as well as the mean unfiltered ^{229}Th signal (in cps) and unfiltered counts. The 6 values are copied and pasted into the age data reduction sheet.

In the age data reduction sheet, the user must input the reduced values from the U and Th data reduction sheets, as well as the chemistry blank ^{238}U, ^{232}Th and ^{230}Th values and errors, the sample weight, the spike weight, the spike ^{233}U and ^{229}Th concentrations, and the machine background mean values for ^{233}U, ^{234}U, ^{235}U in cps and ^{230}Th in cpm.

Absolute concentrations of ^{238}U and ^{232}Th are determined using the $\frac{^{235}U}{^{233}U}$ and $\frac{^{232}Th}{^{229}Th}$ ratios corrected for tailing and fractionation, respectively. The $\frac{^{235}U}{^{233}U}$ ratio is corrected for wash using the ^{233}U unfiltered mean and the ^{235}U wash value, then converted into ^{238}U ppb after correcting for spike and chemistry blank values. The $\frac{^{232}Th}{^{229}Th}$ ratio is also corrected for spike and chemistry blank values, then converted into ^{232}Th ppt. Errors reported for ^{238}U and ^{232}Th concentrations include the effects of spike and sample weight errors. These weight errors are not included in further error propagation.

The absolute concentration of ^{230}Th in ppt is also calculated, though not reported. The tail and fractionation corrected $\frac{^{230}Th}{^{229}Th}$ ratio is further corrected for spike, ^{230}Th wash, and chemistry blank values. The calculated ^{230}Th concentration is divided by the calculated ^{232}Th concentration, to provide the $\frac{^{230}Th}{^{232}Th}$ atomic ratio, and reported in units of ppm. The calculated ^{230}Th concentration is also divided by the calculated ^{238}U concentration, to provide the $\frac{^{230}Th}{^{238}U}$ atomic ratio, which is converted into the activity ratio using the decay constants of ^{230}Th and ^{238}U.

The measured δ^{234}U value is also determined. The tail and fractionation corrected $\frac{^{235}U}{^{233}U}$ ratio is converted into a $\frac{^{234}U}{^{235}U}$ ratio and corrected for spike. The ratio is then converted into a $\frac{^{234}U}{^{238}U}$ ratio using the natural ratio $\frac{^{238}U}{^{235}U}$. The ratio is reported in δ notation using the calculation discussed in Appendix B.4.1.

The uncorrected age is first determined using the age equation discussed in Chapter 1.2.2, and does not take into account the effect of initial ^{230}Th. This equation is set to zero, as shown in Equation B.12, and iteratively solved for time (t). In the Excel data reduction, this entails the use of a Macros program, whereby the program runs through 150 iterations with a maximum change of 1E-11 to determine the most accurate value for variable t. This program attempts to find a variable t where the age equation most closely reaches zero, but due to the program format is capable of settling on values that are near to but not actually zero, thus increasing the age error. In the *Python* data reduction, the *Scipy* submodule function *fsolve* is used, which allows infinite iterations until a zero value is reached. This ensures lower age errors for the *Python* program, and improves data reduction capabilities.

$$0 = (\frac{^{230}Th}{^{238}U})_A - (1 - e^{-\lambda_{230}t} + (\frac{\delta^{234}U_m}{100})(\frac{\lambda_{230}}{\lambda_{230} - \lambda_{234}})(1 - e^{(\lambda_{234} - \lambda_{230})t})) \qquad \text{(B.12)}$$

The corrected age is then determined by including the effects of initial ^{230}Th in the age equation. This correction is set to use the initial $\frac{^{230}Th}{^{232}Th}$ ratio of the bulk earth (4.4E-6), but can be changed by the user. This ratio is used to correct the $\frac{^{230}Th}{^{238}U}$ activity ratio as shown in

Equation B.13, and is again solved iteratively to find the corrected age (t) using Equation B.12.

$$(\frac{^{230}Th}{^{238}U})_A = \frac{^{230}Th\frac{pmol}{g} - (\frac{^{230}Th}{^{232}Th_i}e^{-\lambda_{230}t} *^{232} Th\frac{pmol}{g})}{^{238}U\frac{pmol}{g}} * \frac{\lambda_{230}}{\lambda_{238}} \tag{B.13}$$

Age errors are determined for both uncorrected and corrected ages by iteratively solving for age using the minimum and maximum values for $(\frac{^{230}Th}{^{238}U})_A$ and $\delta^{234}U_m$ in each equation and combining quadratically.

Finally, the initial $\delta^{234}U$ is calculated using the corrected age and decay constant for ^{234}U. Final age is reported in years BP.

The *Python* Age Calculation program includes the data reduction explained above, and significantly reduces user time, expertise, and data management efforts. All calculations are detailed in the source code, making it easier for the user to follow the data reduction process if desired. Figure B.19 illustrates the steps for the *Python* age calculation data reduction for SEM. The user must input the spike used, abundance sensitivity for U run, sample weight, spike weight, sample ID, and row number for age spreadsheet. The program also includes the option of using a different abundance sensitivity for the Th run, in case the U and Th solutions were run on different days. The user must upload their wash and method files for Th and U, with the option of altering method files for Th and U in case solution runs out. Additionally, the chemistry blank Excel file and age spreadsheet Excel file must be uploaded.

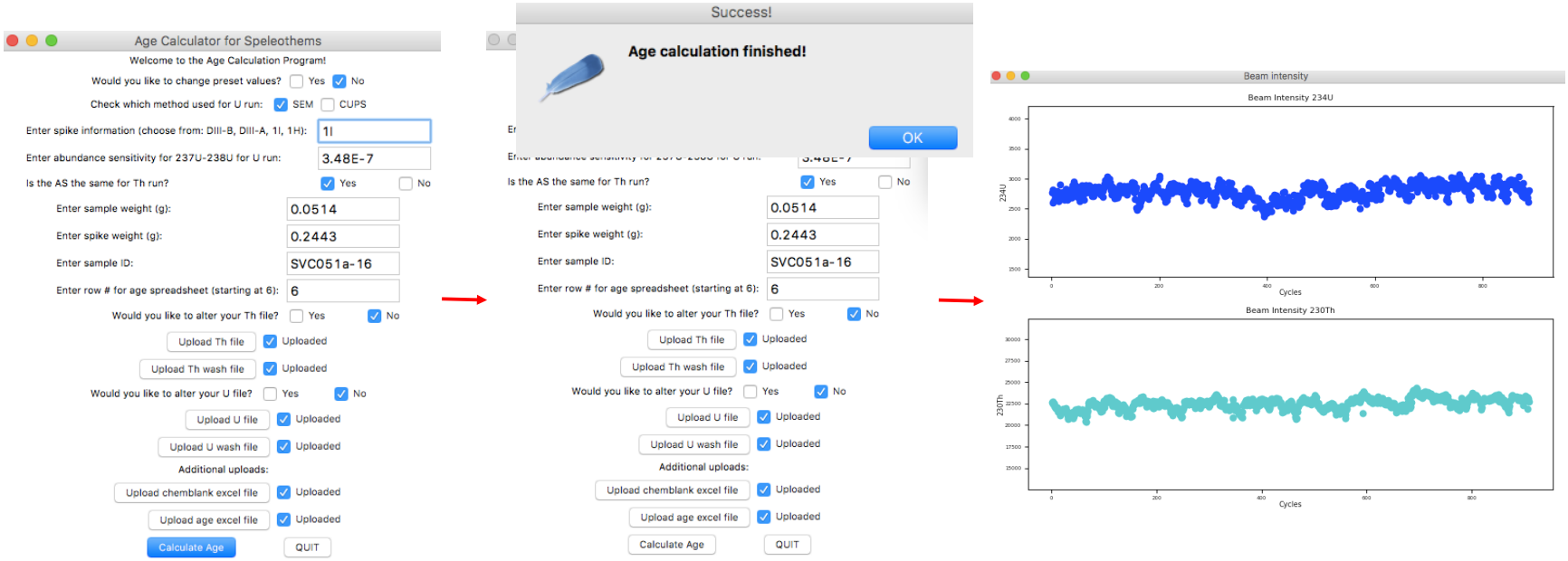

Figure B.19: Example of steps for SEM age calculation using program

As is shown in Figure B.20, the Excel spreadsheet and *Python* program provide the same output data for SEM measurements.

^{230}Th dating results. The error is 2s error.

Sample Number	^{238}U (ppb)	^{232}Th (ppt)	^{230}Th / ^{232}Th (atomic x10^{-6})	d^{234}U* (measured)	^{230}Th / ^{238}U (activity)	^{230}Th Age (yr) (uncorrected)	^{230}Th Age (yr) (corrected)	d^{234}U$_{Initial}$** (corrected)	^{230}Th Age (yr BP)*** (corrected)
SEM data reduction using *Python*									
SVC051a-16	1122.5 ±3.0	4905 ±28	3553 ±19	476.9 ±2.0	0.9415 ±0.0015	102949 ±353	**102871 ±357**	638 ±3	**102804 ±357**
SEM data reduction using Excel									
SVC051a-16	1122.5 ±3.0	4905 ±28	3553 ±19	476.9 ±2.0	0.9415 ±0.0015	102949 ±353	**102871 ±357**	638 ±3	**102804 ±357**

U decay constants: l238 = 1.55125x10-10 (Jaffey et al., 1971) and l234 = 2.82206x10-6 (Cheng et al., 2013). Th decay constant: l230 = 9.1705x10-6 (Cheng et al., 2013).
238U and 232Th errors include sample and spike weight errors
* d234U = ([234U/238U]activity – 1)x1000.
** d234U initial was calculated based on 230Th age (d234Uinitial = d234Umeasured * e^234T).
Corrected 230Th ages assume the initial 230Th/232Th atomic ratio of 4.4 ±2.2 x10-6. Those are the values for a material at secular equilibrium, with the bulk earth 232Th/238U value of 3.8. The errors are arbitrarily assumed to be 50%.
*** B.P. stands for "Before Present" where the "Present" is defined as the year 1950 A.D.

Figure B.20: Results of SEM data reduction using *Python* and Excel

B.5.2 Age Calculation for U on Cups and Th on SEM

Running high intensity beams on Faraday cups results in shorter run times and improved counting, and new methods with 10^{13} Ω resistors has allowed for samples with adequate U and Th concentrations to be run using this method. However, achieving high beam intensities for ^{234}U and ^{230}Th requires large sample sizes, which may not be feasible depending on the sample. As ^{234}U concentration is typically higher than ^{230}Th, there may be scenarios where it is possible to run U on cups but not Th, and Th must be run on a SEM configuration. Current data reduction for this method requires combining the functions of multiple Macros-enabled spreadsheets.

Before U and Th data reduction, the effect of the ^{238}U tail must be accounted for. This is done by analyzing an unspiked standard run, and determining the effect of the tail at each isotope. This is done for the age reduction the same way that it is done for the cups standard reduction, as described in Appendix B.4.2. The analysis results in the $\frac{233}{237}$, $\frac{234}{237}$, $\frac{235}{237}$ and $\frac{236}{237}$ ratios and 2σ errors.

For U cups data reduction, the corrected ^{238}U concentration (in ppb) and δ^{234}U values must be calculated, along with their 2σ errors. U method data is corrected for drift, machine backgrounds, tail, and fractionation in the same way as the concentrated spiked standard, as described in Appendix B.4.2. The tail corrected $\frac{^{236}U}{^{233}U}$ and error will be used in the Th SEM data reduction. The drift, machine background, tail, and fractionation corrected $\frac{^{234}U}{^{233}U}$, $\frac{^{235}U}{^{233}U}$, $\frac{^{238}U}{^{233}U}$, $\frac{^{238}U}{^{235}U}$ and $\frac{^{234}U}{^{238}U}$ ratios are further corrected for spike and chemistry blanks. To correct for spike, the spike specific ratios are merely subtracted from the corrected ratio mean. The correction is no longer element-wise.

To correct for chemistry blanks, chemistry blank ratios must be calculated. The chemistry blank weights of ^{234}U, ^{235}U and ^{238}U are converted into ratios over ^{233}U using the isotopic mass, spike weight, and ^{233}U spike concentration. These are subtracted from the spike

corrected $\frac{^{234}U}{^{233}U}$, $\frac{^{235}U}{^{233}U}$, $\frac{^{238}U}{^{233}U}$ ratios. For the $\frac{^{238}U}{^{235}U}$ and $\frac{^{234}U}{^{238}U}$ ratios, the chemistry blank ratios are converted into the proper ratio using the spike corrected values.

The ^{238}U concentration in ppb is calculated using the $\frac{^{238}U}{^{233}U}$ chemistry blank corrected ratio, spike weight, sample weight, ^{233}U spike concentration and isotopic mass. The 2σ errors with and without sample and spike weight errors are calculated.

The chemistry blank corrected $\frac{^{234}U}{^{238}U}$ ratio is then normalized to the 112A standard. This standard has a $\frac{^{234}U}{^{238}U}$ ratio of 137.832 ± 0.015 (Cheng et al., 2013). The difference between the spiked standard $\frac{^{234}U}{^{238}U}$ ratio, which should be monitored throughout the run time, and the actual 112A $\frac{^{234}U}{^{238}U}$ ratio is subtracted from the chemistry blank corrected $\frac{^{234}U}{^{238}U}$ ratio. The resulting normalized $\frac{^{234}U}{^{238}U}$ ratio is converted to a δ^{234}U value as is the 2σ error after propagation.

The Th data reduction is the same as described in Appendix B.5.1, and results in tail and fractionation corrected $\frac{^{230}Th}{^{229}Th}$ and $\frac{^{232}Th}{^{229}Th}$ ratios and 2σ errors. Additionally, the ^{229}Th unfiltered mean in cps is produced. To first correct for machine background, blank/signal ratios are determined for $\frac{^{229}Th}{^{229}Th}$, $\frac{^{230}Th}{^{229}Th}$, and $\frac{^{232}Th}{^{229}Th}$ by dividing the machine blank ^{229}Th, ^{230}Th, and ^{232}Th beam intensities by the ^{229}Th unfiltered mean. To correct for the blank, Equation B.14 is used, with the $\frac{^{230}Th}{^{229}Th}$ ratio used as an example.

$$\frac{^{230}Th}{^{229}Th}_{mb,corr} = \frac{\frac{^{230}Th}{^{229}Th}_{tail/frac,corr} - \frac{^{230}Th}{^{229}Th}_{mb}}{1 - \frac{^{229}Th}{^{229}Th}_{mb}} \tag{B.14}$$

The machine blank corrected $\frac{^{230}Th}{^{229}Th}$ and $\frac{^{232}Th}{^{229}Th}$ ratios are then corrected for spike by subtracting spike specific isotopic ratios. Chemistry blank ratios of $\frac{^{230}Th}{^{229}Th}$ and $\frac{^{232}Th}{^{229}Th}$ are calculated using the isotopic blank weight, isotopic mass, spike weight, and ^{229}Th spike concentration. These ratios are then subtracted from the $\frac{^{230}Th}{^{229}Th}$ and $\frac{^{232}Th}{^{229}Th}$ spike corrected ratios. The two ratios are also combined to provide the fully corrected $\frac{^{230}Th}{^{232}Th}$ ratio. The corrected $\frac{^{230}Th}{^{229}Th}$ and $\frac{^{232}Th}{^{229}Th}$ ratios are used to calculate the absolute concentrations of ^{230}Th and ^{232}Th in ppt, using the sample weight, spike weight, ^{229}Th spike concentration, and isotopic mass. The relative 2σ errors are also calculated, with two errors for ^{232}Th, both using and not using the contribution of sample and spike weight errors.

Final values from U and Th data reduction are ^{238}U (in ppb and $\frac{pmol}{g}$), ^{232}Th (in ppt and $\frac{pmol}{g}$), ^{230}Th (in ppt and $\frac{pmol}{g}$), δ^{234}U (in δ units), and the $\frac{^{230}Th}{^{232}Th}$ atomic ratio. From the $\frac{pmol}{g}$ values for ^{238}U, ^{232}Th, ^{230}Th, the atomic ratios for $\frac{^{232}Th}{^{238}U}$, $\frac{^{230}Th}{^{238}U}$, and $\frac{^{230}Th}{^{234}U}$ are calculated, and further converted into activity ratios using the decay constants for ^{230}Th, ^{232}Th, and ^{238}U.

The age calculation is the same as described in the previous section (B.5.1). First the $\frac{^{232}Th}{^{238}U}$ activity ratio is used to iteratively solve for time using the age equation. Then the activity ratio is corrected for the effects of initial ^{230}Th and again time is solved iteratively, producing the corrected age.

Current Excel data reduction methods for U on cups and Th on SEM involve six active sheets in a Macros-enabled spreadsheet. This requires significant transfer of data between sheets and knowledge of the reduction methods. The *Python* program significantly reduces user input. The program requires the user to input spike used, abundance sensitivity for Th run, sample weight, spike weight, sample ID, and row number for age spreadsheet. In addition, the user must enter the $\frac{234}{238}$ ratio and error in ppm of the spiked standard run. This value is produced through the *Python* Standard Calculation program. If multiple spiked standards are run throughout the day, the user should use the average. The user must upload the wash and method file for unspiked standard, Th, and U. All three method files have the option to alter them in case solution runs out. This is particularly useful in cups measurements, as often minimal solution is used and sampling time should be as long as possible. As in the SEM data reduction, a chemistry blank Excel file and age spreadsheet Excel file must be uploaded. Figure B.21 illustrates the steps for the *Python* age calculation data reduction for U on cups and Th on SEM.

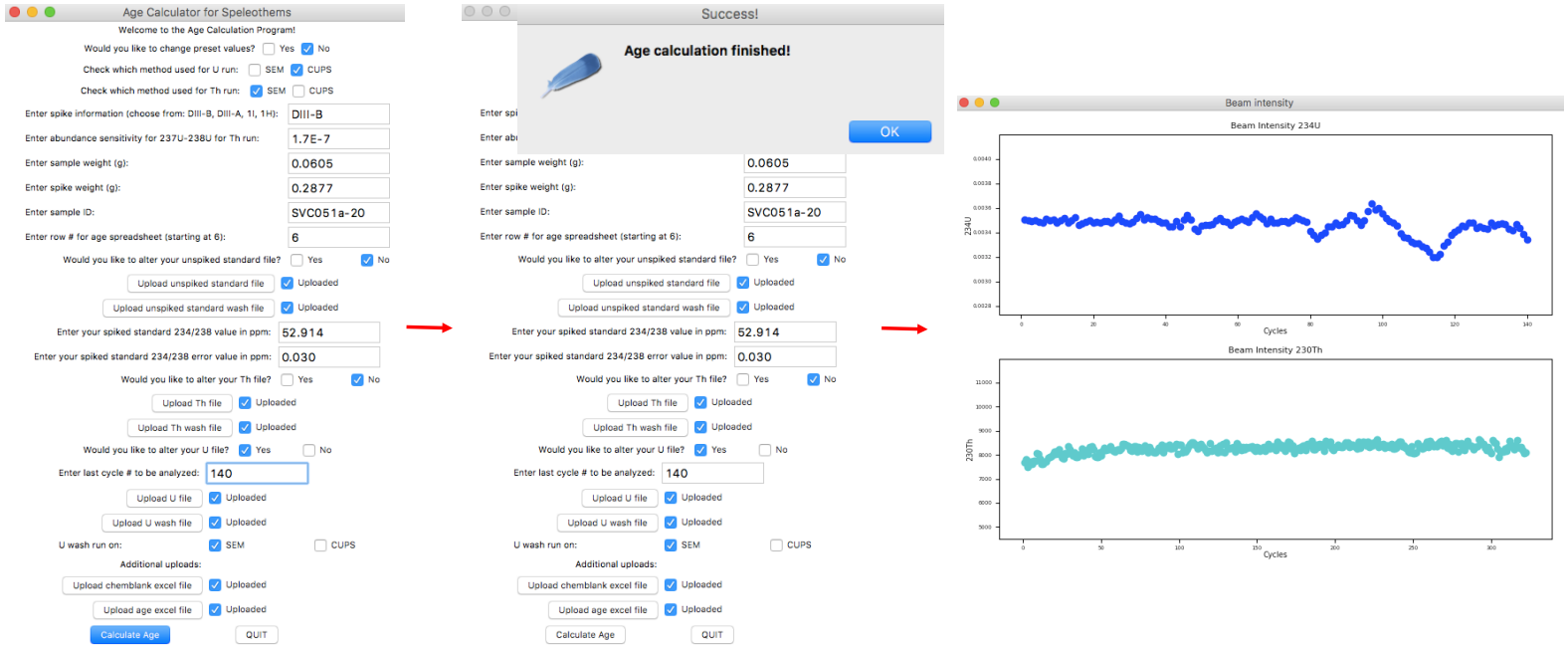

Figure B.21: Example of steps for U on cups and Th on SEM age calculation using program

As is shown in Figure B.22, the *Python* program to reduce data for U on cups and Th on SEM provides the same results as the traditional Excel spreadsheet.

^{230}Th dating results. The error is 2s error.

Sample Number	^{238}U (ppb)	^{232}Th (ppt)	^{230}Th / ^{232}Th (atomic x10^{-6})	d^{234}U* (measured)	^{230}Th / ^{238}U (activity)	^{230}Th Age (yr) (uncorrected)	^{230}Th Age (yr) (corrected)	d^{234}U$_{initial}$** (corrected)	^{230}Th Age (yr BP)*** (corrected)
U on cups and Th on SEM data reduction using *Python*									
SVC051a-20	1128.6 ±2.3	4930 ±27	3582 ±18	633.9 ±1.7	0.9490 ±0.0013	88444 ±227	**88374 ±232**	813 ±2	**88307 ±232**
U on cups and Th on SEM data reduction using Excel									
SVC051a-20	1128.6 ±2.3	4930 ±27	3582 ±18	633.9 ±1.7	0.9490 ±0.0013	88444 ±227	**88374 ±232**	813 ±2	**88307 ±232**

U decay constants: l238 = 1.55125x10-10 (Jaffey et al., 1971) and l234 = 2.82206x10-6 (Cheng et al., 2013). Th decay constant: l230 = 9.1705x10-6 (Cheng et al., 2013).

238U and 232Th errors include sample and spike weight errors

* d234U = ([234U/238U]activity – 1)x1000.

** d234U initial was calculated based on 230Th age (d234Uinitial = d234Umeasured * e^234T).

Corrected 230Th ages assume the initial 230Th/232Th atomic ratio of 4.4 ±2.2 x10-6. Those are the values for a material at secular equilibrium, with the bulk earth 232Th/238U value of 3.8. The errors are arbitrarily assumed to be 50%.

*** B.P. stands for "Before Present" where the "Present" is defined as the year 1950 A.D.

Figure B.22: Results of data reduction for U on cups and Th on SEM using *Python* and Excel

B.5.3 Age Calculation for U and Th on Cups

If the ^{230}Th beam is high enough, it is also possible to run both U and Th on Faraday cups. This method can considerably reduce both user time and age errors. Current data reduction for both Th and U on cups requires a Macros-enabled spreadsheet.

To determine ^{230}Th ages for cups measurements, the unspiked standard, U wash and U method results are reduced using the same procedure as the one outlined in the previous section (Appendix B.5.2). This produces the corrected ^{238}U concentration and error (in ppb) and the corrected δ^{234}U value and error (in δ units). All errors are 2σ, and the ^{238}U errors with and without spike weight errors are calculated. Additionally, the tail corrected $\frac{^{236}U}{^{233}U}$ and the machine blank corrected $\frac{^{237}U}{^{238}U}$ ratios and their respective errors must be determined, as they will be used in the Th data reduction for cups.

Th reduction on cups involves the same corrections as the U method. Drift offset is calculated element-wise for ^{230}Th signal using the ^{230}Th method integration time (1.049 seconds) and amplifier time constant (0.65 sec). The correction is the same as that described in Appendix B.4.2, using the ^{230}Th measured beam rather than the ^{234}U measured beam. The measured $\frac{^{230}Th}{^{229}Th}$ and $\frac{^{230}Th}{^{232}Th}$ ratios are corrected element-wise for drift by dividing the drift offset by the measured ratio.

The drift corrected $\frac{^{230}Th}{^{229}Th}$ and $\frac{^{230}Th}{^{232}Th}$ ratios and the measured $\frac{^{232}Th}{^{229}Th}$ ratio are corrected for machine background values using the calculation described in Appendix B.4.2. However, ratios must be corrected for tailing effects of both ^{232}Th and ^{229}Th. To correct for tailing effects, the tail ratios for tail/229 ($\frac{^{230}Th}{^{229}Th}$ and $\frac{^{232}Th}{^{229}Th}$) and tail/232 ($\frac{^{230}Th}{^{232}Th}$ and $\frac{^{229}Th}{^{232}Th}$) are determined using the $\frac{^{237}U}{^{238}U}$ abundance sensitivity. These tail ratios correct for tailing effects of both ^{232}Th and ^{229}Th element-wise for all three isotope ratios, using slightly different

equations, as shown in B.15, B.16, and B.17. The mean machine blank corrected $\frac{^{232}Th}{^{229}Th}$ ratio is used in all three to correct for the effect of tailing of ^{232}Th and ^{229}Th on each other.

$$\frac{^{230}Th}{^{229}Th}(i)_{tail,corr} = \frac{\frac{^{230}Th}{^{229}Th}(i)_{mb,corr} - \frac{^{230}Th}{^{229}Th\,tail} - (\frac{^{230}Th}{^{232}Th\,tail} * \frac{^{232}Th}{^{229}Th\,mb,corr})}{1 - (\frac{^{229}Th}{^{232}Th\,tail} * \frac{^{232}Th}{^{229}Th\,mb,corr})} \tag{B.15}$$

$$\frac{^{232}Th}{^{229}Th}(i)_{tail,corr} = \frac{\frac{^{232}Th}{^{229}Th}(i)_{mb,corr} - \frac{^{232}Th}{^{229}Th\,tail}}{1 - (\frac{^{229}Th}{^{232}Th\,tail} * \frac{^{232}Th}{^{229}Th\,mb,corr})} \tag{B.16}$$

$$\frac{^{230}Th}{^{232}Th}(i)_{tail,corr} = \frac{\frac{^{230}Th}{^{232}Th}(i)_{mb,corr} - (\frac{^{230}Th}{^{229}Th\,tail} * \frac{^{232}Th}{^{229}Th\,mb,corr})}{1 - \frac{^{230}Th}{^{232}Th\,tail}} \tag{B.17}$$

All three ratios undergo element-wise fractionation correction, using the tail corrected $\frac{^{236}U}{^{233}U}$ ratio, and the mean fractionation corrected ratios are further corrected for spike and chemistry blanks using the method described in the previous section (Appendix B.5.2). The fully corrected $\frac{^{230}Th}{^{229}Th}$, $\frac{^{232}Th}{^{229}Th}$, and $\frac{^{230}Th}{^{232}Th}$ ratios are used to determine absolute isotopic concentrations and the $\frac{^{230}Th}{^{238}U}$ activity ratio. This ratio is then used to calculate the uncorrected and corrected ^{230}Th ages, as previously described. All reduced data is exported into the provided Excel age spreadsheet.

All data reduction methods for cups measurements have been included in the *Python* Age Calculation program. Current procedure involves five active sheets on a Macros-enabled spreadsheet, with considerable data transfer between sheets. The *Python* significantly simplifies cups data reduction, with minimal user input but still allowing for data improvement. The program requires the user to input spike used, sample weight, sample ID, and row number for age spreadsheet, as well as the spiked standard $\frac{^{234}U}{^{238}U}$ ratio and error in ppm. The program requires the wash and method files for the unspiked standard, Th, and U runs to be uploaded. Options to alter any or all of the three method files are offered. Additionally, both Th and U wash files can be run on either a cups or SEM configuration. The user must again upload an Excel chemistry blank file and age spreadsheet file. Figure B.23 shows the steps of the *Python* Age Calculation program for cups. For this sample, the U method file was manually altered to eliminate peak instability, and saved and imported as a .xlsx file.

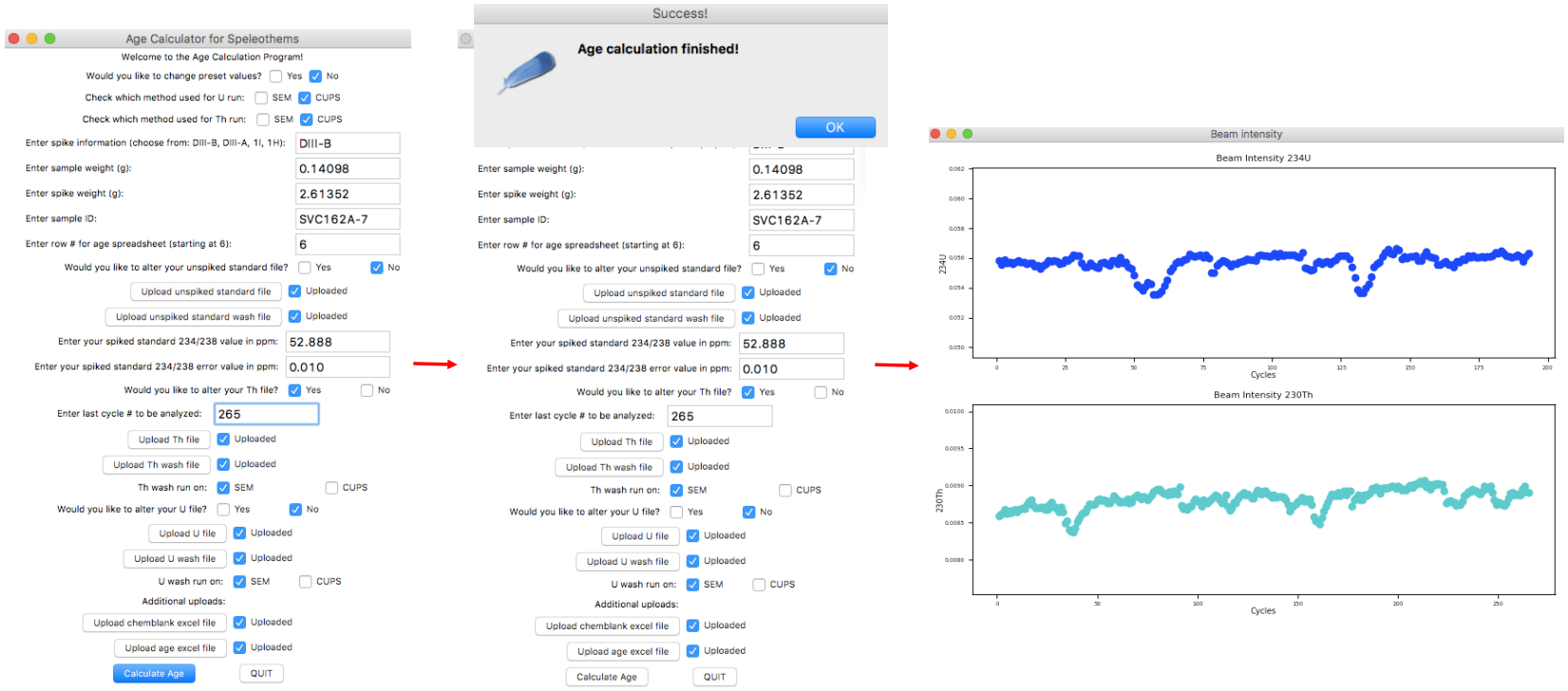

Figure B.23: Example of steps for Cups age calculation using program

As is shown in Figure B.24, the Excel spreadsheet and *Python* program provide the same output data for cups measurements.

^{230}Th dating results. The error is 2s error.

Sample Number	^{238}U (ppb)	^{232}Th (ppt)	^{230}Th / ^{232}Th (atomic x10^{-6})	d^{234}U* (measured)	^{230}Th / ^{238}U (activity)	^{230}Th Age (yr) (uncorrected)	^{230}Th Age (yr) (corrected)	d$^{234}U_{initial}$** (corrected)	^{230}Th Age (yr BP)*** (corrected)
Cups data reduction using *Python*									
SVC162A-7	4566.3 ±3.3	1315 ±1	49215 ±19	486.7 ±0.4	0.8593 ±0.0003	88695 ±58	**88691 ±58**	625 ±1	**88624 ±58**
Cups data reduction using Excel									
SVC162A-7	4566.3 ±3.3	1315 ±1	49215 ±19	486.7 ±0.4	0.8593 ±0.0003	88695 ±58	**88691 ±58**	625 ±1	**88624 ±58**

U decay constants: l238 = 1.55125x10-10 (Jaffey et al., 1971) and l234 = 2.82206x10-6 (Cheng et al., 2013). Th decay constant: l230 = 9.1705x10-6 (Cheng et al., 2013).

238U and 232Th errors include sample and spike weight errors

* d234U = ([234U/238U]activity – 1)x1000.

** d234U initial was calculated based on 230Th age (d234Uinitial = d234Umeasured * e^234T).

Corrected 230Th ages assume the initial 230Th/232Th atomic ratio of 4.4 ±2.2 x10-6. Those are the values for a material at secular equilibrium, with the bulk earth 232Th/238U value of 3.8. The errors are arbitrarily assumed to be 50%.

*** B.P. stands for "Before Present" where the "Present" is defined as the year 1950 A.D.

Figure B.24: Results of data reduction for Cups using *Python* and Excel